Multiple-Particle Positron Emission Particle Tracking (M-PEPT) and its Application to Flows in Porous Media

A Dissertation Presented for the

Doctor of Philosophy

Degree

The University of Tennessee, Knoxville

Cody Stephen Wiggins

August 2019

© by Cody Stephen Wiggins, 2019
All Rights Reserved.

To Gladys and Morris Stout and Georgia and the late George Welton Wiggins

Acknowledgments

I suppose if I were to truly thank all those who have contributed to this work, it would require a document longer than the one that follows. Nonetheless, there are many key contributors to this work whom I would be remiss not to mention.

First, thank you to my advisors, Art Ruggles and Kate Jones. Thank you for guiding me toward the completion of this work while still allowing me to wander where my curiosity has led. I appreciate the knowledge and wisdom you have imparted on me, both regarding this work and academician's life as a whole. To the remaining members of my committee, Soren Sorensen and Tony Mezzacappa, thank you for taking the time to read this document and offer your comments and criticisms. These are neither unwanted nor unnoticed and have contributed greatly to the completion of my education.

To the coworkers I have had along the way, thank you for keeping me humble and showing me the ways in which I err and must rely on the help of others. Mark, I'll never forget our days driving a U-Haul to Texas and my earliest crash-courses in jet mixing studies. Ridley, I think fondly on our time building test sections and spilling their contents while discussing the prior day's MLB outcomes. While I'll likely never be a fan, I'll always have a soft spot for the Detroit Tigers. Seth, thank you for having an imagination that often dwarfs my own and not backing down from the challenge of the impossible. Many facets of this work would have never happened without your willingness to try. Eric, thank you for taking the time to crawl through the caverns of my M-PEPT code and tactfully exposing the flaws therein. Nitant, thank you for maintaining your cheery disposition, even when the toughest times were upon our group. You are truly one of the hardest and most persevering workers I have ever encountered. Roque, thank you for keeping a smile on my face and being willing to battle the beast of GATE when others of us cowered away. Sarah and Emily, thank you for

being the radiochemists I could not be and giving us reasonable hope for the next generation of PEPT tracers. Finally, Zach and Matthew, thank you for your hard work in the last days of our group. Your assistance in conducting the experiments described herein was invaluable.

To the many other professionals who have offered their time and talents to this work and my development, thank you. Diego, thank you for our conversations on the many directions that PEPT could be taken. Your ideas inspired the experiments conducted in this work and opened my mind to the strange world of anomalous transport. Alan, you have been one of the most instrumental contributors to the development of PEPT at the University of Tennessee. Thank you for your flexibility and for gifting us your time and the use of your facilities. In more recent days, thank you for the ways in which you have educated us and assisted us with our first attempts at preclinical imaging. Marsha, Eddie, and Shawn, thank you for helping us to work safely and efficiently and always being willing to assist us with radiation transport. Scott and Ashly, thank you for taking care of the many technical needs of the Nuclear Engineering Department. Chrisanne, thank you for always be willing to answer the many questions I have asked and providing me the resources necessary to navigate graduate school. Melinda and Sarah, thank you for your patience and diligence in my introduction to the field of microbiology. That is a world that I never guessed I would enter, but now it seems that PEPT is destined to make its mark therein. Chris, thank you for exposing me to new ways to study the world of fluid dynamics, both experimental and theoretical. I must also thank Matthew Francis for first introducing a high school student from East Tennessee to nuclear engineering and starting me down the path I have walked these years.

My last words of gratitude are offered to my friends and family who have been with me during both the joys and hardships of this work. To those with whom I have lived, thank you for putting up with my absences and the many times I have neglected household chores in the name of research. To my friends, thank you for staying my friends in spite of all the times I have had to say "no" and rescind my "yes" to your invitations. To those with whom I worship, thank you for your prayers and your warm spirits during the tenure of this work. To my grandparents, thank you for your years of care and concern for me. To my sister, thank you for always being a person I could look up to and strive to be like. To my

parents, thank you for providing the foundations of your own intellect and wisdom for the construction of my education. Thank you for instilling in me a desire to learn and always supporting me in my academic pursuits. Lastly, to Rachel, thank you for bearing with me during the doldrums of this work and rejoicing with me in the times of discovery and elation. Thank you for unconditionally loving and supporting me even when I seem neither lovable nor supportable. I look forward to our life together.

Abstract

Positron emission particle tracking (PEPT) is a method for flow interrogation capable of measurement in opaque systems. In this work a novel method for PEPT is introduced that allows for simultaneous tracking of multiple tracers. This method (M-PEPT) is adapted from optical particle tracking techniques and is designed to track an arbitrary number of positron-emitting tracer-particles entering and leaving the field of view of a detector array. M-PEPT is described, and its applicability is demonstrated for a number of measurements ranging from turbulent shear flow interrogation to cell migration. It is found that this method can locate over 80 particles simultaneously with spatial resolution of order 0.2 mm at tracking frequency of 10 Hz and, at lower particle number densities, can achieve similar spatial resolution at tracking frequency 1000 Hz. The method is limited in its ability to resolve particles approaching close to one another, and suggestions for future improvements are made.

M-PEPT is used to study flow in porous media constructed from packing of glass beads of different diameters. Anomalous (i.e. non-Fickian) dispersion of tracers is studied in these systems under the continuous time random walk (CTRW) paradigm. Pore-length transition time distributions are measured, and it is found that in all cases, these distributions indicate the presence of long waiting times between transitions, confirming the central assumption of the CTRW model. All systems demonstrate non-Fickian spreading of tracers at early and intermediate times with a late time recovery of Fickian dispersion, but a clear link between transition time distributions and tracer spreading is not made. Velocity increment statistics are examined, and it is found that temporal velocity increments in the mean-flow direction show a universal scaling. Spatial velocity increments also appear to collapse to a similar form, but there is insufficient data to determine the presence of universal scaling.

Table of Contents

1 Introduction **1**

2 Background **3**

2.1 PEPT . . . 3

2.1.1 Reconstruction Methods . . . 5

2.1.2 Applications . . . 8

2.1.3 Radiotracers . . . 10

2.1.4 Detectors . . . 12

2.2 Porous Media Flows . . . 14

2.2.1 Continuous Time Random Walk (CTRW) Theory . . . 15

2.2.2 CTRW Experiments . . . 19

2.2.3 Particle Tracking Experiments . . . 22

3 Multiple-Particle PEPT Development **24**

3.1 G-means . . . 25

3.1.1 G-means Clustering . . . 25

3.1.2 G-means example . . . 27

3.1.3 G-means Tests . . . 29

3.1.4 G-Means Drawback . . . 32

3.2 Feature Point Identification . . . 32

3.2.1 Comparison to G-means . . . 36

3.2.2 GATE Simulation Testing . . . 39

3.2.3 Moving Particle Test . . . 44

3.3 Trajectory Linking 48

4 M-PEPT Measurements **53**

4.1 Rectangular Channel 53

4.2 Twisted Tape Swirled Flow 55

4.2.1 Twisted Tape Experiment 56

4.2.2 Results 57

4.3 Turbulent Pipe Flow 60

4.3.1 Pipe Flow Experiment 60

4.3.2 Results 62

4.4 Yeast Cell Tracking 70

4.4.1 Cell Tracking Experiment 71

4.4.2 Results 72

5 Description of Experiment **76**

5.1 PET Scanner 76

5.2 Tracer Particles 84

5.3 Flow Loop and Test Section 87

5.4 Experimental Procedures 96

5.5 Experimental Conditions 101

6 Data Handling **103**

6.1 M-PEPT Reconstruction 103

6.2 Dewarping 105

6.3 Filtering 110

7 Results **115**

7.1 Reconstruction Results 115

7.2 Velocity and Acceleration Statistics 122

7.2.1 Radial Profiles 122

7.2.2 Probability Density Functions 130

7.3 Displacement Statistics 137

7.3.1 CTRW Transition Probability . . . 137
7.3.2 Mean-Squared Displacement . . . 143
7.4 Velocity Correlations . . . 151
7.4.1 Autocorrelation . . . 151
7.4.2 Lagrangian Structure Functions . . . 158
7.4.3 Eulerian Structure Functions . . . 168

8 Discussion and Conclusion **175**
8.1 PEPT Discussion . . . 175
8.2 Porous Media Discussion . . . 181
8.3 Concluding Remarks . . . 184

Bibliography **186**

Appendices **200**
A Other M-PEPT Experiments . . . 201
A.1 Channel with Baffle Plates . . . 201
A.2 Heat Exchanger . . . 203
A.3 Pulsatile Flow . . . 205
B Particle Activation Procedure . . . 209
C Experimental Procedure . . . 213

Vita **220**

List of Tables

2.1 Information on common positron-emitters 10

3.1 A comparison of results obtained for simulated multiple particle tracking using G-Means and FPI methods. 41

4.1 Flow conditions for PEPT pipe flow experiment. 61

5.1 Physical specifications of each test section. 93
5.2 Summary of designed conditions for packed bed experiments. 102
5.3 Summary of activity of tracers used for packed bed experiments. 102

6.1 Summary of reconstruction parameters used for each experiment. 104
6.2 Summary of the linking parameters used for each experiment. 105

7.1 Summary of reconstruction results for porous media experiments. 116
7.2 Average estimated uncertainty and number of coincidence lines (CL) used for detection in each experiment. 122
7.3 Measured flow conditions for $r < 20$ mm for each packed bed experiment. . . 129
7.4 Fitted parameters for stretched exponential fit for x-acceleration. 136
7.5 Fitted parameters for stretched exponential fit for y-acceleration. 136
7.6 Fitted parameters for stretched exponential fit for z-acceleration. 136
7.7 Fitted values of scaling exponent β in CTRW transition probability for each packed bed experiment. 143
7.8 Uncertainty values in each spatial direction for each experiment determined from correction to autocorrelation and Lagrangian velocity structure function. 154

7.9 Integral time scales measured in packed bed experiments. 158

List of Figures

2.1 Visual description of PEPT process. 4
2.2 "Cutpoint" showing 2-D histogram of CL projections 7
2.3 Experimental setup for measuring flow in dishwasher via PEPT 9
2.4 Uptake of ^{18}F by anion exchange resins over time. 12
2.5 ECAT EXACT3D PET scanner housed at PEPT Cape Town 13
2.6 Modular detectors used for PEPT at Birmingham 14
2.7 Schematic representation of differences between normal and anomalous transport. 19
2.8 Experimental setup of flow cell with uniformly heterogeneous packing. 21
2.9 Packing of flow cell with exponentially correlated structure. 22
2.10 PDFs of longitudinal and transverse Lagrangian velocity and acceleration components measured by Holzner et al. 23

3.1 Visual representation of G-means algorithm. 28
3.2 Trajectories measured by PEPT with 17 particles in a polyethylene phantom. 30
3.3 Trajectories measured by PEPT for single particle making eight passes through the bore of the scanner. 31
3.4 Flow chart of PEPT with FPI M-PEPT processing. 33
3.5 Pixel-locking defect. 37
3.6 Particle trajectories calculated from 17 particle dataset using 25 ms time steps with G-means and FPI. 38
3.7 Geometry of GATE model of Siemens Inveon PET scanner. 40

3.8 Particle positions from 100 particle GATE simulation as measured by G-means (a) and FPI (b) methods. 42
3.9 Location accuracy variation with inverse square root of average number of CL used in each time step for multiple particle measurements with FPI. 43
3.10 Trajectories measured in rotating particle experiments. 45
3.11 Measured acceleration, velocity, and filtered position of particle 1 in rotating particle experiment with sinusoidal trend line. 47
3.12 Example of re-linking step. 52

4.1 Rectangular test section as seen from perspective view and in the bore of the P4 scanner. 54
4.2 Trajectories of particles in rectangular test section measured using PEPT. . 55
4.3 Histograms of particle velocity measured in rectangular channel via PEPT and PTV. 56
4.4 Photograph of twisted tape insert. 57
4.5 First 500 trajectories measured in twisted tape experiment. 58
4.6 Axial velocity contour plot at 20D and 30D. 59
4.7 Radial velocity at 20D and 30D with streamlines overlaid. 59
4.8 First 500 trajectories measured via PEPT in pipe flow experiment before and after dewarping and filtering. 63
4.9 Comparison of mean axial velocity measured with PEPT to that of DNS of El Khuory et al. and Wu and Moin. 64
4.10 Comparison of Reynolds stresses measured with PEPT to those of DNS of El Khuory et al. and Wu and Moin. 65
4.11 Comparison of turbulent kinetic energy budget measured with PEPT (symbols) to that of DNS of El Khuory et al. 67
4.12 Comparison of mean acceleration measured with PEPT to that of DNS of Stelzenmuller et al. 68
4.13 Comparison of mean-squared fluctuation of acceleration measured with PEPT to that of DNS of Stelzenmuller et al. 69

4.14 3D trajectories of yeast cells measured via PEPT in the first cell tracking experiment. 73
4.15 Images from first minute of yeast tracking experiment with images at same axial position from first minute of background scan for comparison. 74

5.1 Side and front views of Inveon PET scanner with measured dimensions. . . . 77
5.2 Block diagram of architecture employed by Siemens Inveon. 78
5.3 Photograph of detector used in Siemens Inveon. 78
5.4 Coupling of crystals to light guide in Siemens Inveon. 79
5.5 Block diagram of event routing within FPGA of Siemens Inveon. 80
5.6 Example of window used for Inveon detector setup. 82
5.7 Sensitivity profile of Siemens Inveon recorded using ^{22}Na point source with 425-625 keV energy window. 83
5.8 Noise Equivalent Count Rate for Siemens Inveon measured for two different phantom sizes. 84
5.9 Scanning electron microscope image of anion exchange resin bead. 85
5.10 Photograph of activation equipment in fume hood at UTMC. 86
5.11 Adsorption kinetics of ^{18}F in sample of resin beads. 87
5.12 Diagram of flow loop employed in packed bed experiments. 88
5.13 Photograph of pump head with 2-stop tubing. 89
5.14 Drawing of tube used for packed bed test section. 90
5.15 Size of smallest pore throat created by packing of beads and comparison to tracer particles. 92
5.16 Photograph of test section packing. 93
5.17 Image of dye test performed with 2 mm bead test section. 95
5.18 Photograph of 2, 4, 8 mm bead packed test section with labels. 95
5.19 Photograph of assembled flow loop in bore of Inveon PET scanner. 98
5.20 Final assembly of flow loop in PET scanner with shielding in place. 99

6.1 Radial astigmatism defect for imaging sources near radial edge of PET scanner. 106
6.2 Point source and positioning system used to generate dewarping map. 108

6.3 Comparison of M-PEPT reconstructed positions before and after dewarping to real positions for point source location in Siemens Inveon. 109
6.4 xy-projection of trajectories reconstructed from first 30 minutes of experiment 2_ReMid. 111
6.5 Plots of velocity and acceleration versus filter width for experiment 2_ReMid. 113
6.6 Comparison of unfiltered and filtered position time series for two subsets of two trajectories from case 2_ReMid. 114

7.1 Filtered trajectories from experiment 2_ReLow, colored according to velocity magnitude. 117
7.2 First 200 filtered trajectories from experiment 2_ReMid, colored according to velocity magnitude. 118
7.3 First 200 filtered trajectories from experiment 2_ReHigh, colored according to velocity magnitude. 119
7.4 First 200 filtered trajectories from experiment 2,4_ReMid, colored according to velocity magnitude. 120
7.5 First 200 filtered trajectories from experiment 2,4,8_ReMid, colored according to velocity magnitude. 121
7.6 Variation of measured uncertainty with axial (z-) position for case 2_ReMid. 123
7.7 Velocity and acceleration profiles from experiment 2_ReLow. 124
7.8 Velocity and acceleration profiles from experiment 2_ReMid. 125
7.9 Velocity and acceleration profiles from experiment 2_ReHigh. 126
7.10 Velocity and acceleration profiles from experiment 2,4_ReMid. 127
7.11 Velocity and acceleration profiles from experiment 2,4,8_ReMid. 128
7.12 Comparison of velocity probability density functions for all 2 mm cases. . . . 131
7.13 Comparison of velocity probability density functions for all ReMid cases. . . 132
7.14 Comparison of acceleration probability density functions with stretched exponential fits for all 2 mm cases. 134
7.15 Comparison of acceleration probability density functions with stretched exponential fits for all ReMid cases. 135

7.16 Transition probability distributions measured in experiment 2_ReLow with exponential fits to late-time tails. 138
7.17 Transition probability distributions measured in experiment 2_ReMid with exponential fits to late-time tails. 139
7.18 Transition probability distributions measured in experiment 2_ReHigh with exponential fits to late-time tails. 140
7.19 Transition probability distributions measured in experiment 2,4_ReMid with exponential fits to late-time tails. 141
7.20 Transition probability distributions measured in experiment 2,4,8_ReMid with exponential fits to late-time tails. 142
7.21 Correction to mean-squared displacement caused by correlated uncertainties. 145
7.22 Mean-squared displacement curves for case 2_ReLow with different exponential scalings shown. 146
7.23 Mean-squared displacement curves for case 2_ReMid with different exponential scalings shown. 147
7.24 Mean-squared displacement curves for case 2_ReHigh with different exponential scalings shown. 148
7.25 Mean-squared displacement curves for case 2,4_ReMid with different exponential scalings shown. 149
7.26 Mean-squared displacement curves for case 2,4,8_ReMid with different exponential scalings shown. 150
7.27 Correction to velocity autocorrelation caused by correlated uncertainties. . . 152
7.28 Velocity autocorrelation curves of 2_ReMid case before and after correction for correlated uncertainties. 153
7.29 Measured x-velocity autocorrelation curves for all packed bed experiments. . 155
7.30 Measured y-velocity autocorrelation curves for all packed bed experiments. . 156
7.31 Measured z-velocity autocorrelation curves for all packed bed experiments. . 157
7.32 Correction to Lagrangian velocity structure function caused by correlated uncertainties. 159

7.33 Lagrangian velocity structure functions of 2_ReMid case before and after correction for correlated uncertainties. 160
7.34 Measured x-direction Lagrangian velocity structure functions with $\tau^{1/4}$ scaling for comparison. 161
7.35 Measured y-direction Lagrangian velocity structure functions with $\tau^{1/4}$ scaling for comparison. 162
7.36 Measured z-direction Lagrangian velocity structure functions with $\tau^{1/2}$ scaling for comparison. 163
7.37 Measured x-direction Lagrangian velocity structure functions compensated by $(\tau^{1/4} v_x'^{9/4} d_{bead}^{-1/4})$. 165
7.38 Measured y-direction Lagrangian velocity structure functions compensated by $(\tau^{1/4} v_y'^{9/4} d_{bead}^{-1/4})$. 166
7.39 Measured z-direction Lagrangian velocity structure functions compensated by $(\tau^{1/2} v_z^{5/2} d_{bead}^{-1/2})$. 167
7.40 Measured longitudinal Eulerian velocity structure functions with $r^{2/3}$ scaling for comparison. 170
7.41 Measured transverse Eulerian velocity structure functions with $r^{1/3}$ scaling for comparison. 171
7.42 Longitudinal Eulerian velocity structure functions compensated by $(r^{2/3} \bar{v'}^2 d_{bead}^{-2/3})$. 172
7.43 Transverse Eulerian velocity structure functions compensated by $(r^{1/3} \bar{v'}^2 d_{bead}^{-1/3})$. 173

8.1 Axial frame from smoothed CL grid showing images of close particles. 177
8.2 All possible combinations of coincidence lines for a single axial slice of a ring-type PET scanner with 24 detector elements. 178
A.1 Test section region of interest in baffle flow experiment. 202
A.2 Trajectories of particles in baffle induced flow. 202
A.3 Time-averaged downstream velocity measured via PEPT and PTV in baffle flow experiment. 203
A.4 Photograph of stainless steel heat exchanger studied via PEPT. 204

A.5 Trajectories measured in heat exchanger experiment, colored by downstream velocity. 204
A.6 Elastic tube pinched with spring clamp in pulsatile flow experiment. 206
A.7 Trajectories from three frames of pulse cycle from open geometry pulsatile flow experiment, colored by downstream velocity. 207
A.8 Trajectories from three frames of pulse cycle from pinched geometry pulsatile flow experiment, colored by downstream velocity. 208

Nomenclature

β Late-time scaling exponent of CTRW transition time distribution

$\psi(\mathbf{s}, t)$ CTRW transition probability distribution

$\rho(\tau)$ Lagrangian velocity autocorrelation

d_{bead} Average bead diameter for packed bed test section

$D_{ii}(\tau)$ 2nd-order Lagrangian velocity structure function in the i-direction

$D_{LL}(r)$ 2nd-order longitudinal Eulerian velocity structure function

$D_{NN}(r)$ 2nd-order transverse Eulerian velocity structure function

Re Reynolds Number

t^* Average bead transit time for packed bed test section

$t_{1/2}$ Half-life

A-D Anderson-Darling

ADC Analog-to-digital converter

ADE Advection-Diffusion Equation

BGO Bismuth germanate

CL Coincidence line(s)

CLT Crystal Lookup table

CTRW Continuous time random walk

DI Deionized

DNS Direct numerical simulation

EPM Event processing module

FOV Field of view

FPGA Field programmable gate array

FPI Feature point identification

FPTD First pass time distribution

LSO Lutetium oxyorthosilicate

M-PEPT Multiple-particle positron emission particle tracking

MSD Mean-Squared Displacement

NECR Noise equivalent count rate

PDF Probability Density Function

PEPT positron emission particle tracking

PET Positron emission tomography

PSPMT Position-sensitive photomultiplier tube

RMS Root mean square

SERF Science and Engineering Research Facility

TKE Turbulent kinetic energy

UTK University of Tennessee, Knoxville

UTMC University of Tennessee Medical Center

Chapter 1

Introduction

A complete understanding of the phenomenology of fluid flow remains an outstanding question in the world of physics. While the Navier-Stokes equations, the equations governing the motion of fluids, have been known for nearly 200 years, these equations have proven difficult, and perhaps even impossible, to solve. The computational scaling of direct numerical simulations (DNS) of the Navier-Stokes equations often makes DNS impractical for complex and high Reynolds number flow. As such, simplified models of fluid flow are often employed, and these require proper validation via experiment.

In many cases, flows of interest lack optical access, either due to system geometry or the nature of the flowing medium. These systems are often prohibitively difficult to study via optical imaging methods, as they require either the use of surrogate materials and fluids or significant alteration of the system with subsequent inference of any quantities of interest. A number of experimental methods have been proposed that do not require optical access to the fluid, including methods based on ultrasonics [1], magnetic resonance [2], and radiography [3, 4]. Among these, positron emission particle tracking (PEPT) is a means of assessing fluid flow by recording the trajectories of radiolabelled fluid tracers in the system. This method revolves around the detection of 511 keV gamma rays and does not require the use of transparent materials.

Study of flows in porous media suffers from the drawback of lack of optical access, and measurements are often limited to bulk flow properties at the large scales of the flow that neglect flow phenomena at the pore scale or small scale flow properties that neglect

longer range correlations. It has been seen in a number of porous flows that these systems often exhibit anomalous dispersion in which the spreading of concentrations does not fall in line with that predicted by Fick's law (see Section 2.2). A proper understanding of this dispersion phenomenon is needed for modeling of dispersive processes in groundwater transport, petroleum recovery, transmission through building material, and movement in chemical reactors, among others [5]. Models that view dispersion as the continuum limit of single-particle processes require particle tracking data for validation. As such, PEPT is a prime candidate for interrogation of porous media flows. However, previous PEPT methods have been limited to tracking one to a few particles simultaneously. This both inhibits the data collection rate of PEPT for single particle statistics and prevents the use of PEPT for multiple-position, same-time measurements of the flow.

In this work, methods for multiple-particle positron emission particle tracking (M-PEPT) are presented and explored. These are shown to have similar spatiotemporal resolution to previous PEPT methods and are employed to study a number of apparatuses. Using these novel techniques, porous media flows are studied to determine a connection between single particle statistics and anomalous dispersion.

This dissertation will first discuss past methods for PEPT and studies of porous media flows (Chapter 2). Novel M-PEPT methods will be discussed (Chapter 3), including examples of experiments performed with M-PEPT (Chapter 4). An experiment to study single-particle statistics in PM flows is described, including details of experimental set-up and procedures (Chapter 5) and data handling (Chapter 6). The results of this experiment are then presented (Chapter 7), and the outcomes of this work are discussed (Chapter 8).

Chapter 2

Background

2.1 PEPT

Positron emission particle tracking was first proposed in a patent by Robert Shaw in 1984 [6]. He envisioned PEPT as means for measuring blood flow around the heart; however, this has proven prohibitively difficult. Instead, PEPT has become a tool used for imaging of flows for a number of chemical and industrial applications, with only a few biological applications demonstrated.

Similar to its predecessor, positron emission tomography (PET), PEPT relies on using the detection of the coincident gamma rays produced by positron-election annihilation as a means of determining the distribution of a radioisotope. The basic principle of PEPT is described graphically in Figure 2.1. A tracer particle is labelled with a positron- (e^+-) emitting radioisotope. This tracer is then introduced to the fluid of interest, and a detector array is placed around the flow apparatus. As the tracer moves with the fluid, emitted positrons annihilate with nearby electrons, and this annihilation event produces back-to-back coincident gamma rays of energy 511 keV that are detected by the detector array. Coincidence lines (CL) are drawn between the detection sites of coincident gamma rays, and a time series of CL is examined to determine the position of the tracer. Tracer positions from individual time steps can then be linked in to continuous particle trajectories.

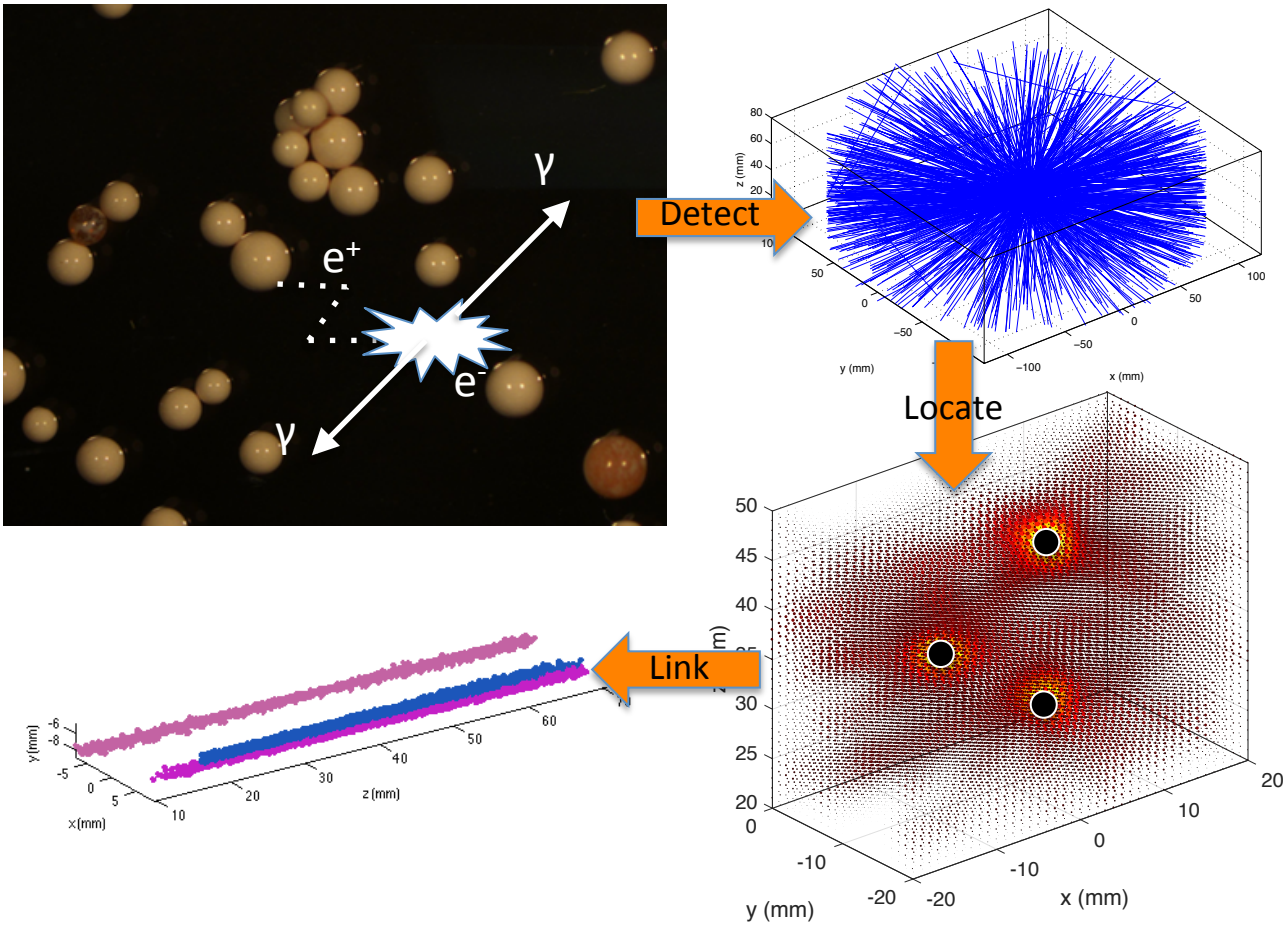

Figure 2.1: Visual description of PEPT process. (Clockwise from top-left) Radiolabelled tracer particles are introduced to a flowing media. Positrons annihilate near tracers and produces back-to-back gamma rays that are detected by a detector array. CL are drawn between detection sites and used to locate particles at different time steps. Particle positions from individual time steps are then linked into trajectories.

2.1.1 Reconstruction Methods

The processes used for the reconstruction of tracer position from CL have seen some evolution since the inception of PEPT, with the majority of PEPT reconstruction being done with one of three methods: the Birmingham method, the Bergen method, and the Cape Town method. These are named herein for the university at which they were developed and are detailed below. New methods have been developed that will be described and used later in this work.

Birmingham Method

The oldest and most prominent method for PEPT reconstruction is the Birmingham Method of Parker et al. [7], developed at the University of Birmingham in the United Kingdom. This and other methods work under the assumption that uncorrupted coincident gamma rays should form a cluster of CL in the near vicinity of the tracer particle. As such, an iterative method is used to localized the tracer particle.

CL are considered in sets, S, of N events, constituting a single time step for reconstruction. A least squares minimization is then used to determine the point in space, $m(S)$, that minimizes the sum, $D(S)$, of distances to all events in S,

$$D(S) = \sum_{D} \delta_i(m), \tag{2.1}$$

where $\delta_i(m)$ is the distance from the ith CL to a point m. It is then assumed that the events farthest away from m_S are from corrupt gamma rays or false coincidences, so those greater than $k \times d(S)$ are removed from the set S. Here, k is a fixed parameter set by the user (usually between 1 and 1.5) and $d(S)$ is the average distance between $m(S)$ and all CL in S. The point $m(S)$ is then recalculated, and the process is repeated iteratively until only some fraction f of the original N CL remains. This final $m(S_F)$ calculated from the reduced set S_F is then taken to be the position of the tracer and the time of detection is taken to be

$$t = \sum_{S_F} t_i, \tag{2.2}$$

where t_i is the time of detection of the ith CL. The uncertainty of the tracer position is seen to vary as $1/\sqrt{fN}$, so the parameters f and N must be set large enough to collect sufficient CL for detection and small enough to reject noise from corrupt CL and reduce smearing of the CL distribution by particle motion. This means that f should be set lower for data sets in which more scatter is anticipated (i.e. measurements in dense, high-Z materials), and N should be set lower for faster flows.

This method has primarily been employed for studies using only one tracer particle; however, a multiple particle variant has been developed by Yang et al. [8]. This method was used to track up to three particles of significantly different activities (ratio 1:2:4). The previously described Birmingham method is used to first isolate the particle having the highest activity, and the final set of CL associated with this particle are then neglected, and the process is repeated to find the particle of the second highest activity and subsequently repeated to find the third. In this way, an ordering is established so that the three particles are easily distinguished, and detections of particles in each time step are linked into trajectories. This method requires that the number of particles in the system is known, and the need for particles of very different activities limits the number of particles that can be tracked simultaneously. The lowest activity particle must be active enough to be accurately triangulated, while the total activity in the detector field of view must be low enough to prevent saturating the detectors.

Bergen Method

The method for PEPT reconstruction employed at the University of Bergen, Norway examines 2-D "cutpoints" of CL in evenly divided time steps [9]. CL from a time step are projected onto a 2-D plane, and the number of line crossings is binned in a 2-D grid, as seen in Figure 2.2. The position of the particle in these two dimensions is calculated by a weighted averaging of these bins and an iterative reduction of the window size. A final window size of 16×16 mm^2 is seen to produce results with the lowest standard deviation, based on the imaging of a stationary particle across $\mathcal{O}(10^6)$ detections. The position of the particle in the third dimension is found via the same 2-D cutpoint triangulation in an

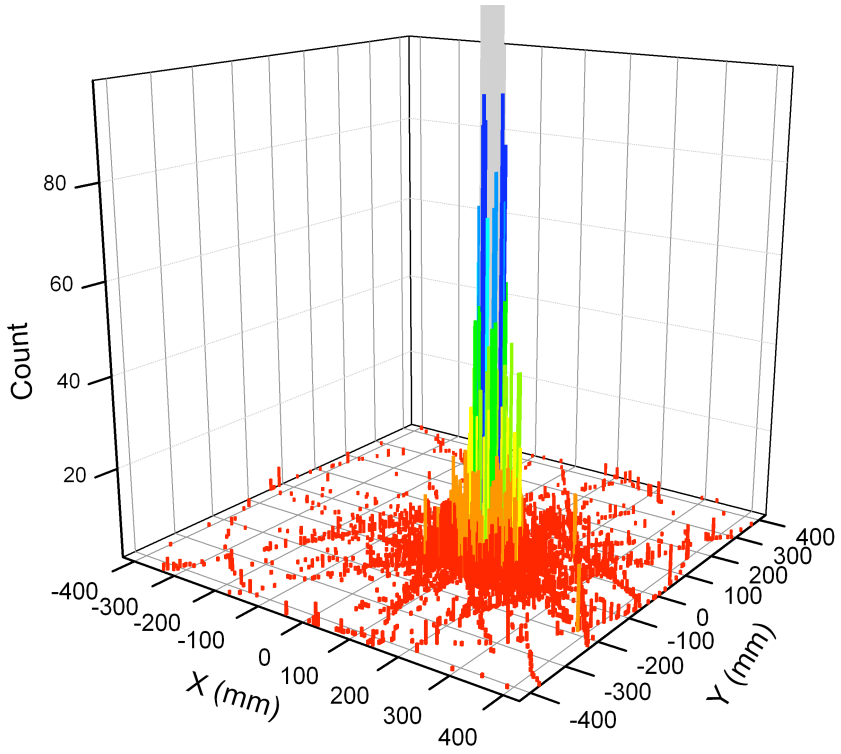

Figure 2.2: "Cutpoint" showing 2-D histogram of CL projections [9].

orthogonal plane. Similar to the Birmingham method, the precision afforded by the Bergen method depends on the number of CL used for reconstruction.

To the author's knowledge, this method has only been used for single-particle PEPT, but it warrants mentioning that this method has achieved the highest spatial resolution cited in literature for a PEPT system. Using ion exchange resin beads of size 560-700 μm and activity $\sim$1 mCi, Chang and Hoffman [10] cited positioning uncertainties of less than 100 μm in each spatial direction; however, the flow conditions and temporal resolution under which this was achieved were not reported.

Cape Town Method

The method of Bickell et al. [11] was developed at the University of Cape Town, South Africa and works similarly to the Bergen method in that it relies on the tracing of CL from a given time step onto a grid; however, this method traces CL onto a 3-D grid. Once this "line density" grid is constructed, the grid element having the greatest line crossing value is

identified, and the particle's position is found via 1-D Gaussian fits across each dimension of the grid, centered on this maximum. For single-particle studies, this method was shown to be of similar accuracy to the Birmingham method.

This method was also extended to multiple-particle tracking in the case that the number and initial positions of the particles are known *a priori*. The initial particle positions are used as inputs for the reconstruction, and the algorithm only searches for maxima in the line-crossing grid in the neighborhood of these inputs. Particle positions are then calculated via the same 1-D Gaussian fitting routine described previously, and these positions are used as inputs for the local maxima search in the next time step, allowing tracking of multiple particles over multiple time steps. This method was shown to be capable of tracking up to 16 particles.

2.1.2 Applications

PEPT has seen great use for interrogating flows lacking optical access. The majority of these works have used the Birmingham method. Wildman et al. [12] used PEPT to study grain motion in vibrating granular beds. Chiti et al. [13] studied flow around a Rushton turbine. Griffiths et al. [14] studied the movement of inclusions in castings of low melting point alloys. Mihailova et al. [15] used PEPT and magnetic resonance imaging to examine flow in a static mixer. Pérez-Mohedano et al. [16] studied flow in a commercial dishwasher to examine periodic flow throughout the washing cycle. Figure 2.3 shows this experimental set-up, with the dishwasher being placed in the field of view of the two-panel PEPT camera used at the University of Birmingham. Boucher et al. [17] studied size and density effects on particle trajectories in an iron-ore slurry flow. A recent work by Parker [18] offers a review on the applications of PEPT for studies in granular media. The M-PEPT method of Yang et al. [8] has been used to study the tumbling of cubed potatoes in rotating cans [19].

At the University of Cape Town, the majority of PEPT measurements have also been conducted using the Birmingham method. Volkwyn et al. [20] studied particle motion in tumbling mills as a tool for quantifying PEPT uncertainty as a function of tracer activity. Morrison et al. [21] further looked at the effect of rotation speed on particle residence times and bed shapes in rotating drums.



Figure 2.3: Experimental setup for measuring flow in dishwasher via PEPT [16]. Shown is commercial dishwasher between parallel plate detectors.

The Bergen method has been used for studying flows in processing equipment. Chang et al. [9] studied flow in a hydrocyclone via PEPT, and Chang et al. [22] later used PEPT as a means of validating computational fluid dynamics (CFD) models of hydrocyclone flow. Chang and Hoffman [10] later used PEPT to study the effect of inlet velocity on particle radial and tangential velocity in a hydrocylcone. Balakin et al. [23] studied the effects of flow straighteners on particle trajectories in a pneumatic conveying system.

The demonstrated applications of PEPT to biological research have been limited. In a Master's thesis from the University of Birmingham, Chou [24] investigated the feasibility of radiolabelling red blood cells with ^{11}C and subsequently tracking them via PEPT. He found that due to a low specific activity of the radioisotope and inefficiency of the labelling technique employed, this was not feasible. Lee et al. [25] used simulations to study the efficacy of *in vivo* single-cell tracking for an arbitrary activated cell using a modified version of the Birmingham method with B-spline fitting of CL positions to trajectories. They demonstrated that cell tracking is possible given the proper balance of cell activity and movement speed but is unlikely using detectors made of lutetium oxyorthosilicate (LSO)

Table 2.1: Information on common positron-emitters. Mean and maximum positron energy (E) and range (R) of positrons in water are given. Data are compiled from [27, 28].

Isotope	$T_{1/2}$	E_{mean} (keV)	E_{max} (keV)	R_{mean} (mm)	R_{max} (mm)
^{18}F	109.8 min.	252	635	0.66	2.6
^{11}C	20.3 min.	390	970	1.1	4.5
^{22}Na	2.6 yr.	220	674	0.53	2.3
^{64}Cu	12.7 h.	278	653	0.56	2.9
^{68}Ga	68 min.	844	1899	3.6	10.3

due to the background decay of ^{176}Lu. Later, Ouyang et al. [26] demonstrated the feasibility of single-cell tracking with PEPT using bismuth germanate (BGO) detectors.

2.1.3 Radiotracers

PEPT relies on the use of positron-emitting radioisotopes. Table 2.1 contains information on the most common isotopes used for PEPT. When selecting an isotope for measurement, it is desired that the half-life, $t_{1/2}$, of the isotope is long enough to allow for sufficient data collection, but short enough to prevent prolonged contamination of test equipment. As the activity, A, of a particle is

$$A = \frac{ln(2)}{t_{1/2}} N, \tag{2.3}$$

where N is the number of atoms of the radioisotope attached to a particle, it is also desired that half-life be short enough to allow sufficient activity for tracking. A short positron range is beneficial to PEPT reconstruction, as it leads to a more localized cluster of CL around each tracer. ^{18}F is the most commonly used isotope for PEPT, due to its intermediate half-life of 110 min., short positron range, and the fact that it emits no gamma rays in its decay chain that could cause false coincidence detections with the desired 511 keV annihilation photons. Tracer activation is performed by either direct or indirect methods.

In direct activation, the tracer particle itself consists of the positron-emitting radioisotope. In this way, it can be viewed as a volumetric activation. Often direct activation is performed via the irradiation of a stable sample. For example, particles containing oxygen

compounds can be activated via irradiation by a ^{3}He beam through the reactions

$$^{16}O(^{3}He, p)^{18}F \tag{2.4}$$

and

$$^{16}O(^{3}He, n)^{18}Ne \rightarrow {}^{18}F. \tag{2.5}$$

Through direct activation, particles of size larger than 1 mm can be produced [29, 30]. The amount of activity that can be achieved in a particle is a function of the beam current, the particle size, and the irradiation time. It is found that the activity is proportional to the diameter-squared of the particle, i.e. proportional to its cross-sectional area. Current and irradiation time must be great enough to sufficiently activate a particle but low enough to prevent physical damage of the particle.

Indirect activation is performed through chemical means, in which a radioisotope is attached to a non-radioactive particle, usually through ion-exchange techniques. Anion exchange resins can be labelled with ionic ^{18}F, and cation exchange resins can be labelled with ^{61}Cu and ^{66}Ga [30]. Both weak and strong base anion exchange resins can be used for adsorption of ^{18}F, but uptake is greatly affected by solution pH for weak bases. For this reason, strong base anion exchange resins are more commonly used for PEPT [29, 30].

The affinity subsequence for anions to a strong base exchange resin is as follows:

$$SO_4^{2-} > HSO_4^- > I^- > NO_3^- > Br^- > Cl^- > HCO_3^- > HSiO_3^- > F^- > OH^-. \tag{2.6}$$

The first implication of this is that hydroxide-form (OH-form) resins must be used for the uptake of ^{18}F to occur. If chloride-form resins are used, conversion to hydroxide-form must be performed before activation with ^{18}F can be done. Furthermore, this affinity subsequence implies the necessity to work in a medium without any free anions during both activation and experiment. Figure 2.4 shows the effect of free Cl^- and CO_3^{2-} on ^{18}F uptake during activation. Here it can be seen that presence of free anions greatly cripples the ability of the resin to uptake ^{18}F [29, 30].

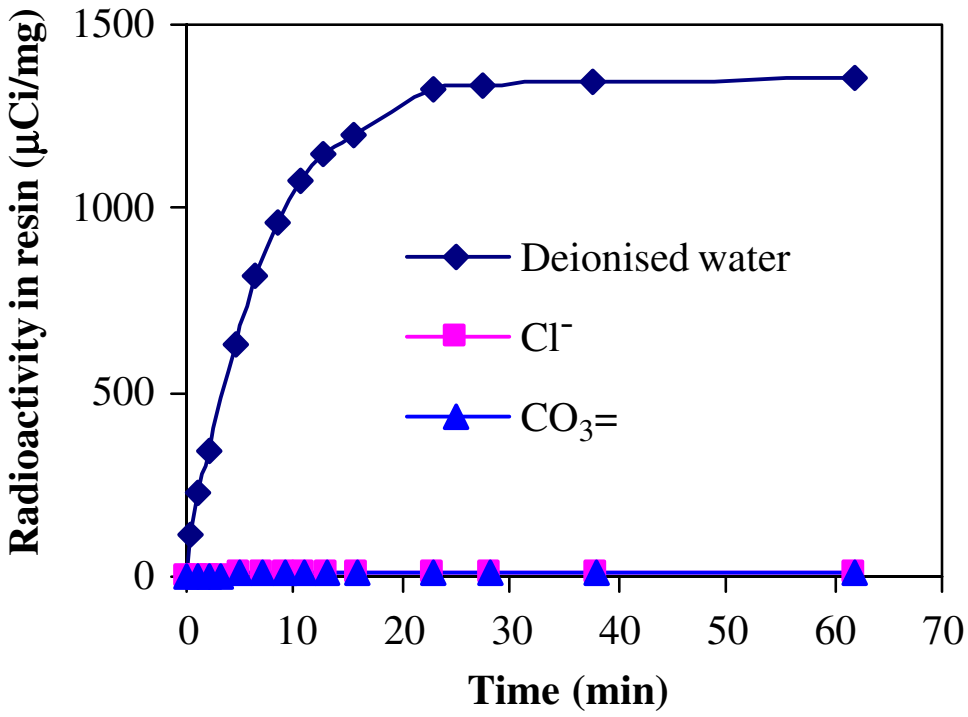

Figure 2.4: Uptake of ^{18}F by anion exchange resins over time. Different curves indicate presence of different ions in activation medium [29].

2.1.4 Detectors

A number of different detector configurations have been used for PEPT. The earliest PEPT measurements were carried out using two parallel plate detectors, as shown in Figure 2.3. In this set up, the system of interest is placed between the plates, and this open design accommodates measurement of a wide range of engineering systems.

Many commercially available PET scanners have also been used for PEPT studies. These have a cylindrical detector array surrounding a central bore as seen in the image of the ECAT EXACT3D PET scanner housed at PEPT Cape Town, shown in Figure 2.5. In this configuration, detector blocks consisting of high-Z scintillators are arranged in a ring, allowing for increased sensitivity and count rate performances over parallel plate geometries. However, these systems are limited to studies of systems that can fit inside the bore of the detector array. For clinical PET scanners, the bore is generally of the order of 70 cm diameter [18], while for preclinical scanners, the bore is of order 10 cm [31].

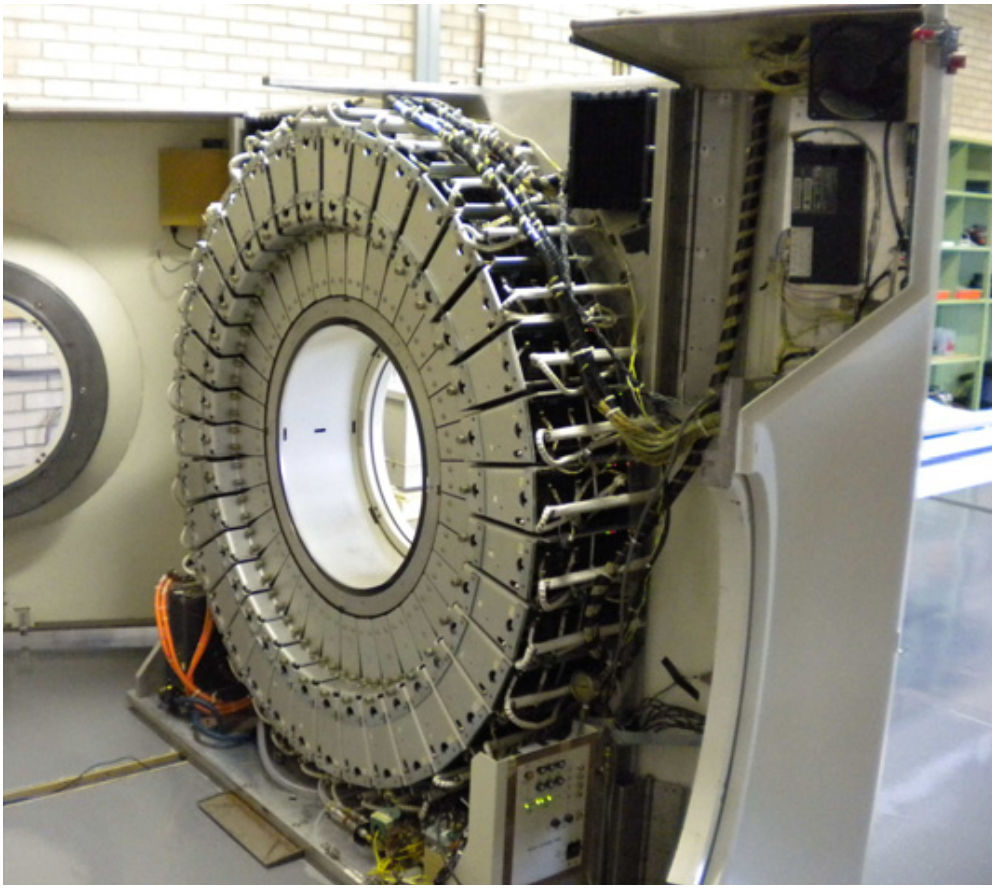

Figure 2.5: ECAT EXACT3D PET scanner housed at PEPT Cape Town [20].

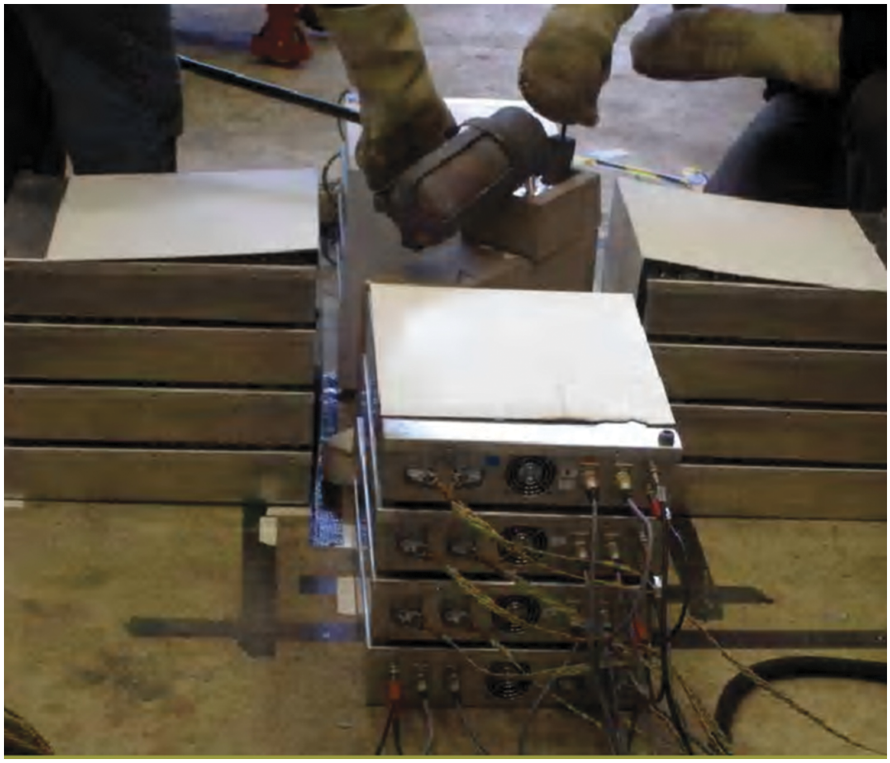

Figure 2.6: Modular detectors used for PEPT at Birmingham [18].

Modular detector arrays have also been employed for PEPT studies [18]. These can either feature custom detectors and electronics or are constructed using detector blocks from a commercial PET system. Individual detectors are removed from the scanner gantry and arranged in modules that can be reconfigured to any desired geometry. Figure 2.6 shows a rectangular detector array constructed of detector blocks removed from an ECAT950 PET scanner.

2.2 Porous Media Flows

Flow in porous media occurs in a number of engineering and natural systems [5]. In porous media, the Darcy equation is commonly used to describe macroscopic flow properties:

$$\vec{v} = -\frac{k}{\mu}\nabla P, \tag{2.7}$$

where $\vec{v}$ is the average fluid velocity, k is the permeability, μ is the fluid dynamic viscosity, and P is the pressure [32]. The Darcy equation follows from the Navier-Stokes equations when inertial effects and energy dissipation are neglected. This holds in extremely low Reynolds number regimes in which viscous forces in the fluid dominate inertial forces. For flows in porous media, the Reynolds number, Re, is defined as

$$Re = \frac{\rho v l_c}{\mu}, \tag{2.8}$$

where ρ is the fluid density, l_c is some characteristic length scale of the flow, and v is the average velocity in the pores [33]. In the case of porous media flows, l_c is usually taken to be the average pore diameter or the average bead diameter in the case of packed bed systems. It is generally accepted that flow can be considered Darcy when $Re < 1$.

In the absence of inertial effects, it is expected that the spreading of the concentration C of a solute in porous media flow will be governed by the advection-diffusion equation (ADE). For 1-D flow, the ADE is

$$\frac{\partial C}{\partial t} = D\frac{\partial^2 C}{\partial x^2} - V\frac{\partial C}{\partial x}, \tag{2.9}$$

where D is the dispersion coefficient [34]. In this equation, it is assumed that the dispersion of the solute is governed by Fick's law

$$\frac{\partial C}{\partial t} = D\frac{\partial^2 C}{\partial x^2}. \tag{2.10}$$

Under Fickian transport, it is expected that the concentration of a solute will spread linearly in time. However, it has been observed that this is not always the case for flows in porous media, even at extremely low Reynolds numbers. For this reason, such flows are often referred to as "non-Fickian".

2.2.1 Continuous Time Random Walk (CTRW) Theory

Several models have been proposed to solve the problem of non-Fickian transport, including fractional derivative [35] and variable dispersion coefficient [36] models. Another attempt at

solving this problem is a generalization of random walk theory called the continuous time random walk (CTRW).

The concept of the random walker was formally introduced by Karl Pearson in *Nature* in 1905 [37]. He posed the problem of a man walking l yards in a straight line, turning through any angle, walking another l yards, and repeating the whole process N times. He sought the probability that the walker is a final distance between x and $x+dx$ from his starting position after N steps. In one dimension, if p is the probability that the walker moves to the right, then the probability that the walker is m steps from the starting point (with $-N \leq m \leq N$) is

$$P_N(m) = \frac{N!}{\frac{N+m}{2}!\frac{N-m}{2}!} p^{\frac{N+m}{2}} (1-p)^{\frac{N-m}{2}}. \tag{2.11}$$

If we then let $x = ml$ and take a large number of steps (large N limit) this probability becomes the Gaussian distribution

$$P(x)dx = \frac{1}{\sqrt{2\pi}\sigma} \exp\left(-\frac{(x-\mu)^2}{2\sigma^2}\right) dx \tag{2.12}$$

with $\sigma = 2l\sqrt{Np(1-p)}$ and $\mu = (2p-1)Nl$.

This concept can be further generalized by not restricting the step distance to a single value. Let $w(s)ds$ be the probability that a jump is between a distance of s and $s+ds$. Then, it can be shown that after a large number, N, of steps, the Gaussian distribution of Equation 2.12 applies once again with $\mu = N\overline{s}$ and $\sigma^2 = N\overline{(\Delta s)^2}$. The only requirement for this to hold is that the moments of $w(s)$

$$\overline{s^n} = \int_{-\infty}^{\infty} w(s)^n ds \tag{2.13}$$

are finite [38]. As the spreading, σ^2, of the distribution varies linearly with the number of steps (a surrogate for time), this is analogous to Fickian dispersion.

The continuous time random walk (CTRW) is a further generalization of the classical random walk formalism in which discrete time (N) steps or transitions are replaced by continuous time (t) transitions in which the transition times are themselves represented by some probability distribution. We can reconsider the probability distribution of Equations

2.11 and 2.12 by a recursion relation between times N and $N-1$:

$$P_N(m) = \sum_{m'} p(m,m) P_{N-1}(m') \tag{2.14}$$

where $p(m,m')$ is the probability of transition from position m' to position m and is related to $w(s)$ above. We can then consider the same transitions but with a continuous time variable:

$$R(\mathbf{s},t) = \sum_{\mathbf{s}} \int_0^t \psi(\mathbf{s}-\mathbf{s}', t-\tau) R(\mathbf{s}',\tau) d\tau \tag{2.15}$$

where $\psi(\mathbf{s},t)$ is the probability per unit time of a transition of distance $\mathbf{s}$ in a time t, and $R(\mathbf{s},t)$ is the probability of a walker arriving at a position $\mathbf{s}$ at time t [39, 40]. Note that in this case, according to the formalism of Berkowitz et al. [40], spatial transitions are still discrete, corresponding to transitions on a lattice [41].

Now, as $R(\mathbf{s},t)$ is a probability of arrival, it is useful to then consider the probability $P(\mathbf{s},t)$ of finding a walker at position $\mathbf{s}$ at time t:

$$P(\mathbf{s},t) = \int_0^t \Pi(t-\tau) R(\mathbf{s},\tau) d\tau \tag{2.16}$$

with

$$\Pi(t) = 1 - \int_0^t \psi(\tau) d\tau \tag{2.17}$$

being the probability of staying stationary for a time t [39]. In the above equation,

$$\psi(\tau) = \sum_{\mathbf{s}} \psi(\mathbf{s},\tau). \tag{2.18}$$

Equation 2.15 can alternatively be viewed as a convolution in time and space and can be recast and solved via Fourier and Laplace transforms:

$$\mathcal{R}(\mathbf{k},u) = \frac{1}{1-\Lambda(\mathbf{k},u)} \tag{2.19}$$

with $\mathbf{k}$ and u being the Fourier and Laplace variables, respectively, and

$$\Lambda(\mathbf{k}, u) = \mathcal{F}\{\psi^*(\mathbf{s}, u)\} = \sum_{\mathbf{s}} \exp(i\mathbf{k} \cdot \mathbf{s})\psi^*(\mathbf{s}, u) \tag{2.20}$$

$$\psi^*(\mathbf{s}, u) = (L)\{\psi(\mathbf{s}, u)\} = \int_0^\infty \exp(-ut)\psi(\mathbf{s}, t)dt. \tag{2.21}$$

From this, one can then solve for the distribution of the walker's position:

$$P(\mathbf{s}, t) = \mathcal{F}^{-1}\{\gamma(\mathbf{k}, t)\} \tag{2.22}$$

where

$$\gamma(\mathbf{k}, t) = \mathcal{L}^{-1}\left\{\mathcal{R}(\mathbf{k}, u)\frac{1 - \psi^*(u)}{u}\right\} \tag{2.23}$$

with $\psi^*(u)$ the Laplace transform of $\psi(\tau)$.

The probabilities of finding a walker at a given position at a given time (Equations 2.12 and 2.22) can be viewed in a macroscopic limit as the concentration distribution of some solute introduced into a solution. In theory, even for the CTRW case, this can be calculated if one has knowledge of the microscopic transition rate $\psi(\mathbf{s}, t)$.

For this reason, of central importance to these formulations is the transition probability $\psi(\mathbf{s}, t)$. Anomalous (i.e. non-Fickian) transport will arise when the long-time tails of $\psi(\mathbf{s}, t)$ decay algebraically [42]:

$$\psi(\mathbf{s}, t) \sim t^{-1-\beta}, \qquad t \to \infty. \tag{2.24}$$

The exponent β describes the shape of the probability distribution of long waiting times between steps and may be a function of a number of conditions (pore sizes, Reynolds number, etc.).

If $\beta > 2$, the moments of this distribution will be finite and classical diffusion will be recovered. In the case that there is a biasing of the distribution (such as the pressure gradient forcing a flow field), it is found that for $1 < \beta < 2$, the mean position of the walker varies linearly with time while the distribution is asymmetric and has long late time tails. For $0 < \beta < 1$ at long times, the walker's mean position and variance will vary as $\mu \sim t^\beta$ and $\sigma^2 \sim t^{2\beta}$, respectively. In this case, the mean walker position moves more slowly than in

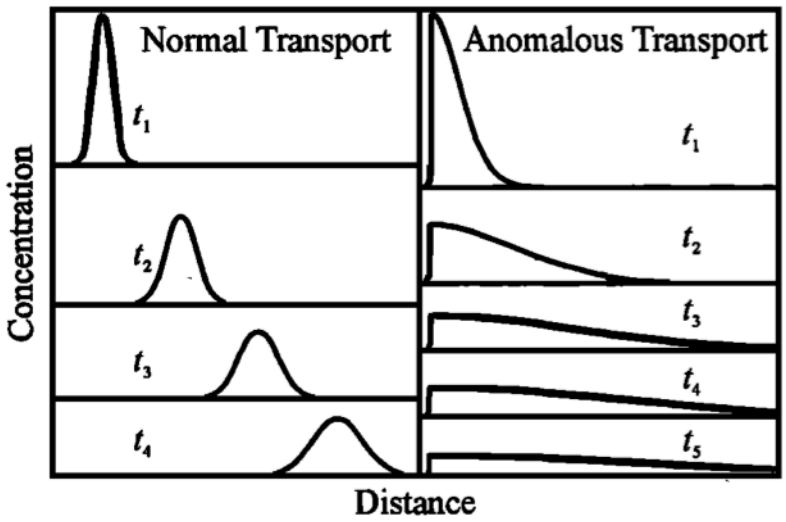

Figure 2.7: Schematic representation of differences between normal and anomalous transport [40].

the normal walker case where both μ and σ^2 vary linearly with time, as in Equation 2.12 (recall that in the discrete case, the variable N is analogous to time) [34]. This phenomenon is demonstrated in Figure 2.7.

2.2.2 CTRW Experiments

Many experiments have focused on measuring the first pass time distribution (FPTD) of a solute as a means of calculating the exponent β of the long-time transition probability. The FPTD, $F(\mathbf{s}, t)$, is the probability that a walker first arrives at a position $\mathbf{s}$ at a time t and is defined by the relation

$$R(\mathbf{s}, t) = \delta_{\mathbf{s},\mathbf{0}}\delta(t-0) + \int_0^t F(\mathbf{s}, t)R(0, t-\tau)d\tau. \tag{2.25}$$

This can once again be solved by Laplace transforms as

$$F(\mathbf{s}, t) = \mathcal{L}^{-1}\left\{\frac{R^*(\mathbf{s}, u) - \delta_{\mathbf{s},\mathbf{0}}}{R^*(0, u)}\right\} \tag{2.26}$$

where $R^*(\mathbf{s}, u)$ is the Laplace transform of $R(\mathbf{s}, t)$ [39, 43].

To date, experiments have considered the late time limit of $F(\mathbf{s}, t)$, corresponding to that after many individual transitions. In a system with a mean flow direction x, one averages over all directions perpendicular to x and considers the quantity

$$f(L, t) = \langle F(\mathbf{s}, t) \rangle \tag{2.27}$$

where angle brackets represent a spatial average over the directions perpendicular to x. In the lab, this quantity represents an average distribution of solute over a plane perpendicular to x at a distance L in the x-direction from some starting point x_0 at a time t. This can then be measured for the injection of a uniform concentration, C_0, of solute at position x_0 at time $t = 0$, as the concentration at L will be [40]

$$C(L, t) = C_0 \int_0^t f(L, t - \tau) d\tau \tag{2.28}$$

As such, the concentration distribution downstream of an injection point is a cumulative form of the FPTD. This can then be related back to the original transition probability $\psi(\mathbf{s}, t)$ in the large t domain (or small u if working in Laplace space) to determine the exponent β in its asymptotic form.

Using this framework, Berkowitz et al. [40] reexamined the experiments of Silliman [44] and Silliman and Simpson [45] in which flow was induced across a flow cell having heterogeneous packing of fine sand and coarse sand, as seen in Figure 2.8. A tracer solution was introduced upstream of the flow cell, and its concentration was measured at five downstream positions by measuring electrical resistance. They show that using a value of $\beta = 0.87 \pm 0.01$, the concentration distributions calculated via a CTRW formalism better match the data than those calculated under a classical advection-diffusion equation (ADE) formalism [40].

Levy and Berkowitz [34] used a similar experimental setup to study tracer movement through three different porous media: sand packed homogeneously, two different sized sands packed with a "uniform heterogeneity" (similar to that studied by [45]), and three different sands packed in an "exponentially correlated" structure (see Figure 2.9). Tracer was injected,

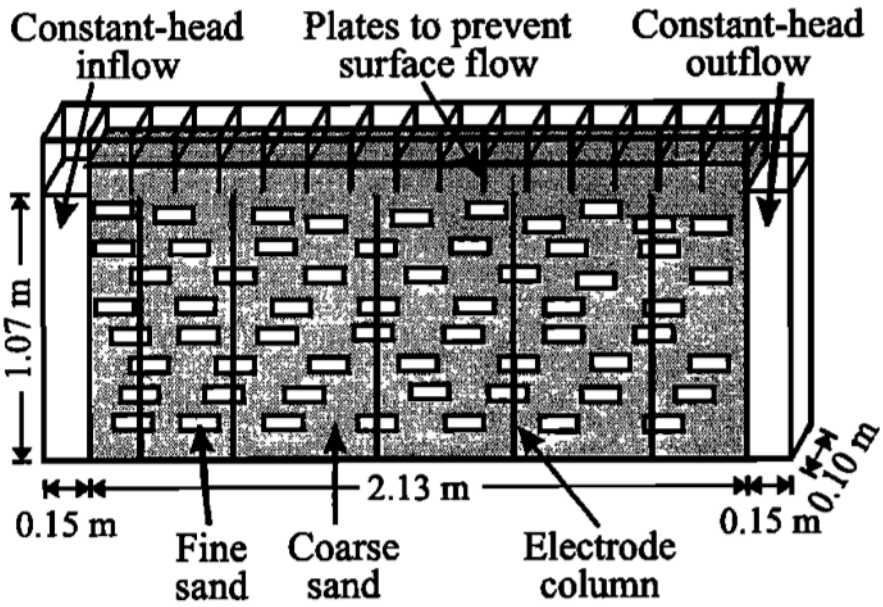

Figure 2.8: Experimental setup of flow cell with uniformly heterogeneous packing examined by Silliman and Simpson [45] and reexamined by Berkowitz et al. [40]. Image is taken from the latter.

and concentration distributions were measured in each packed bed at various mean flow rates and used to infer the late time shape of the CTRW transition time distribution. The homogeneous system showed values of β ranging from 1.65 to 1.89, with the latter being at the lowest flow rate, indicating an approach to classical diffusion. Similarly, for the uniformly heterogeneous system, β ranged from 1.45 at the highest flow rate to 1.71 at the lowest flow rate. Lastly, in the exponentially correlated system, β ranged between 1.59 and 1.67.

Edery et al. [43] examined transport of nonreactive and reactive solutes in a porous medium consisting of acrylic polymer beads that were index-of-refraction-matched to water. A 1-D column was first used to fit a value of β for the system, and using this value, 2-D simulations were performed using a CTRW particle tracking formulation and compared to experimental results from a 3-D flow cell (averaged over depth). The simulations recreated experimental results well in both the nonreactive and reactive cases without the need for reaction model parameter fitting in the reactive case. Small-scale differences between experiment and simulation in both cases were attributed to preferential flow paths typical of systems displaying anomalous diffusion.

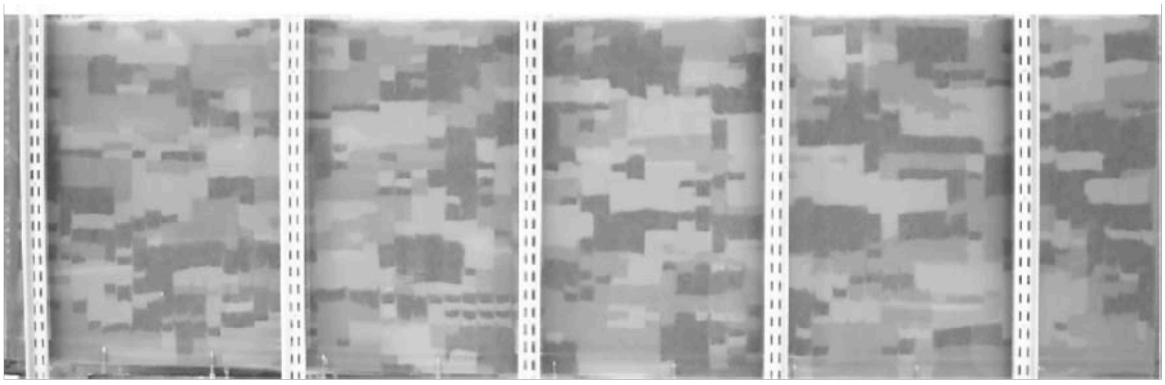

Figure 2.9: Packing of flow cell with exponentially correlated structure. Small, medium, and large grain sands correspond to the light, intermediate, and dark colors, respectively [34].

2.2.3 Particle Tracking Experiments

The CTRW formalism lends itself to the analysis of trajectories of flow tracers (the "random walkers"). Such studies are considered Lagrangian in that they follow individual tracers as they move with the flow (in contrast to Eulerian measurements in which a spatially fixed region of the flow field is examined). However, due to the opaque nature of most natural porous media, few optical particle tracking studies have been performed in porous media. In these works, care must be taken to match the indices of refraction of the porous media and the working fluid to prevent distortions.

Moroni and Cushman [46] used a packed bed of 1.9 cm Pyrex spheres with glycerol fluid and small air bubbles as the fluid tracer. These bubbles were illuminated with a high power lamp and recorded using two cameras, and their 3-D trajectories were reconstructed from these two images. Bubbles were tracked across a field of view of length 22 cm and Darcy Reynolds number was varied from 0.05 to 0.13. They found that the probability distribution functions (PDFs) of the the Lagrangian velocity were Gaussian in the transverse direction but non-gaussian in the longitudinal direction. They also observed that dispersion was tending toward the Fickian limit at late times but was non-Fickian at the scale of the experiment.

Holzner et al. [47] studied both Lagrangian velocity and acceleration statistics in a packed bed of Nafion grains of size 3.7 mm and 0.5 mm. A 24%-by-volume aqueous solution of isopropanol was used as the working fluid, and silver particles of 15 μm were used as

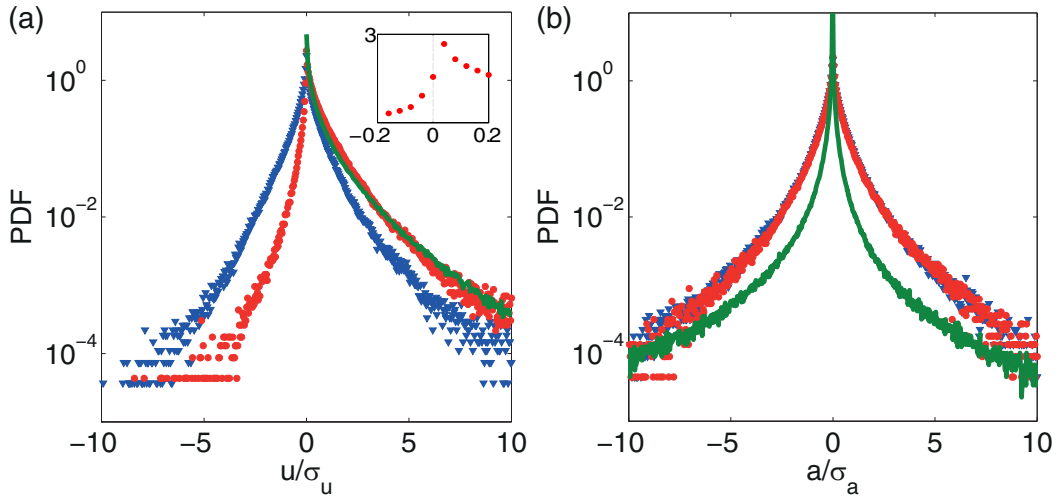

Figure 2.10: PDFs of longitudinal (red circles) and transverse (blue triangles) Lagrangian velocity (a) and acceleration (b) components measured by Holzner et al. [47]. Longitudinal velocity and acceleration from CTRW model shown with green line. Inset in (a) is a closeup near zero of longitudinal velocity.

tracers. An argon laser was used to illuminate the flow field, and a 50 Hz camera with a four-way image splitter was used to mimic a multiple camera particle tracking system. They observed non-Gaussian longitudinal velocity and acceleration at the pore scale, as seen in Figure 2.10 and related this to anomalous dispersion at the lab scale. Furthermore, they showed that their results are in agreement with a CTRW model for particle dynamics.

Chapter 3

Multiple-Particle PEPT Development

The majority of past PEPT experiments have only tracked a single particle at a time. A few methods for multiple-particle PEPT (M-PEPT) have been attempted, but these have been quite limited [8, 11]. Past methods have been able to track up to sixteen particles simultaneously [11] but have been limited in that they require *a priori* knowledge of the number of particles present in the field of view (FOV) of the detectors or require knowledge of the initial positions of the particles.

A less restrictive version of M-PEPT is sought. By allowing tracking of an arbitrary number of particles, one opens up the possibility of flow measurement in systems where tracers enter and leave the FOV of the detectors, such as test sections in a recirculating flow loop. This allows for the collection of a greater number of individual particle trajectories and improved statistical analysis of the underlying flow. This chapter will focus on the development of such a method.

In particle tracking, two major steps are present: a detection step and a linking step. In the detection step, particles in an individual time frame are located. During the linking step, particles located in different frames are associated to the same physical particles from other time steps and linked into trajectories spanning many frames. Two methods for multiple-particle detection are presented herein: the G-means method and the the feature point identification (FPI) method, with emphasis being placed on the latter.

3.1 G-means

The G-means method for M-PEPT reconstruction was first presented in a work by the author [48]. This method is based on the "line density" method developed at the University of Cape Town [11] and uses clustering to identify particles. As with the Cape Town method, one begins by dividing coincidence event data into time steps and counting the number of CL crossings at each point in a Cartesian grid for each time step. The next step is to filter the data before beginning the clustering process. First, a check is made to determine whether there are any particles in the FOV of the detectors. A user-input threshold is set on the maximum number of CL crossings in an individual grid element in given time step. If this threshold condition is met, a preset fraction of this maximum value is subtracted from each point in the count grid, and any point having fewer counts than this fraction being are to zero. This fraction is determined by the user based on knowledge of the activity of each particle relative the background and is usually set somewhere in the range of 0.25-0.5. The remaining data can thus be viewed as points in $\mathbf{R}^3$ with a multiplicity corresponding to the number of line crossings at each point. These data can be grouped into k clusters with the centroid of each cluster taken to be the location of a tracer particle. However, such clustering can be quite difficult if the number of clusters (and thus particles) k is not known prior to calculation. Due to the isotropic distribution of positron emission about each tracer, it is expected that each cluster of CL crossings should be normally distributed about the true particle position, and this feature can be used to discriminate between true and false clusters. For this reason, the method of G-means clustering is employed.

3.1.1 G-means Clustering

Gaussian-means (G-means) clustering is an adaptation of the well-established k-means algorithm [49] that allows clustering when the number of natural clusters in a dataset is unknown. In this method, developed by Hamerly and Elkan [50], principal component analysis and goodness-of-fit testing are used to determine the number of clusters k in a dataset as well as their locations. The method begins by performing a k-means clustering of the dataset with $k = 1$ (or a higher number if there is *a priori* information of the system)

and subsequently splitting or accepting each cluster based on its adherence to a Gaussian fit. In this way, the number of clusters in the dataset grows until it reaches the number of natural clusters. In the case of this M-PEPT method, calculations are always started with a $k = 1$ clustering, i.e. a universal centroid calculation. As such, this method is deterministic and does not risk the potential false convergence error of k-means clustering caused by poor initialization.

The splitting process is performed based on a statistical testing of each cluster for normality. If the data appear to be normally distributed, the cluster is accepted. If they do not, the cluster is split into two. The statistical test is performed based on the adherence of the cluster to a one-dimensional Gaussian fit. This process is described as follows.

Consider a dataset S of points in d-dimensional space (in the case of this method, $d = 3$) with the data already divided into k clusters, $X_j \subset S$, where $j \in \mathbf{J} = \{1, 2, ...k\}$. Now consider a specific cluster, X_m, where $m \in \mathbf{J}$, containing n points. The main principal component of X_m is found by using a power iteration routine [51] to find the greatest eigenvalue λ and corresponding eigenvector of the covariance matrix of this cluster. This eigenvector is the main principal component, and two daughter centroids, c_1 and c_2, are initialized along this vector, a distance $\pm\sqrt{2\lambda/\pi}$ from the centroid of X_m. k-means clustering is performed on X_m with $k = 2$ and c_1 and c_2 as the initial cluster centers. After c_1 and c_2 converge on new values, c_1' and c_2', one defines the line $v = c_1' - c_2'$. A one-dimensional projection of the data in X_m is taken along v such that $x_i' = (x_i \cdot v)/\|v\|^2$. This new data set X_m' is a one-dimensional representation of the data in X_m and is then transformed so that it has mean 0 and variance 1.

A one-dimensional Anderson-Darling (A-D) test [52] is then performed on the data in X_m' to test if it is normally distributed. For each of the n values $x_i' \in X_m'$, let $z_i = F(x_i')$, where F is the $N(0, 1)$ cumulative distribution function. Then the A-D statistic, A^2, is defined as

$$A^2(Z) = -\frac{1}{n}\sum_{i=1}^{n}(2i-1)[\ln(z_i) + \ln(1 - z_{n+1-i})] - n. \tag{3.1}$$

It has been shown [53] that for datasets where the mean and variance are estimated from the data itself, a correction must be applied to the A-D statistic as follows:

$$A^2_*(Z) = A^2(Z)\left(1 + \frac{4}{n} - \frac{25}{n^2}\right). \tag{3.2}$$

In the case of this method, if the A-D statistic is below a given critical value, the original cluster X_m is accepted. If it is not, the cluster is split, and a k-means clustering of the entire dataset S is performed with $k' = k + 1$, and centroids are initialized at the daughter centroids of X_m, c'_1 and c'_2, and the centroids of the remaining subsets X_n, $(n \neq m)$. This process is continued until all clusters pass the A-D test. For a finite number of points in the set S, this clustering will always converge; however, the number of clusters determined by G-means is sensitive to the selection of the A-D critical value.

As previously stated, the final positions of particles in each time step are taken to be the centroids of these clusters. As in the Cape Town method [11], 3-D Gaussian fits are applied to the clusters, and uncertainty in position is taken to be the full width at half maximum of a cluster divided by the square root of the number of CL used in that cluster.

3.1.2 G-means example

Figure 3.1 shows an example of the splitting of clusters achieved by the G-means algorithm. The example uses actual 3-dimensional data acquired from a MicroPET P4 preclinical PET scanner [54] with three activated particles placed near the center of the FOV of the scanner. with three particles, it can be seen that the filtered line-density dataset has three natural clusters. In this case, the critical value for the A-D test is taken to be 20, based on experience.

First the universal centroid is calculated (Figure 3.1 top-left). In the first run of G-means, the daughter centers are found, the A-D statistic for the cluster is calculated as 143.2, and splitting is accepted (top-right). The daughter centers and A-D statistics are then found for the lower cluster, and it is found that $A^2_* = 84.25$, meaning that this cluster is split as well (bottom-left). On the final iteration, all three clusters are examined, and their A-D values are found to be 0.902, 6.089, and 2.627. As all three of these values are less than 20, all three

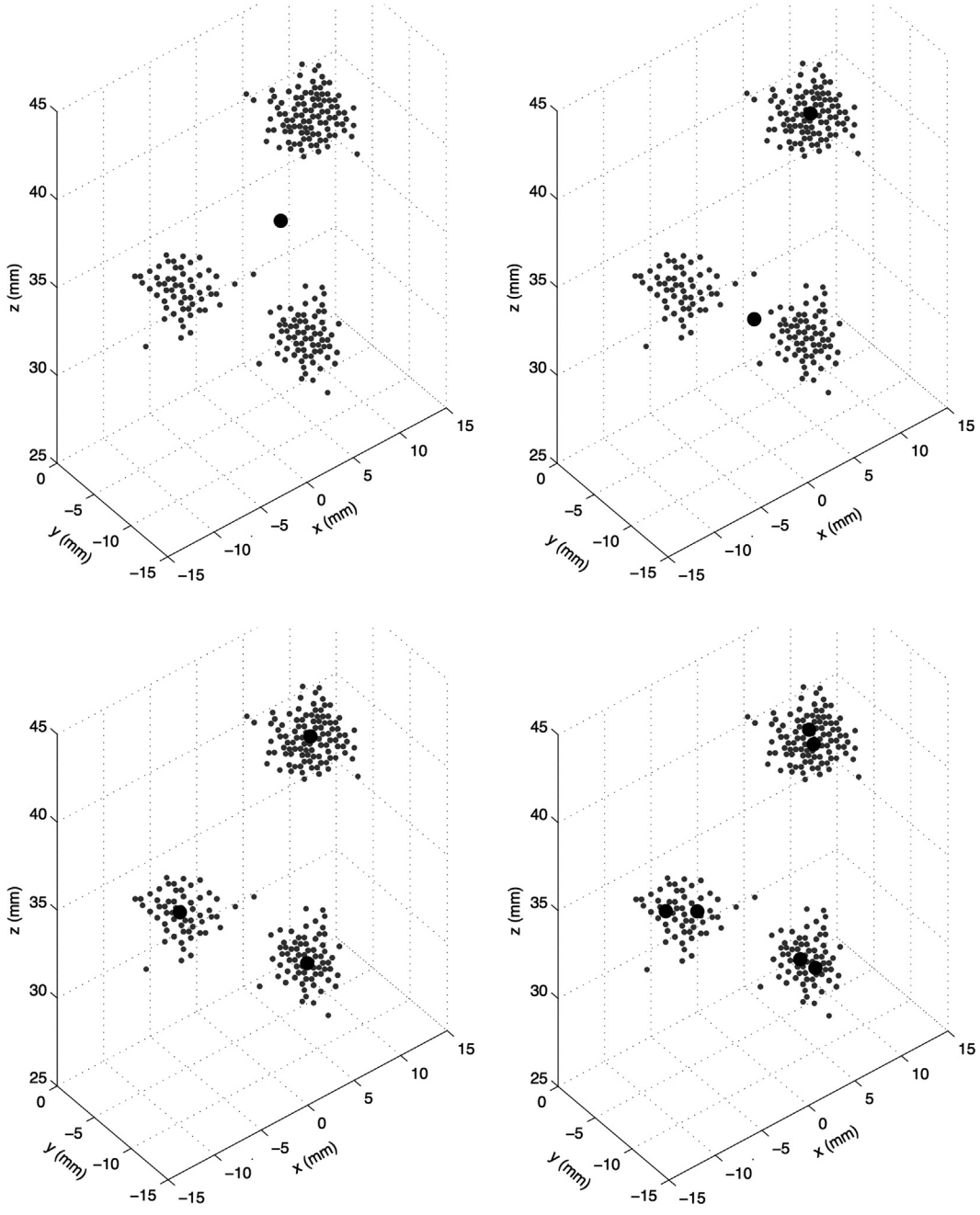

Figure 3.1: Visual representation of G-means algorithm. Clustering begins with one cluster (top-left) and proceeds to two clusters (top-right) and three clusters (bottom-left). Further splitting (bottom-right) is rejected.

splits (bottom-right) are rejected, and the three clusters are accepted. Thus, as expected, $k = 3$ for this dataset.

3.1.3 G-means Tests

A series of experiments was designed and conducted using a MicroPET P4 preclinical PET scanner [54] to test this method. The P4 is a ring-type scanner consisting of 168 segmented LSO detectors with a cylindrical FOV of length 7.8 cm and diameter 19 cm. Tracers used are ion exchange resins of roughly 1 mm diameter and labelled with 20-50 μCi of ^{18}F , unless otherwise stated. The G-means reconstruction program was written by the author using C++.

In the first test conducted, a single tracer particle was left stationary in the center of the FOV of the scanner and tracked over the course of 1 s using 1 ms time steps and a grid of size 2×2×2 mm^3 for reconstruction. For this experiment, the particle was activated to 430 μCi, resulting in an acquisition rate of roughly 140 CL per ms. Knowledge of this data-rate is necessary to facilitate comparison to other PEPT methods. The mean and standard deviation of these 1000 measurements was found to be (1.13, -5.19, 39.5) ± (0.32, 0.36, 0.32) mm in the x-, y-, and z-directions, respectively. Here, z denotes the axial direction, x is the horizontal transaxial, and y is the vertical transaxial, with the origin located in the radial center of the bore, aligned to its front axial edge. This same dataset is then analyzed using the Birmingham method with 140 CL used per reconstruction. The position measured in this way is (1.20, -5.41, 39.6) ± (0.41, 0.27, 0.37) mm. This comparison shows the accuracy of the G-means method is comparable to that of the Birmingham method. The runtimes for these two analyses were 9.65 and 1.09 s, respectively, with reconstruction executed on an Apple MacBook Pro computer with 2.66 GHz Intel Core 2 Duo processor. The increased computational time is expected, given the relative simplicity of the Birmingham method compared to this clustering method.

Next, 17 particles were placed in a polyethylene phantom with an average separation of 20 mm and moved slowly through the bore of the scanner using its built-in bed motion controls (speed of roughly 3 mm/s). Using a $1 \times 1 \times 1$ mm^3 grid and 100 ms time steps, the trajectories of these particles were reconstructed using an average of 230 CL per particle per

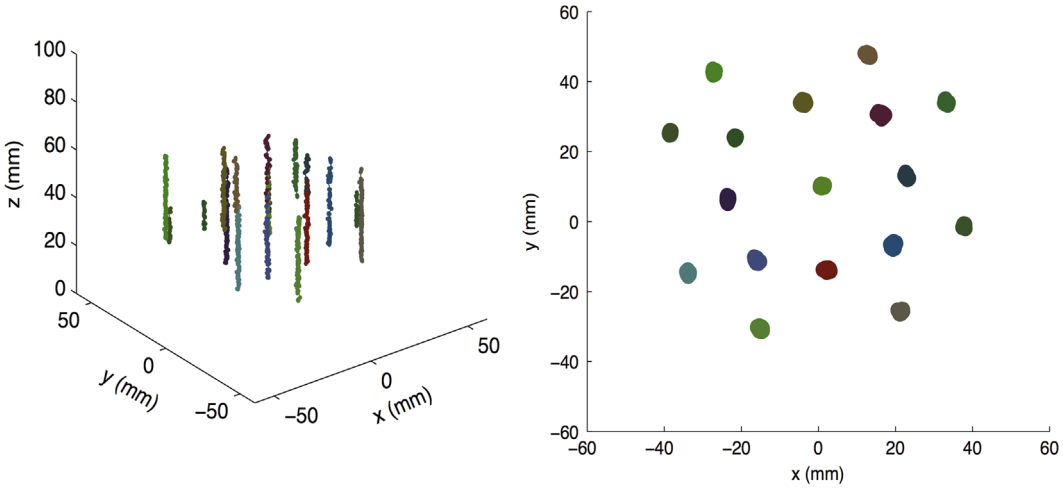

Figure 3.2: Trajectories measured by PEPT with 17 particles in a polyethylene phantom. Left: 3-dimensional representation of trajectories. Right: x-y (transaxial) projection of trajectories. Different colors correspond to different particles and are consistent across frames.

time step. These trajectories can be seen in Figure 3.2. This represented a new record of number of particles tracked simultaneously with PEPT.

To test the ability of this algorithm to track particle entering and leaving the bore, as well as its ability to measure irregular trajectories, an experiment was performed in which an activated particle was attached to the end of a rod and moved in an out of the scanner by hand. The particle was made to enter and leave the FOV of the scanner 8 times, and these 8 trajectories can be seen in Figure 3.3. These trajectories were reconstructed using a $2\times2\times2$ mm^3 grid with 10 ms time steps.

Lastly, an experiment was performed to test the resolving power of this method in which one particle was held stationary, and another was moved toward it until the two touched. Using $2 \times 2 \times 2$ mm^3 grid elements and time steps of 25 ms (roughly 400 CL per time step), the particles were distinguishable down to a separation of 5 mm. Below this, the particles were seen as one entity at their mutual centroid.

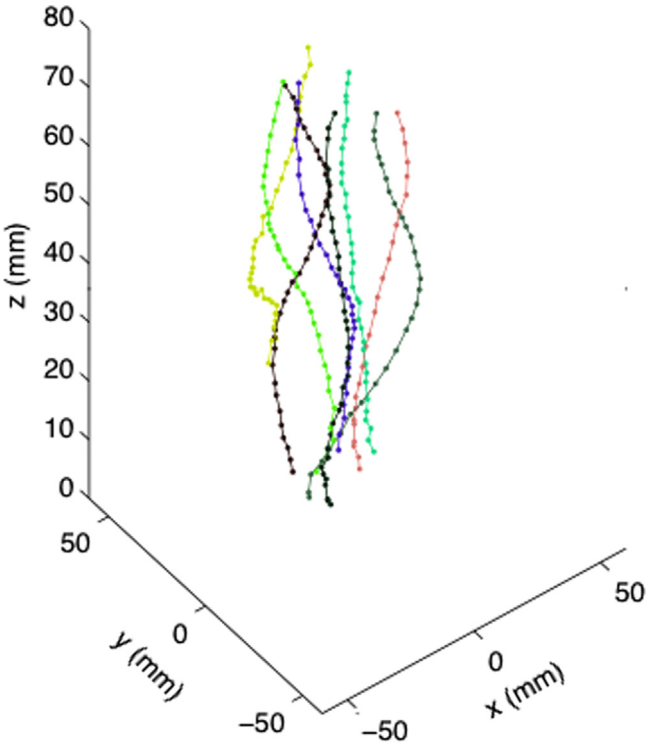

Figure 3.3: Trajectories measured by PEPT for single particle making eight passes through the bore of the scanner.

3.1.4 G-Means Drawback

While the G-means method has proven useful for M-PEPT reconstruction, it has a significant drawback. Results of reconstruction are very sensitive to the selection of the critical A-D value. Standard values based on confidence of fit are given by Stephens [53], but these are based on clustering of continuous data. In the case of the binned (i.e. discrete) data of CL crossings, these values are found to be too restrictive, preventing G-means clustering from converging on the correct number of clusters. As such, the A-D critical value must be selected based on experience and without mathematical foundation. This creates issues in reconstructions with many particles, as G-means tends to create too many or too few clusters. For this reason, another method for M-PEPT has been developed that does not exhibit such an acute sensitivity to input parameters.

3.2 Feature Point Identification

The feature point identification (FPI) method for M-PEPT is based on optical particle tracking techniques and is described by the author in [55]. As this is the method for M-PEPT reconstruction used in this work, a more detailed explanation is given here. A visual representation of FPI processing is given in Figure 3.4.

As before, this method begins with the segregation of coincidence events into time steps and a line density tallying of CL crossings on a Cartesian grid at each time step. In this case, it is helpful to view each grid element as a 3-D analog to the pixel referred to as a "voxel", with the number of line crossings being analogous to a greyscale value. This verbage and procedure are similar to the backprojection procedure employed in PET reconstruction [56]. With this voxel imagery in mind, optical particle tracking methods can then be naturally adapted for use in PEPT. The method used herein is adopted from the techniques of Crocker and Grier [57] and Sbalzarini and Koumoutsakos [58]. The identification portion of this reconstruction is carried out in three steps: smoothing, position estimation, and position refinement.

After the CL grid is generated for a given time step, we can consider $N^t(x, y, z)$ to be the number of line crossings at the voxel at position (x, y, z) during time frame t. The grid

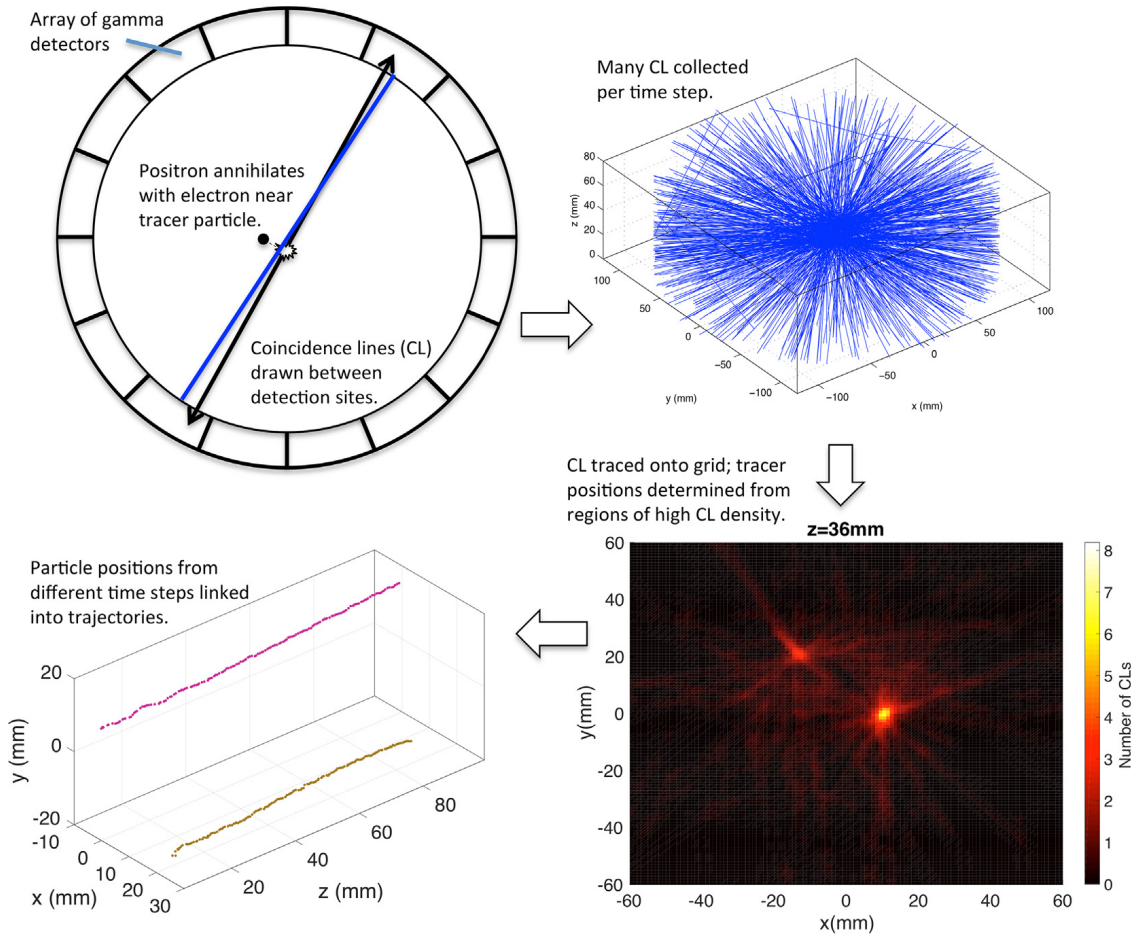

Figure 3.4: Flow chart of PEPT with FPI M-PEPT processing. (Clockwise from top-left) Positrons annihilate with electrons near the tracer particle, producing back-to-back coincident gamma rays of energy 511 keV. Coincidence lines (CL) are drawn between detector elements within which these photons interact. Data from the duration of the scan are divided into time steps containing tens to hundreds of CL each. These are traced onto a 3-D Cartesian grid and examined via image processing techniques. Here, a single axial slice containing two particles is shown. Local maxima are considered to be particle locations, and final positions are determined via Gaussian fits about these maxima. Finally, particle positions from individual time steps are linked into trajectories.

is first smoothed via convolution with a boxcar kernel of width $2f+1$:

$$N'^{t}(x,y,z) = \frac{1}{(2f+1)^3} \sum_{i=-f}^{f} \sum_{j=-f}^{f} \sum_{k=-f}^{f} N^{t}(x+i, y+j, z+k) \tag{3.3}$$

where f is the smoothing size. In most studies, f is set to 1 (minimal smoothing) or 0 (no smoothing). In the above operation, the outer f elements are neglected in each dimension. Crocker and Grier [57] and Sbalzarini and Koumatsakos [58] convolve each frame with a Gaussian surface of rotation of half-width 1 pixel to further reduce camera pixelation noise, and use convolution with a larger boxcar kernel as a means to estimate background in each frame. An analog has been implemented for M-PEPT reconstruction using a Gaussian volume of rotation. In this case, we set $f = r$, and the final smoothed grid is taken to be

$$N^{t,F}(x,y,z) = \frac{1}{K_0^3} \sum_{i=-r}^{r} \sum_{j=-r}^{r} \sum_{k=-r}^{r} N^{t,*}(x+i, y+j, z+k) \exp\left(-\frac{i^2+j^2+k^2}{2\lambda^2}\right), \tag{3.4}$$

with

$$N^{t,*}(x,y,z) = \begin{Bmatrix} N^{t} - N'^{t}, & (N^{t} - N'^{t}) > 0 \\ 0, & (N^{t} - N'^{t}) \leq 0 \end{Bmatrix} \tag{3.5}$$

and normalization

$$K_0 = \sum_{i=-r}^{r} \exp\left(-\frac{i^2}{2\lambda^2}\right). \tag{3.6}$$

The smoothing width λ is usually taken to be

$$\lambda = \frac{Crystal\ Width}{2 \times (Grid\ Size)}, \tag{3.7}$$

referencing the width of the detector crystal elements and the size of the grid employed for CL tallying. In this way, the weight of any given CL is effectively blurred into a Gaussian "tube" to account for uneven sampling of the CL grid by the crystal geometry. In general, the addition of this second level of smoothing is not seen to offer significant benefit but only serves to increase computational cost. As such, the smoothed grid $N^{t,F}$ is only used in cases of large background radiation. The grid N'^{t} is used otherwise.

Next, particle positions are estimated by finding local maxima in the smoothed grid N'^t. Local maxima are taken to be voxels having CL crossing values in the upper rth-percentile of their given frame and having value greater than any of their neighbors within a cube of width $2w+1$. The value r is adjusted based on the amount of noise in an experiment, as well as the distribution of activities of particles used in an experiment.

The parameter w serves as an apparent particle radius where the virtual particle can be viewed as a cloud of high CL density in voxel-space. It is desired that this search radius be greater than the typical virtual radius of a particle. In voxel-space, typical virtual diameters of particles are of order 4-6 voxels (based on full width at half maximum of line crossing distributions with 1 mm voxels). A particle appears larger in image space than its physical size due to the nonzero positron range and spreading of the CL distribution by scattering of coincident photons before detection.

This parameter also limits the between-particle separation that can be resolved in a given frame to w times the voxel size. Below this separation, only the particle that appears brightest in voxel space (i.e. the one corresponding to the highest CL crossing peak) will be detected, and any other particles will be ignored but will bias the measured position toward the centroid of the particles involved. Thus, in the case of two particles approaching closely, it is likely that the trajectory of the higher activity particle will be continued while there will be a break in the measured history of the other. As such, w can also be adjusted in a given experiment according to expected particle number density so that it is less than the anticipated between-particle spacing. In searching for local maxima, the outer w elements are neglected in each dimension. This prevents bias along the edges of the scanner but restricts the useable FOV of the scanner.

Ties in the local maxima search are handled on a "first come, first serve" basis. If two grid elements of identical smoothed CL crossing value are identified as local maxima and are found in the same cubic region of side length $2w+1$ voxels, the first one detected by the algorithm will be accepted as a particle position estimate, and the second will be rejected. It is expected that any bias introduced here is reduced or eliminated during the particle position refinement stage. Furthermore, the frequency of such ties is reduced by the use of the aforementioned smoothing filter.

In the earliest implementations of the FPI method, final particle positions were calculated according to a weighted-average centroid calculation over a cubic region of side length $2w+1$ centered at each estimate. Recent work has revealed that this centroid calculation results in a pixel-locking defect. This is analogous to the effect discussed by Brady [59] as it biases positioning results toward the centers and edges of voxels. For this reason, particle positions calculation is now performed via 1-D Gaussian fits in each spatial direction, centered about each local maximum. An example of this pixel-locking defect before and after this correction is shown in Figure 3.5. The position of each particle is taken to be the mean of the Gaussian, and the uncertainty is calculated from the fitted standard deviation σ as $\Delta x = \sigma/\sqrt{N_{CL}}$, where N_{CL} is the number of CL used for position reconstruction. N_{CL} is estimated as the number of CL passing within a distance $(w+0.5)$ voxels from each calculated position.

3.2.1 Comparison to G-means

As with G-means, a series of analyses were performed to test the capability of the FPI method. Selected experiments were analyzed via the FPI method and compared to results from G-means. Experiments were conducted using the MicroPET P4 scanner. Both methods were implemented by the author as C++ programs and executed on an Apple Macbook Pro computer with 2.66 GHz Intel Core 2 Duo processor. These tests were documented by the author [55] and used the original weighted-averaging approach to final particle localization.

First, FPI was used to analyze the stationary particle dataset described in Section 3.1.3. The position of a particle of activity 430 μCi was reconstructred using a $2 \times 2 \times 2$ mm^3 grid, 1 ms time steps, and reconstruction parameters $f = 1$, $r = 0.3$, and $w = 3$. Over 1000 histories, the mean position $\pm$ standard deviation of the particle was found to be (1.22, -5.49, 39.4)$\pm$(0.51,0.48,0.24) mm in the x-, y-, and z-directions, respectively, where z is the axial, x the horizontal transaxial, and y the vertical transaxial direction. The origin of the coordinate system is placed at the radial center of the bore, aligned to its front axial edge. Recall that the G-means result for the location of this particle was (1.22, -5.19, 39.5)$\pm$(0.32, 0.36, 0.32) mm. Thus, the two methods are in agreement, with G-means displaying a lower transaxial variance, and FPI displaying a lower axial variance. The runtime for FPI was 7.48 s, compared with 9.65 s for G-means.

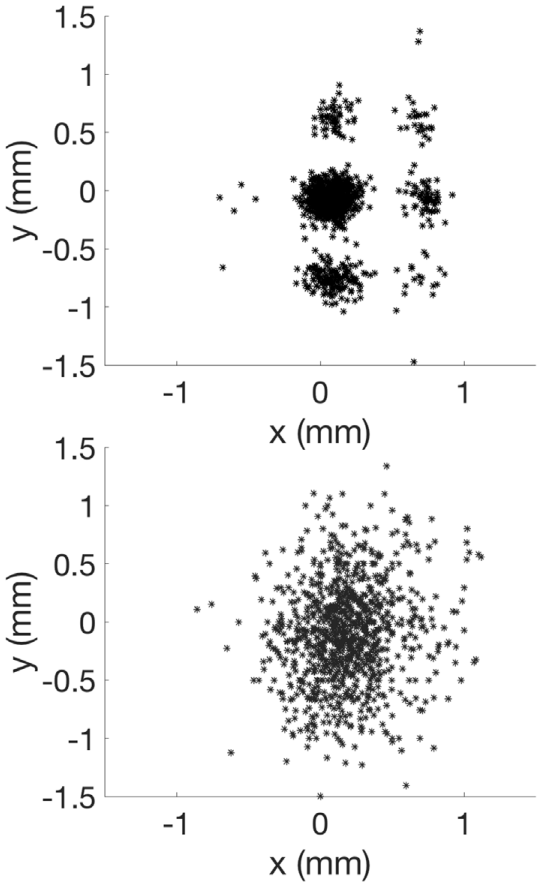

Figure 3.5: Pixel-locking defect. 2-D projection of detected PEPT positions for single stationary particle in scanner FOV before (top) and after (bottom) correction of pixel-locking defect. Top frame shows significant bias toward centers and edges of grid elements. $1 \times 1 \times 1$ mm^3 grid is used for reconstruction herein.

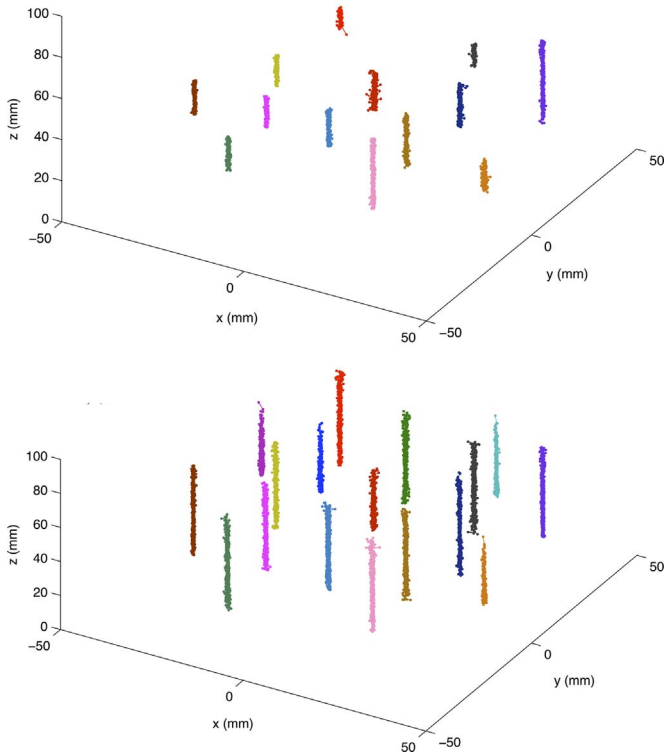

Figure 3.6: Particle trajectories calculated from 17 particle dataset using 25 ms time steps with G-means (top) and FPI (bottom).

Next, the dataset of 17 particles in a polyethylene phantom was examined with FPI. Using a $1 \times 1 \times 1$ mm^3 grid and 100 ms time steps, FPI showed very similar results to those previously seen with G-means. However, when 25 ms time steps were used (resulting in about 60 Cl per particle per time step), FPI significantly outperformed G-means. Figure 3.6 shows the reconstruction results of FPI compared to those of G-means. Here it is seen that the FPI method was able to successfully identify and track all 17 particles, whereas G-means only found 13 of the particles. Furthermore, G-means was only able to detect particles near the axial center of the FOV, while FPI tracked the particles throughout. This shows that the FPI method is better capable of determining particle positions with fewer coincidence events.

Lastly, the two approaching particles dataset was analyzed with FPI. Using the search radius $w = 3$ and grids of size $1 \times 1 \times 1$ mm^3 and $2 \times 2 \times 2$ mm^3, the two particles were resolved down to a separation of 2.7 mm and 4.5 mm, respectively. Recall that using a

$2 \times 2 \times 2$ mm^3 grid, G-means resolved particles down to a 5 mm separation. These minimum resolved separations are slightly lower than the values of 3 mm and 6 mm expected based on the selected search radius and mesh size. It is believed that the nearness of the two particles resulted in a biasing during the position refinement step, with initial particle guesses outside the expected resolving limit, and final particle positions shifted toward the center of the two-particle system during the refinement step.

3.2.2 GATE Simulation Testing

In order to further test the FPI and G-means methods for higher particle numbers, a GEANT4 Application for Tomographic Emission (GATE) [60] model of a Siemens Inveon PET scanner [31] developed by Lee et al. [61] was employed. The Inveon is a different preclinical PET scanner of cylindrical geometry and is further described in Section 5.1. An image of the model geometry is shown in Figure 3.7. Simulations were conducted using 25, 50, 75, and 100 particles randomly distributed in a cylinder of water of diameter 80 mm and length 80 mm centered in the bore of the scanner and aligned axially with the scanner bore. The simulated particles were ^{22}Na point sources of activity 5 μCi each in cubic volumes of side length 0.5 mm. Energy blurring was induced via random assignment of detector resolution between 15% and 35% based on a reference energy of 511 keV. In each case, the particles were left stationary and scanned for 10 s using an acquisition energy window of 425-625 keV and the default coincidence timing window of 3.432 ns.

It should be noted that such GATE models have been seen to overpredict the number of CL generated by a source during a scan [62, 25]. Lee et al. [25] determined the magnitude of this overprediction and rejected a number of the simulated CL based on a Bernoulli random process. In the case of our work, simulated dead time began to affect the outcomes of the simulations with higher particle numbers, making rejection of events in post-processing unphysical. For this reason, all CL generated by GATE were kept, but results will be cited in terms of the number of CL used for particle location, not the actual activity of the particles.

For each of the four aforementioned cases, particle locations were determined using both G-means and FPI with 100 ms time steps. For the 25, 50, 75, and 100 particle cases, this resulted in an average of 1012, 770, 575, and 417 CL used per particle per time step for

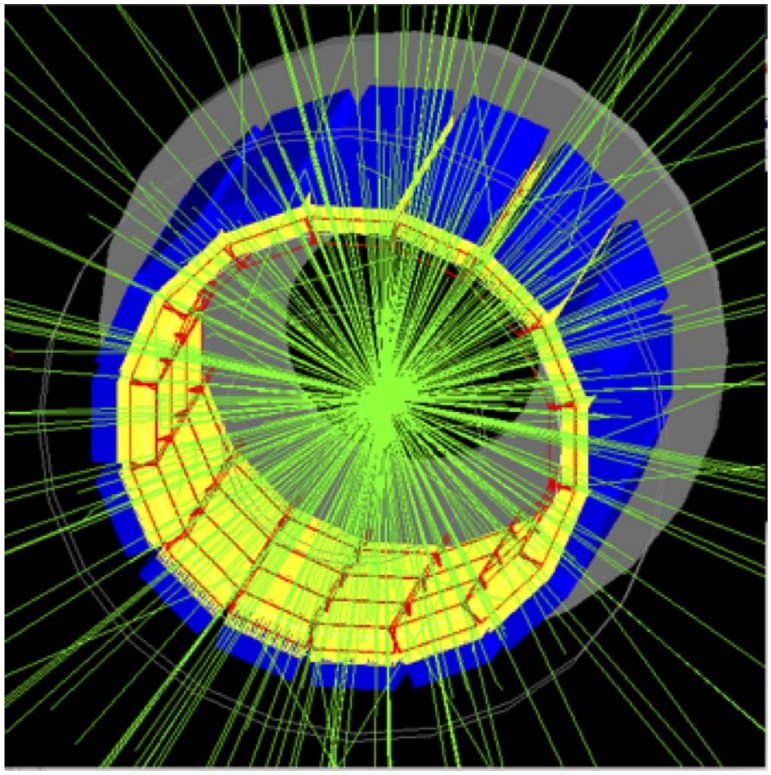

Figure 3.7: Geometry of GATE model of Siemens Inveon PET scanner. Gamma rays are shown as generated by a source particle in the center of the FOV of the scanner.

Table 3.1: A comparison of results obtained for simulated multiple particle tracking using G-Means and FPI methods. All results obtained using CL time slices of 100 ms tallied over $0.5 \times 0.5 \times 0.5$ mm^3 grid.

	G − Means				
Number of Particles	Found	Gaps	Δx(mm)	Δy(mm)	Δz(mm)
25	25	13	0.28	0.25	0.26
50	46	6	0.21	0.29	0.22
75	60	8	0.32	0.38	0.30
100	13	2	0.28	0.22	0.22
	FPI				
Number of Particles	Found	Gaps	Δx(mm)	Δy(mm)	Δz(mm)
25	25	0	0.11	0.12	0.14
50	50	0	0.14	0.17	0.19
75	75	0	0.16	0.19	0.23
100	100	8	0.26	0.27	0.33

location, respectively. In both methods, a $0.5 \times 0.5 \times 0.5$ mm^3 grid was used for CL crossing tallying, along with a filtering value of $r = 0.3$. For all cases, G-means used an A-D critical value of 10, and FPI used parameters $f = 1$ and $w = 6$.

Results were evaluated based on the number of particles found and the continuity and accuracy of the detection. In these simulations, a particle was deemed "found" if it was located at least 20 times in the 100-frame set, and these locations were properly associated to the same particle by a common linking algorithm. In this way, any detected short, spurious trajectories were treated as false positives and rejected. Furthermore, instances where a given particle was tracked in time, lost for a number of time steps, and then found again were treated as "gaps" in trajectories. Accuracy was determined in the x- (radial, horizontal) direction by comparing the measured position of each particle, $x_{m,i}$, to that of the original simulated position, $x_{s,i}$ by

$$\Delta x = \sqrt{\frac{1}{N}\sum_{i=1}^{N}(x_{m,i} - x_{s,i})^2} \tag{3.8}$$

and similarly for the y (radial, vertical) and z (axial, horizontal) directions, where N is the number of detections of a given particle. A summary of results is given in Table 3.1.

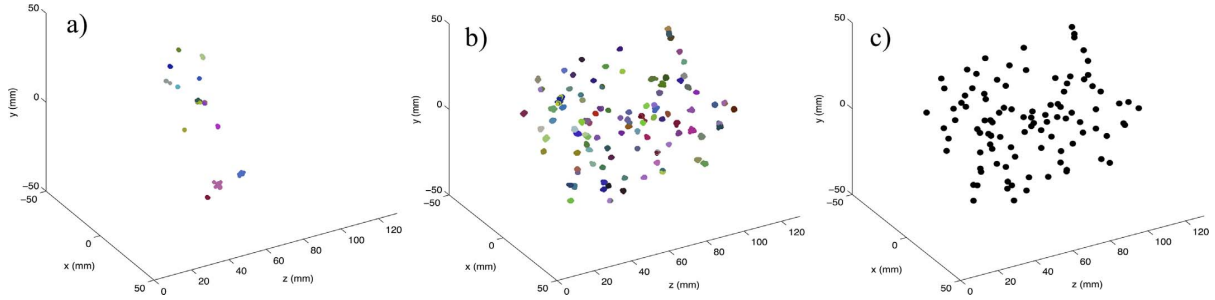

Figure 3.8: Particle positions from 100 particle GATE simulation as measured by G-means (a) and FPI (b) methods using 100 ms time steps and $0.5 \times 0.5 \times 0.5$ mm^3 grid. Each different color indicates a different particle, as measured. Panel (c) shows the true particle positions input into GATE.

It can be seen that the FPI method was more capable of finding individual particles, with G-means showing extreme deterioration in the 100 particle case. Furthermore, in all but the 100 particle case, FPI also outperformed G-means in terms of gaps in tracking and average measurement accuracy, with the comparison between the 100 particle cases being skewed by the disparity of particles detected by G-means. The requirement that all trajectories must be at least 20 frames long eliminated all false positives for both methods. For a visual comparison of results, Figure 3.8 shows the particles detected by G-means and FPI along with true particle positions for the 100 particle case. It is easily observed that the FPI reconstruction of the particle distribution closely resembles the true particle distribution, while G-means only captures a fraction of the distribution.

For previous PEPT methods, it has been shown or postulated that accuracy varies as $1/\sqrt{N}$ where N is the average number of CL used for each detection [7, 11]. To asses this for the FPI method, these four GATE simulations were further examined using varying time steps. All other detection parameters were held the same as the previous test, but time steps were varied from 10 ms to 100 ms in 10 ms steps. The accuracy of the measurement was then assessed via the average of total detection error

$$\Delta r = \sqrt{\Delta x^2 + \Delta y^2 + \Delta z^2} \tag{3.9}$$

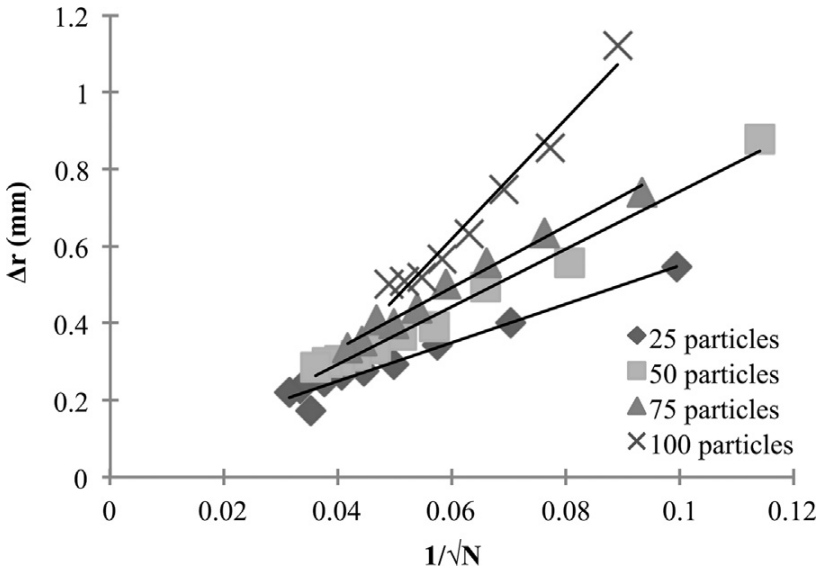

Figure 3.9: Location accuracy variation with inverse square root of average number of CL used in each time step for multiple particle measurements with FPI using $0.5 \times 0.5 \times 0.5$ mm^3 grid.

over all particles. Figure 3.9 shows the average error for each run plotted against the inverse of the square root of the average number of CL used for detection, with trendlines added. For the 100 particle simulation with 10 ms and 20 ms time steps and the 75 particle simulation with 10 ms time steps, results were exceptionally poor and deemed unusable. For this reason, these three cases are omitted from this figure and the following discussion.

Here, one can see that in each case, average error varied linearly with $1/\sqrt{N}$, as expected, with linear fits to the 25, 50, 75, and 100 particle cases having R^2 values of 0.97, 0.99, 0.99, and 0.97, respectively. Also, it is seen that this dependence was stronger for higher particle cases; however, the constant of proportionality is still unknown and is expected to be a function of many factors (number of particles, velocity, scanner geometry, test section materials, parameters f and w, etc.). A user must select time steps that allow for time resolution suitable for a given application while maintaining an ample number of CL per time step for location accuracy.

3.2.3 Moving Particle Test

An experiment was performed to test the ability of the FPI method to track particles with circular motion, similar to those performed in tests of previous PEPT methods [7, 11]. In this experiment, two ^{22}Na sources of activity 7 μCi each were attached to the ends of a rod, and the rod was rotated about a point near its midpoint with a drill. An acquisition scan was performed in a Siemens Inveon preclinical PET scanner with the drill mounted to the bed of the scanner and the sources inside the scanner bore. The axis of rotation was aligned with the axis of symmetry of the scanner bore. The radii of rotation of the two particles were measured with a caliper and found to be 26 $\pm$ 2 mm and 24 $\pm$ 2 mm. The particle at the larger radius will be referred to as "particle 1" and the other as "particle 2". The uncertainty was due to uncertainty of the exact location of the sources within their mounts. The frequency of rotation was measured with a laser triggering system and found to be 6.9 Hz. As such, the expected velocities of the two particles were 1.1 $\pm$ 0.1 m/s and 1.0 $\pm$ 0.1 m/s, and the expected accelerations were 48 $\pm$ 4 m/s^2 and 43 $\pm$ 4 m/s^2, respectively.

PEPT data were analyzed with FPI in time steps of 3 ms, resulting in the use of 30 CL per particle per detection, on average. CL crossings were tallied across a $1 \times 1 \times 1$ mm^3 grid, and FPI parameters of $r = 0.4$, $f = 1$, and $w = 10$ are used. 3D representations of the measured trajectories and a sample of the measured radial coordinates (x and y) of the particles are seen in Figure 3.10.

Here it can be seen that the FPI method is capable of tracking the motion of the particles. The x and y coordinates of each particle were fitted to functions of the form

$$x = x_0 + R\cos(\omega t + \phi) \tag{3.10}$$

$$y = y_0 + R\sin(\omega t + \phi). \tag{3.11}$$

Best fit curves are shown in Figure 3.10. The radii of the trajectories measured via this best fit were 23.9 mm for particle 1 and 23 mm for particle 2. Such a slight underprediction of the radius of particle 1 may be caused by the motion of a particle in an arc during a finite

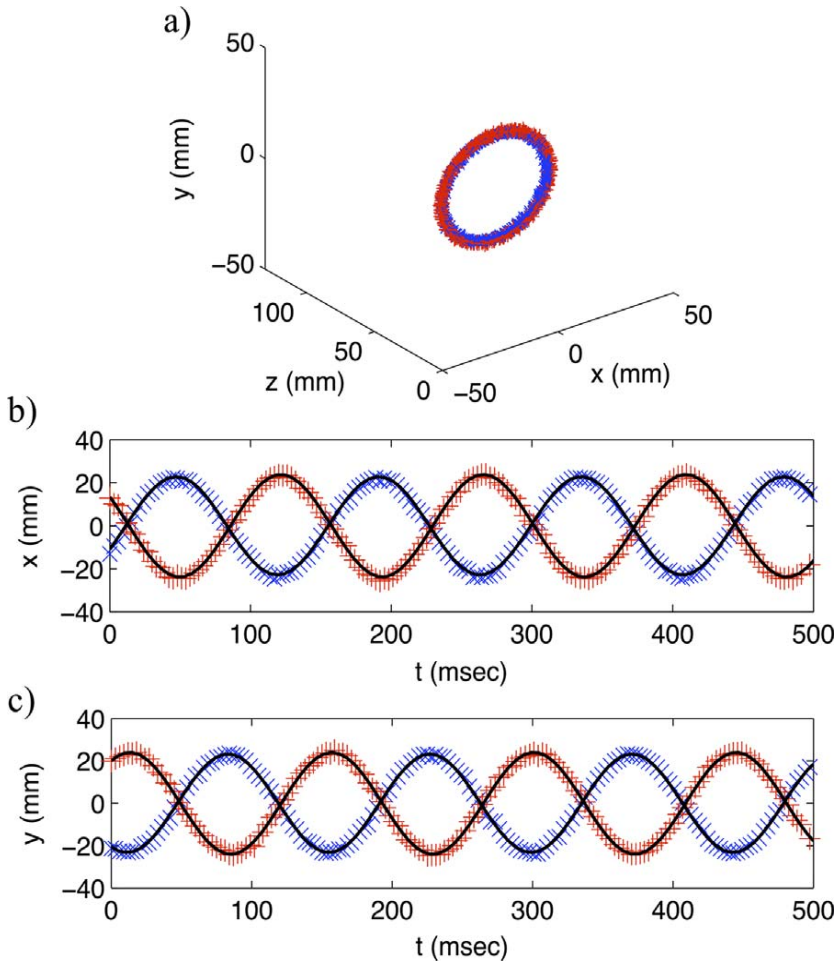

Figure 3.10: Trajectories measured in rotating particle experiments for particle 1 (red +) and particle 2 (blue ×). Shown are 3D representation (a) and radial coordinates, x (b) and y (c), over the first 1/2-second of measurement with sinusoidal trendlines in black.

time biasing the centroid of its CL distribution radially inwardly, as predicted by Parker et al.[7]. It is also known that in PET measurements, there is a biasing of measurement toward the radial center of the scanner that increases as one moves away from the radial center due to the depth of interaction of photons within detector crystals [63]. The latter effect is dealt with later in this work (see Section 6.2).

To make use of PEPT for Lagrangian flow measurements, velocity and acceleration must be extracted from measured trajectories. Voth et al. [64] emphasize that one must use a low-pass filter on position data before using it for calculation of velocity and acceleration information. Both the filtering and differentiation of the position signal can be achieved via convolution with Gaussian kernels, as was done by Mordant et al. [65]. Kernels of the form

$$k(\tau) = A \exp\left(-\frac{\tau^2}{\sigma^2}\right) \tag{3.12}$$

$$k'(\tau) = A'\tau \exp\left(-\frac{\tau^2}{\sigma^2}\right) \tag{3.13}$$

$$k''(\tau) = A''\left(\frac{2\tau^2}{\sigma^2} - 1\right) \exp\left(-\frac{\tau^2}{\sigma^2}\right) + B \tag{3.14}$$

are used to find filtered position, velocity, and acceleration, respectively. Here normalization constants are selected so that $k \star 1 = 1$, $k' \star \tau = 1$, $k'' \star 1 = 0$, and $k'' \star \tau^2 = 2$, i.e. proper filtering and first and second derivatives of simple functions are achieved, where "$\star$" is the convolution operation. The filter width, σ, can be adjusted for best results, as shown by Berg et al. [66].

The previously shown rotating particle data were filtered and differentiated in this way. The filtered position, velocity and acceleration time histories of particle 1, with sinusoidal trend lines added, are seen in Figure 3.11. Here, convolution has been performed with kernels of filter width $\sigma = 2$ time steps.

Velocity and acceleration values were obtained from sinusoidal fits to data and found to be 1.0 m/s and 45.4 m/s^2 for particle 1 and 0.99 m/s and 43.7 m/s^2 for particle 2, respectively. These agree with the values expected from the measured particle radii and drill frequency, within uncertainty.

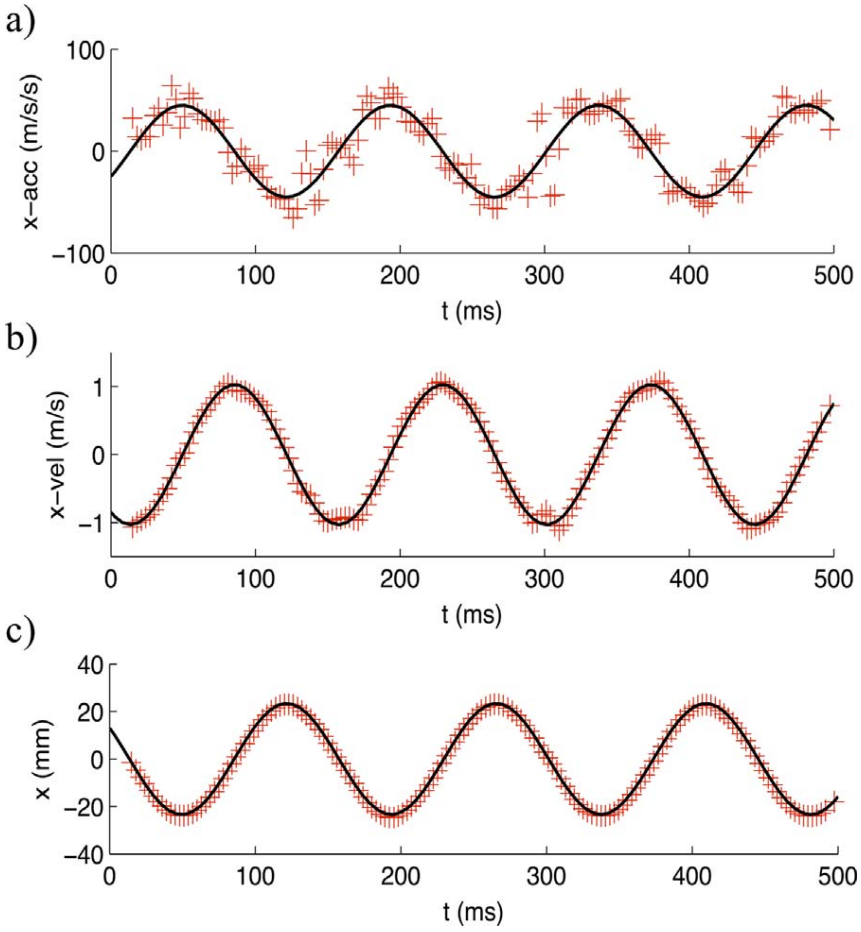

Figure 3.11: Measured acceleration (a), velocity (b), and filtered position (c) of particle 1 in rotating particle experiment with sinusoidal trend line shown in black. Data are obtained via convolution with Gaussian kernels of filter-width $\sigma = 2$.

It is seen in Figure 3.11 that there was a large amount of erraticism in the differentiated data, especially acceleration. This is expected for the calculation of derivatives, and finer time resolution is desired to reduce noise in measurements of fluid velocity and acceleration. In order to achieve this, higher activity tracer particles are used in physical measurements. In this experiment, sources were of activity 7 μCi, while in flow experiments, tracers are usually of order 50-1000 μCi.

3.3 Trajectory Linking

After particles are located, particles from individual time steps must be linked together into trajectories. The earliest linking method employed by our group is described by the author in [48]. Particle linking is performed on a frame-by-frame basis by finding the particle matching that reduces the overall sum of displacements between particle pairs. Consider two consecutive time frames t_k and t_{k+1}, having n and m particles, respectively. In each of these frames are particle positions $\mathbf{x}_i$ and $\mathbf{y}_j$, respectively, with $i = (1, 2, ..., n)$, and $j = (1, 2, ..., m)$. We do not assume $m = n$ so that particles entering and leaving the FOV can be properly addressed. A cost matrix c_{ij} is defined by the displacement for each possible particle pairing between frames t_k and t_{k+1},

$$c_{ij} = |\mathbf{x}_i - \mathbf{y}_j| \tag{3.15}$$

Using the time steps over which CL are collected and a maximum velocity, v_{max}, as input by the user, a maximum cost, c_{max}, is calculated for linking as

$$c_{max} = (t_{k+1} - t_k) \times v_{max}. \tag{3.16}$$

In the case that $m \neq n$, the smaller dimension of c_{ij} is padded with the value c_{max} until it is square. Without loss of generality, assume $m > n$. In this case, we would pad c_{ij} such that

$$c_{ij} = c_{max}; \quad i = (n+1, n+2, ..., m), \;\; j = (1, 2, ..., m). \tag{3.17}$$

After this cost matrix has been created, the well-established Kuhn-Munkres algorithm [67, 68, 69] is used to find the single-link matching pairs that reduce the total cost of this system. If the cost of any individual link is greater than or equal to c_{max}, this link is considered to be false. In the case where $m \neq n$, padding the cost matrix as described above will guarantee that at lease one false-link will be found. In the case of a false-link, the particle in frame t_{k+1} is considered a new particle, and a new trajectory is begun. A "ghost" particle is then inserted into frame t_{k+1} at the position of the unlinked particle from frame t_k that will then be used for linking between frames t_{k+1} and t_{k+2}. The time difference $t_{k+2} - t_k$ will be used when determining the appropriate maximum cost for this particle. Using this ghost particle technique, occlusion in trajectories can be accounted for up to some number of user defined frames (usually 2-5 time steps). If no match is found for a particle after this many frames, the trajectory is ended. All ghost particles are removed from final time histories of particles, meaning that only true detections of particles are used in final data analysis.

For most cases, this method of two-frame, nearest-neighbors linking is adequate and preferred due to its simplicity over more robust four-frame methods [70] or methods based on local smoothness [71, 72]. For the case of more complicated flows with larger particle numbers, a modification has been made to this method that uses information across multiple frames, similar to the method of Hassan and Canaan [70] and described by Patel et al. [73]. The two frames t_k and t_{k+1} are considered as before. Now, for each particle position $\mathbf{x}_i$, $i = (1, 2, ..., n)$ in frame t_k, let l_i be the number of histories in the trajectory corresponding to $\mathbf{x}_i$. For each position, its location in t_{k+1} is estimated as

$$\mathbf{x}_i' = \begin{Bmatrix} \mathbf{x}_i, & l_i = 1 \\ \mathbf{x}_i + \mathbf{v}_i \Delta t, & l_i = 2 \\ \mathbf{x}_i + \mathbf{v}_i \Delta t + \frac{1}{2}\mathbf{a}_i \Delta t^2, & l_i > 2 \end{Bmatrix} \tag{3.18}$$

where $\Delta t = t_{k+1} - t_k$, and $\mathbf{v}_i$ and $\mathbf{a}_i$ are the velocity and acceleration of particle i at time t_k, estimated by backward divided differencing. In other words, the estimated position is taken to be the last position if only one history exists, is estimated based on a velocity projection if two histories exist, and is projected based on velocity and acceleration if more than two histories exist.

Using these projected positions and the measured positions from frame t_{k_1}, the cost matrix c_{ij} is then defined by

$$c_{ij} = |\mathbf{x}'_i - \mathbf{y}_i|, \tag{3.19}$$

and the previously described Kuhn-Munkres algorithm with padding is employed to find the single-link matching pairs that minimize the total cost of the system.

In this case, the maximum allowed cost is defined as

$$c_{max} = k_i \times \Delta t \times v_{max}, \tag{3.20}$$

where k_i is a scalar value that depends on the number of histories of particle i from frame t_k. Typical values used are

$$k_i = \begin{Bmatrix} 1, & l_i = 1 \\ 0.5, & l_i = 2 \\ 0.3, & l_i > 2 \end{Bmatrix}, \tag{3.21}$$

meaning that a stricter cost is imposed for the projected positions. If the cost of any individual link is greater than or equal to c_{max}, the previously described ghost particle procedure is carried out until the trajectory is ended.

In the experiments conducted herein, particles remain in the FOV of the scanner until they have passed through the bore. As such, there is no occlusion from a particle physically going out of frame, as occurs in 2-D particle tracking [58]. Instead, occlusion tends to occur due to a combination of factors. The first of these is similar to the 2-D out-of-frame problem and is due to the sensitivity gradient across the FOV of a scanner, as detailed by Tai et al. [54]. It is possible that a particle can move to an area of the scanner with low sensitivity, causing the CL counts associated with this particle to fall below the filters set on a given time step. As particles pass close to one another, it is also expected that the particle of less activity will not be detected in a given time step but will be located again after the two particles have moved apart. For these reasons, some post-processing is also performed to account for these situations.

After all linking has been performed, trajectories with very few histories are removed from the dataset. The threshold for this operation is usually set to 2-5 time steps (i.e. the

same value used in the ghost particle process) and eliminates the majority of noise caused by spurious detections.

Next, the first and last points of all trajectories are considered. If it is found that any two trajectories are within the maximum displacement allowed by v_{max} and separated in time by less than the ghost particle inclusion limit, these two trajectories are linked into one. In the case that their time difference is zero, the average position of the two locations is used in the splicing. An example of this is shown in Figure 3.12. Such a situation is usually caused by false-positive detection in the near vicinity of a true (or projected) particle, causing a link to be established between a trajectory in a previous frame and this false-positive. This will result in a slight kink in the trajectory, but as the acceptance criteria for relinking is based on v_{max}, the magnitude of the kink will be less than level of noise accepted in the normal linking step, and the kink will be mostly removed during trajectory smoothing.

After this relinking step is performed, a stricter filter is applied to each dataset that eliminates trajectories of fewer histories than a larger threshold (usually 10 to 20). This eliminates any remaining spurious trajectories from the dataset. When setting this threshold, a user must be aware of the expected number of time steps a particle will be in the FOV of the detector system and make sure the threshold is set well below this value. This final, more strict filtering will decrease the chance of false-positive trajectories but will increase the chance of true-negatives. In most cases, it is desired that no (or very few) false-positives enter the final statistical analysis, and the loss of a few true trajectories is accepted. If the opposite outcome is desired, this final filtering step can be skipped by a user.

When selecting a value for v_{max}, it is important that the user has an idea of the maximum physical velocity that will be present in the flow being studied and sets v_{max} to be just above this value. However, in the case of very slow moving flows, this heuristic often fails. For most studies, the average uncertainty of M-PEPT reconstruction has been seen to be of order 0.5 mm. If the frequency of detection and speed of flow are such that particles move less than this between each time step, one should adjust v_{max} such that $(v_{max} \times t_{step})$ is greater than 0.5 mm. If larger uncertainties are observed in an experiment, v_{max} should be further increased.

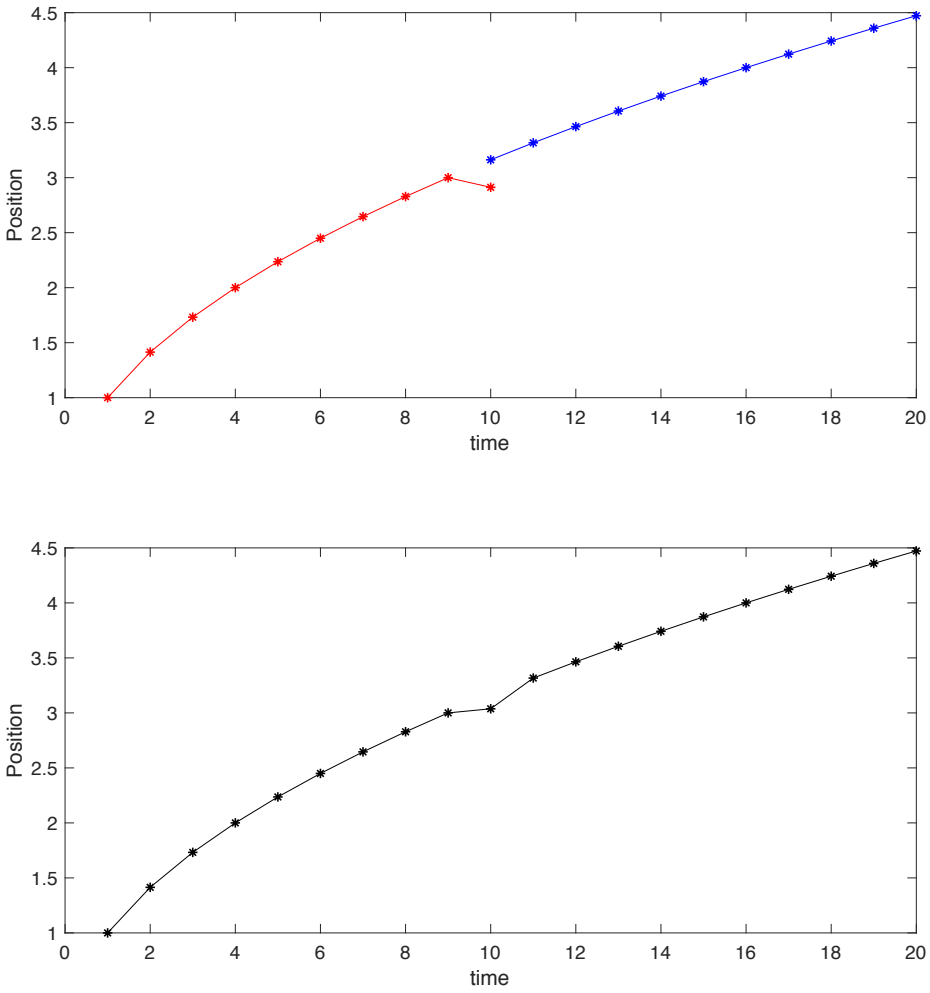

Figure 3.12: Example of re-linking step. Two trajectories shown in top frame are merged into single trajectory in bottom frame.

Chapter 4

M-PEPT Measurements

A number of measurements have been performed with the M-PEPT methods described herein. As a major purpose of this dissertation is the introduction of these methods, selected experiments are presented that highlight the capabilities of M-PEPT. For information on other experiments conducted during the term of this study, the reader is referred to Appendix A. Unless otherwise stated, the author led or assisted in preparing and performing each of these experiments. In all cases, the author performed M-PEPT reconstruction of particle trajectories and subsequent analysis.

4.1 Rectangular Channel

While the FPI method has largely replaced G-means for M-PEPT analysis, the G-means method has been used for analysis of two PEPT experiments. The first of these is detailed here, and the second is described in Appendix A. This experiment is significant in that it was the first experiment to implement multiple-particle tracking with arbitrary numbers of particles for fluid flow measurement and was validated against optical particle tracking measurements.

In this experiment (performed by Langford, Tenpenny, and Ruggles and analyzed by the author) once-through flow in a rectangular test section of cross section 19.05 mm $\times$ 57.15 mm was examined using a MicroPET P4 PET scanner [74]. This test section and the scanner are shown in Figure 4.1.

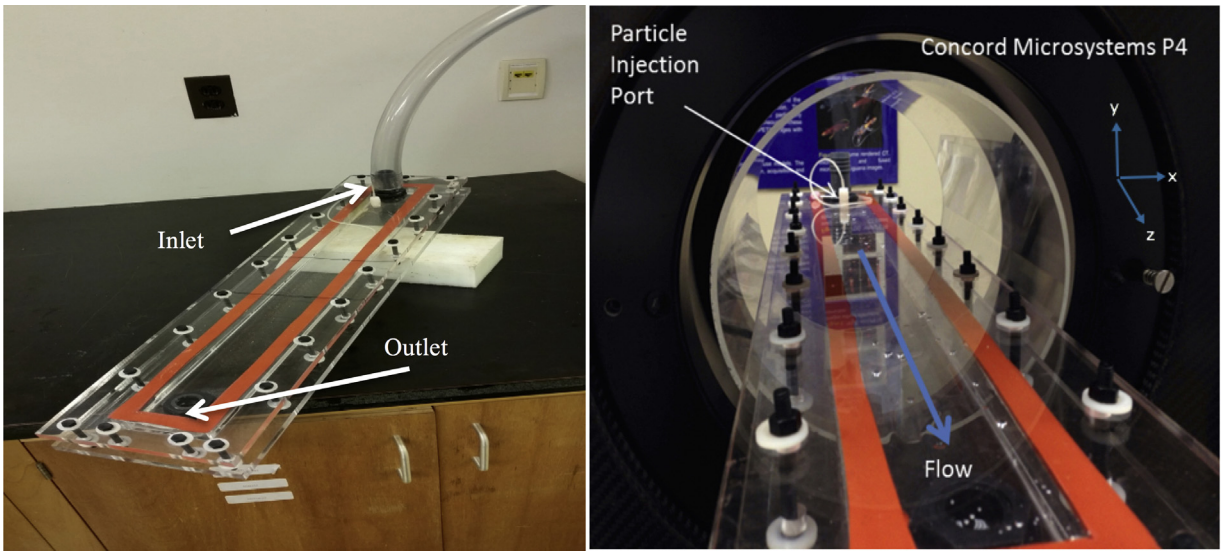

Figure 4.1: Rectangular test section as seen from perspective view (left) and in the bore of the P4 scanner (right).

Water was used as the working fluid, and flow was driven by a centrifugal pump at a mean velocity of 0.38± 0.01 m/s, resulting in a Reynolds number of 10,700 ± 300. Roughly 15 particles of activity 1 mCi each were injected into the test section upstream of the scanner FOV. Trajectories were reconstructed using 3 ms time steps, a 2×2×2 mm^3 CL counting grid and an A-D critical value of 12. The resulting trajectories are shown in Figure 4.2. The measured raw trajectories were smoothed using a moving average filter of size 5 time steps, and velocity was calculated along each trajectory by finite differencing.

The trajectories were qualitatively compared to those generated by computational fluid dynamics (CFD). A shear stress turbulence (SST) model of flow through this test section was created using COMSOL Multiphysics. A particle tracking study was included in this model, and both the modeled trajectories and those measured in PEPT revealed the presence of counter-rotating vortices on the outer edges of the test section [75].

This measurement was further validated against optical particle tracking velocimetry (PTV) and particle image velocimetry (PIV) measurements of flow in the same test section. These techniques are optical in nature, with PIV giving a 2-D Eulerian (spatially-fixed) picture of the flow field and PTV giving a 2-D Lagrangian (moving with the flow) picture

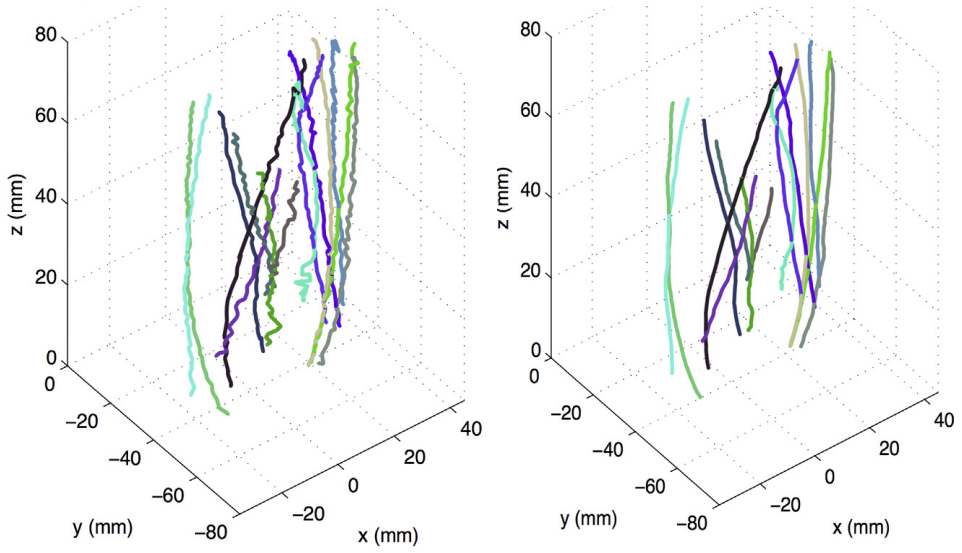

Figure 4.2: Trajectories of particles in rectangular test section measured using PEPT. Left: unfiltered trajectories. Right: Trajectories smoothed using moving-average filter.

of the underlying flow. Similar to PEPT, PTV reconstructs trajectories of individual flow tracers and is expected to offer the most similar results to PEPT.

PEPT, PIV, and PTV measured mean velocities are 0.38±0.09 m/s, 0.37±0.03 m/s, and 0.38±0.07 m/s respectively. Furthermore, the histograms of Lagrangian velocity measured via PEPT and PTV were similar, as seen in Figure 4.3. As PIV is natively Eulerian, a similar histogram of individual particle velocities is not available for PIV. The similarity among the measured mean velocities and between PEPT and PTV velocity distributions suggest the validity of the PEPT method.

4.2 Twisted Tape Swirled Flow

Twisted tape inserts are commonly used to enhance performance in heat transfer devices. Such a device is planned to be used for heat removal from plasma facing components in nuclear fusion reactors W7-X and ITER [76, 77]. Recent computational work by Clark et al. [78, 79] has predicted the presence of secondary flows in pipe flow swirled by a twisted

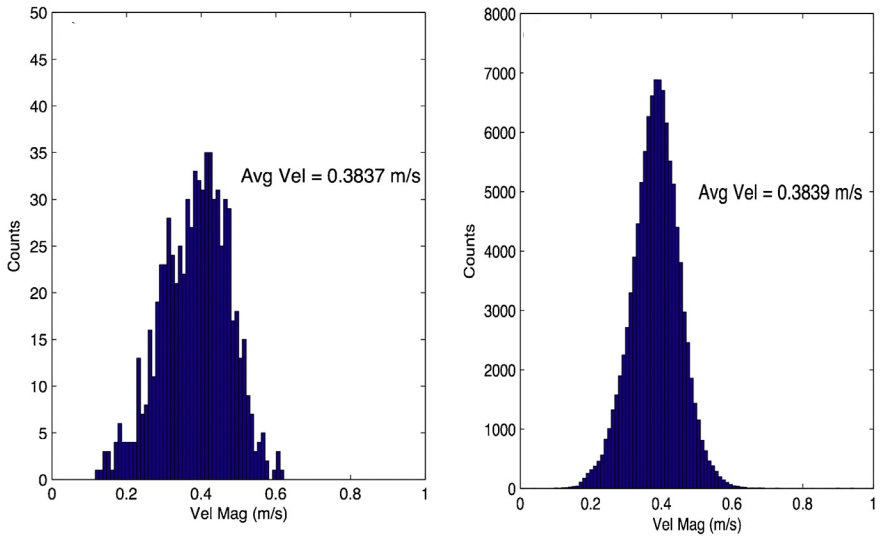

Figure 4.3: Histograms of particle velocity measured in rectangular channel via PEPT (left) and PTV (right).

tape. Such secondary flows can lead to boundary layer separation and local hot spots on pipe walls in high heat flux environments, which could lead to component failure.

Due to the opaque nature of the tape itself, measurement of twisted tape swirled flows is difficult for optical methods. As such, most measurements are of integral quantities such as pressure drop and heat transfer coefficient but neglect local flow information [80]. The ability of PEPT to image in opaque systems poises it as a prime candidate for twisted tape flow measurement. For this reason, a PEPT experiment was devised and performed by the author and others to search for the predicted secondary flows.

4.2.1 Twisted Tape Experiment

A flow loop was constructed to deliver flow of water swirled by a twisted tape insert. The test section consisted of a clear polyvinyl chloride (PVC) pipe of inner diameter 40.9 mm (1.61 in.) with the twisted tape insert shown in Figure 4.4. This tape is made of stainless steel and has a twist ratio of 3 diameters per twist and a diameter of 38.1 mm (1.5 in.). As this is less than the inner diameter of the tube, this experiment is considered a measurement with a loose-fitting twisted tape.

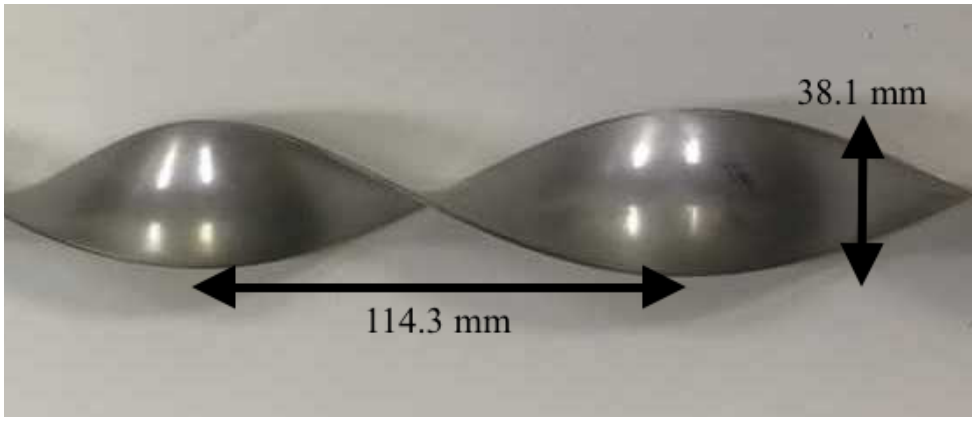

Figure 4.4: Photograph of twisted tape insert.

PEPT measurements were performed with a Siemens Inveon Preclinical PET scanner. The flow tracers were anion exchange resins of mean diameter 690 μm and density 1.2 g/cc activated to 800 μCi with ^{18}F ions. Flow was delivered at 37.9 L/min (10 gal/min), corresponding to a Reynolds number of 13,000, based on the hydraulic diameter of the active flow region. Two experiments were performed at this flow condition, with each consisting of 30 minutes of scanning. The first experiment was carried out with the upstream edge of the scanner bore located 20 pipe diameters (20D) from the start of the twisted tape, and the second was carried out at 30 pipe diameters (30D).

4.2.2 Results

The data were processed using the FPI method with 1 ms time steps and a $1 \times 1 \times 1$ mm^3 grid. After trajectories were reconstructed, a dewarping routine was carried out (see Section 6.2), and data were transformed to the rotating frame of the swirled flow. For the latter operation, maximum and minimum measured x- and y- (radial horizontal and radial vertical) positions were used to find the centerline of the pipe. Using the knowledge that the twist ratio, T, is 3 diameters per twist, measured positions were rotated about the pipe centerline by an angle that varies with the z- (axial) position as

$$\theta = \frac{\pi z}{TD}, \tag{4.1}$$

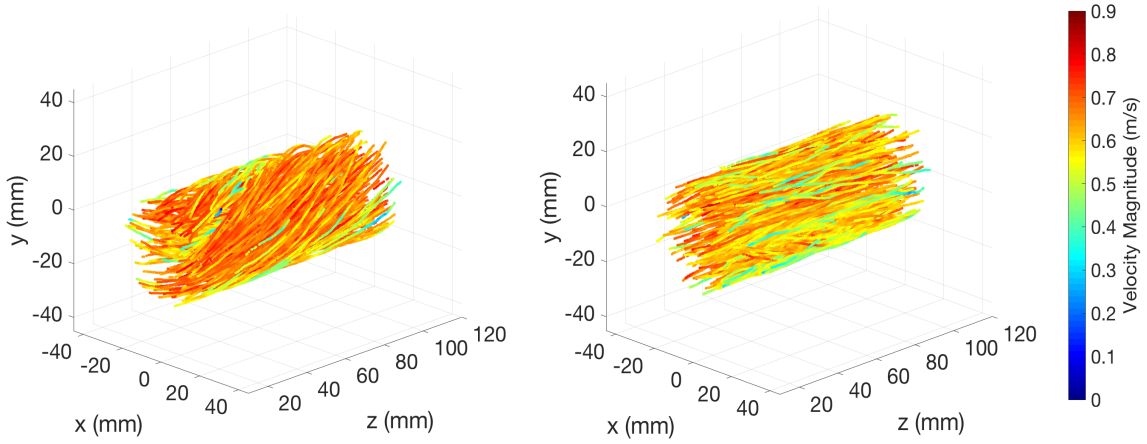

Figure 4.5: Left: first 500 trajectories measured in twisted tape experiment at 20D, colored according to velocity magnitude. Right: same trajectories after transformation to rotating frame.

where z varies from 0 mm at the entrance of the scanner FOV to 127 mm at its far axial edge. The first 500 trajectories measured at the 20 diameter location are shown in Figure 4.5, before and after this unwinding. After this, the Gaussian kernels described in Equations 3.12 and 3.13 were used to smooth the trajectories and calculate instantaneous velocity.

A total of 8,147 trajectories were recorded at 30D, and 12,932 trajectories were recorded at 20D. To examine mean flow characteristics, data were averaged onto a single axial plane and binned onto a grid of 0.5 mm $\times$ 0.5 mm elements to examine mean flow characteristics. Figure 4.6 shows the axial velocity contours at each measurement station. Here it can be seen that the rotation caused the point of maximum flow velocity to shift away from the areal center of each semi-circular region. Furthermore, the flow patterns were not symmetric across the twisted tape divider, likely due to slight differences in the inlet conditions between each channel. It is also evident that some flow patterns have changed between the 20D and 30D cases.

Secondary flows were also measured in this experiment. Figure 4.7 shows the radial velocity at each measurement station. Vortices were observed in the corners of each channel, as evidenced by the overlaid streamlines. Similar to the axial flow, these secondary flows were seen to be asymmetric across the separation and still developing between 20 and 30

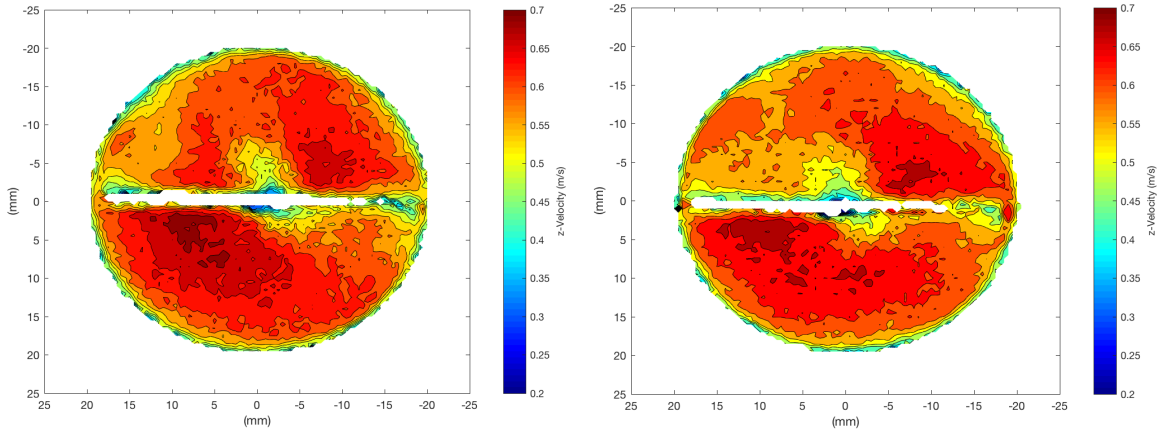

Figure 4.6: Axial velocity contour plot at 20D (left) and 30D (right).

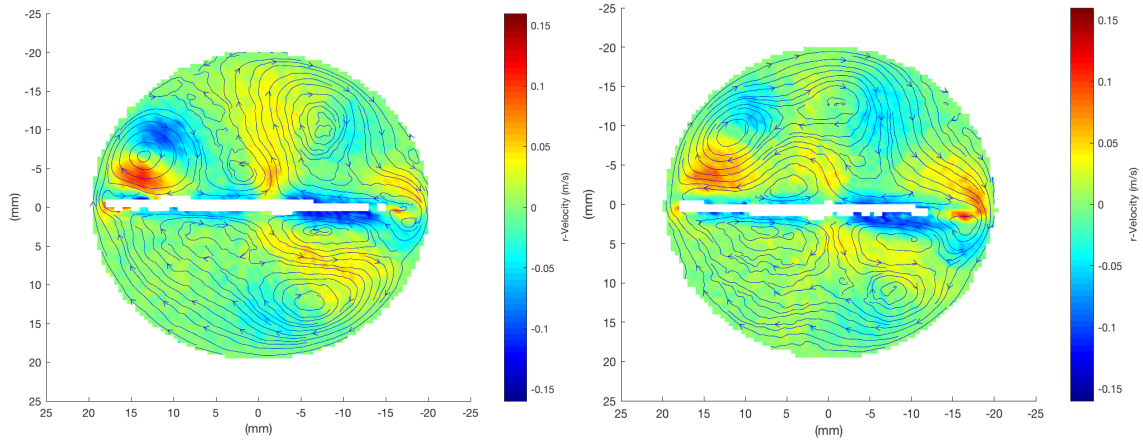

Figure 4.7: Radial velocity at 20D (left) and 30D (right) with streamlines overlaid.

diameters. There are two vortices present in the upper channel (as depicted in Figure 4.7) at 20D that appear to be merging into a single vortex at 30D.

In this measurement, PEPT was used to confirm the presence of asymmetric secondary flows in pipe flow swirled by a twisted tape insert. This is a measurement that has proven prohibitively difficult for optical measurements and highlights the ability of PEPT to image flows lacking optical access. Furthermore, this measurement revealed that the time averaged flow structures in twisted tape swirled flow are not fully developed at 20 diameters, and future work is needed to understand the developing flow region of twisted tape flow.

4.3 Turbulent Pipe Flow

In an experiment conducted by the author and others [81], the capability of M-PEPT for measuring parameters of interest to turbulence modeling were demonstrated via a measurement of turbulent pipe flow. Turbulent pipe flow has been examined since the seminal work of Osborne Reynolds [82] on the transition from laminar to turbulent flow, with more recent work focusing on the dynamics of pipe flow at extremely high Reynolds number [83, 84, 85]. This system is of particular importance for M-PEPT measurement as existing direct numerical simulation (DNS) data [86, 87, 88] can be used to test measurement outcomes. These data were compared to M-PEPT reconstruction of time-average characteristics of the flow-field such as mean velocity, Reynolds stress, turbulent kinetic energy (TKE) budget, and acceleration to test the applicability of M-PEPT for such measurements.

4.3.1 Pipe Flow Experiment

A flow loop was designed to deliver flow of water in a pipe at Reynolds numbers up to 60,000. The test section was a PVC pipe of inner diameter 73.7 mm (2.9 in.) with the center of the measurement volume located 1.84 m (about 25 diameters) downstream of the test section entrance. Measurements were performed with a Siemens Inveon preclinical PET scanner.

Anion exchange resin beads of mean diameter 90 μm and density 1.2 g/cc were used as flow tracers in this experiment. Smaller particles were used to mitigate the inertial response of the particles, quantified by the Stokes number, St, defined as

$$St = \frac{1}{18}\frac{\rho_p}{\rho_f}\left(\frac{d_p}{\eta}\right)^2, \tag{4.2}$$

where ρ_p is the particle density, ρ_f is the fluid density, d_p is the particle diameter, and η is the Kolmogorov length scale. These particles were activated with ^{18}F to 50 μCi per particle. As shear flow was studied in this work, dissipation rate ϵ and subsequently the length scale η varied radially within the pipe. St was determined using $\eta = \left(\frac{\nu^3}{\epsilon}\right)^{1/4}$ based on the average value of ϵ and the kinematic viscosity ν of water. ϵ was determined via a balance of the TKE

Table 4.1: Flow conditions for PEPT pipe flow experiment. Listed values for Re_λ, η, and τ are averages for $y^+ > 200$.

Experimental Condition	Value
Bulk Reynolds Number, Re_D	42,600
Average Flow Speed (m/s)	0.50
Scan Time (min.)	30
Tracer Diameter (μm)	90
Number of Tracers	$\sim$325
Activity per Tracer (μCi)	50
Temperature, T (^{o}C)	26
Kinematic Viscosity, ν (m^2/s)	8.7×10^{-7}
Friction Velocity, u_τ (m/s)	0.026
Friction Reynolds Number, Re_τ	1100
Taylor Scale Reynolds Number, Re_λ	240
Kolmogorov Length Scale, η (μm)	130
Kolmogorov Time Scale, τ_η (ms)	22
Stokes Number, St	0.032

budget. St was found to be 0.032. As $St << 1$, these tracers were considered fluid tracers, and inertial effects were ignored.

The details of the flow conditions in this experiment are given in Table 4.1. The friction velocity, u_τ, is used to nondimensionalize the distance from the wall as $y^+ = (R - r)/\frac{u_\tau}{\nu}$, where r is the radial coordinate, and R is the pipe radius. Listed values of Taylor-scale Reynolds number (Re_λ), Kolmogorov length scale (η), and Kolmogorov time scale (τ_η) are average values for flow away from the wall ($y^+ > 200$).

At the start of this experiment, water was circulated for 2 hours to allow the water temperature to equilibrate. A bulk flow velocity of 0.50 m/s, corresponding to a Reynolds number of 42,600, was chosen to facilitate comparison to the DNS data of El Khuory et al. [87] (Re=37,700) and Wu and Moin [86] (Re=44,000). Coincidence event scans were performed with a coincidence window of 3.438 ns and energy window of 425-625 keV.

After data collection, trajectories were reconstructed using the FPI method with a $1 \times 1 \times 1$ mm^3 grid. Overlapping time steps were employed for this reconstruction, as done by the author's group [89]. 5 ms of data were used with 4 ms overlap between time steps. In this way, 5 ms of CL data were used for each position determination, but an effective time resolution of 1 ms was achieved. This creates the effect of a moving average filter on

the underlying data, but as the overall window size was smaller than the Kolmogorov time ($\tau_\eta = 22$ ms), it is not expected that this intrinsic filter negatively impacted results. The use of this 1 ms effective time steps reduced between-frame displacement of particles and aided in the linking process. The average data rate observed across the duration of this experiment was 44 CL per particle per millisecond, implying an average of 220 events used for each individual particle position reconstruction.

Dewarping was performed to correct for the photon depth of interaction defect described in Section 6.2. Trajectories were then translated and rotated such that the centerline of the pipe was aligned to the z-axis, where the z-direction is the axial direction, and the x- (y-) direction is the horizontal (vertical) radial direction. Filtering and differentiation were performed via convolution with the Gaussian kernels described by Equations 3.12-3.14.

4.3.2 Results

After all processing, a total of 4,024 trajectories were recorded, corresponding to 5.2×10^5 individual position, velocity, and acceleration measurements. Figure 4.8 shows the first 500 measured trajectories before and after dewarping, filtering, and differentiation. Average uncertainties of position locations were calculated as 0.165 mm, 0.165 mm, and 0.132 mm, in the x-, y-, and z-directions, respectively.

Velocity data were sorted into radial bins and averaged to examine radial distributions of various quantities. Radial bins were sized such that each bin contained an equal fraction of the cross-sectional area of the pipe. The bins can be viewed as annuli bounded by circles of radii

$$r_i = \left\{0, \frac{1}{\sqrt{N}}R,\ \frac{1}{\sqrt{N}}\sqrt{2}R,\ ...,\ \frac{1}{\sqrt{N}}\sqrt{N-1}R,\ R\right\}, \tag{4.3}$$

where N is the number of bins used, and R is the radius of the pipe. A total of 50 radial bins were used for averaging, resulting in bins of radial extent ranging from 5.2 mm at the pipe centerline to 0.37 mm at the wall. An even distribution of traces in bins was observed, as desired.

Average velocity is shown as a function of distance from the wall in Figure 4.9. The data were normalized by the friction velocity, u_τ, and kinematic viscosity, μ, listed in

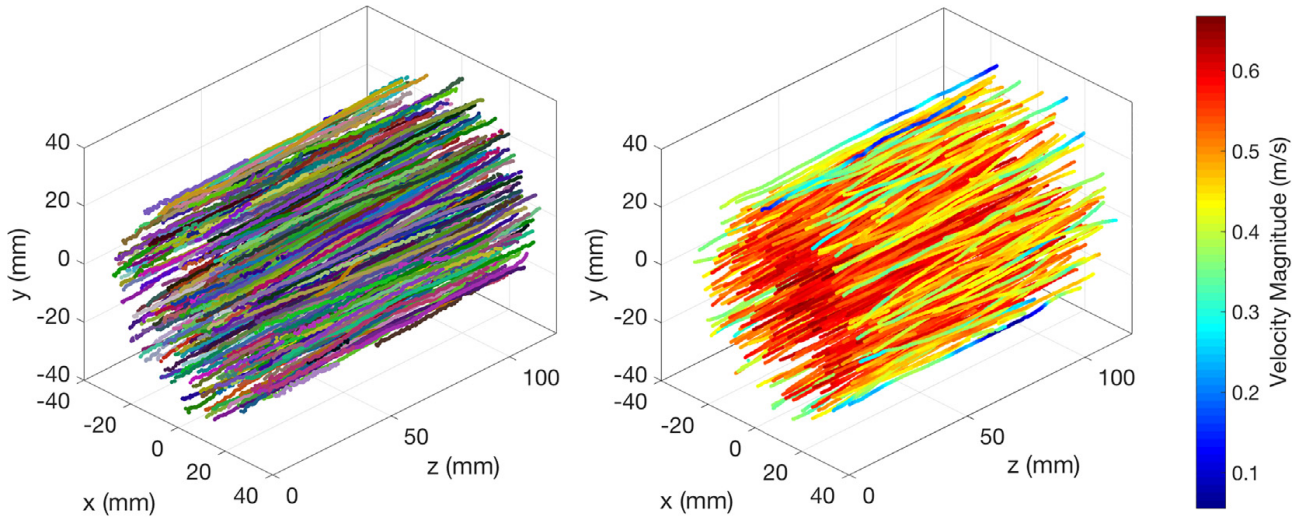

Figure 4.8: First 500 trajectories measured via PEPT in pipe flow experiment before (left) and after (right) dewarping and filtering. In left frame, different colors indicate different trajectories. In right frame, colors indicate instantaneous velocity magnitude.

Table 4.1. DNS data of El Khuory et al. [87] and Wu and Moin [86] are shown for reference. As these data were from direct numerical solutions of the Navier-Stokes equations with no modeling assumptions, they can be considered adequate benchmarks against which to validate. Furthermore, these two DNS datasets agree well outside a slight deviation at the centerline, and the dataset of Wu and Moin [86] has itself been validated against the Princeton Superpipe data of Zagarola and Smits [90]. PEPT data matched DNS data well throughout, with the largest discrepancy occurring at the point nearest the wall.

The next quantities considered were the Reynolds stresses, $\langle u_i' u_j' \rangle$, where the Reynolds decomposition $u_i = U_i + u_i'$, with instantaneous velocity u_i and mean velocity U_i, has been employed. Here, $\langle \cdot \rangle$ indicates an ensemble average. For pipe flow, the only nonzero off-diagonal term in this matrix is the term $\langle u_r' u_z' \rangle$. Measured Reynolds stress profiles are shown in Figure 4.10, with comparison to DNS data. Here, it is seen that Reynolds stress profiles agreed well throughout, with the exception of a major discrepancy between measurement and DNS for the axial (z) component in the near wall region. It is believed that this was largely due to the inability to resolve the mean velocity in the near-wall region, causing further error in the evaluation of fluctuations about that mean.

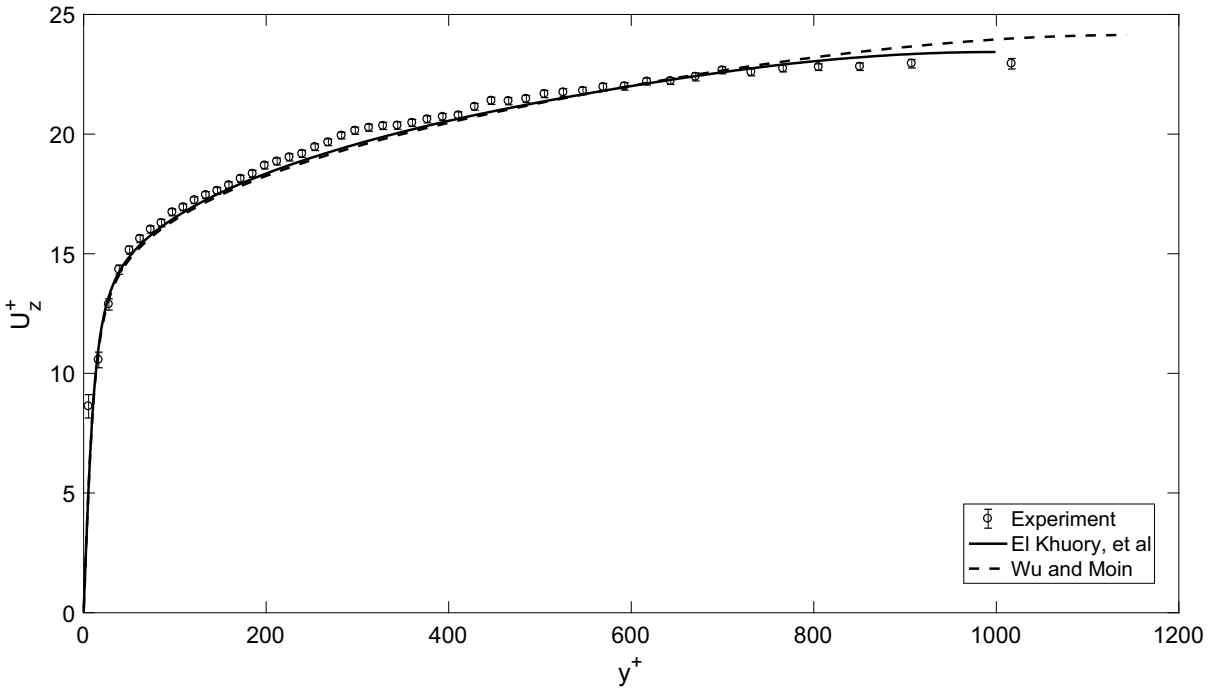

Figure 4.9: Comparison of mean axial velocity measured with PEPT (symbols) to that of DNS of El Khuory et al. [87] (solid line) and Wu and Moin [86] (dashed line) as a function of distance from the wall. Velocity is normalized as $u^+ = u/u_\tau$. Positions are normalized as $y^+ = y/(\frac{u_\tau}{\nu})$, where y is the distance from the wall.

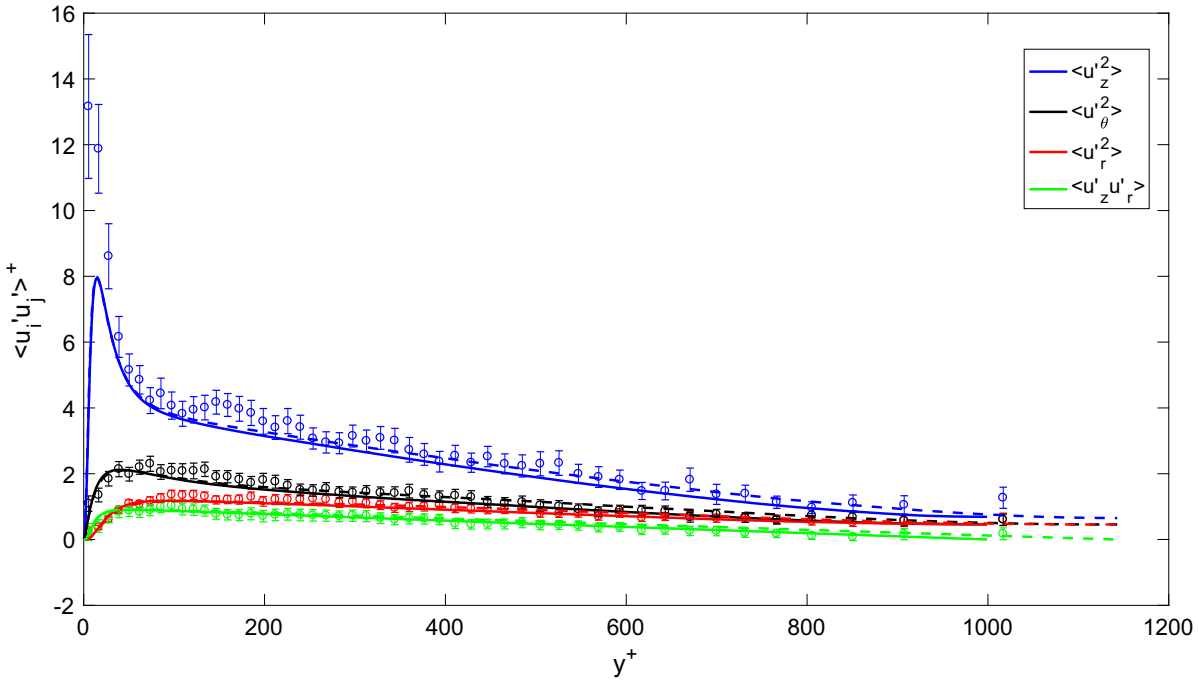

Figure 4.10: Comparison of Reynolds stresses measured with PEPT (symbols) to those of DNS of El Khuory et al. [87] (solid line) and Wu and Moin[86] (dashed line) as a function of distance from the wall. Reynolds stresses are normalized as $\langle u_i' u_j' \rangle^+ = \langle u_i' u_j' \rangle / u_\tau^2$. Positions are normalized as $y^+ = y/(\frac{u_\tau}{\nu})$, where y is the distance from the wall.

Key terms in the turbulent kinetic energy (TKE) budget were also calculated. TKE is defined as $k = \frac{1}{2}\langle u_i' u_i' \rangle$, where the Einstein summation convention is assumed for tensors. The equation governing the evolution of this quantity can be derived directly from the Reynolds-averaged Navier-Stokes equations as

$$\frac{Dk}{Dt} = P^k + \epsilon + \Pi^k + D^k + T^k, \tag{4.4}$$

where $\frac{D}{Dt} = \frac{\partial}{\partial t} + U_i \frac{\partial}{\partial x_i}$ is the mean-flow material derivative, $P^k = -\langle u_i' u_j' \rangle \frac{\partial U_i}{\partial x_j}$ is production, $\epsilon = -\nu \langle \frac{\partial u_i'}{\partial x_j'} \frac{\partial u_i'}{\partial x_j} \rangle$ is dissipation, $\Pi^k = -\frac{1}{\rho} \frac{\partial \langle p' u_i' \rangle}{\partial x_j}$ is pressure diffusion, $D^k = \frac{\nu}{2} \frac{\partial^2 \langle u_i' u_i' \rangle}{\partial x_j^2}$ is viscous diffusion, and $T^k = -\frac{1}{2} \frac{\partial \langle u_i' u_i' u_j' \rangle}{\partial x_j}$ is turbulent diffusion. Using PEPT data, the terms P^k, D^k, and T^k were measurable. In this analysis, the turbulence was considered steady $\left(\frac{Dk}{Dt} = 0\right)$ and the term Π^k was neglected, as the DNS data show it to be negligible throughout the pipe. As such, dissipation was calculated as the balance of the remaining TKE budget terms,

$$\epsilon = -P^k - D^k - T^k. \tag{4.5}$$

Figure 4.11 shows the measured TKE budget profiles compared to the DNS results of El Khuory et al. [87]. The DNS of Wu and Moin [86] were not considered in this analysis, as they did not present a TKE budget. These profiles have been expanded near the wall to reveal features. Measured profiles matched simulated profiles well for $y^+ > 50$. Below this, the profiles maintained the qualitative shape of those seen in simulation, but discrepancies began to appear in all terms. The matching of the measured and simulated dissipation in the turbulent core of the flow corroborated the estimation of the mean dissipation rate for this system by PEPT measurements.

As PEPT data are natively Lagrangian, differentiation can be performed twice along trajectories to yield time-resolved acceleration information. Acceleration data were sorted into the radial bins described by Equation 4.3, and radial profiles of the mean acceleration A_i and mean-squared fluctuation $\langle a_i'^2 \rangle$ are plotted in Figures 4.12 and 4.13, respectively, where the Reynolds decomposition has been once again employed to described the instantaneous acceleration. These data were compared to the DNS results of Stelzenmuller et al. [88],

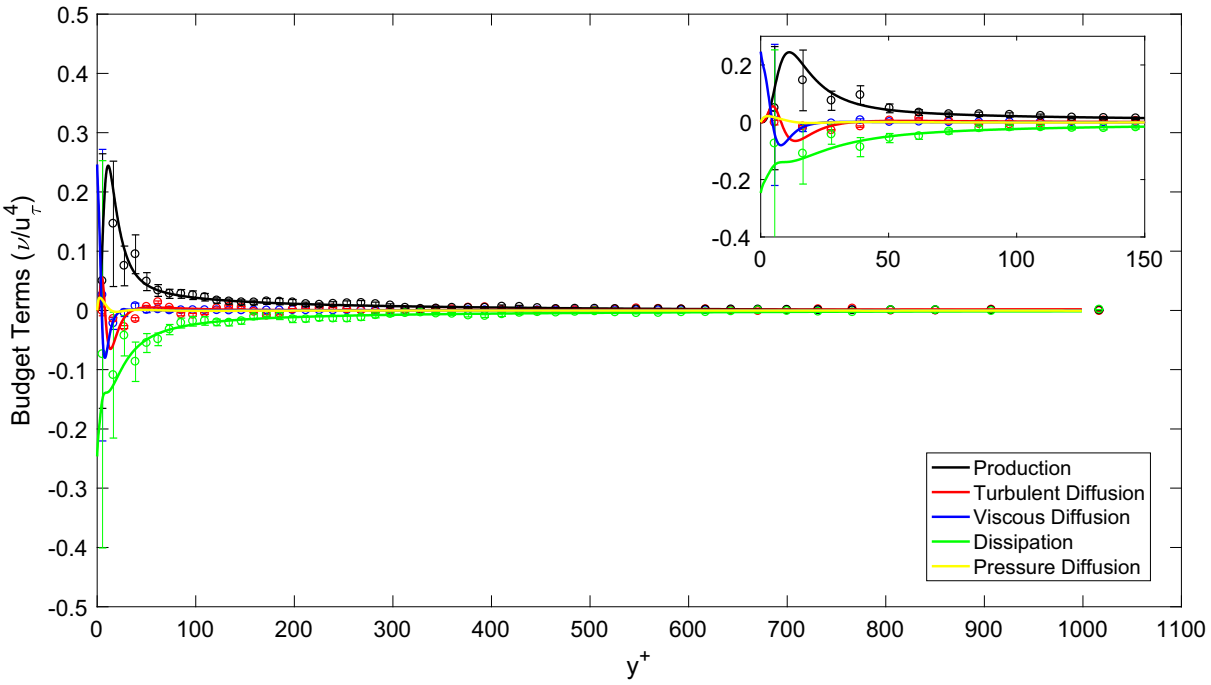

Figure 4.11: Comparison of turbulent kinetic energy budget measured with PEPT (symbols) to that of DNS of El Khuory et al. [87] (solid line) as a function of distance from the wall. The inset shows the same data zoomed in on near-wall region to reveal detail. Budget terms are normalized by (ν/u_τ^4). Positions are normalized as $y^+ = y/(\frac{u_\tau}{\nu})$, where y is the distance from the wall.

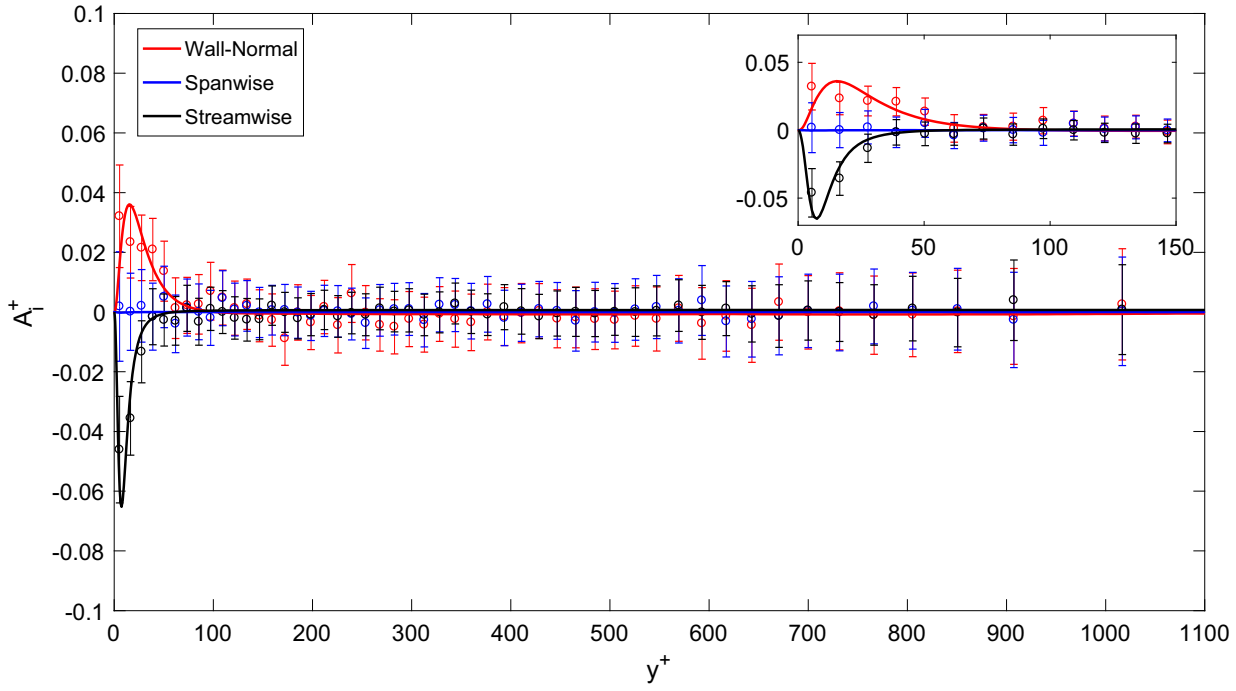

Figure 4.12: Comparison of mean acceleration measured with PEPT (symbols) to that of DNS of Stelzenmuller et al. [88] (solid line) as a function of distance from the wall. The inset shows the same data zoomed in on near-wall region to reveal detail. Accelerations are normalized as $a^+ = a/\left(\frac{u_\tau^3}{\nu}\right)$. Positions are normalized as $y^+ = y/(\frac{u_\tau}{\nu})$, where y is the distance from the wall.

who considered rectangular channel flow at $Re_\tau = 1440$ (compared to $Re_\tau = 1100$ in this work). Measured data in the r-, θ-, and z-directions are plotted as wall-normal, spanwise, and streamwise to facilitate comparison with channel geometry. The wall-normal (i.e. the "r-") component of the measured acceleration is plotted as negative ($-a_r'$) to match the coordinate system of the simulation, which measured distances outwardly from the wall.

It can be seen that the measured mean acceleration matched well that of the DNS. The shape of the measured mean-squared fluctuation curve was also similar to that of the simulation; however, the magnitude of the normalized values differed more than expected from the given Reynolds number mismatch. It is possible that this discrepancy is due to the difference in geometry between the experiment (cylindrical) and simulation (rectangular). In an experimental study of pipe flow at $Re_D = 10,300$, Oliveira et al. [91] observed that acceleration variance did not approach zero toward the centerline. They also observed the

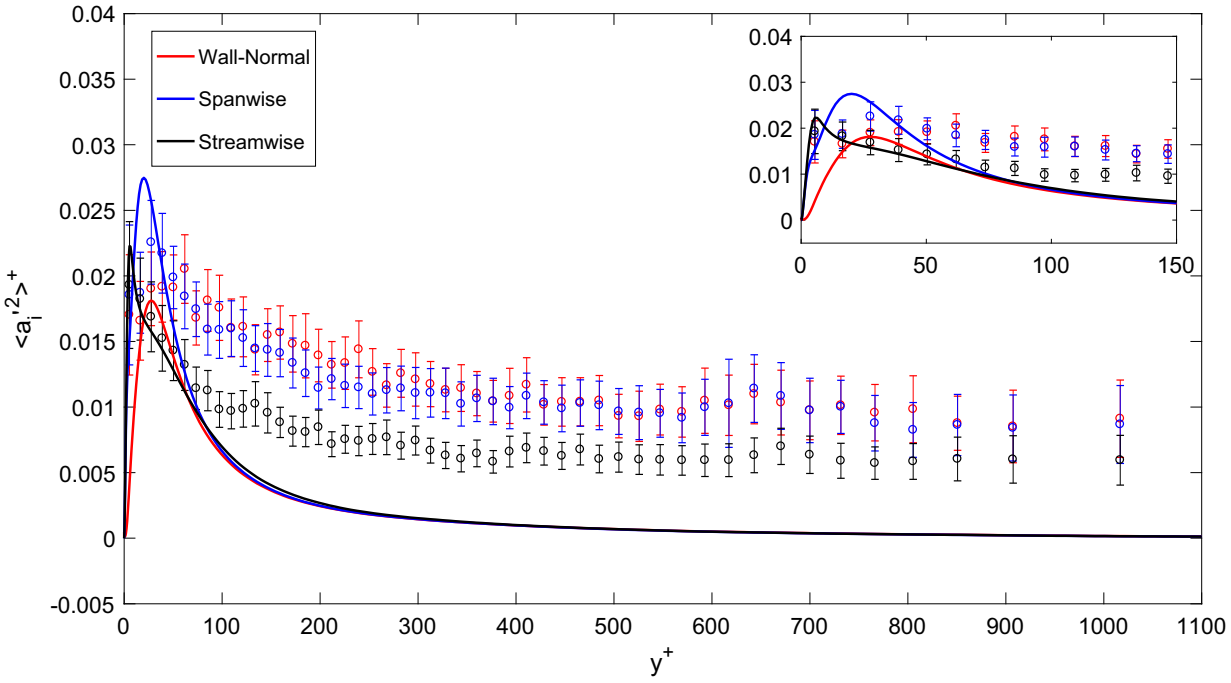

Figure 4.13: Comparison of mean-squared fluctuation of acceleration measured eith PEPT (symbols) to that of DNS of Stelzenmuller et al. [88] (solid line) as a function of distance from the wall. The inset shows the same data zoomed in on near-wall region to reveal detail. Acceleration variances are normalized as $\langle a_i'^2 \rangle^+ = \langle a_i'^2 \rangle / \left(\frac{u_\tau^3}{\nu} \right)^2$. Positions are normalized as $y^+ = y/(\frac{u_\tau}{\nu})$, where y is the distance from the wall.

streamwise acceleration variance to be the largest of the three components, contrary to what is seen here.

This work showed the usefulness of M-PEPT for measurement of turbulence quantities of interest in wall-bounded shear flow. Results indicated that measurements were accurate away from the wall in this flow field. Defects near the wall are not entirely understood, but it is possible that inertial effects were at work. As the Kolmogorov time scale τ_η is known to vary as $\epsilon^{-1/2}$, the increased dissipation in the boundary layer leads to a decrease of the smallest time scales of the flow, which would correspond to an increased St in the boundary layer.

Furthermore, PEPT spatial resolution may have come into play for measurements in the near-wall region, especially as measurement error propagated into the calculation of 2nd- and 3rd-order statistical quantities like Reynolds stress and TKE budget terms. The average spatial uncertainty calculated for this work was of the order 0.1 mm in each spatial direction, comparable to the width of the smallest near-wall bins ($\sim$0.4 mm). The development of tracers of small diameter and high activity is a line of research for the improvement of spatial resolution.

Despite these observed drawbacks, M-PEPT's utility for measurement in shear flow was demonstrated. As such M-PEPT can be employed as a tool for measurement of such quantities of interest to turbulence modeling as mean velocity and Reynolds stress in flow systems without the need for optical access. M-PEPT is also useful for the measurement of mean acceleration values, but it is not recommended that it be used for measuring higher moments of acceleration unless measurement noise can be shown to be of significantly less magnitude than the smallest scales of interest in the flow.

4.4 Yeast Cell Tracking

The last capability of M-PEPT described in this chapter realized the biological science application of PEPT, albeit in a different way than that envisioned by Shaw [6]. Past studies have been conducted with positron emission tomography (PET) to image large groups of cells [92, 93, 94, 95, 96]. However, conventional PET is not suitable for tracking individual cells.

Lee et al. [25] explored tracking of a single cell using a PET scanner and a specialized particle-tracking algorithm that fits CL data to cubic splines. They demonstrated via a Monte Carlo simulation of a Siemens Inveon preclinical PET scanner, that single-cell tracking should be possible when cell activity exceeds 10 Bq. The model was further validated with data using a 1000 Bq point source in a Siemens Inveon PET scanner; however, they also noted that the presence of the isotope ^{176}Lu in the lutetium oxyorthosilicate (LSO) crystals of the Inveon PET scanner causes a background count rate not represented in their Monte Carlo model. They conclude that tracking of low activity sources using the Inveon scanner, with intrinsic ^{176}Lu decays causing random coincidence count rate near that associated with a 100 Bq positron-emitting source, was not feasible and have since showed the ability of their method to track low activity sources in a scanner without LSO [26].

Goertzen et al. [97] showed that using a restricted energy acceptance window with lower bound of at least 400 keV nearly removes the random coincidence count rate attributable to ^{176}Lu decay in a MicroPET R4 scanner. However, this restriction of the energy window causes some reduction in the scanner sensitivity.

Using a restricted energy window of 425-625 keV, an experiment was performed to track individual yeast cells in a Siemens Inveon preclinical PET scanner. A population of roughly 125,000 cells was activated to 55 Bq/cell with ^{18}F, and 16 of these were tracked *in vitro* in a bottle of water.

4.4.1 Cell Tracking Experiment

An experiment was devised by Langford et al. [89] in which genetically modified yeast cells were activated and tracked using PEPT. The author assisted with the cell activation and performed all data analysis in this work. For this study, a cell was needed that could be activated with a positron-emitting radioisotope. ^{18}F was selected due to its ready availability and intermediate half-life of 109.8 minutes. Ideally, a cell would be able to uptake the radioisotope and be unable to export it. To accommodate this, the yeast *Saccharomyces cerevisiae*, strain BY4741-SSY3 [98] was grown with the Fluoride EXporter (FEX) gene deleted. Deletion of this gene prohibited the efflux of ^{18}F from the cell while maintaining normal influx.

Activation of the cells was carried out in a manner similar to the ion exchange procedure. In short, cells were introduced to an aqueous ^{18}F ionic solution of volume 20 μL and activity 1.3 GBq (35 mCi). A 40% glucose buffer solution was added to encourage uptake of fluoride ions by the cells. After incubation in the solution for 8 minutes, cells were removed from the suspension via centrifugation and washed via repeated rinsing and centrifuging to remove any excess ^{18}F not taken up by the cells. In this way, a final population of 125,000 cells were activated to 55 Bq/cell.

Cells were then transported to a test facility. After a series of dilutions, 17±4 activated cells were added to a 500 mL bottle of DI water, and this bottle was placed in the bore of a Siemens Inveon preclinical PET scanner. Two scans were performed for 5 minutes each using the aforementioned 425-625 keV energy window. At the time of the first scan, the activity of the cell sample had decayed to 32 Bq/cell.

Coincidence scan data were analyzed using the FPI method with a grid size of $2 \times 2 \times 2$ mm^2. Overlapping time steps were employed with CLs being processed in time windows of length 60 s, moved 3 s at each time step (i.e. with 57 s of overlap). Given an average activity of 32 Bq/cell and a peak sensitivity of 5.2% (measured for this scanner in an independent experiment), a coincidence event rate of 1.7 events per cell per second was expected. As such, this time window size allowed for 100 CL per cell for each position reconstruction.

4.4.2 Results

Figure 4.14 shows a 3D representation of the cell trajectories measured via PEPT from the first experiment. In total, 16 cells were identified and tracked during the first scan, and 18 trajectories were identified during the second scan. Average calculated localization uncertainties were 0.56 mm, 0.56 mm, and 0.50 mm in the x-, y-, and z-directions, respectively, in the first scan and 0.58 mm, 0.59 mm, and 0.52 mm in the second scan. Visual inspection of the results of the second scan indicated that there were likely two instances of occlusion (detection, loss, and subsequent detection of the same cell) in the second scan, implying that only 16 cells were found

This detection and tracking were performed using activity well below that used in conventional PET [97]. For this reason, an individual frame from this experiment was

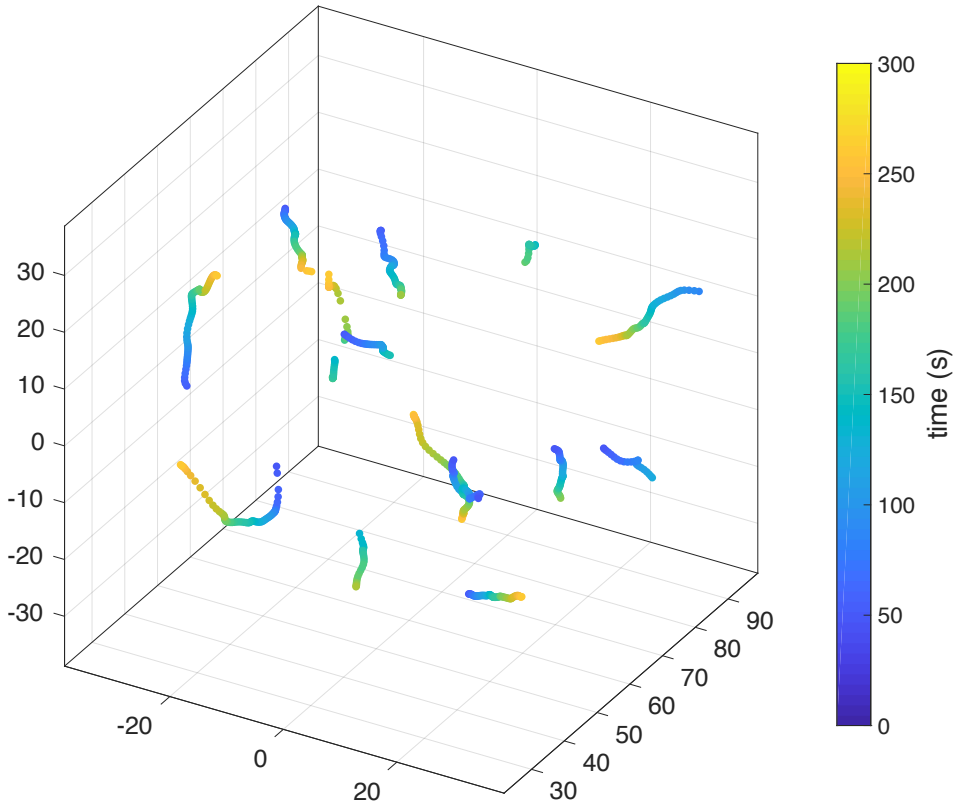

Figure 4.14: 3D trajectories of yeast cells measured via PEPT in the first cell tracking experiment. Time of detection is indicated by color along each trajectory.

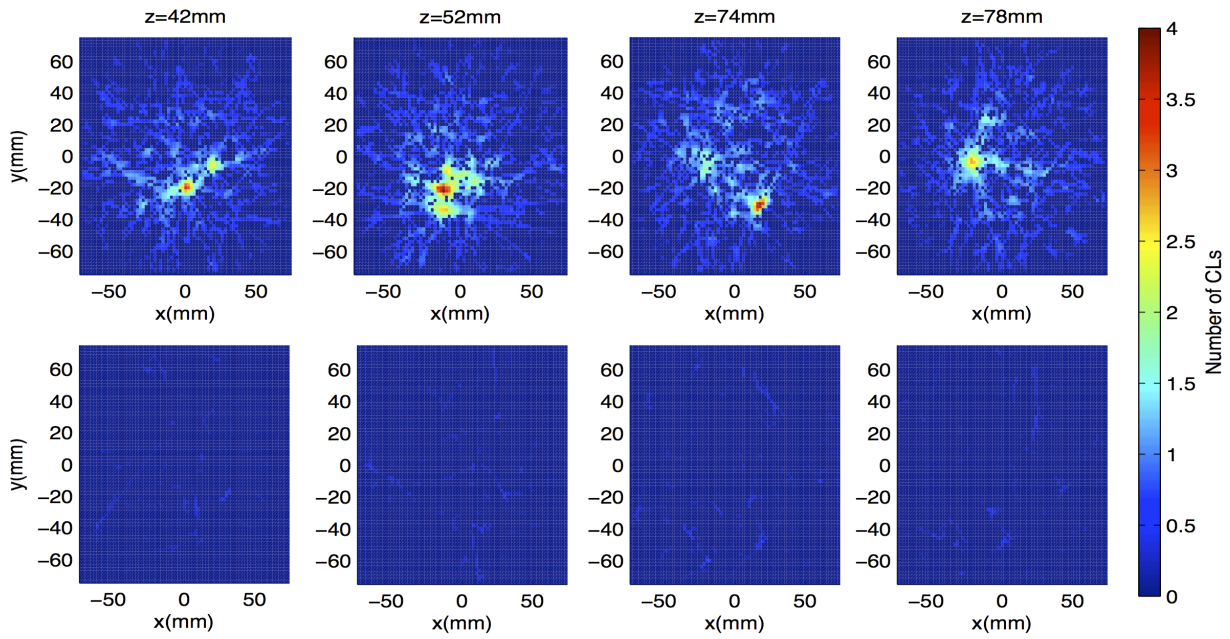

Figure 4.15: Top Row: Images from first minute of yeast tracking experiment. Four axial locations show particle images. Bottom Row: For comparison, images at same axial position from first minute of background scan are shown.

compared to the measured background radiation. A background scan was performed for 6 hours using the Siemens Inveon and CL crossings were tallied across a $2 \times 2 \times 2$ mm^3 grid, as was done for this experiment, and normalized to show average numbers of CL crossings per minute. The random coincidences occurring from ^{176}Lu decay create a broad distribution of CL throughout the FOV. In contrast, the yeast cell scans showed very localized regions of high CL density. Figure 4.15 shows four axial slices from the smoothed line density grid of the first scan compared to four one-minute slices from the background scan. Here it can be seen that the virtual images of the yeast cells are readily apparent above background. In the cell-tracking experiment, an average peak value of smoothed line density of 4.5 CL per voxel was measured, compared to only 0.56 CL per voxel in the background scan.

In this work, it was suspected that radiation exposure led to cell death, based on dose calculations carried out with MCNP6 [99]. Future work is planned to determine methods to activate cells to trackable levels without causing cell death.

This work displayed the first time positron-imaging has been used for individual cell tracking. In the future, it is desired that this method can be ported to a system of more

biological interest. Currently, activation and tracking of yeast cells *Candida Albicans* is being explored using the same means demonstrated herein. Fungal infections caused by this yeast cause serious medical problems with approximately 400,000 systemic infections per year in the U.S and a mortality rate of about 50% [100]. These infections often progress before the cause of infection is identified. It is desired that with PEPT, the modes and paths of propagation of this infection can be better understood. We have demonstrated that these cells can be activated to trackable levels and are currently pursuing *in vivo* imaging of this infection in a mouse.

Furthermore, it has been shown that certain stem cells can be activated using hexadecyl-4-[^{18}F] fluorobenzoate to individual activities that should be trackable through PEPT [96, 95]. *In vivo* tracking of such cells could provide novel insight into individual cell dynamics in stem cell therapies and allow monitoring of the administration of these therapies. If suitable radiolabelling techniques can be engineered, this method could be further extended to tracking of leukocytes for the study of infection and inflammation [101], cancer cells for study of migration and metastasis [102], and a number of other cells of interest for cell-based therapies [103].

Chapter 5

Description of Experiment

An experiment was designed to study Lagrangian dynamics of flow in porous media. Particle tracking studies in porous media have been conducted by optical means [46, 47]. These experiments require the use of index of refraction matched materials and are often limited to examination of particle trajectories over only a few pore lengths. In this work, we sought to study the long range dynamics of particles traveling in porous media with PEPT.

Toward this end, a flow loop was designed that allows delivery of flow to a number of test sections. Experiments were conducted in the Science and Engineering Research Facility (SERF) at the University of Tennessee, Knoxville (UTK). A Siemens Inveon preclinical PET scanner was used for coincident gamma ray detection, and anion exchange resins were used as tracers. Test sections were constructed with packed bed geometries. Details of this experimental setup follow.

5.1 PET Scanner

A Siemens Inveon preclinical PET scanner was used for all PEPT measurements described herein. An image of the Inveon is shown in Figure 5.1. The Inveon consists of 64 detector blocks arranged in four rings. Each block consists of a 20 $\times$ 20 array of LSO crystals of size 1.51 mm $\times$ 1.51 mm (detector face) $\times$ 10.0 mm (depth), such that the entire system is comprised of 25,600 individual detector elements. The crystal ring is of diameter 16.1



Figure 5.1: Side (Left) and front (Right) views of Inveon PET scanner with measured dimensions [104].

cm, and the length of the FOV is 12.7 cm. The transaxial FOV is limited to a diameter of 10.0 cm due to the encasing around the detector elements [31].

A brief description of the detector system of the Inveon follows. For a full treatment of this system, the reader is referred to [105, 106, 107, 108, 109, 110, 111, 112]. A block diagram of the full Inveon architecture (detector, electronics, and interface with host PC) is given in Figure 5.2 [109].

The detector block used in the Inveon is shown in Figure 5.3. In each block, a 20 × 20 LSO crystal array is coupled by a tapered 14 × 14 element light guide to a position-sensitive photomultiplier tube (PSPMT). Crystals are arranged such that for all but the outer elements, there is a 9 to 4 (3 × 3 to 2 × 2) multiplexed coupling of crystals to light-guides. This coupling scheme is shown in Figure 5.4. This tapered structure allows for the coupling of many scintillating elements to a single detector block and allows detector blocks to be arranged without a gap between the detection elements of adjacent blocks [106].

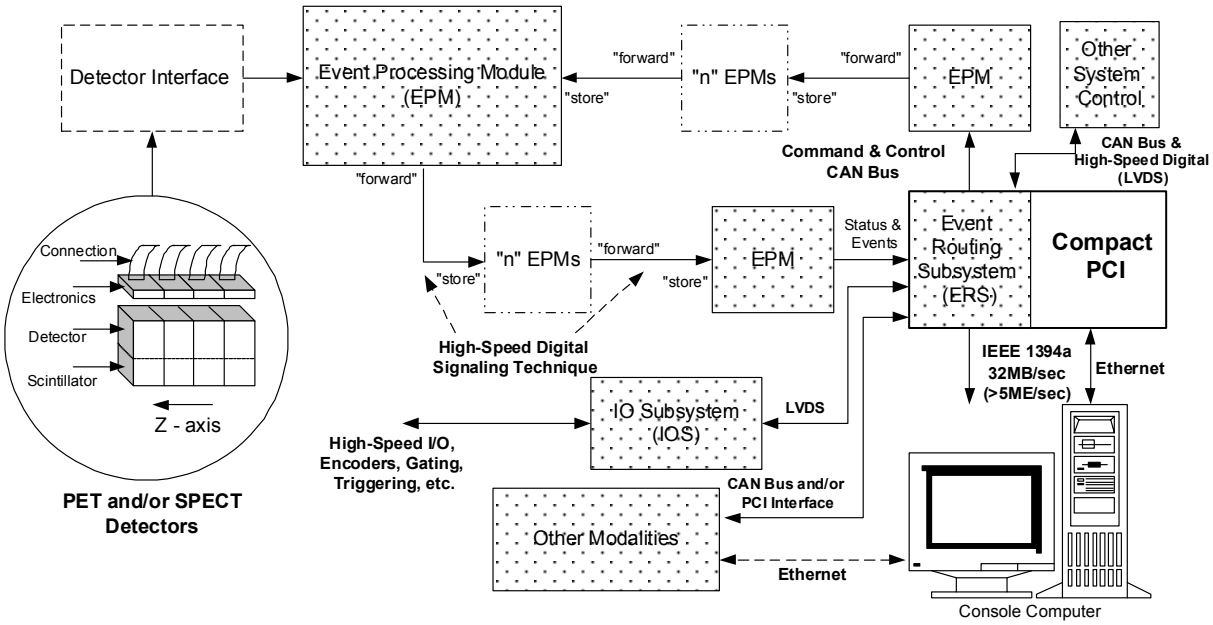

Figure 5.2: Block diagram of architecture employed by Siemens Inveon [109].

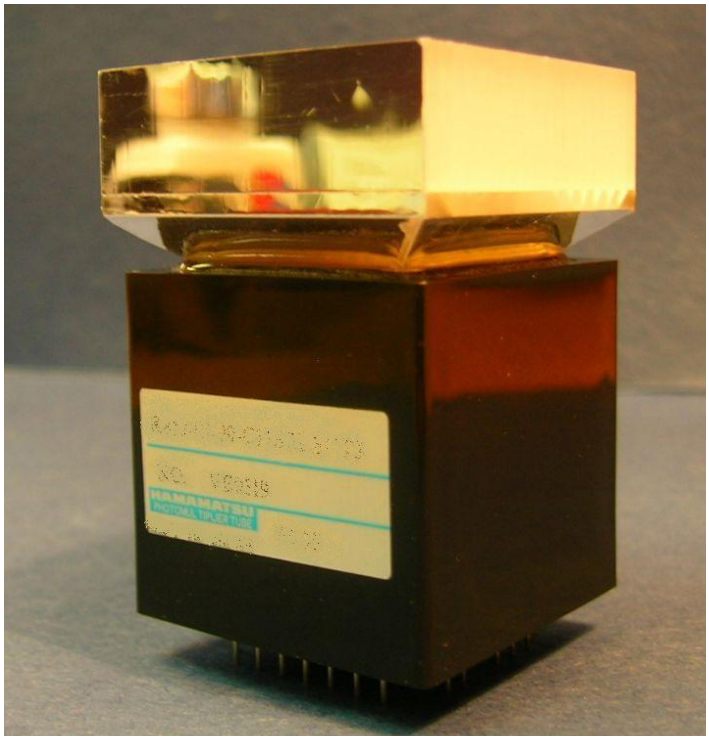

Figure 5.3: Photograph of detector used in Siemens Inveon [106].

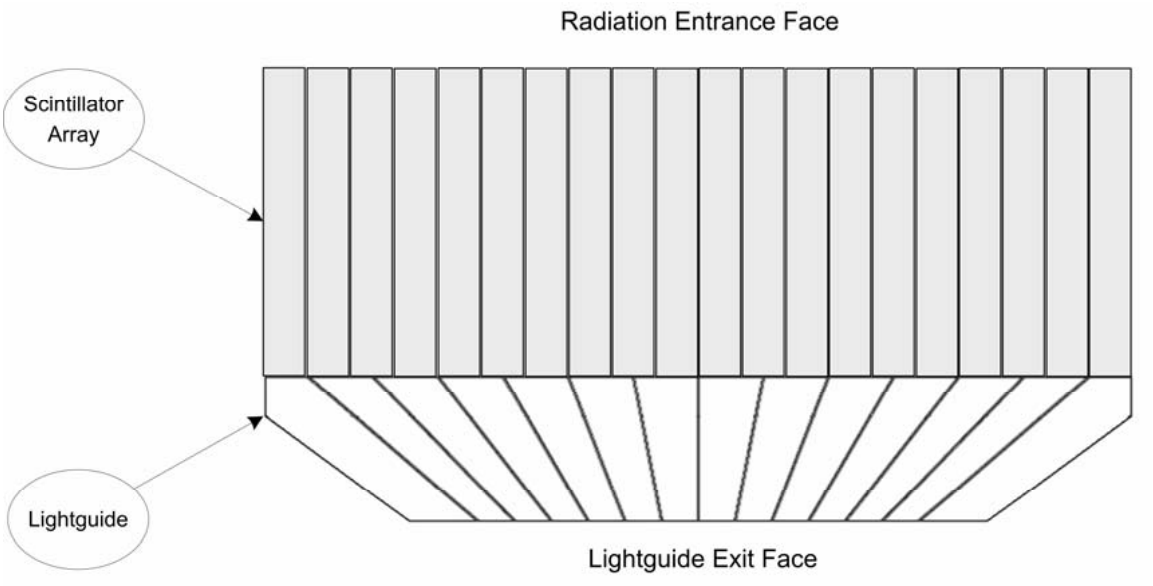

Figure 5.4: Coupling of crystals to light guide in Siemens Inveon [106].

Analog readouts from PSPMTs are sent to one of the event processing modules (EPMs). Each EPM is coupled to four detector blocks, giving a total of 16 EPMs in the system arranged in a ring. Here an analog to digital converter (ADC) first digitizes signals and passes them to a field programmable gate array (FPGA). These signals include information on the location and energy of the radiation interaction in the detector as well as a 312 ps time stamp. Event processing within the FPGA is described in Figure 5.5. The position and energy information are passed to a crystal lookup table (CLT) that returns a specific crystal address to the FPGA. This crystal address is used to query an energy and time correction lookup table that is used to correct the signal. This lookup table contains information of upper and lower bounds for allowed energy. If a signal is found to have energy within these bounds, a crystal-specific time correction is applied [105].

This signal is then processed for coincidence determination. Coincidence determination is performed between events that originate on a given EPM and those received from other EPMs as seen in the bottom panel of Figure 5.5 [105]. Signals are passed between EPMs in a "store and forward" architecture in which the information is first stored locally on an EPM and then passed to an adjacent EPM [109]. Events from other EPMs are processed on first-in-first-out (FIFO) buffers and are compared to those stored locally on an EPM.

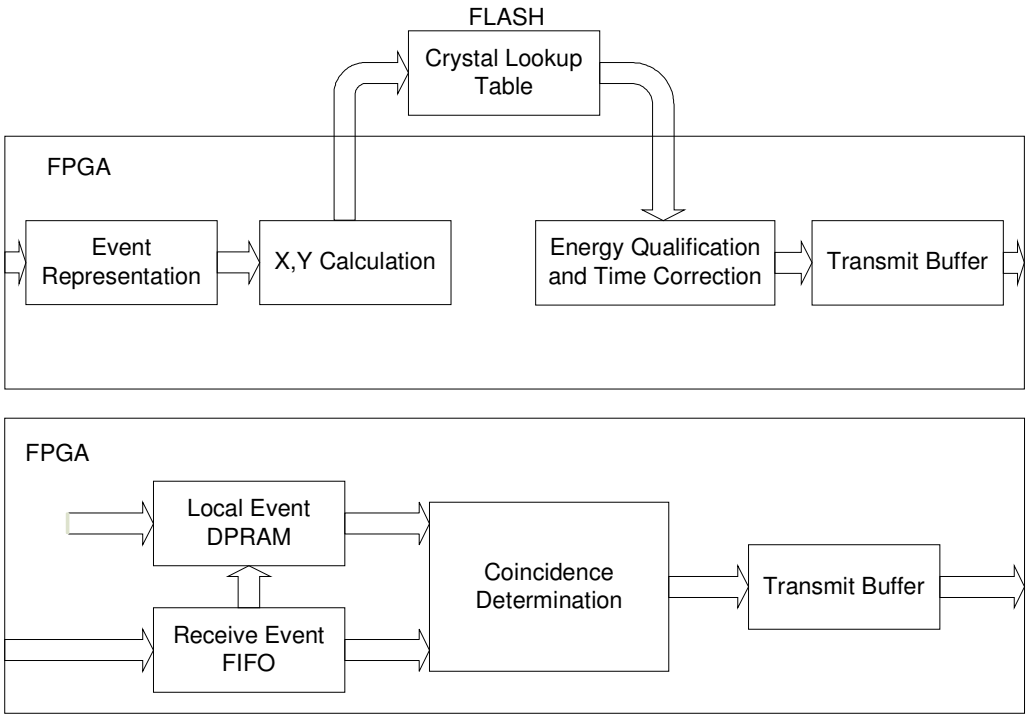

Figure 5.5: Block diagram of event routing within FPGA of Siemens Inveon. Top: singles even processing. Bottom: Coincidence determination [105].

If the time stamps of two events are found to be within the preset coincidence window, a coincidence event is created and transmitted to the event routing subsystem (ERS) [105]. The ERS then translates the signal to a listmode data format and outputs the data stream to a listmode file [112]. This listmode file is written to a host computer where it can be used for PET reconstruction using software provided by the manufacturer or offloaded for PEPT or other forms of processing.

Each coincidence event is written to the listmode file as a word containing information on the crystal addresses of both crystals involved in the event. Time marks are inserted into the listmode stream every 200 μs and are used to sort the data. This currently serves as the limit on temporal resolution in our PEPT experiments and does not represent the overall timing resolution of 1.2 ns of the detection electronics of the Inveon [105]. An external TTL trigger can be also be sent to the Inveon via BNC ports on the front of the scanner. In this case, trigger event words are inserted into the listmode at the rising or falling edge of the TTL signal, depending on user specification. No external triggering is used in this work.

Crystal lookup tables and crystal energy maps are generated via a detector setup routine in which a cylindrical ^{68}Ge source (positrons emitted by ^{68}Ga after decay $^{68}\text{Ge}\rightarrow{}^{68}\text{Ga}+e^{-}+\bar{\nu_e}$) is used for calibration. A scan of this source is performed until each detector has recorded 10,000 events. At this point, PSPMT readouts are examined for each detector, and regions of the readout are assigned to each crystal in a detector, as seen in Figure 5.6. Histograms of energy recorded by each detector are examined, and the 511 keV energy peak is identified in each for calibration.

With a cylindrical detector geometry, the sensitivity of the Inveon is seen to vary greatly with axial position. Figure 5.7 shows the axial sensitivity profile of the Inveon recorded using a ^{22}Na source and the restricted energy window of 425-625 keV [113]. Here, the efficiency is defined as the number of CL recorded per second divided by the activity of the point source (in Bq). It can be seen that the Inveon is a great deal more sensitive at its center of FOV than at its axial edge. In the case of PEPT measurements (in which measurement accuracy varies inversely with the square root of the number of CL recorded), this means that recorded positions will be significantly more accurate at the axial center of the scanner

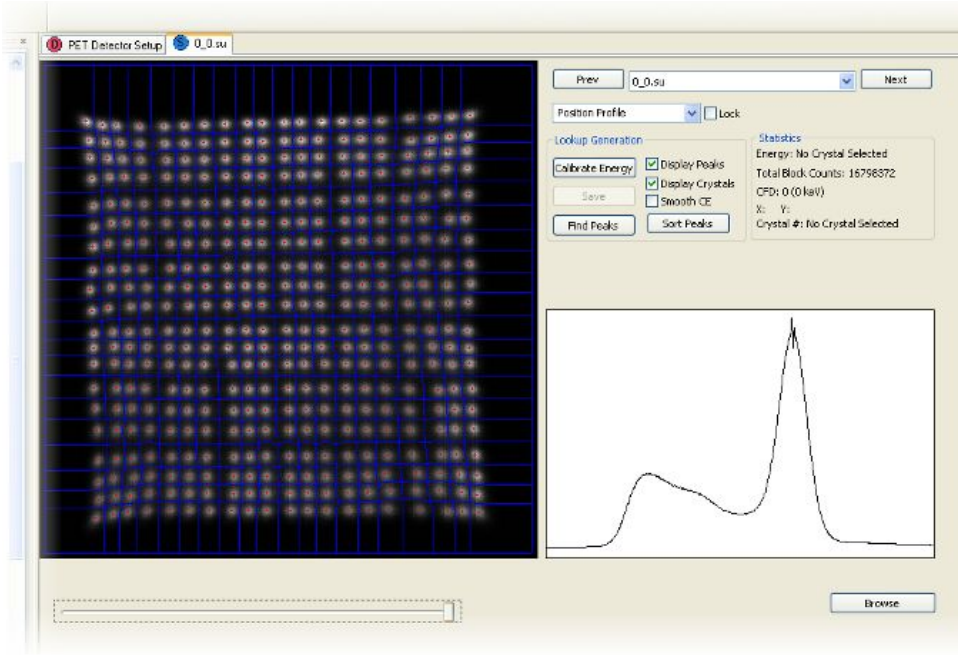

Figure 5.6: Example of window used for Inveon detector setup. On the left is an example of a generated crystal lookup table. On the right is an example of detector energy readout with 511 keV energy peak clearly identifiable [104].

than at the edges, and this must be considered in data analysis. The peak (center FOV) sensitivity is measured to be 5.2%.

The 425-625 keV energy window is more restrictive than that usually used for PET scans [31]. While this reduced energy window reduces the sensitivity of the scanner, it has been shown to greatly reduce the number background events associated with ^{176}Lu decay in the LSO crystals [97]. Experience has shown that the gains achieved by this noise reduction outweigh the losses associated with reduced sensitivity.

In order to quantify scanner performance as a function of the activity present in the FOV, one considers the noise equivalent count rate (NECR) of the scanner, defined as

$$NECR = \frac{R_{true}^2}{R_{total} + R_{random}}. \tag{5.1}$$

Here, each R indicates a count rate, and the random count rate is determined using a delayed coincidence window [31]. As the activity present in the bore increases, the number of random coincidences will also increase. As such, the NECR serves as a means of quantifying the

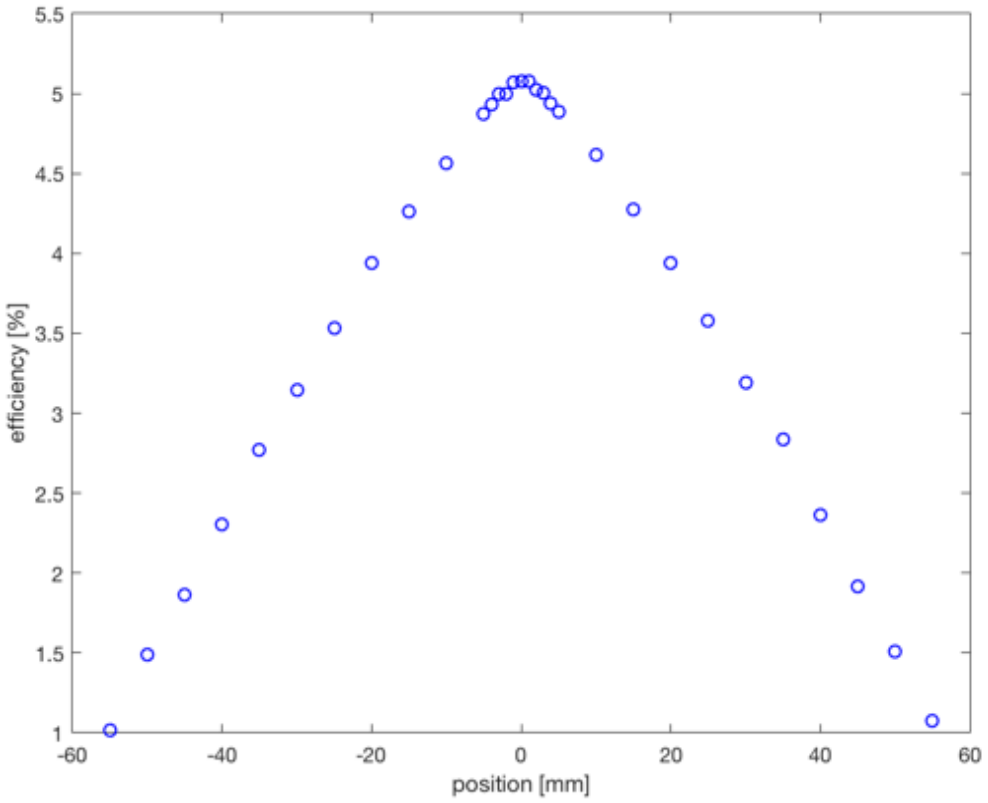

Figure 5.7: Sensitivity profile of Siemens Inveon recorded using ^{22}Na point source with 425-625 keV energy window [113].

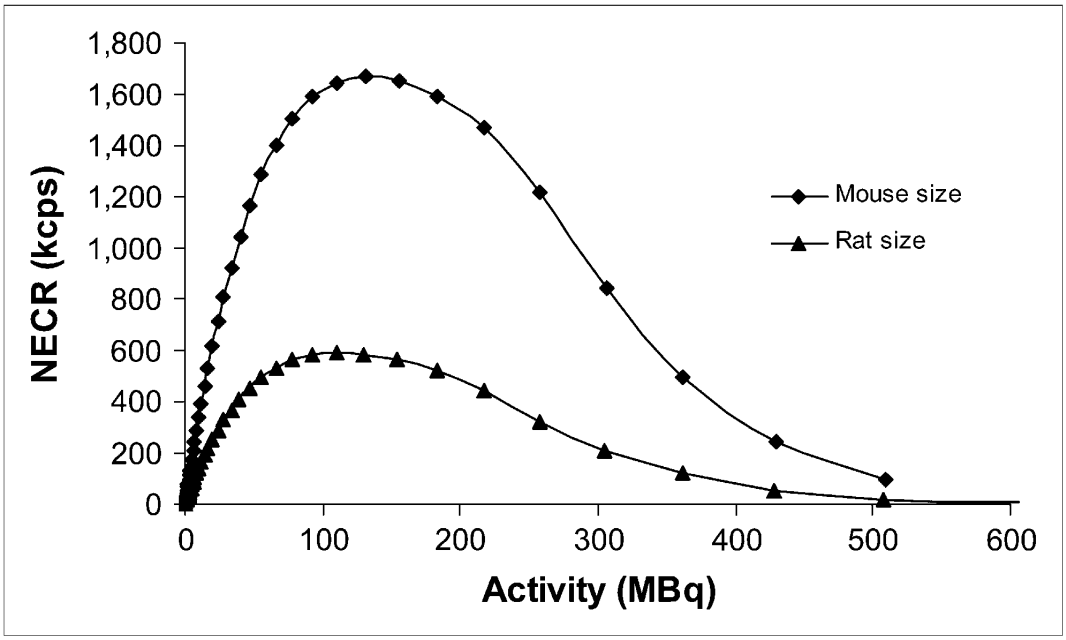

Figure 5.8: Noise Equivalent Count Rate for Siemens Inveon measured for two different phantom sizes [31].

true count rate performance of the scanner, adjusted for the background caused by random coincidences. The measured NECR relative to activity present in the bore of the Inveon for two different phantoms is shown in Figure 5.8. For both phantom sizes, the NECR peaks between 100 and 150 MBq (2.7-4.1 mCi). This means that above ∼4 mCi, increasing the amount of activity in the bore will primarily serve to increase the random coincidence background. For this reason, it is desired that the amount of total activity present in the scanner FOV be kept under 4 mCi for any PEPT experiment.

5.2 Tracer Particles

Amberlyst OH-form anion exchange resin were used as tracers for these experiments. A scanning electron microscope image of such a resin is shown in Figure 5.9. The particle pictured is from a set of larger resins of diameter 596-789 μm (middle 80%), as measured by a Mastersizer 3000 laser particle size analyzer. The tracers used in this work were of the same physical characteristics but were of diameter 69-120 μm. The smaller diameter allowed these tracers to pass through the constructed porous media and be more representative of the

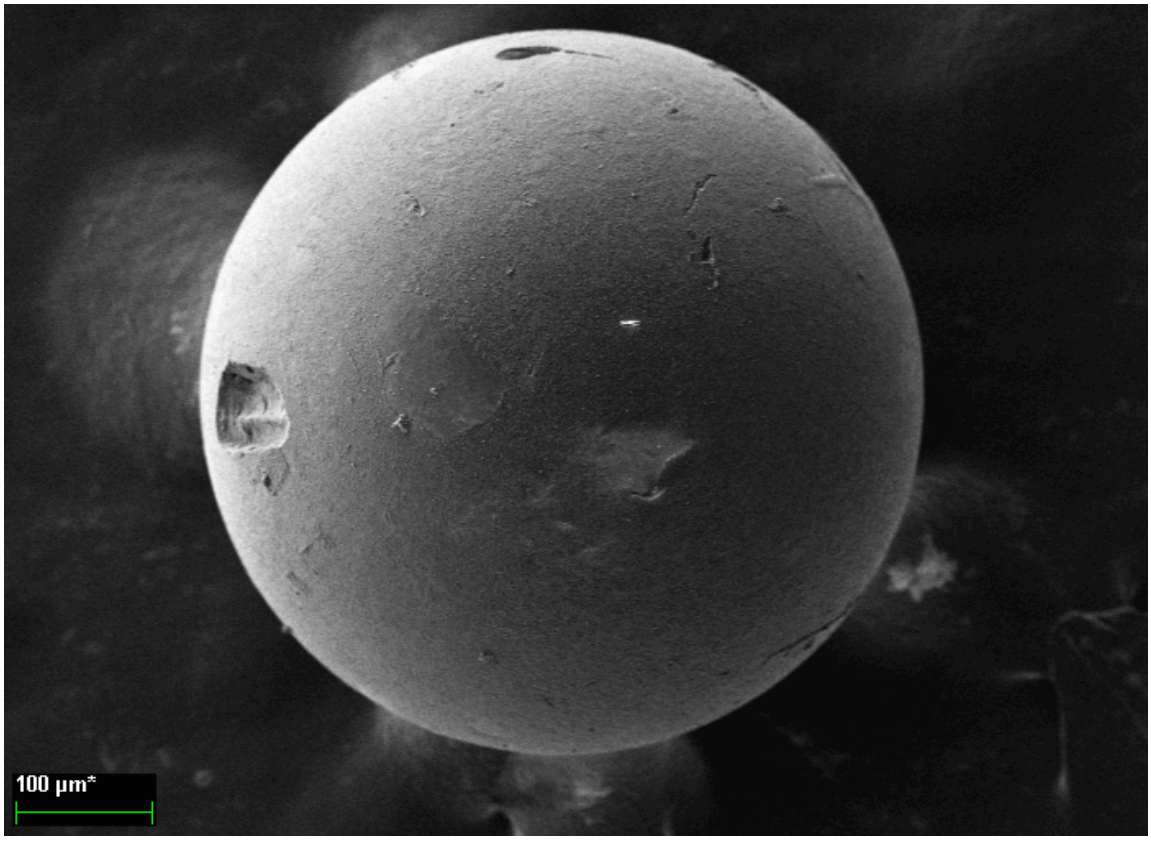

Figure 5.9: Scanning electron microscope image of anion exchange resin bead.

motion of the underlying fluid elements. These particles have a wet density of approximately 1.205 g/cc, measured via suspension of particles in sucrose solutions of varying density (see Section 5.3).

Particles were activated with ^{18}F at the University of Tennessee Medical Center (UTMC). ^{18}F was chosen due to its short positron range in water (0.66 mm), intermediate half-life (109.8 min.), and ready availability. This half-life allows for several minutes to a few hours of data collection before particle activity is too low to facilitate tracking. As upwards of 30 mCi total activity was used in these experiments, this half-life is also sufficiently short to allow decay of all activity after only several hours. As such, cleanup of experiments can be conducted two days after experiments without the need to treat materials as radioactive.

The isotope ^{18}F was produced by technicians at UTMC by irradiating ^{18}O-enriched water with a medical cyclotron via the reaction ^{18}O(p,n)^{18}F . This creates an aqueous solution of

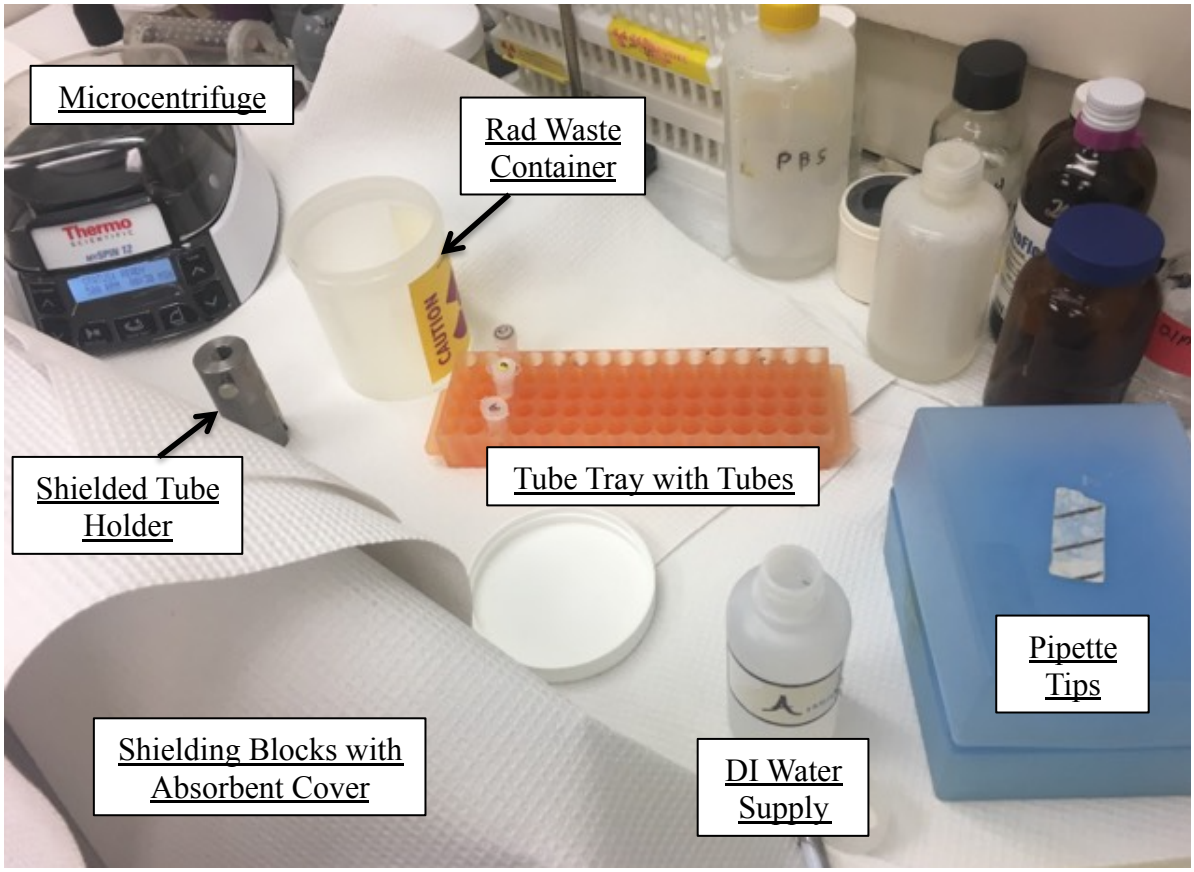

Figure 5.10: Photograph of activation equipment in fume hood at UTMC.

^{18}F ions that can be attached to the OH-form resins, as described in Section 2.1.3. A brief description of this activation procedure follows. For the full procedure, see Appendix B.

Before arriving at UTMC, a suspension of tracer particles in deionized (DI) water of concentration 100 particles per μL was prepared. At UTMC, the activation procedure was then carried out behind lead shielding blocks in a fume hood, as pictured in Figure 5.10. The radioactive ^{18}F solution was provided by UTMC and was of volume $\sim$30 μL and activity $\sim$30 mCi.

5 μL of the stock suspension (500 particles) was mixed with the activity in an Eppendorf tube and placed in a tungsten-shielded tube holder (see Figure 5.10) to incubate for 20 minutes with intermittent agitation. A 20 minute activation time was chosen, as this was found to allow sufficient adsorption of radioactive fluoride ions onto the particles without significant loss of activity due to radioactive decay. This is in line with the adsorption kinetics observed by Fan et al. [29], as seen in Figure 5.11.

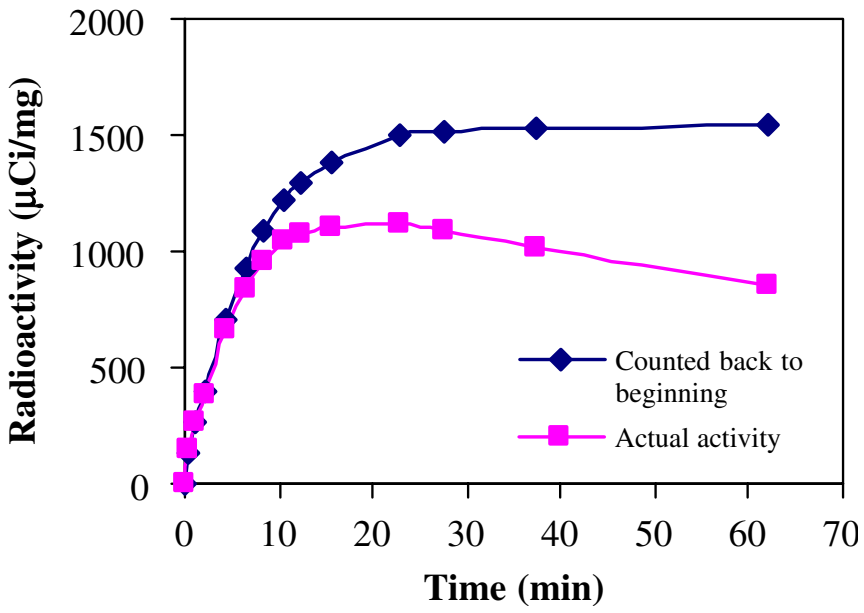

Figure 5.11: Adsorption kinetics of ^{18}F in sample of resin beads [29].

After the activation period, tracers were washed via a series of rinses and dryings with a microcentrifuge. All washes were performed with DI water to prevent exchange of ^{18}F from the particles with free ions in the wash. Finally, particles were resuspended in a DI sugar-water solution of density 1.205 g/cc and transported to the test facility at SERF.

Under this protocol, approximately 500 particles are activated up to 50 μCi per particle. After transport, typical activities at the start of an experiment are 30-40 μCi. Given the peak (center FOV) sensitivity of the Inveon of 5.2%, this corresponds to a peak data collection rate of 58,000-77,000 coincidence events per second. At this data rate, position reconstruction can be performed with time steps on the order of milliseconds [81].

5.3 Flow Loop and Test Section

To facilitate measurements of flow in porous media, a flow loop was constructed with three interchangeable packed bed test sections. A diagram of this flow loop is seen in Figure 5.12. Here, flow is driven by a peristaltic pump through five flexible tubing lines at the same flow rate. Of these lines, four are connected to a header tank, and the fifth is connected to a

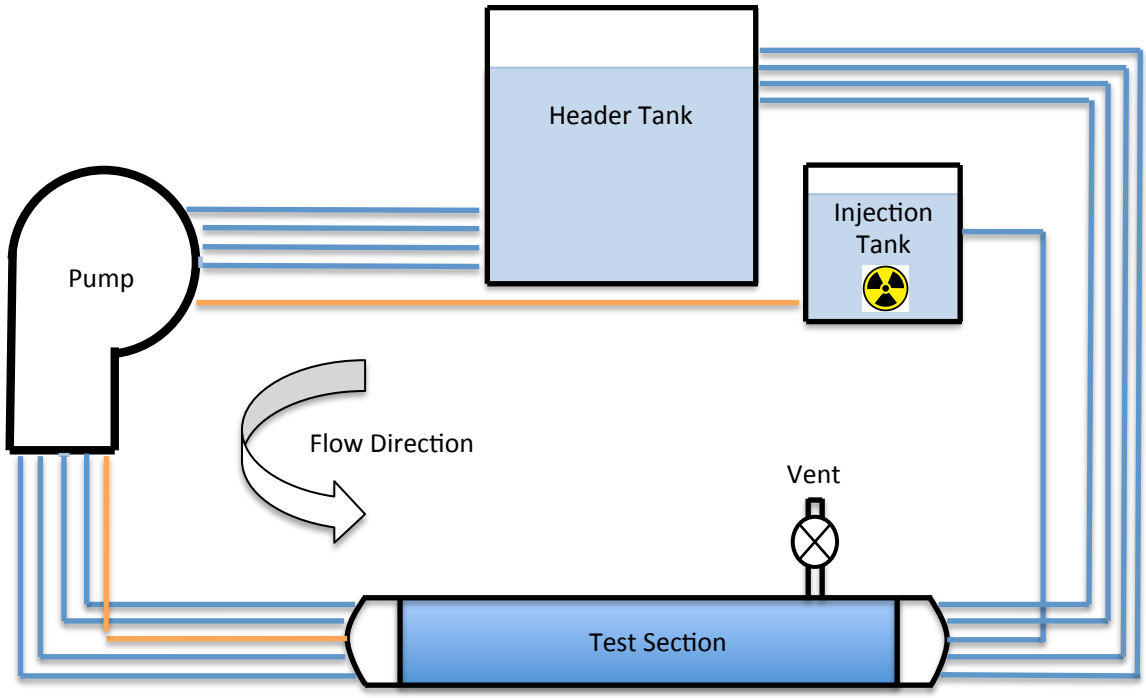

Figure 5.12: Diagram of flow loop employed in packed bed experiments. Orange line indicates injection line that delivers radioactive particles to the test section.

separate, smaller tank used for particle injection. This "injection" line delivers flow to the radial center of the test section,

A Masterflex L/S Precision Variable Speed peristaltic pump drive model MK-07557-00 with Masterflex L/S Multichannel Pump Head model 7535-08 was used to drive the flow. This pump head is a 6-roller design and can be driven between 6 and 600 RPM using the aforementioned drive. It is recognized that the use of a peristaltic pump will create small vibrations in the flow; however, the six-roller design minimizes pulsing, and such a pump drive has been used previously in porous media research [43]. Dye tests were performed to ensure that all vibrations had been damped out by the time flow reached the measurement region.

Masterflex L/S 14 flexible tubes of platinum-cured silicone and inner diameter 1.6 mm were used to connect the test section to the header tanks and were hooked into the pump head via Masterflex L/S 14 platinum-cured silicone 2-stop tubing. An image of this tie-in to

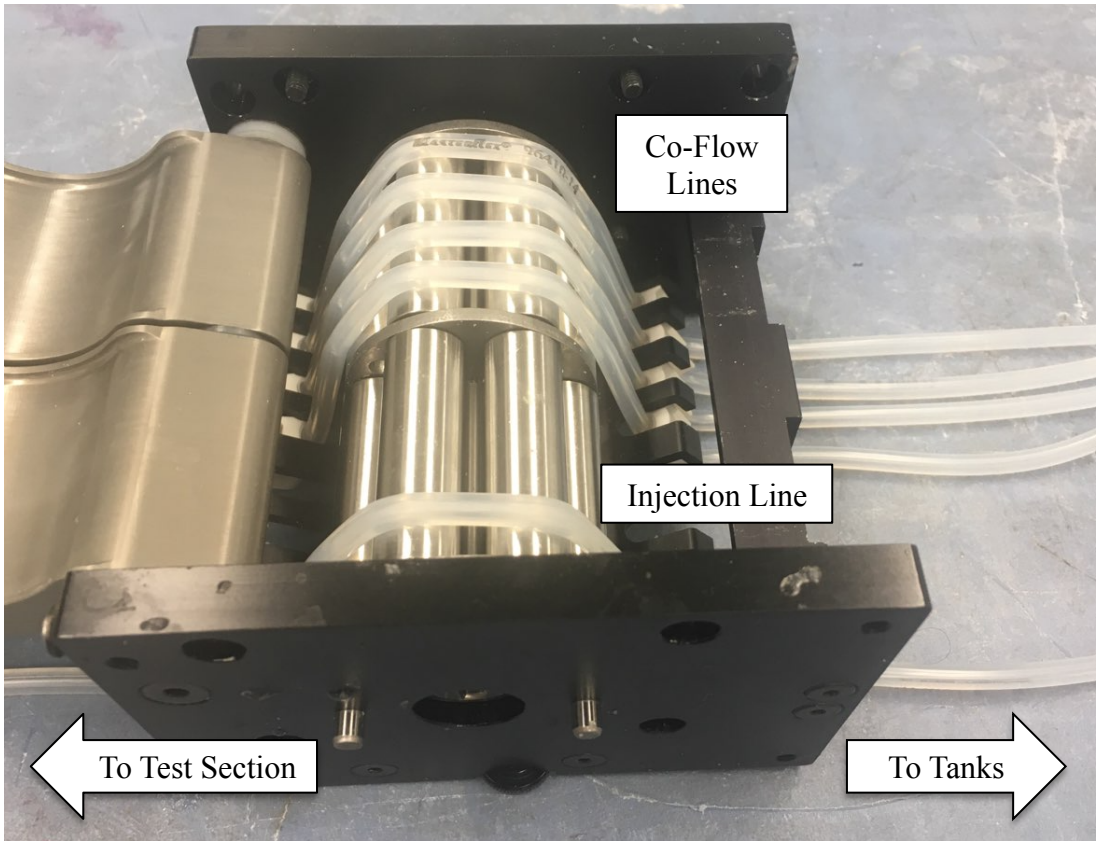

Figure 5.13: Photograph of pump head with 2-stop tubing.

the pump head is shown in Figure 5.13. All connections used were polypropylene to reduce contamination of the deionized water used in these experiments.

The test section itself was constructed from 3-inch nominal diameter Schedule-80 clear PVC pipe. An engineering drawing of this test section is offered in Figure 5.14. The actual inner diameter of this tube is 73.7 mm (2.9 in.). The tube was cut to length 58.4 cm (23 in.), and a 1/2-in. An NPT threaded hole was tapped near the outlet, as shown in Figure 5.14. A 15.2 cm (6 in.) clear PVC threaded nipple was tied into this hole, and a ball-valve is attached to this nipple to vent the test section. This length of tube was selected to allow ample flow development length between the inlet and the portion of the test section in the FOV of the scanner and to permit access to the vent line downstream of the scanner bore.

At either each end of the tube, socket-type PVC end caps are fixed in place with silicone sealant. Stainless steel wire screens of mesh size 20 (mesh spacing 0.85 mm) were inserted between the central tube and the caps to prevent any shifting of the packed beads. A wire

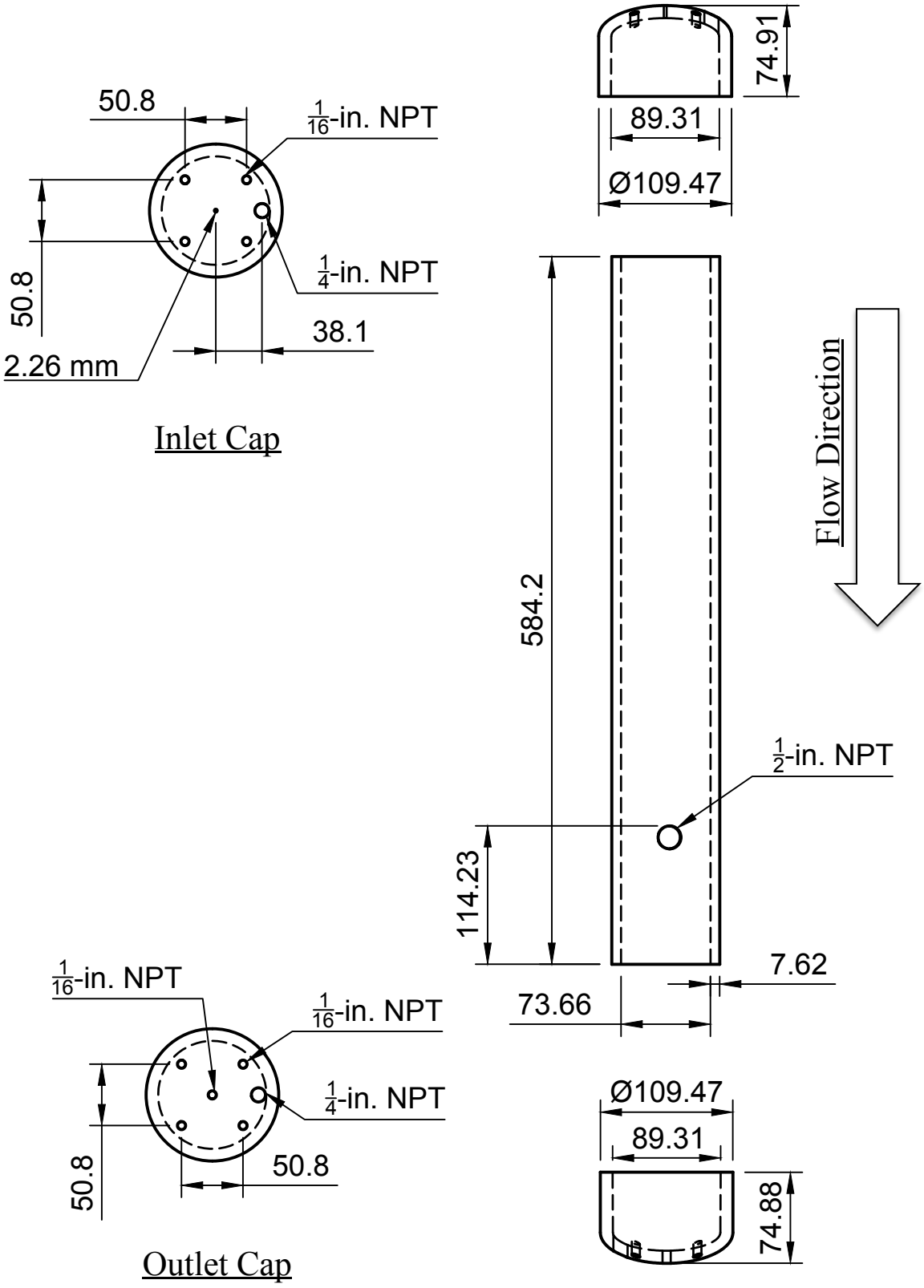

Figure 5.14: Drawing of tube used for packed bed test section. Listed dimensions are in mm, and threads are according to National Pipe Threads (NPT) standards.

screen was also added between the test section and the threaded nipple to prevent beads from escaping into the vent. In the outlet cap, five 1/16-in. NPT holes were tapped in the pattern seen in Figure 5.14. In the inlet cap, four 1/16-in. NPT holes were tapped with a central, untapped hole of diameter 2.26 mm. This central hole allows the insertion of a 14 gauge (inner diameter 1.6 mm), stainless steel needle, trimmed to length 43 mm. This needle is attached to the injection line via a barbed, polypropylene, luer-lock coupling and is used to inject radiotracers into the test section beyond the wire screens. In each of the aforementioned 1/16-in. tapped holes, polypropylene barbed fittings were inserted to connect the test section to the Masterflex tubing. As shown in Figure 5.14, 1/4-in. NPT holes were also tapped in each end cap for connection to pressure transducers, but these were plugged for this work.

Beds were packed with glass or plastic beads of different sizes to create the porous media. 2 mm and 4 mm diameter beads of soda lime glass and 8 mm diameter imitation pearl (plastic) beads were used. The density of the glass beads is 2.5 g/cm^3, and the density of the plastic beads is 1.0 g/cm^3. These bead sizes were chosen for dilational symmetry of the created pore lengths, with the smallest bead size being chosen to allow passage of the tracers. Figure 5.15 shows the smallest pore throat that can be created by packing of beads of diameter d. The width of this smallest throat is $\left(\frac{\sqrt{3}-1}{2}\right) \times d = 0.366 \times d$. In this case, that throat size is 0.732 mm. As the tracers employed are of diameter $\sim$90 μm, they will be able to pass through all pores created by this packing; however, it is possible that tracers can get stuck in the corners of these channels. This is considered in the data analysis.

The beds were packed in 3 different configurations: 2 mm beads alone; 2 mm and 4 mm beads; and 2 mm, 4 mm, and 8 mm beads. In the mixed bead cases, equal volumes of each bead were used.

Packing of a test section proceeded as follows: first, the empty tube and all its components were weighed. With the inlet cap attached and vent line in place, the test section was turned on end and beads were added slowly and intermittently packed via tamping, as shown in Figure 5.16. In this way, beads were added up to the outlet, and the outlet cap was fixed in place. The test section was placed in its normal, horizontal orientation with the vent line pointing up, and the nipple was removed. Beads were then further packed into the vent line

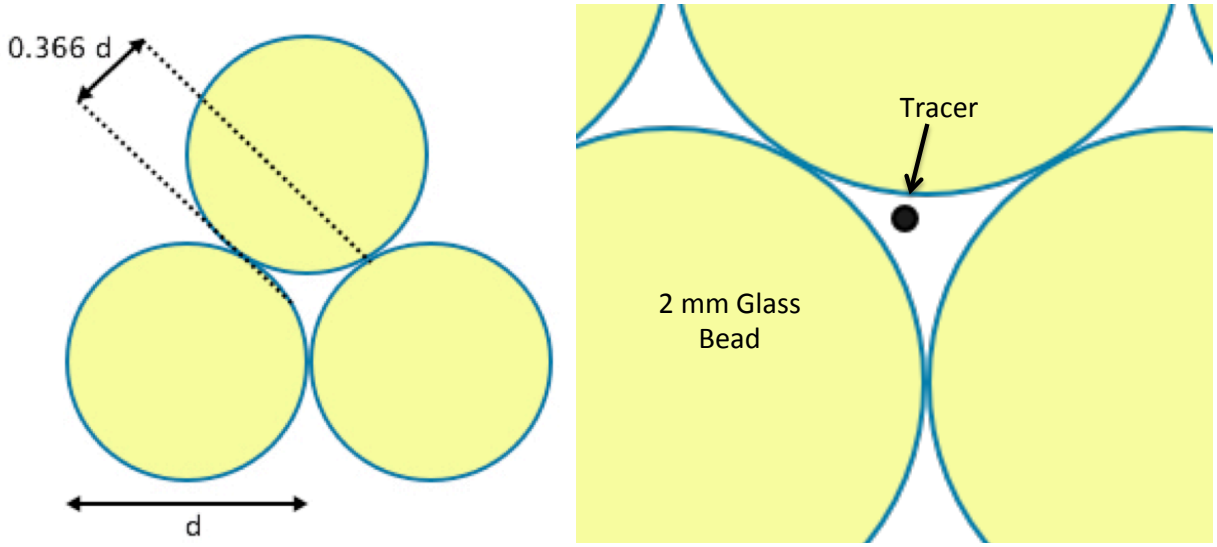

Figure 5.15: Left: Size of smallest pore throat created by packing of beads of diameter d. Right: Comparison of tracer particles of size 90 μm to pores created by beads of diameter 2 mm.

until the test section was as tightly packed as can be achieved. The fully packed test section was weighed, and the weight of the beads taken to be the difference between the weight of the packed test section and the weight of all the test section components before packing. Using the density of the beads, the volume of the solid phase V_{solid} was determined, and the porosity, ϕ, of the test section was calculated as

$$\phi = \frac{V_{TS} - V_{solid}}{V_{TS}}. \tag{5.2}$$

Here, the volume of the test section, V_{TS}, is modeled as a cylinder with two spherical domes representative of the inlet and outlet caps. The inner dimensions of each tube are measured independently to account for slight variations between each constructed test section. The final specifications of each test section are given in Table 5.1. The average bead diameter in each test section was calculated based on number, N_i, of each bead present, where the equal volume requirement creates bead number ratios

$$N_{8mm} : N_{4mm} : N_{2mm} = 1 : 8 : 64. \tag{5.3}$$

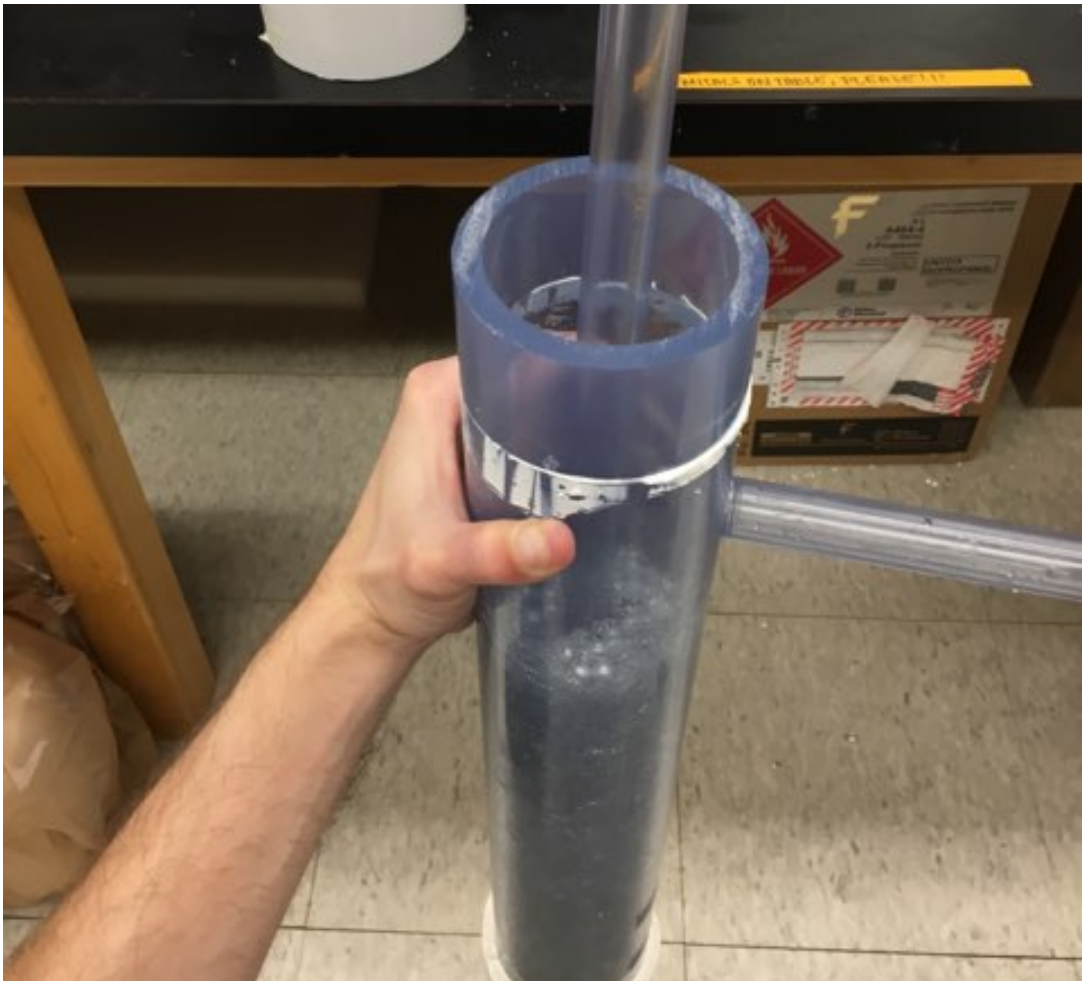

Figure 5.16: Photograph of test section packing.

Table 5.1: Physical specifications of each test section.

Bead Size	Average Diameter (mm)	ϕ
2 mm	2 mm	0.39
2 mm, 4 mm	2.22 mm	0.36
2 mm , 4 mm, 8 mm	2.3 mm	0.30

By packing beads tightly, one prevents shifting of beads during experimental setup. If the beads are not packed tightly, a gap can form at the top of the test section, and flow will preferentially sample the top of the test section. Extra care was taken in packing of the mixed bead cases to ensure an even distribution of the the bead sizes. In these cases, if beads are not packed tightly, the larger beads will migrate to the top of the test section over time. Such a stratification of grains of different sizes is colloquially referred to as the "Brazil nut effect" [114] and can also lead to preferential flow at the top of the test section. Dye tests were performed to check for any issues in each test section. An example of such a dye test is shown in Figure 5.17. In these, dye was added to the injection line to ensure that the plume coming from this line (indicative of the distribution of radiotracers) was spreading evenly and moving with uniform velocity by the time this plume reaches the region of the test section that is present in the scanner FOV. In cases where these criteria were not met, the test section was disassembled and repacked. An image of a fully packed test section is shown in Figure 5.18.

For these experiments, an aqueous sucrose solution was used as the working fluid. This solution was chosen due to the ability to adjust its density without introducing free ions to the water. Matching the density of the tracers to the fluid is crucial in these experiments, as the flow is extremely slow and does not have enough inertia to entrain significantly density-mismatched particles.

A series of tests were performed to determine the density at which the tracer particles employed were neutrally buoyant in the solution. Sucrose solutions of different densities were prepared, and particles were introduced to the solutions. Each sample was stirred, and the settling/floating of the particles was monitored over several hours. It was found that there was a slight variance in density across any sample of these particles, i.e. there was no sample in which all particles remained neutrally suspended for many hours. Instead, it was found that over a narrow range of densities (1.205-1.220 g/cc) some particles would migrate to the top of the container, and some would migrate to the bottom of the container, while most remained suspended over the course of several hours. A density of 1.205 g/cc was chosen for use, as it is at the lower end of this range, and our testing showed that it was likely for particles to remain entrained in the flow if they were slightly heavier than the

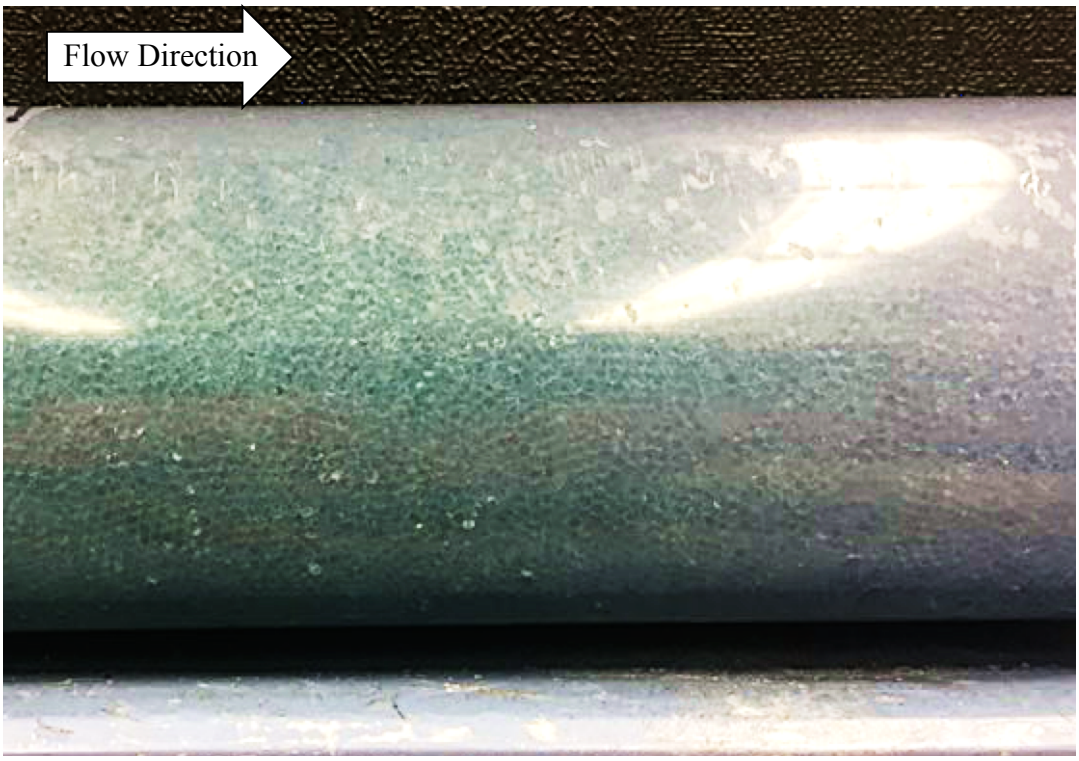

Figure 5.17: Image of dye test performed with 2 mm bead test section. Flow is left to right, and injection plume is dyed green. Tape on top of test section shows start of scanner FOV when test section is in place for PEPT measurement.

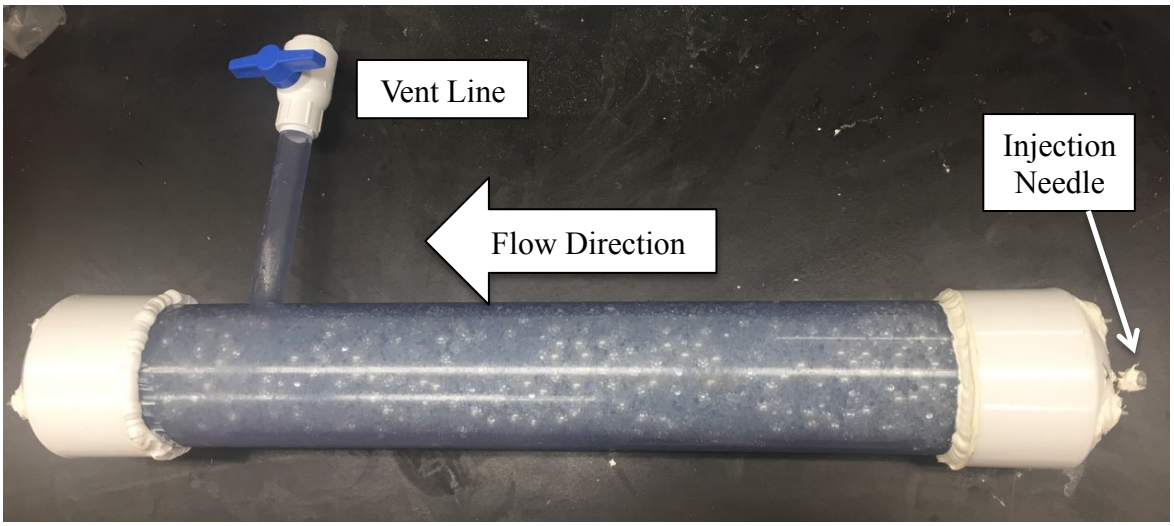

Figure 5.18: Photograph of 2, 4, 8 mm bead packed test section with labels.

fluid, while light particles tended to get stuck at top of the test section. Experiments using a test section without any packed beads showed that the particle did not drift vertically in a sucrose solution of this density.

A sucrose solution of density 1.205 g/cc consists of 53.7% water and 46.3% sugar, by weight. To make a batch, 2500 g of DI water and 2155.5 g of sugar were weighed out using a scale of accuracy ±0.05 g. These were mixed to form a solution of volume 2.5 L and density 1.205 g/cc. This solution was prepared the day before the experiment and stored in a polyethylene container to prevent leaching of stray ions into the solution. This waiting period allows any bubbles that formed in the solution during the mixing process to migrate out of the solution before any experiment. The density of the solution was measured before each experiment.

The sugar-water was stored at 21° C, and all experiments were conducted at this temperature. The kinematic viscosity of sucrose water at this concentration and temperature is 8.2×10^{-6} m^2/s. This value is strongly dependent on temperature [115], so the temperature was checked before each experiment.

It is found that the flow rate generated by the pump is strongly dependent on the amount of wear of the 2-stop tubing used to connect flow lines to the pump. For this reason, the 2-stop tubing was changed after each experiment, and the flow rate was recalibrated. The flow rate is determined by measuring the time it takes the pump to move a given volume of sugar water from one container to another. The pump speed (in RPM) was adjust until the desired flow rate for a given experiment was achieved. This recalibration was performed the night before each experiment, and the pump was not used again until the experiment to prevent any further wear to the 2-stop tubes.

5.4 Experimental Procedures

A description of the experimental procedure employed for each packed bed flow experiment follows. For a step-by-step procedure, see Appendix C. All experiments were carried out in the Science and Engineering Research Facility (SERF) at UTK.

On the day before an experiment, fresh DI water was procured from a Millipore Milli-Q filter system, sugar water was prepared, and the pump was calibrated, as described in Section 5.3. DI water was then used to clean all equipment, and the equipment used for activation of tracer particles was staged.

On the morning of the experiment, temperature and density of the sugar water were measured and recorded. A baseline radiation survey was performed to check for any pre-existing radioactive sources. The scanner was turned on over an hour before being used to allow internal electronics to reach equilibrium temperature. The flow loop was then assembled as pictured in Figure 5.19. The test section was placed on the bed of the scanner, outside the bore. A plastic sheath was placed in the bore of the scanner to protect the scanner in the event of leaks. Plastic drop cloths were also put down on the scanner for the same purpose. The injection tank was placed on a magnetic stirrer to ensure that tracers were well-mixed into the solution and delivered to the test section. Both tanks were elevated on blocks so that their water level remained above that of the test section throughout the experiment.

After the flow loop was assembled, particle activation was carried out at UTMC, as described in Section 5.2. The activated particles were transported to SERF by UTK Radiation Safety personnel. The flow loop was then filled with the DI sugar water solution. The outlet of the test section was elevated during filling so that air could escape the test section through the outlet. Once the water level reached the vent line, the vent valve was closed and throttled thereafter to remove any air remaining in the test section. It is desired that the test section be free of air, so the test section was agitated, and the vent valve was throttled until no more bubbles were visible in the flow. After filling and degasing the test section, the pump was turned off. At this point, the test section was moved into the bore of the scanner via the bed motion controls. The test section was positioned so that the FOV of the scanner is 150 mm downstream of the particle injection point (i.e. the end of the needle). This corresponds to 75, 68, and 65 bead diameters for the 2 mm, 2 and 4 mm, and 2, 4, 8 mm bead packings, respectively.

Tracer particles were delivered in a suspension of about 500 particles in sugar water in a 2 mL centrifuge vial. A few drops of glycerine were added to this vial at SERF, as this has

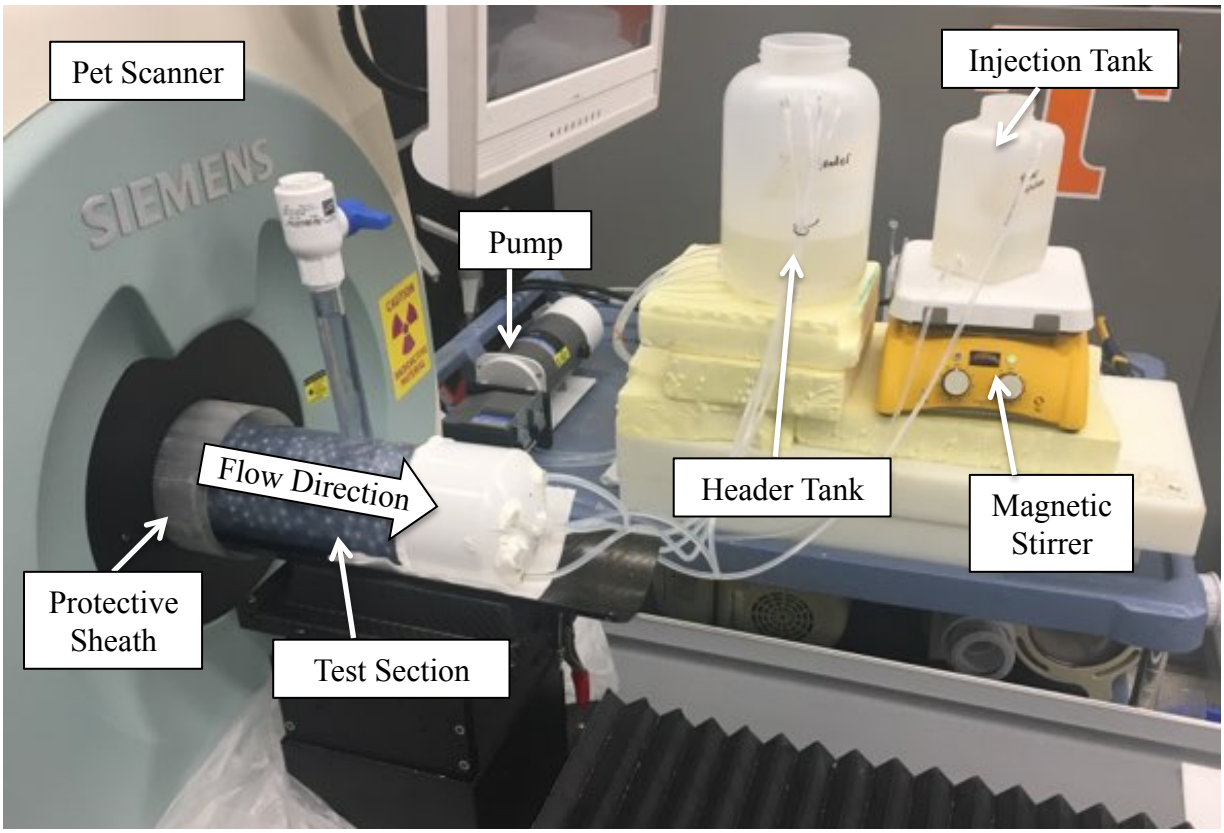

Figure 5.19: Photograph of assembled flow loop in bore of Inveon PET scanner. Shown is the 2, 4, 8 mm mixed packing bed.

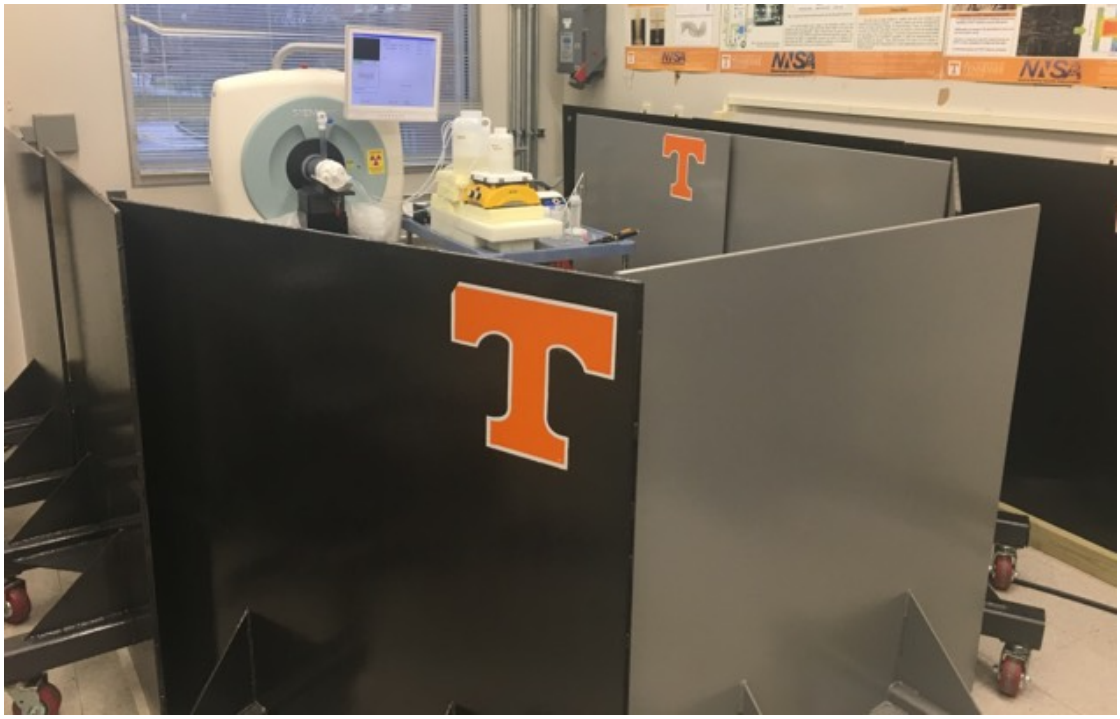

Figure 5.20: Final assembly of flow loop in PET scanner with shielding in place.

been found to help prevent particles from sticking to surfaces throughout the test section. The magnetic stirrer was turned on, and the particles were added to the injection tank. The tank was also stirred by hand at this point. The pump was set to the speed determined during calibration and started. Portable lead shielding was placed around the test area, as seen in Figure 5.20.

Flow was allowed to circulated for about one minute, and then the scan was begun. Scans were performed using the Inveon in emission modality for 30 minutes each. After each scan, the test section was inspected to check for leaks and the buildup of gas, and the header tank was stirred. Other than this time, all personnel remained outside the shielded area to mitigate radioactive dose. In the case of one experiment (referred to as "2_ReHigh" using the nomenclature introduced in Section 5.5) 15 minute scans were used. In this instance, a higher flow rate was used, and the shorter scans allowed more frequent stirring to encourage recirculation of tracers.

The default coincidence window of 3.438 ns and the restricted energy acceptance window of 425-625 keV were used for coincident gamma ray collection. No PET attenuation

correction or reconstruction was performed as only the raw list mode files of coincidence data are needed for PEPT reconstruction.

After each scan, subsets of the list mode data were analyzed via PEPT. Each experiment was conducted until trajectories were no longer being recorded. In general, this resulted in data being collected for one to two hours (two to four scans) before a given experiment was terminated.

The loss of data-rate over this time span occurs for three primary reasons. First, the activity of the tracers decays with a half-life of 109.8 minutes. As such, we expect that the signal will decrease by a factor of two roughly every two hours; however, the loss of signal observed in most experiments was more drastic than this.

A second factor contributing to declining signal is leaching of activity from the tracers. As demonstrated by the affinity subsequence given in Equation 2.6, the ion exchange resins used in this experiment have a greater affinity for Cl^- and other common ions than F^-. Thus, the presence of free anions in the flow loop is likely to result in the tracers exchanging their radiolabel for these free anions. To combat this, deionized water was used for all experiments; however, this is easily contaminated as free ions leach from the test section materials into the water, for example, Cl^- ions from PVC. Materials used in test section construction were chosen to mitigate leaching into DI water, but these only delay contamination. Leaching of activity from tracers has been studied, but no exact rate has been determined. This remains an open line of research.

Lastly, data collection rate decreases as tracers get stuck while traversing the packed bed. As demonstrated in Figure 5.15, bead sizes were chosen so that tracers can pass through the centers of all pores; however, beads can get trapped in the corners of the pores. The flow loop was constructed to allow for the recirculation of tracers, but it was found that very few tracers made a second pass through the test section, indicating that most got stuck during their first transit. A number of particles were seen to get stuck in the scanner FOV, and this must be considered during data handling.

After each experiment was concluded, the test section was removed from the scanner bore using the bed motion controls. The pump was run in reverse to drain the test section, and a second survey was conducted to check for spills and monitor radiation levels throughout the

lab. All radioactive materials were left to decay behind the portable shielding for two days. After this, a survey was conducted to ensure that all radiation had decayed to background levels, and all materials were cleaned up. Similarly, all contaminated activation equipment was retrieved from UTMC after radiation had decayed to background levels.

5.5 Experimental Conditions

A number of experimental conditions were explored with varying Reynolds numbers and bead packings. In this work, five of these cases are considered. These are described in table 5.2. These experiments are named according to the bead sizes used ("2", "2,4", and "2,4,8") and the Reynolds number used ("ReLow", "ReMid", "ReHigh"). A summary of these conditions is given in Table 5.2. The three Reynolds number conditions correspond to $Re = 0.135$, $Re = 0.27$, and $Re = 0.54$, respectively. Reynolds numbers are kept below 1 to ensure Darcy flow. All experiments used the aforementioned 46.3 % by weight sucrose solution of density 1.205 g/cc. This working fluid was kept at 21° C to ensure a kinematic viscosity of 8.2×10^{-6} m^2/s.

Reynolds number variation is only presented using the 2 mm bead test section. Experiments were performed using different Reynolds numbers with each bead pack; however, many of the experiments were inconclusive due to either a lack of trajectories or a strong biasing of the trajectories to the top of the test section caused by the uneven packing defect described in Section 5.3. If the latter persisted even after a given test section passed dye tests, the test section was disassembled and repacked again. Furthermore, the flow conditions listed in Table 5.2 are the designed conditions. After examination of all trajectories in a given test, the mean flow velocity and subsequently the Reynolds numbers were reassessed for each case. The corrected Reynolds numbers are given in Section 7.2 and differences are discussed therein.

In each experiment, a slight variation of activity of tracers was observed. This is summarized in Table 5.3. The number of tracers is based on the efficiency of transfer of activated tracers from the activation medium to the vials used for transport and was

Table 5.2: Summary of designed conditions for packed bed experiments. Reynolds number (Re), volume flow rate ($\dot{V}$), and mean axial velocity ($\overline{v}$) are those intended for each experiment.

Experiment	Bead Sizes (mm)	Re	Pump Speed (RPM)	$\dot{V}$ (mL/min.)	$\overline{v}$ (mm/s)
2_ReLow	2	0.135	80	55	0.55
2_ReMid	2	0.27	167	110	1.1
2_ReHigh	2	0.54	369	220	2.2
2,4_ReMid	2, 4	0.27	138	95	1.0
2,4,8_ReMid	2, 4, 8	0.27	113	74	0.96

Table 5.3: Summary of activity of tracers used for packed bed experiments.

Experiment	Est. Number of Tracers	Activity per Tracer (μCi)
2_ReLow	475	36
2_ReMid	450	44
2_ReHigh	450	46
2,4_ReMid	500	50
2,4,8_ReMid	500	58

estimated from the measured activities of the transport vials relative to those of the activated samples.

Chapter 6

Data Handling

All data collected during experiments were analyzed using in-house software. M-PEPT reconstruction was implemented in C++, and all post-processing routines were implemented in C++ and Matlab. Apple LLVM 9.0 and MATLAB_R2017a were used for C++ and Matlab compilation, respectively.

6.1 M-PEPT Reconstruction

Raw coincidence event data from the Siemens Inveon are stored in listmode files. These files contain a series of binary words with each giving the the locations of the crystals used in a coincidence location. Events are sorted by time, and time stamp words are placed into the stream every 200 μs. For reasons of propriety, the exact formatting of these files is withheld.

Data were analyzed using the *MultiPEPT* software created at UTK. This code was written in C++ and is maintained by the author. It has been audited as part of a Master's thesis by Eric Moore [116]. Minor changes to the code have been made since this audit, but major functions have not changed.

The primary purpose of this program is to read list mode files and produce text files containing tracer location information for each trajectory. One file is created for each recorded trajectory. These files contain time, the x-, y-, z-locations, and the calculated x-, y-, z-uncertainties for each detection. In the coordinate system used hereafter, the x-, y-, and z-directions correspond to the radial horizontal, radial vertical, and axial directions,

Table 6.1: Summary of reconstruction parameters used for each experiment. Experiment labels are given according to sizes of beads employed (in mm). All parameters are described in Section 3.2. CL_{LLD} refers to the threshold CL crossing value used to determine if any particles are present in a given time step or not.

Exp.	Time Step (ms)	Voxel Size (mm)	CL_{LLD}	w (voxels)	r
2_ReLow	100	1	5	3	0.05
2_ReMid	100	1	4	3	0.08
2_ReHigh	100	1	5	3	0.05
2,4_ReMid	100	1	5	3	0.08
2,4,8_ReMid	100	1	4	4	0.05

respectively. The coordinate system is aligned such that the origin is located at the front axial edge of the scanner FOV, aligned with the centerline of the bore. A separate file of all particle positions found in each time step, without linking into trajectories, is also created to allow the user to adjust any linking parameters without the need to rerun the particle detection step.

All reconstruction was performed using the FPI method described in Section 3.2. A summary of the reconstruction parameters used for each case is given in Table 6.1. 100 ms time steps were chosen to ensure ample CL per detection for reconstruction. Given the mean flow velocities of ∼1 mm/s being studied, this was deemed sufficient time resolution. A $1 \times 1 \times 1$ mm^3 grid was employed in all cases for CL crossing studies, and the Gaussian smoothing described by Equation 3.4 was used. It was observed that a background of CL noise develops throughout the experiments, likely due to leaching. For this reason, it was beneficial to use the boxcar filtering as a means of background measurement and the Gaussian kernel for image smoothing. The other parameters used for reconstruction were determined iteratively by examining subsets of the data and adjusting parameters to allow for a maximum number of particles detected while reducing the number of spurious detections. Using these parameters, an average of 564, 602, 663, 508, and 838 CL were used for each detection for the cases 2_ReLow, 2_ReMid, 2_ReHigh, 2,4_ReMid, and 2,4,8_ReMid, respectively.

The linking parameters were adjusted in a similar manner, accounting for spurious detections associated with incorrect linking. A summary of the linking parameters used is given in Table 6.2. Linking was performed using the 2-frame nearest neighbors technique

Table 6.2: Summary of linking parameters used for each experiment. Experiment labels are given according to sizes of beads employed (in mm). N_{ghost} is the number of ghost frames a particle is allowed to remain undetected until its trajectory is discontinued. N_{min} is the minimum number of position locations that each trajectory must contain to be considered valid. Low, middle, and high Reynolds number cases refer to $Re = 0.135$, $Re = 0.27$, and $Re = 0.54$, respectively.

Exp.	v_{max}	N_{ghost}	N_{min}.
2_ReLow	0.03	3	20
2_ReMid	0.02	3	30
2_ReHigh	0.02	3	30
2,4,_ReMid	0.02	3	20
2,4,8_ReMid	0.03	3	30

described in Section 3.3. The more robust projection method was not found to be beneficial for these experiments.

6.2 Dewarping

As noted by Moses [63], a radial astigmatism defect is present in cylindrical geometry PET scanners due to the depth of interaction of coincident photons in detector elements. For sources near the radial edge of a scanner, gamma rays are likely to strike a given crystal face at an oblique angle such that they pass through this crystal and interact in a neighboring crystal. This will create a CL distribution that will have an extended tail toward the center of the scanner. A pictorial representation of this is shown in Figure 6.1. This defect will result in a radially inward biasing of PEPT-measured particle positions, with increased magnitude near the radial edges of the scanner. This has been noted by previous PEPT researchers [10], but the first correction was applied by the author and others [81]. In the experiments documented herein, data were collected out to a radial extent of 36.8 mm (i.e. the pipe radius). As this is a significant percent of the detector array radius of 80.5 mm, it is expected that some degree of defect will be present and should be corrected.

A series of scans was performed with a calibration source to create a dewarping map for positions reconstructed via PEPT. This procedure is analogous to those performed for the calibration of PIV experiments [117, 118, 119]; however, this calibration uses a series of point locations in lieu of a single image of a target, as is commonly used for PIV calibration. A

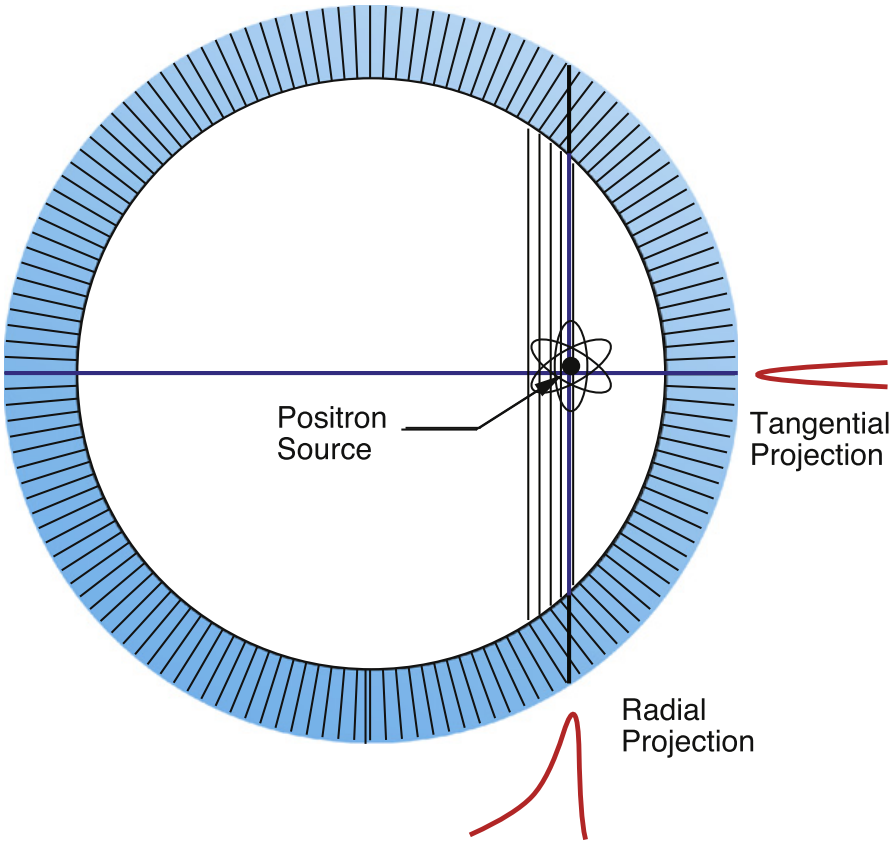

Figure 6.1: Radial astigmatism defect for imaging sources near radial edge of PET scanner [63].

^{22}Na point source of activity 3.4 μCi encased in a polyethylene cube of side length 12.7 mm was attached to an x-y positioning table with accuracy 0.05 mm by a plastic rod, as shown in Figure 6.2. Assuming that all biasing due to the depth of interaction occurs away from the center, M-PEPT reconstruction was used to place the source in the center of the FOV to within 0.04 mm in each spatial direction. Then, the positioning system was used to move source in the positive x- and z-directions in 10 mm increments until the source reached the axial and radial edges of the FOV. It is assumed that all biasing will be a result of axial and radial displacement from the center, and thus data from only one quadrant of the x-z plane are sufficient for building the dewarping map. At each location, 30 second scans were performed. M-PEPT was used to locate the source, and this reconstructed position compared to the actual position determined with the positioning table. The real and reconstructed positions are shown in Figure 6.3. Biasing of up to 3 mm in the radial direction occurs at the radial edge, and biasing of up to 0.6 mm in the axial direction occurs at the axial edge.

Similar to the method of Van Doorne and Westerweel [119], a third-order polynomial in r- and z-directions was fitted using the Matlab Curve Fitting Toolbox to transform from measured (subscript M) to real (subscript R) coordinates:

$$\begin{aligned} r_R = {} & a_{0,r} + a_{1,r} r_M + a_{2,r} z_M + a_{3,r} r_M^2 + a_{4,r} z_M^2 + a_{5,r} r_M z_M \\ & + a_{6,r} r_M^3 + a_{7,r} z_M^3 + a_{8,r} r_M^2 z_M + a_{9,r} r_M z_M^2 \end{aligned} \tag{6.1}$$

$$\begin{aligned} z_R = {} & a_{0,z} + a_{1,z} r_M + a_{2,z} z_M + a_{3,z} r_M^2 + a_{4,z} z_M^2 + a_{5,z} r_M z_M \\ & + a_{6,z} r_M^3 + a_{7,z} z_M^3 + a_{8,z} r_M^2 z_M + a_{9,z} r_M z_M^2. \end{aligned} \tag{6.2}$$

Here, the axes are aligned so that the origin is at the center of the scanner FOV.

It is assumed that there is no radial biasing away from $r = 0$ and no axial biasing away from $z = 0$, and thus the coefficients $a_{0,r}$, $a_{2,r}$, $a_{4,r}$, and $a_{7,r}$ are forced to zero, and $a_{0,z}$, $a_{1,z}$, $a_{3,z}$, and $a_{6,z}$ are forced to zero. After fitting, this polynomial was used to correct the measured positions from the calibration experiment. These dewarped positions are shown in Figure 6.3. After dewarping, the average difference between corrected and true positions is 0.09 mm in the radial direction and 0.04 mm in the axial direction.

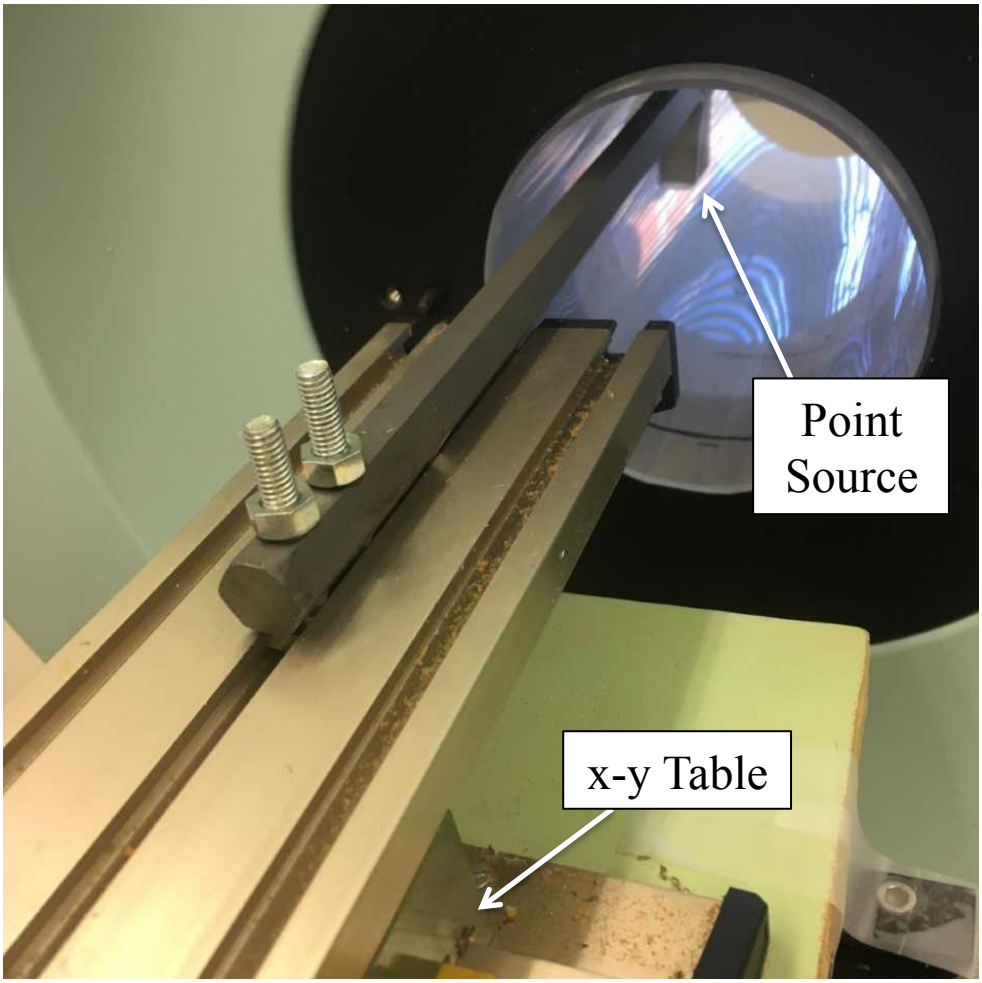

Figure 6.2: Point source and positioning system used to generate dewarping map.

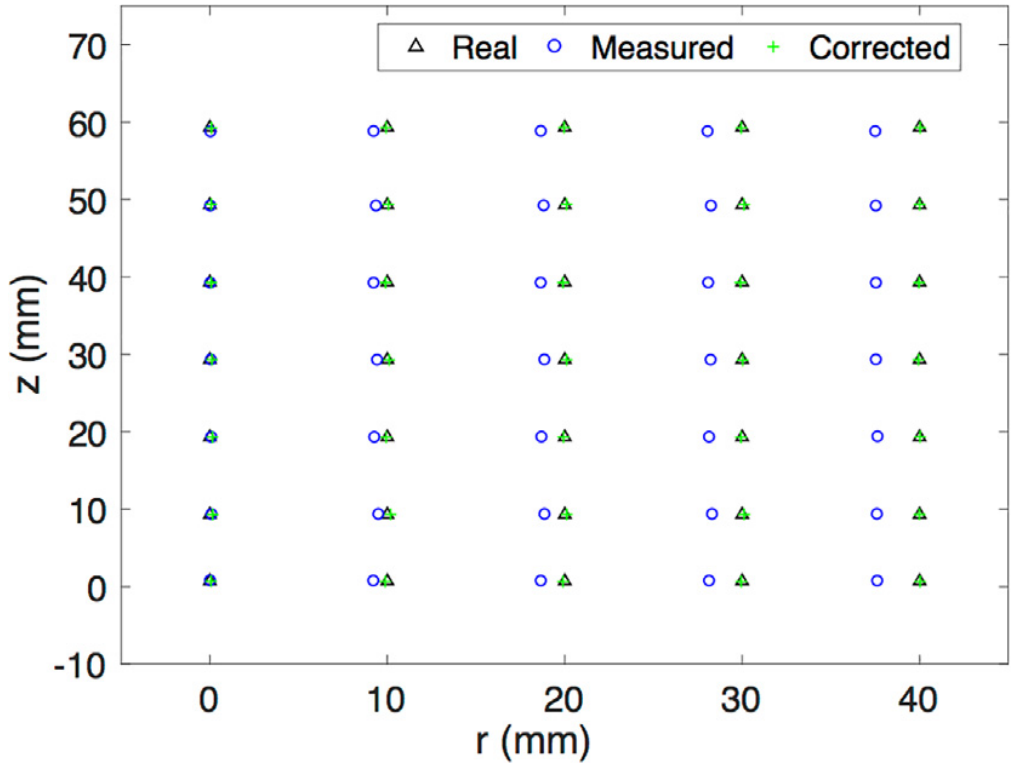

Figure 6.3: Comparison of M-PEPT reconstructed positions before (circles) and after (crosses) dewarping to real positions (triangles) for point source location in Siemens Inveon.

.

As the detector elements within the scanner remain stationary with respect to the scanner bore, it is expected that only a single calibration experiment is needed for a given PET scanner or equivalent system. This calibration only accounts for distortions due to depth of interaction of photons in detector crystals and does not account for other potential distortions in PEPT.

The polynomials Equation 6.1 and Equation 6.2 were used to transform all trajectories measured in this experiment. Dewarping is carried out after trajectories are reconstructed and before any further filtering is applied. In contrast, some PET software models the penetration of photons and corrects for it during image reconstruction [63]. This may be implemented in future versions of the *MultiPEPT* software.

6.3 Filtering

Filtering of the dataset was performed in multiple steps. After dewarping, trajectories of particles that get stuck in the scanner FOV were removed from the dataset. To do this, any trajectory that had a standard deviation in position of less than 2 mm across its length was removed. Next, if any trajectory had a subset of its history of 200 consecutive positions with a standard deviation of less than 0.2 mm, it was identified. The first measure accounts for any particle that remains stuck in the FOV throughout its history. It is not uncommon for a particle to get stuck and remain in the FOV for the duration of an experiment but be occasionally lost by the reconstruction algorithm and found again. As such, a single stuck particle may account for several trajectories removed from the dataset. The second measure accounts for any particle that gets stuck during its history, even if only temporarily. In this case, the trajectory is kept until it gets stuck, and the remainder of the trajectory is discarded.

The next filtering step is to transform the trajectories from a given experiment so that the centerline of the pipe falls on the z-axis for the coordinate system used herein. To do so, the xy-projections of all dewarped trajectories from an experiment are first plotted. As an example, trajectories from the 2_ReMid case are shown in Figure 6.4. Positions along the outer edge of the test section are identified and fit to a circle of radius 36.8 mm to find the

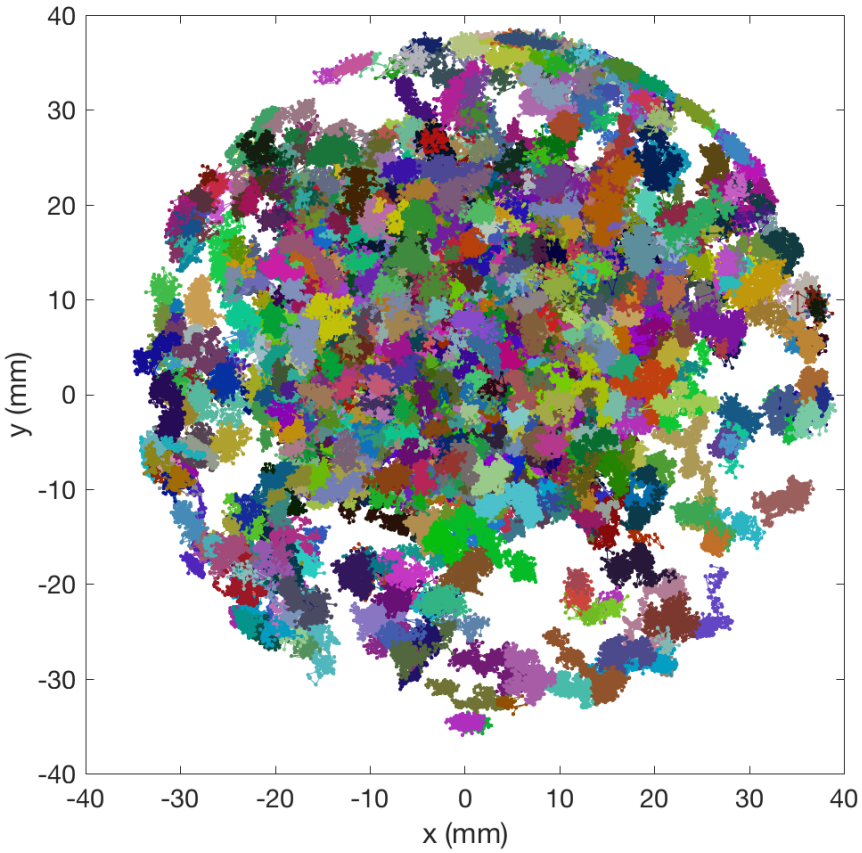

Figure 6.4: xy-projection of trajectories reconstructed from first 30 minutes of experiment 2_ReMid.

center. In the case shown, the center was determined to be (x_0, y_0)=(2.9 mm, 1.5 mm). The x- and y-coordinates of all the trajectories are transformed as $x' = x - x_0$ and $y' = y - y_0$.

As this experiment was analyzed in Cartesian coordinates, the primary purpose in identifying the centerline is rejection of data near the pipe walls. As such, errors in this transformation do not propagate into statistics considered in this analysis.

Lastly, trajectories were filtered and differentiated by convolution with the Guassian kernels given in Equations 3.12, 3.13, and 3.14. When using such filters, an optimal kernel half-width σ must be chosen that sufficiently rejects noise without smoothing out any real fluctuations in the trajectories. To do so, we use the method described by Berg et al. [66] in which one looks for an "elbow" in the plots of the standard deviation of velocity and acceleration versus filter size. This plot for the case 2_ReMid is shown in Figure 6.5. In these studies, σ was varied from 0.5 to 6 time steps in 0.5 time step increments. To calculate

velocity and acceleration standard deviations, only measured accelerations calculated from data points with radial position $r < 20$ mm were considered to eliminate aberrations caused by wall effects.

In all cases observed, the only elbow-like features occur in the plots of velocity standard deviation. For all experiments, an elbow appears at $\sigma = 2$ time steps. For this reason, a filter width of $\sigma = 2$ time steps was used for all cases. The acceleration plots do not show a clear elbow, and for this reason, all acceleration statistics considered herein are normalized by root mean square (RMS) acceleration. Figure 6.6 shows the effect of a filter of this size on time series data of the x-, y-, and z-locations of two particles. This filter appears to remove much of the erraticism of each trajectory while maintaining much of the underlying structure. The kernel is constructed with support $4\sigma + 1$ time steps. Thus, a support of 9 time steps was used in this work.

The lack of convergence of acceleration statistics with filter width reveals a potential drawback of the use of smoothing kernels for filtering and differentiating. An alternative form of filtering based on the use of penalized B-splines has been suggested [120, 121]. Calculated acceleration statistics are seen to more quickly converge with filter width with such a filter [121]. A B-spline filtering routine has been implemented; however, it has been seen that it does not sufficiently remove noise from the trajectories measured via PEPT. The investigation of different filtering and differentiating methods for PEPT is left to future work.

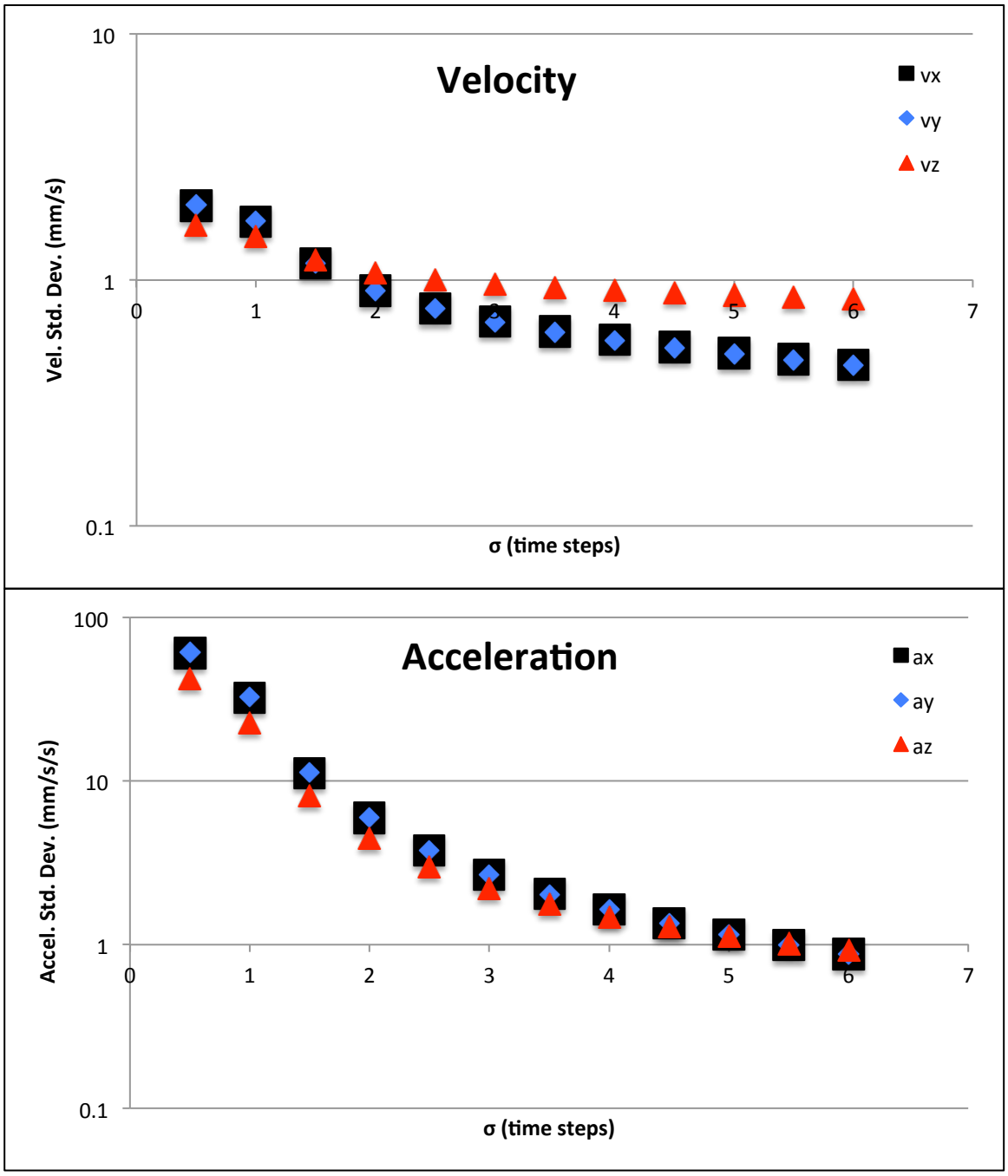

Figure 6.5: Plots of velocity (top) and acceleration (bottom) versus filter width for experiment 2_ReMid. Filter width is varied in 100 ms time steps.

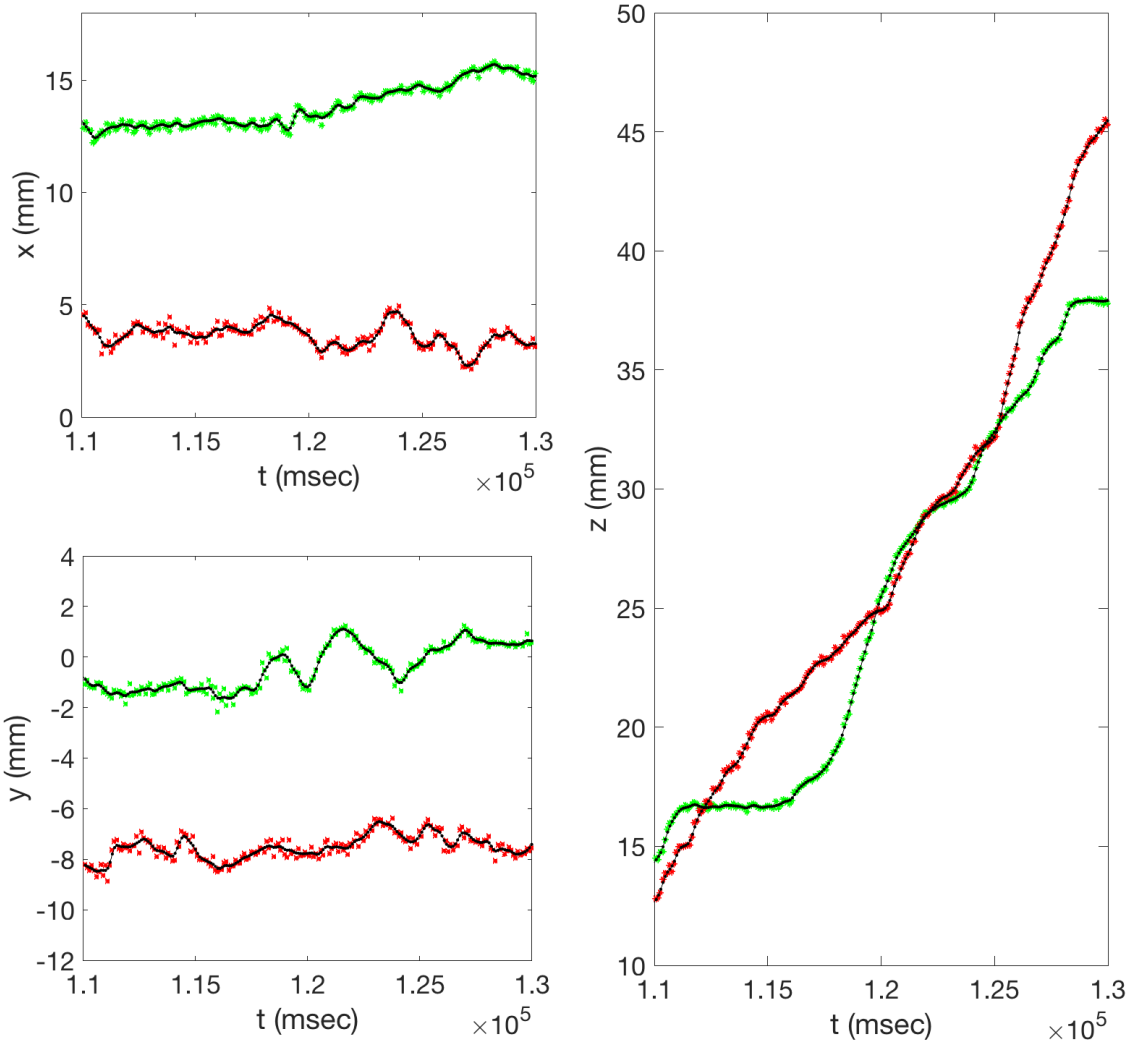

Figure 6.6: Comparison of unfiltered and filtered position time series for two subsets of two trajectories from case 2_ReMid. These trajectories appeared 2 minutes into data collection. Colored asterisks are unfiltered data and black dots are data filtered using Gaussian kernel of size $\sigma = 2$ time steps.

Chapter 7

Results

After M-PEPT reconstruction, a number of analyses were performed using particle trajectories. The data were analyzed to examine characteristics of the underlying porous media flow including bulk velocity and acceleration statistics, particle transport statistics, and velocity correlations. These results follow.

7.1 Reconstruction Results

Table 7.1 gives a summary of the reconstruction results for the five experiments. In this work, a new record for experimental multiple-particle tracking with PEPT was achieved. The 85 particles tracked simultaneously during experiment 2,4_ReMid is a five-fold increase in multiple-particle tracking performance over the previous high of 17 particles demonstrated by the author [48, 55].

It was found that the number of trajectories detected varied greatly among the different experiments, with the cases 2_ReLow and 2,4,8_ReMid showing the fewest trajectories. In both of these cases, very few particles were seen to pass through the test section, and the exact reason for this is unclear. It seems likely that this was largely due to particles getting stuck upstream of the FOV, but no solution for this problem was found. An unknown source could have also contaminated the water with free ions, leading to early onset of leaching of the radiolabel from the tracer particles. Before each scan, water quality was assessed with a conductivity meter, but no difference was observed among different experiments.

Table 7.1: Summary of reconstruction results for porous media experiments. Number of filtered trajectories refers to the number of trajectories remaining after stuck particle trajectories are removed. Maximum number detected refers to the maximum number of particles tracked simultaneously during the experiment.

Exp.	Data Used (min.)	No. of Traj.	No. of Filtered Traj.	Max No. Detected
2_ReLow	30	267	73	19
2_ReMid	60	6,116	2,090	80
2_ReHigh	45	3,585	946	82
2,4_ReMid	30	5,310	2,256	85
2,4,8_ReMid	30	678	262	30

The first 200 filtered trajectories recorded from each experiment are shown, colored according to instantaneous velocity magnitude, in Figures 7.1-7.5. In the case of experiment 2_ReLow (Figure 7.1), all trajectories are shown, as only 73 filtered trajectories were found. A few qualitative features of these scans should be noted.

We see that the plume of particles is less spread out in the case of the 2 mm packed test section than in the case of the mixed bead sizes test section, indicating that dispersion of tracers is happening more slowly in the 2 mm cases. Secondly, we note that the cases 2_ReLow and 2,4,8_ReMid appear to preferentially sample the upper portion of the test section. It is possible that this is caused by some further settling of the packed beads during the time between dye tests and the experiment. While not detrimental, this defect does create more trajectories in the near-wall region near the top of the test section that will be rejected during data analysis. Lastly, many trajectories in all cases show regions of intense acceleration and deceleration, indicated in these figures by changes of color. These signs of acceleration intermittency will be reflected in the discussion of acceleration statistics in Section 7.2.

Recall from Section 3.2 that the uncertainty in the location of a particle can be estimated as the standard deviation of the Gaussian fit to a particle image divided by the square root of the number of CL that went into that particle image. The average number of CL used per detection and average estimated uncertainty in each spatial direction are given in Table 7.2. In each experiment, the estimated uncertainty is seen to be of the order of 0.1 mm in each spatial direction. The trend of decreased uncertainty with increased number of CL is observed except in the case of experiment 2_ReLow. It is believed that the lower uncertainty

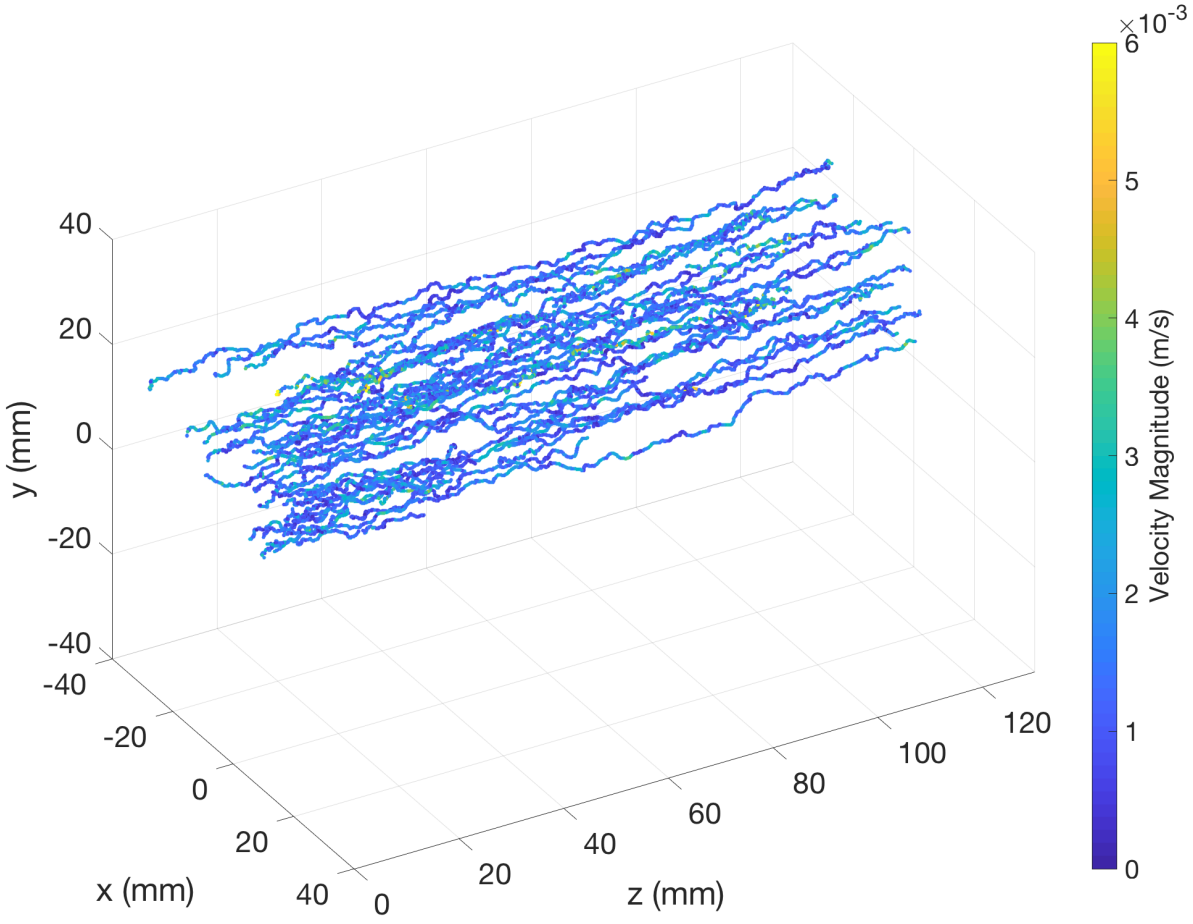

Figure 7.1: Filtered trajectories from experiment 2_ReLow, colored according to velocity magnitude. Flow direction is left to right.

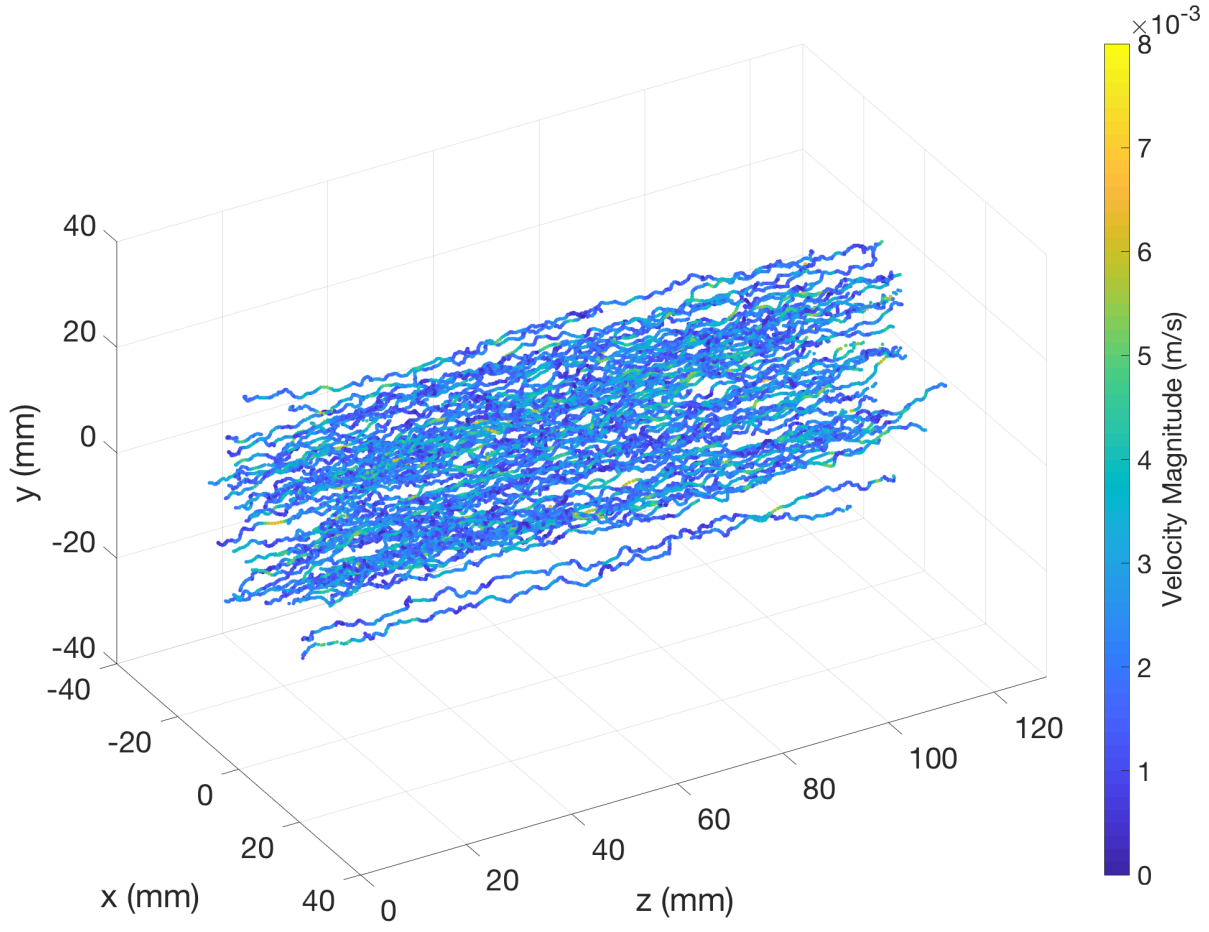

Figure 7.2: First 200 filtered trajectories from experiment 2_ReMid, colored according to velocity magnitude. Flow direction is left to right.

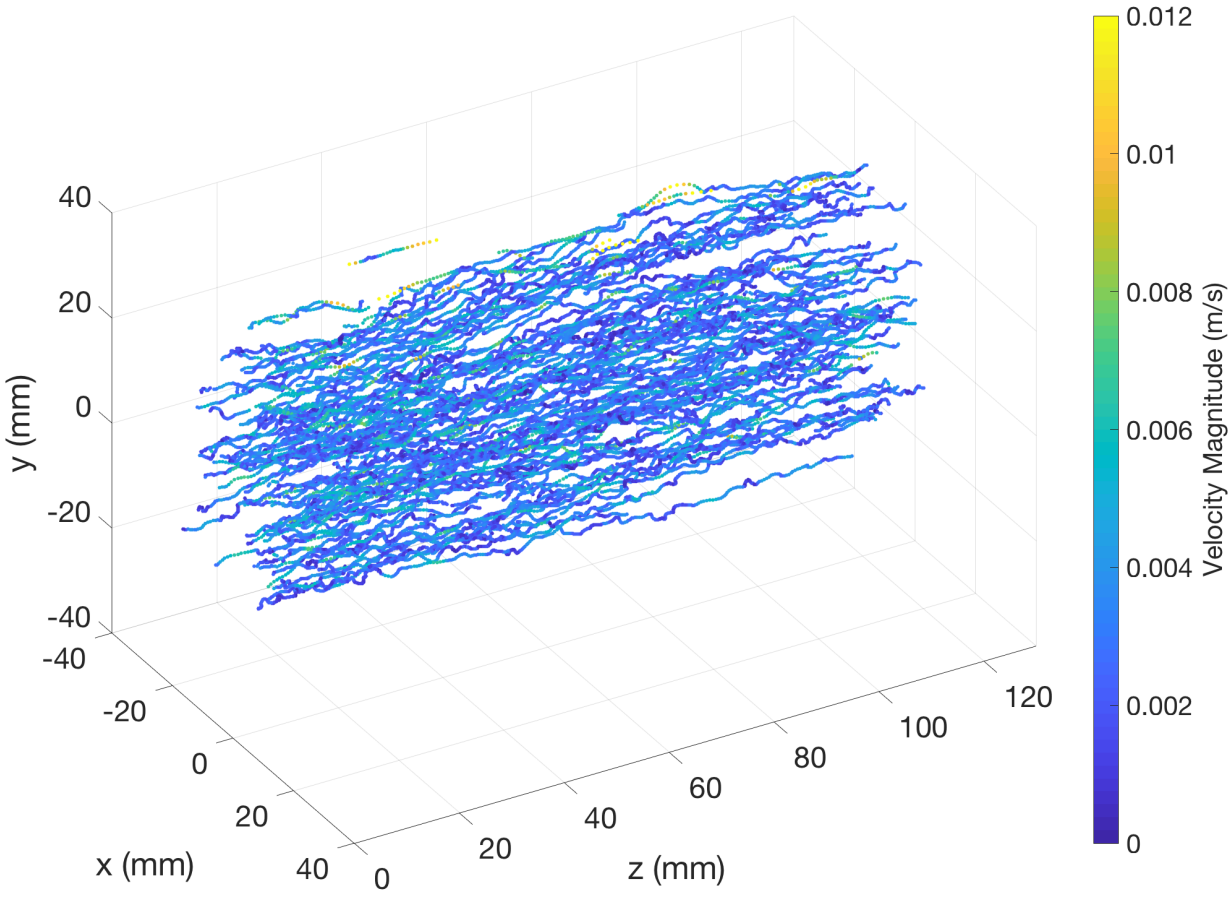

Figure 7.3: First 200 filtered trajectories from experiment 2_ReHigh, colored according to velocity magnitude. Flow direction is left to right.

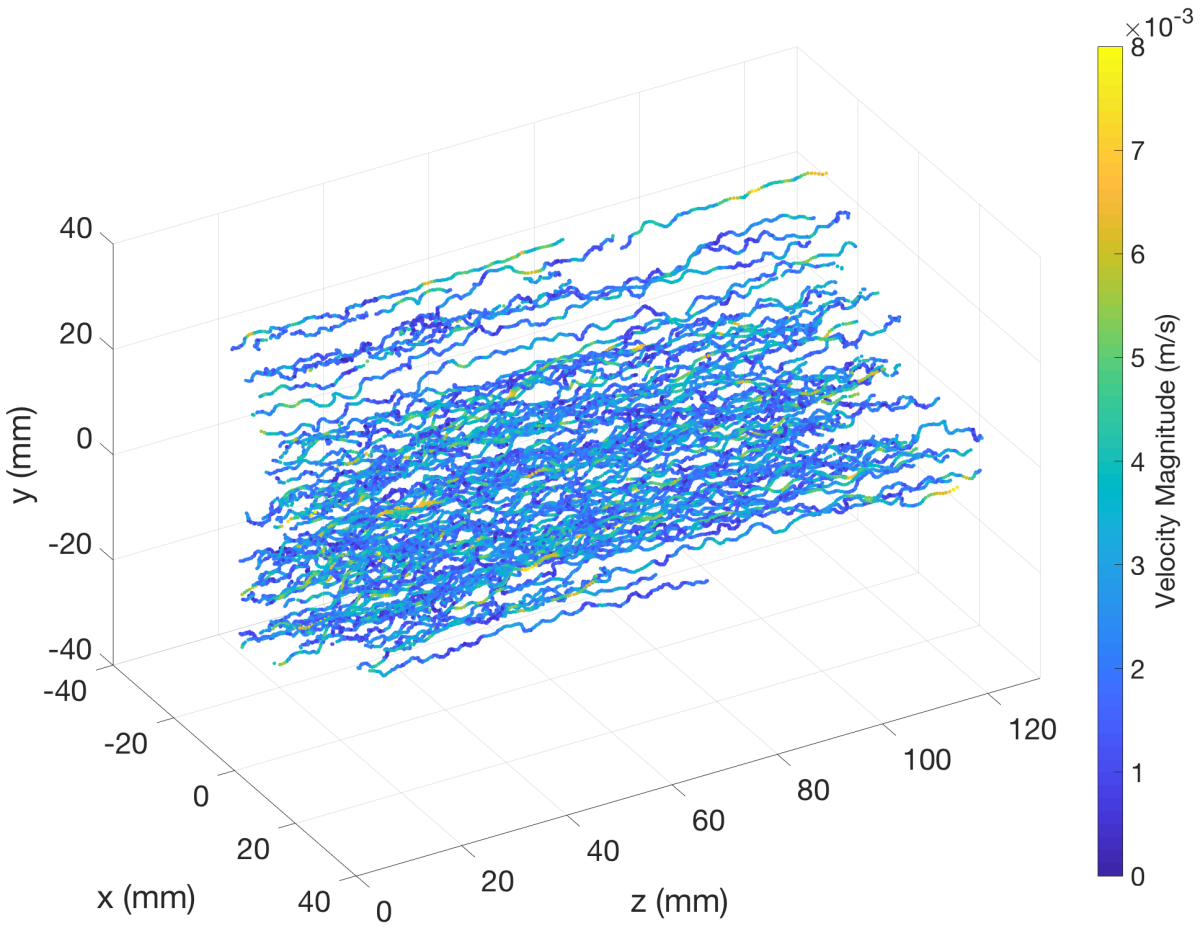

Figure 7.4: First 200 filtered trajectories from experiment 2,4_ReMid, colored according to velocity magnitude. Flow direction is left to right.

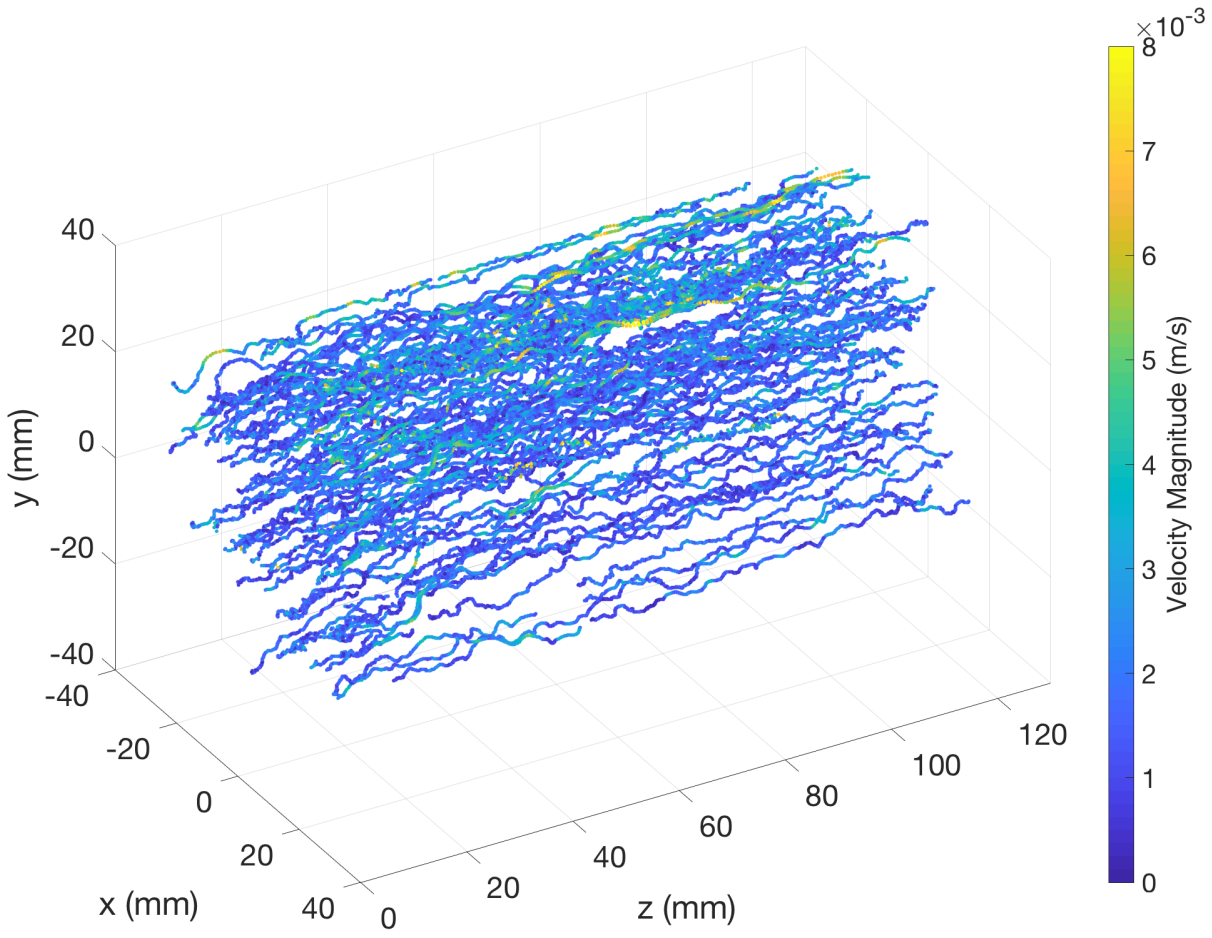

Figure 7.5: First 200 filtered trajectories from experiment 2,4,8_ReMid, colored according to velocity magnitude. Flow direction is left to right.

Table 7.2: Average estimated uncertainty and number of coincidence lines (CL) used for detection in each experiment.

Exp.	Δx (mm)	Δy (mm)	Δz (mm)	No. of CL
2_ReLow	0.079	0.098	0.061	564
2_ReMid	0.094	0.092	0.066	602
2_ReHigh	0.089	0.092	0.064	663
2,4_ReMid	0.098	0.103	0.072	508
2,4,8_ReMid	0.086	0.087	0.060	822

seen in this experiment is due to the uneven sampling of the trajectories within the test section. As more particles were detected near the top of the test section, less scatter of coincident gamma rays is expected than for particles in the radial center of the pipe, as all but the downwardly directed gamma rays have less solid material through which to travel. This would result in a tighter spread of the CL used to create each particle image.

An axial variability of measured uncertainty is also observed. Figure 7.6 shows measured uncertainty in each direction as a function of axial location for the 2_ReMid case. Measurement uncertainty peaks at the axial edges and is lowest in the center of the FOV. This is the mirror of the axial sensitivity profile of the scanner (see Figure 5.7), reflecting the inverse relationship between uncertainty and the number of CL recorded by the scanner. Due to the increased uncertainty near the axial edges, the outer 10 mm of data in each axial direction was neglected during statistical analysis.

The scanner sensitivity profile shows little variation with radial position except very near to the radial edge of the FOV. As such, no radial trend in calculated uncertainty was observed.

7.2 Velocity and Acceleration Statistics

7.2.1 Radial Profiles

We first examine average velocity and acceleration statistics within each test section. To do so, all individual velocity and acceleration measurements (i.e. each time step within each trajectory) are sorted into radial bins, as was done in the experiment described in Section 4.3.

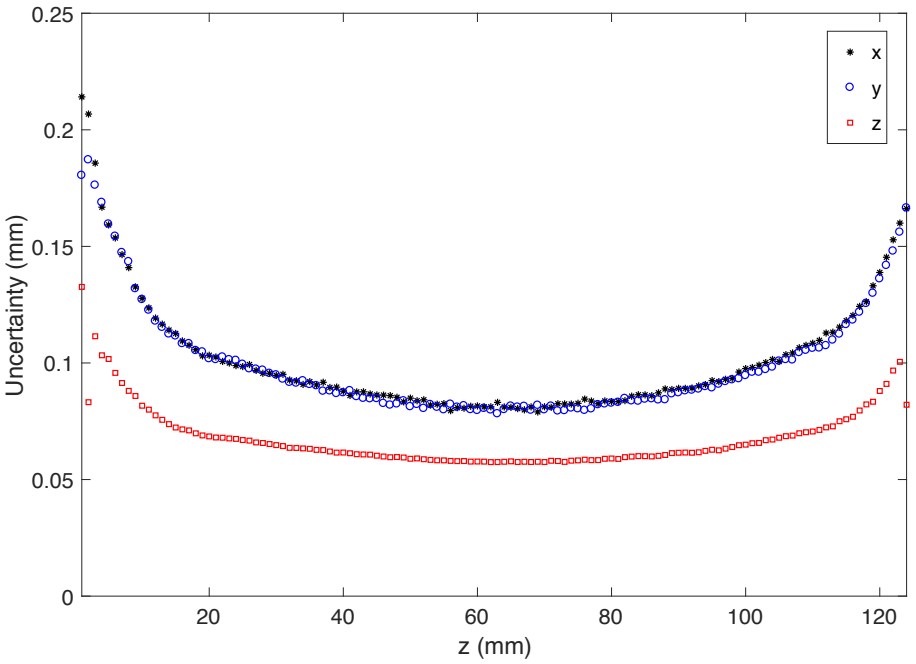

Figure 7.6: Variation of measured uncertainty with axial (z-) position for case 2_ReMid.

Bins are divided by circles of radii

$$r_i = \left\{0, \frac{1}{\sqrt{N}}R, \ \frac{1}{\sqrt{N}}\sqrt{2}R, \ ..., \ \frac{1}{\sqrt{N}}\sqrt{N-1}R, \ R\right\}, \tag{7.1}$$

where $N = 50$ bins are used, and R is the radius of the pipe. This segmenting gives all bins the same cross-sectional area.

Plots of mean and fluctuating velocity and mean and RMS acceleration are shown in Figures 7.7-7.11. Uncertainty was calculated as the standard deviation of the mean of each quantity. The fluctuating velocity component v_i' is shown, where the Reynolds decomposition, $v_i(t) = \langle v \rangle + v_i'(t)$ is used, and angle brackets indicate ensemble-averaging. Fluctuating velocity variance is shown to keep with the form of the Reynolds stress tensor $R_{ij} = \langle v_i' v_j' \rangle$. A few things are to be noted from the plots of these quantities.

We note that in each case velocity and acceleration statistics appear to be mostly constant below $r = 20$mm. Breaks from this tendency are observed in the RMS acceleration profiles of case 2,4,8_ReMid that continues to fluctuate down to the core. The cause for this is unknown but could be related to the biasing of trajectories toward the top of the test section. Due

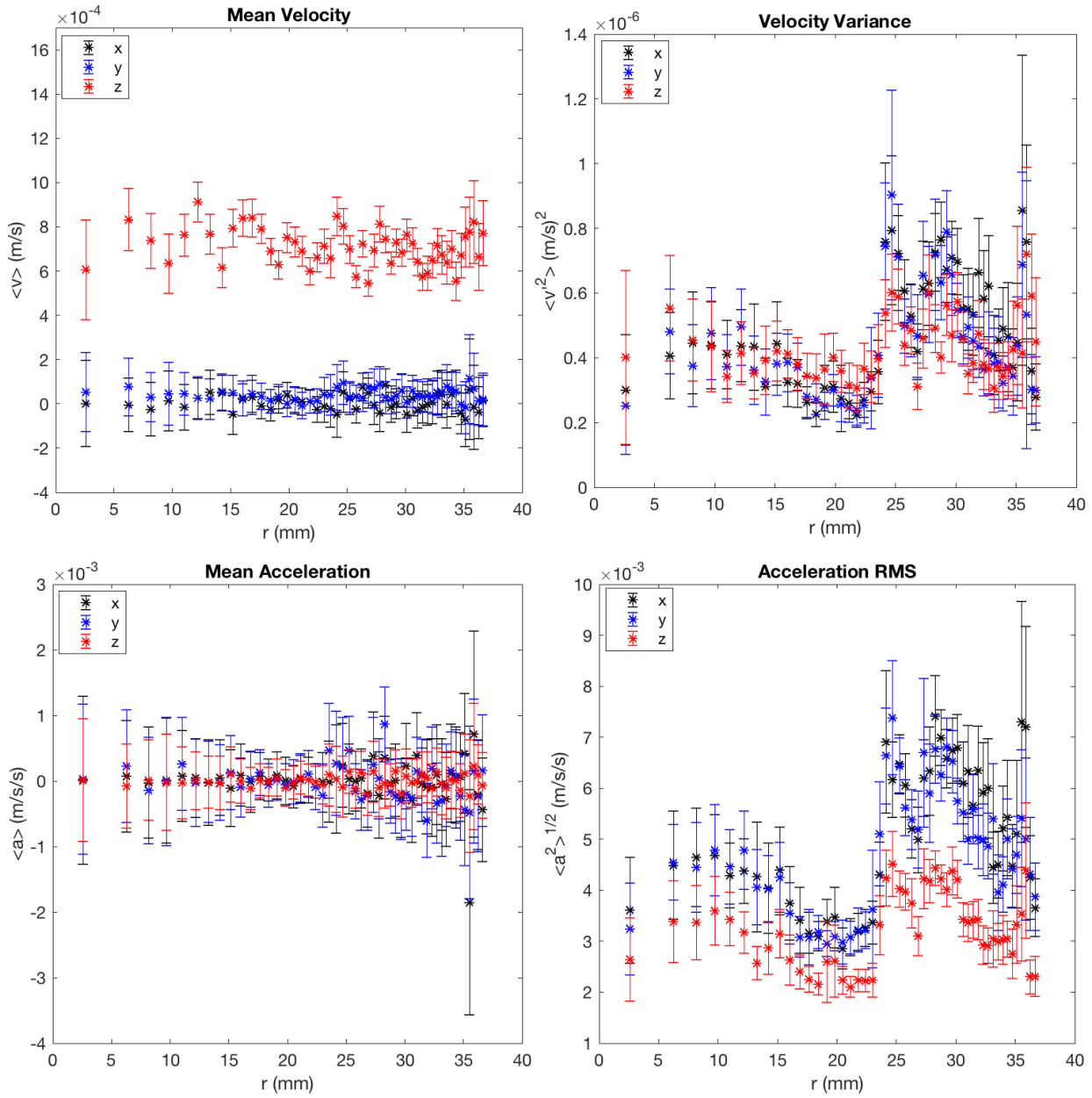

Figure 7.7: Velocity and acceleration profiles from experiment 2_ReLow. Clockwise from top left: mean velocity, velocity fluctuation variance, root mean squared acceleration, and mean acceleration.

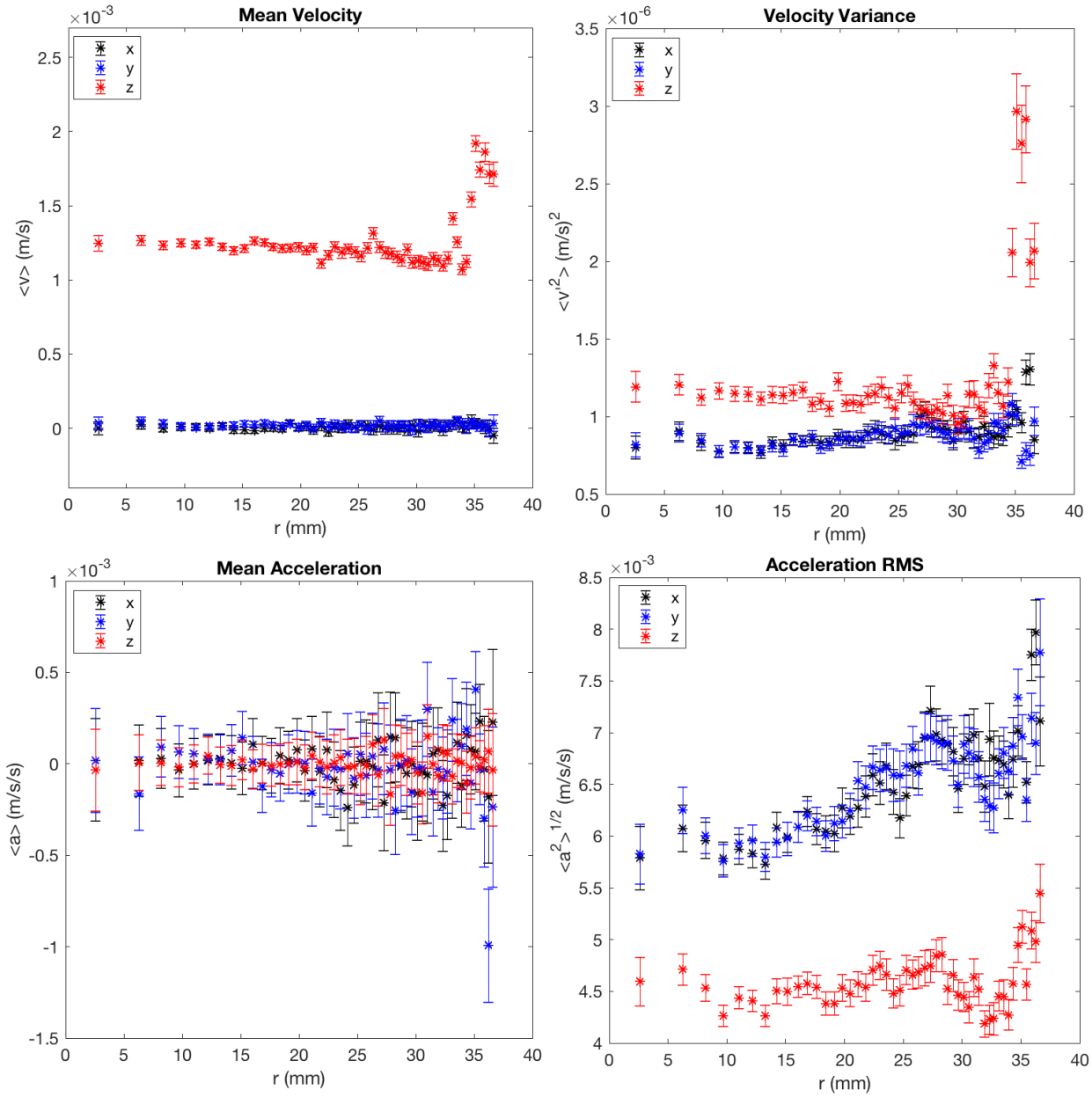

Figure 7.8: Velocity and acceleration profiles from experiment 2_ReMid. Clockwise from top left: mean velocity, velocity fluctuation variance, root mean squared acceleration, and mean acceleration.

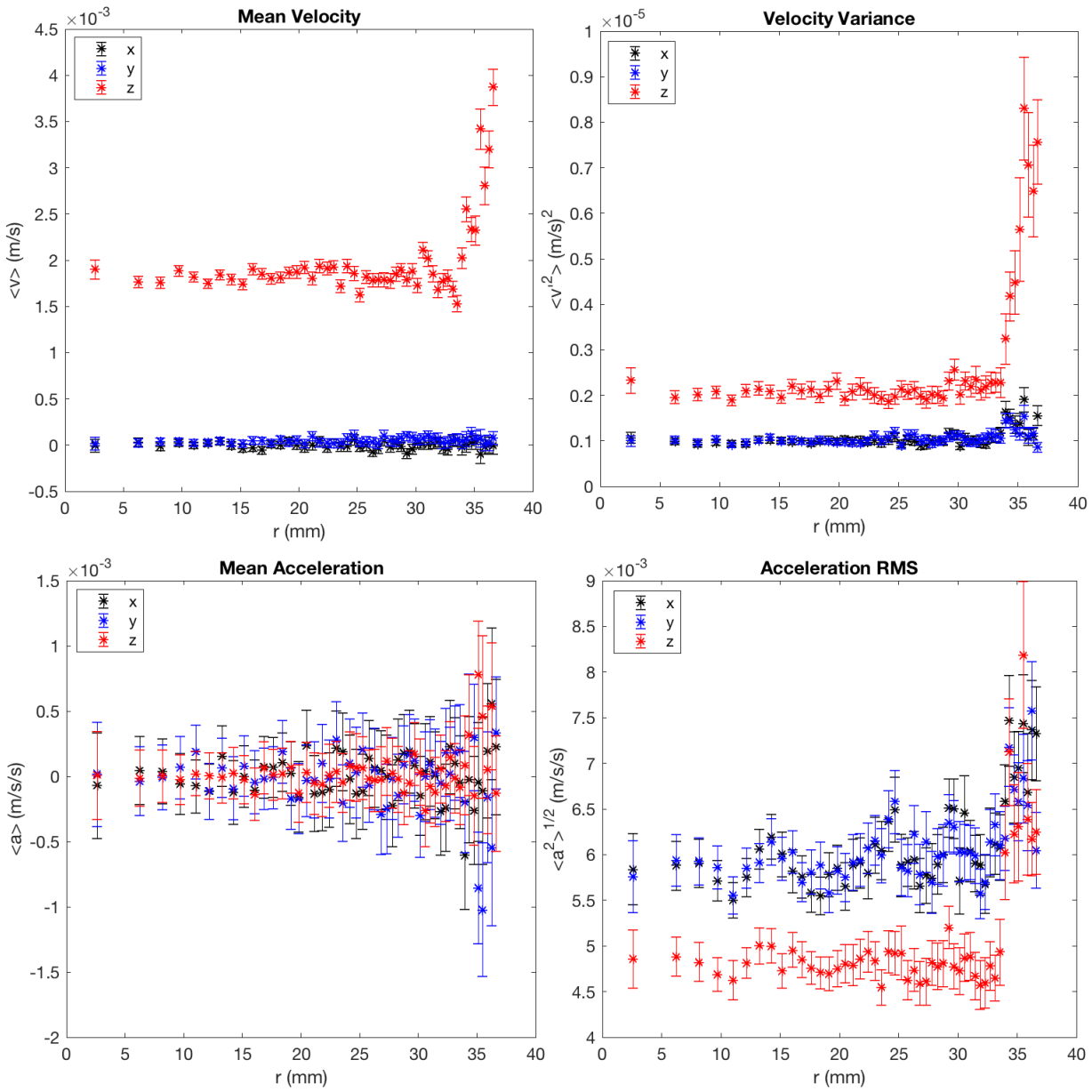

Figure 7.9: Velocity and acceleration profiles from experiment 2_ReHigh. Clockwise from top left: mean velocity, velocity fluctuation variance, root mean squared acceleration, and mean acceleration.

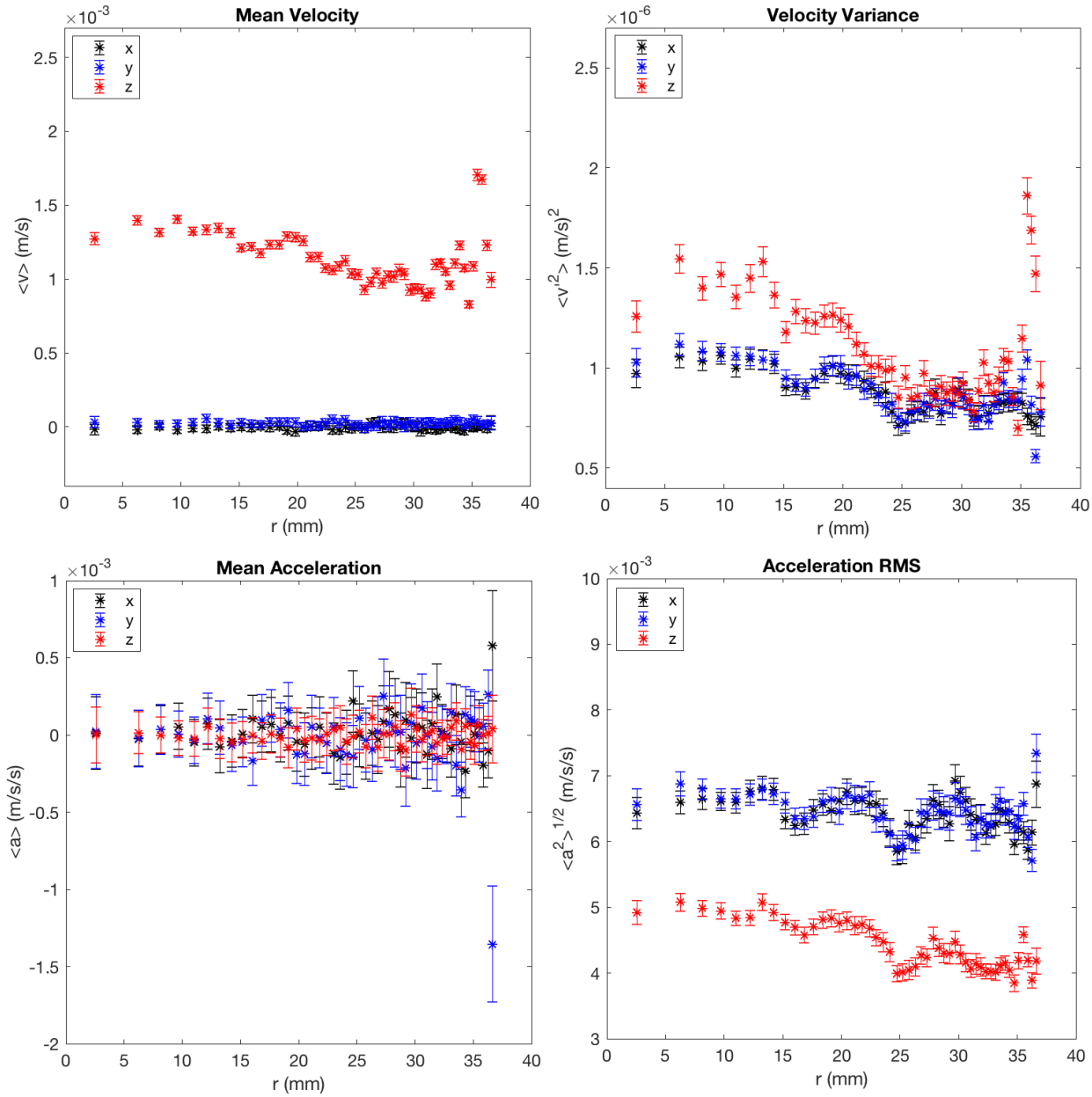

Figure 7.10: Velocity and acceleration profiles from experiment 2,4_ReMid. Clockwise from top left: mean velocity, velocity fluctuation variance, root mean squared acceleration, and mean acceleration.

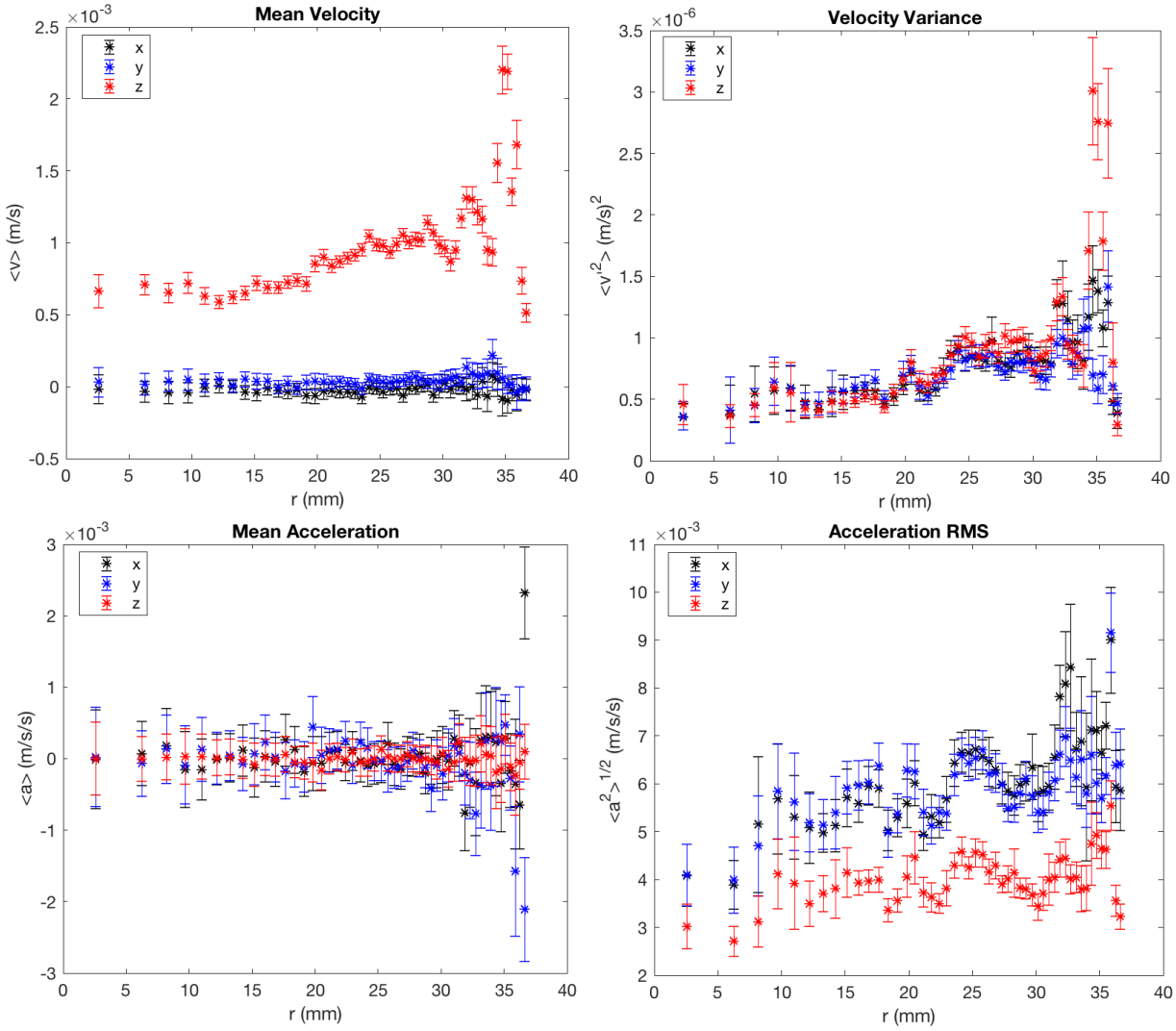

Figure 7.11: Velocity and acceleration profiles from experiment 2,4,8_ReMid. Clockwise from top left: mean velocity, velocity fluctuation variance, root mean squared acceleration, and mean acceleration.

Table 7.3: Measured flow conditions for $r < 20$ mm for each packed bed experiment. Re is reassessed based on measured $\langle v_z \rangle$, and mean t^* is mean bead-diameter transit time. Recall that intended Reynolds numbers for Low, Mid, and High cases were 0.135, 0.27, and 0.54, respectively.

Exp.	d_{bead} (mm)	$\langle v_z \rangle$ (mm/s)	Re	t^* (s)
2Re_Low	2	0.7	0.18	2.7
2Re_Mid	2	1.2	0.30	1.6
2Re_High	2	1.8	0.44	1.1
2,4Re_Mid	2.22	1.3	0.35	1.7
2,4,8Re_Mid	2.3	0.7	0.19	3.4

to the convergence of statistics in this region, only data coming from the $r < 20$mm region of each test section will be considered in statistical analysis hereafter. In most cases, the wall effects are most extreme in the outer 5 mm (∼2 bead diameters) of the flow field (recall that the pipe radius is 36.83 mm). Past works have suggested the heuristic of using a test section of diameter 10 bead diameters as a means of mitigating wall effects [122, 123], and it appears the diameter to bead ratios of 18.4, 16.6, and 16.0 kept wall-effects from affecting the entire flow field in these experiments.

In each experiment, the measured mean velocity for $r < 20$ mm was then used to reassess the Reynolds number. Table 7.3 shows the measured mean velocity in the region of interest of each test section. It is seen that in each case, the desired Reynolds number was not achieved. In most cases, it is believed that this was caused by the modulation of flow rate at the edges of the test section. In the cases 2_ReHigh and 2,4,8_ReMid, the measured Reynolds numbers in the middle of the test section were well below those intended. This is reflected by the sharp increase in axial velocity near the radial edges seen in Figures 7.9 and 7.11, respectively. The increased flow at the edges indicates that the overall mean flow velocity is near that intended, while the velocity in the center is less than desired. With this, the Reynolds number of case 2,4,8_ReMid is actually closer to that of case 2_ReLow than the other ReMid cases. The name 2,4,8_ReMid will be kept, but the break of this case from the other ReMid cases will be considered throughout analysis.

Table 7.3 also lists the mean bead transit time t^*, defined as

$$t^* = \frac{d_{bead}}{\langle v_z \rangle}, \tag{7.2}$$

where d_{bead} is the mean bead diameter for each test section. Recall that for the mixed-bead cases, d_{bead} was determined for each test section as the average diameter of all beads present, based on the bead number ratios expected from an equal volume distribution. The time and length scales t^* and d_{bead} will be used to normalize results in this analysis to facilitate comparison between different cases.

7.2.2 Probability Density Functions

The probability density functions (PDFs) of velocity, $P(v_i)$, and acceleration, $P(a_i)$, are considered for each experiment. Figure 7.12 shows a comparison of velocity PDFs for all 2 mm cases. Velocities are normalized by the RMS velocity for each case. We see that in all cases, x- and y-velocity distributions are non-Gaussian, with long tails. These transverse velocity distributions are similar in all cases with the low Reynolds case possibly showing a broader distribution. Due to the lack of data in this case, it is difficult to tell the exact nature of the tails of this distribution. In the case of axial (z-) velocity, we see that all cases show a significant negative (backward) velocity region, indicating regions of flow reversal in the packed bed. This region is more pronounced for the lower Reynolds number cases and is slightly less significant for the high Reynolds number case.

Figure 7.13 shows velocity distributions for all ReMid cases. There is little noticeable difference between the 2 mm and 2,4 mm cases. The 2,4,8 mm case shows broader tails and higher probability of negative axial velocity. It is unclear if these features are caused solely by the different bead configuration or if the lower Reynolds number of the 2,4,8 mm case contributes.

We note that these are less sharply cusped than the distributions measured by Holzner et al. [47] (shown in Figure 2.10). While the tracer particles used in this experiment ($\sim$90 μm diameter) are significantly smaller than the packed beads, they are still unable to sample the slow flow near the surface of each bead. It is believed that this undersampling of the low-speed flow regions creates this lack of a sharp cusp near $v = 0$.

Figure 7.14 shows a comparison of acceleration PDFs for all 2 mm cases, while Figure 7.15 shows the same for all ReMid cases. These are normalized by the RMS acceleration for each case. Once again, these are distinctly non-Gaussian, but lack the sharp peak observed

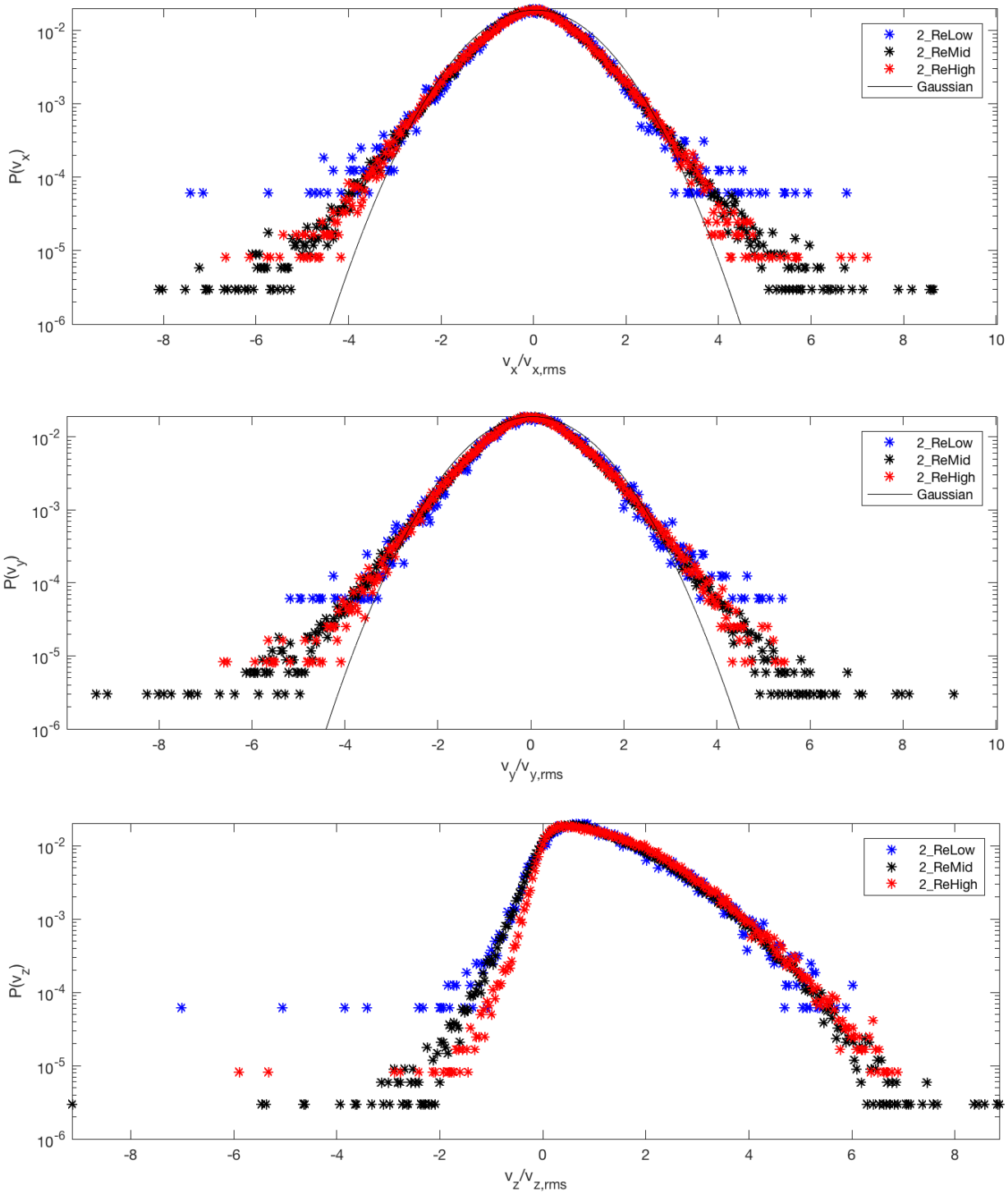

Figure 7.12: Comparison of velocity probability density functions for all 2 mm cases. Top to bottom: x-, y-, and z-velocity PDFs. Gaussian distribution shown for reference.

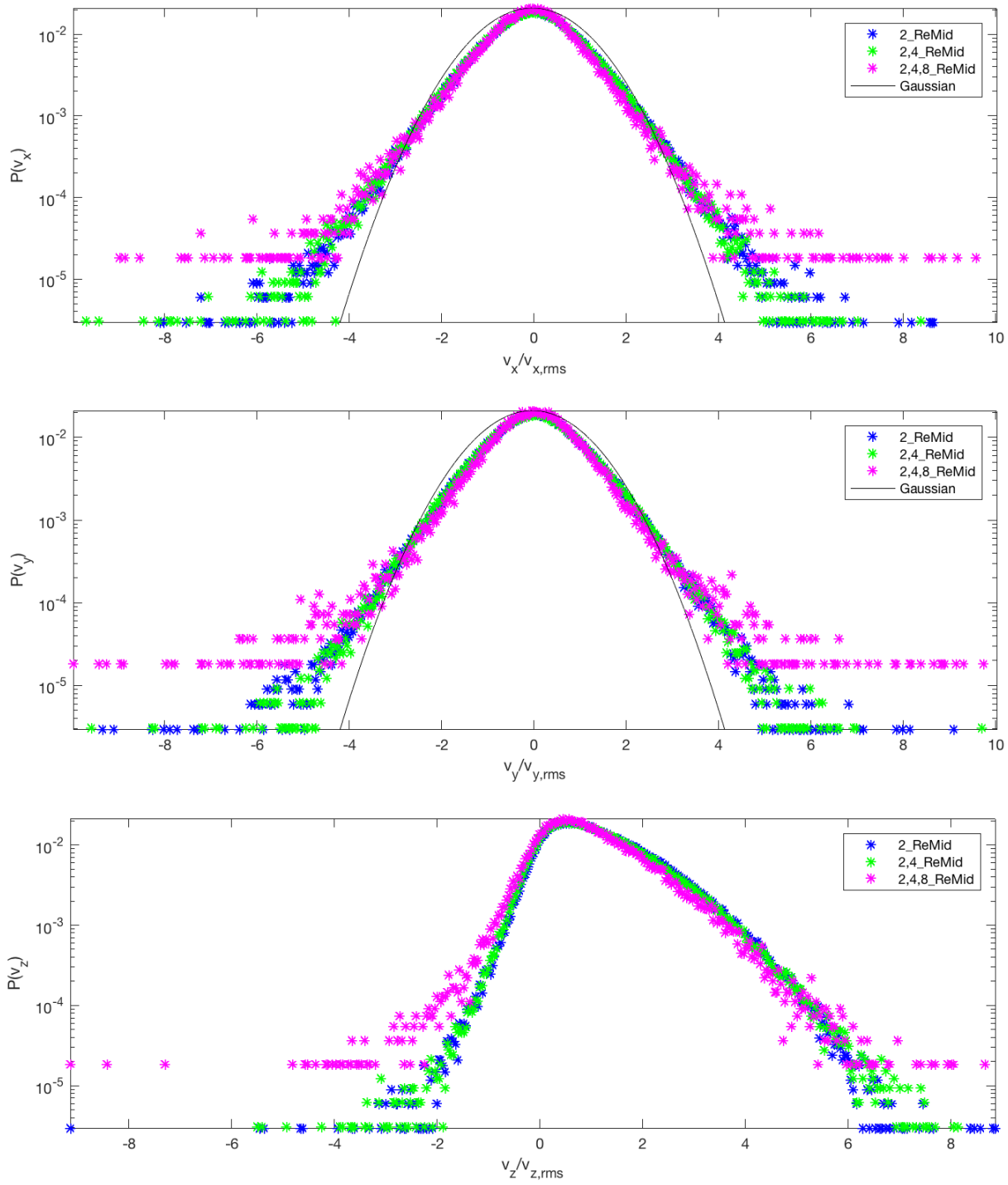

Figure 7.13: Comparison of velocity probability density functions for all ReMid cases. Top to bottom: x-, y-, and z-velocity PDFs. Gaussian distribution shown for reference.

by Holzner et al [47]. The lack of near-boundary resolution is believed to be at play again. We see that the low Reynolds number 2 mm case appears to have broadened tails, but it is difficult to tell to what degree this is caused by lack of data.

Comparing different bead packings, we see that the 2,4,8 mm case demonstrates significantly broader tails of the acceleration PDFs with a more distinct cusp near $a = 0$ when compared to the other cases. This may be associated with the lower Reynolds number, but this sharper cusp is not seen in the 2_ReLow case.

In lieu of a Gaussian fit, acceleration distributions were fitted to the stretched exponential distribution proposed by Voth et al. [64] and Mordant et al. [65] for describing the acceleration distributions observed in turbulent flow:

$$P(a) = C \exp\left(-\frac{a^2}{(1 + |a\chi/\sigma|^\gamma)\sigma^2}\right), \tag{7.3}$$

where C is a normalization constant and σ, χ, and γ are fit parameters. With this fit, the shape of the distribution tail is dominated by the parameter γ and behaves as $P(a) \sim \exp\left(-|a|^{2-\gamma}\right)$. Fitting was performed with the Matlab Curve Fitting Toolbox and included a 95% confidence interval on each fit parameter. Stretched exponential fits are shown for each curve in Figures 7.14 and 7.15. This parameterization is seen to describe the measured data quite well.

The values for the fit parameters in the x-, y-, and z-directions are given in Tables 7.4, 7.5, and 7.6, respectively. The values of γ measured in the lower Reynolds number cases (2_ReLow and 2,4,8_ReMid) reflect the broader tails observed in their distributions.

In the work of Mordant et al. [65], fit parameters of $\sigma = 0.563$, $\gamma = 1.600$, and $\chi = 0.513$ were found for the acceleration distribution of turbulent von Kármán flow (flow driven by two counter-rotating disks) of Taylor-scale Reynolds number 690. The distributions measured in the current work differ from this in many aspects as to be expected; however, we see that the transverse (x- and y-) γ values, and thus the shapes of the tails, of cases 2_ReLow and 2,4,8_ReMid are similar to those measured in turbulent flow.

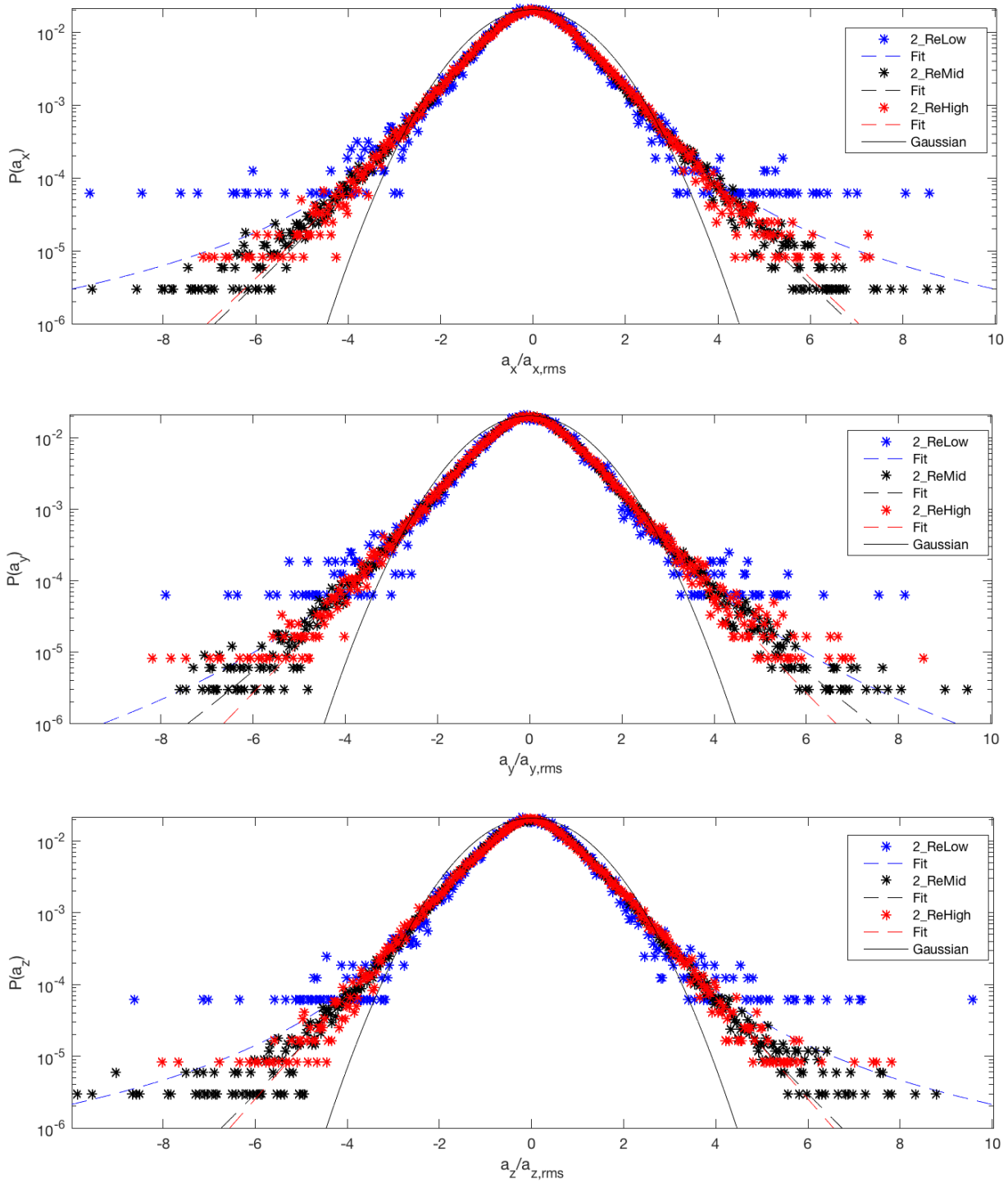

Figure 7.14: Comparison of acceleration probability density functions with stretched exponential fits for all 2 mm cases. Top to bottom: x-, y-, and z-acceleration PDFs. Gaussian distribution shown for reference.

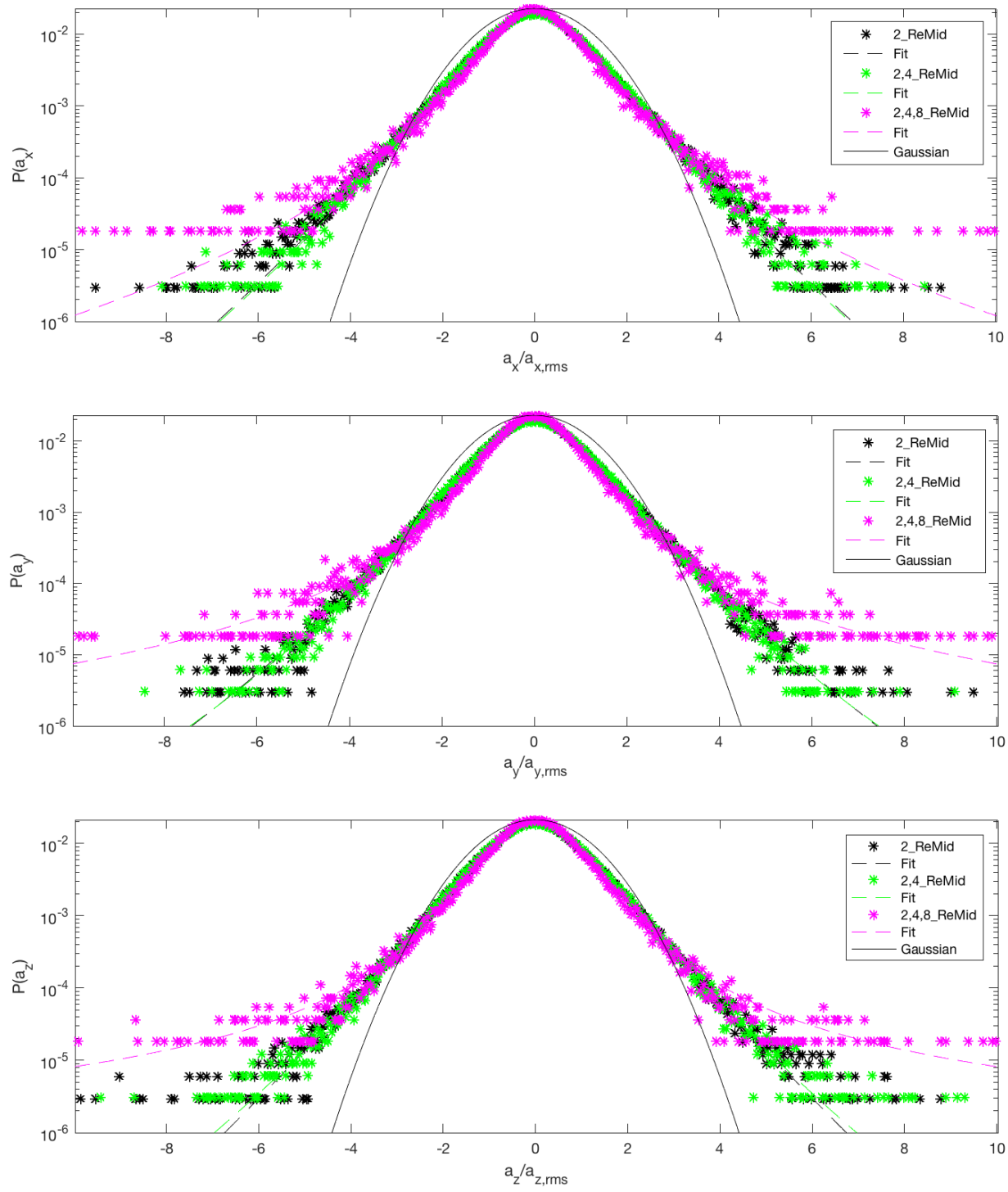

Figure 7.15: Comparison of acceleration probability density functions with stretched exponential fits for all ReMid cases. Top to bottom: x-, y-, and z-acceleration PDFs. Gaussian distribution shown for reference.

Table 7.4: Fitted parameters for stretched exponential fit for x-acceleration.

Exp.	σ_x	γ_x	χ_x
2_ReLow	0.97 ± 0.04	1.78 ± 0.29	0.38 ± 0.04
2_ReMid	0.86 ± 0.01	1.24 ± 0.05	0.49 ± 0.02
2_ReHigh	0.86 ± 0.03	1.22 ± 0.09	0.51 ± 0.04
2,4_ReMid	0.96 ± 0.02	1.32 ± 0.08	0.41 ± 0.02
2,4,8_ReMid	0.80 ± 0.02	1.57 ± 0.11	0.45 ± 0.02

Table 7.5: Fitted parameters for stretched exponential fit for y-acceleration.

Exp.	σ_y	γ_y	χ_y
2_ReLow	0.98 ± 0.05	1.65 ± 0.35	0.38 ± 0.03
2_ReMid	0.88 ± 0.01	1.32 ± 0.05	0.48 ± 0.01
2_ReHigh	0.84 ± 0.03	1.16 ± 0.08	0.54 ± 0.04
2,4_ReMid	0.98 ± 0.01	1.44 ± 0.07	0.40 ± 0.01
2,4,8_ReMid	0.80 ± 0.01	1.74 ± 0.08	0.43 ± 0.01

Table 7.6: Fitted parameters for stretched exponential fit for z-acceleration.

Exp.	σ_z	γ_z	χ_z
2_ReLow	1.00 ± 0.10	1.80 ± 0.37	0.36 ± 0.02
2_ReMid	0.87 ± 0.02	1.19 ± 0.06	0.50 ± 0.02
2_ReHigh	0.65 ± 0.03	0.99 ± 0.06	0.93 ± 0.01
2,4_ReMid	1.00 ± 0.02	1.39 ± 0.08	0.39 ± 0.01
2,4,8_ReMid	0.90 ± 0.01	1.83 ± 0.11	0.39 ± 0.01

7.3 Displacement Statistics

7.3.1 CTRW Transition Probability

We examine the motion of trajectories using the continuous time random walk (CTRW) formalisms described in Section 2.2. Recall that under this framework, the primary controlling factor is the transition probability $\psi(\mathbf{s}, t)$ that a walker takes a step of length $\mathbf{s}$ in a time t. It is predicted that anomalous transport will arise when at late times this scales as $\psi(\mathbf{s}, t) \sim t^{-1-\beta}$, with β <2. For the case of flow driven in a single direction (as is the case herein), an exponent $1 < \beta < 2$ suggests that the walker's mean position will vary linearly in time, while its variance will not vary linearly and will have long tails. For the case of $0 < \beta < 1$, it is predicted that mean position of the walker and its variance will scale as t^{β} and $t^{2\beta}$, respectively [34].

To determine this scaling, we consider the distributions of transition times of length one bead diameter, d_{bead}, in each direction for each experiment. Recall that d_{bead} was 2 mm, 2.22 mm, and 2.3 mm for the 2 mm, 2,4 mm, and 2,4,8 mm cases, respectively. Figures 7.16-7.20 show the transition time distributions for each of the experiments. The tails of these distributions were fitted starting at 1.5 times the mean transition time using the Matlab Curve Fitting Toolbox to determine the scaling exponent β. These fitted curves are shown in each figure.

It is seen that in all cases, $\beta < 2$, predicting the presence of anomalous transport. Values of the fitted exponents with 95% confidence intervals are given in Table 7.7. For transitions in the axial (z-) direction, we see that β primarily depends on the bead packing, indicating that CTRW statistics in the mean-flow direction are primarily controlled by the geometry of the porous media over the Reynolds number range examined.

The transition times in the transverse directions are seen to be much longer and more widely distributed than those in the axial direction. The latter is especially evident in the higher Reynolds number cases (2_ReMid, 2_ReHigh, and 2,4_ReMid) as demonstrated by the relative magnitudes of the peaks of the axial and transverse distributions. In all cases, the transverse transition times have scaling exponents $\beta \sim 1$, placing them on the cusp

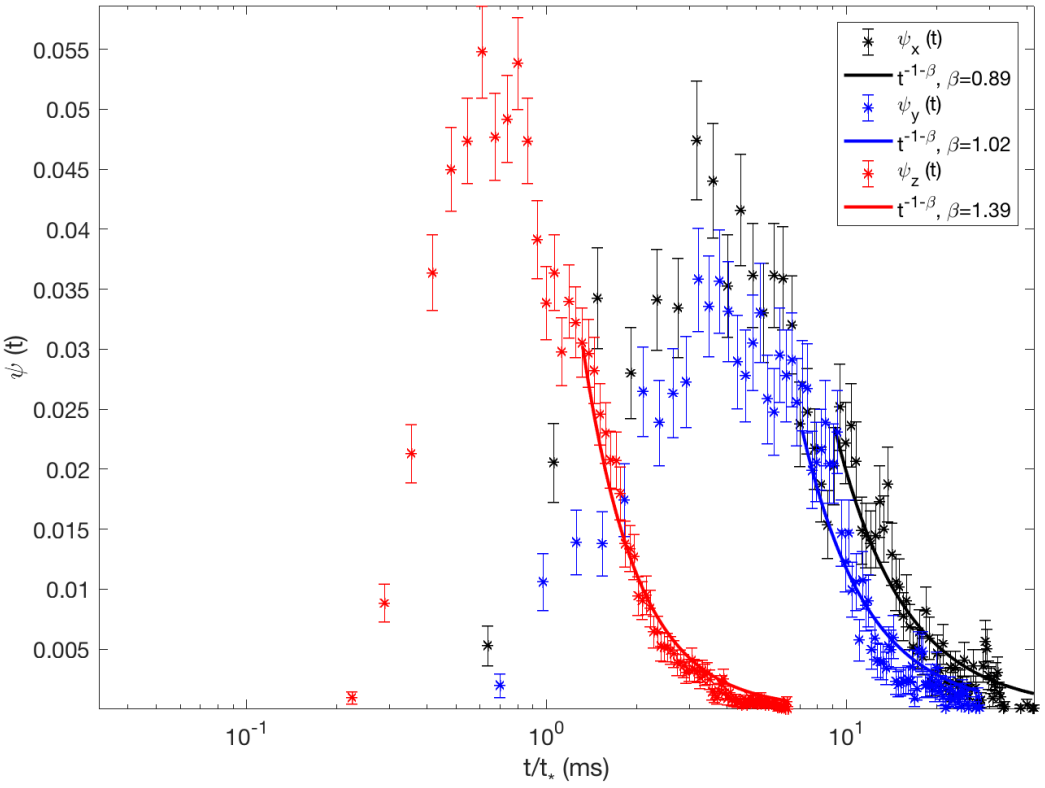

Figure 7.16: Transition probability distributions measured in experiment 2_ReLow with exponential fits to late-time tails.

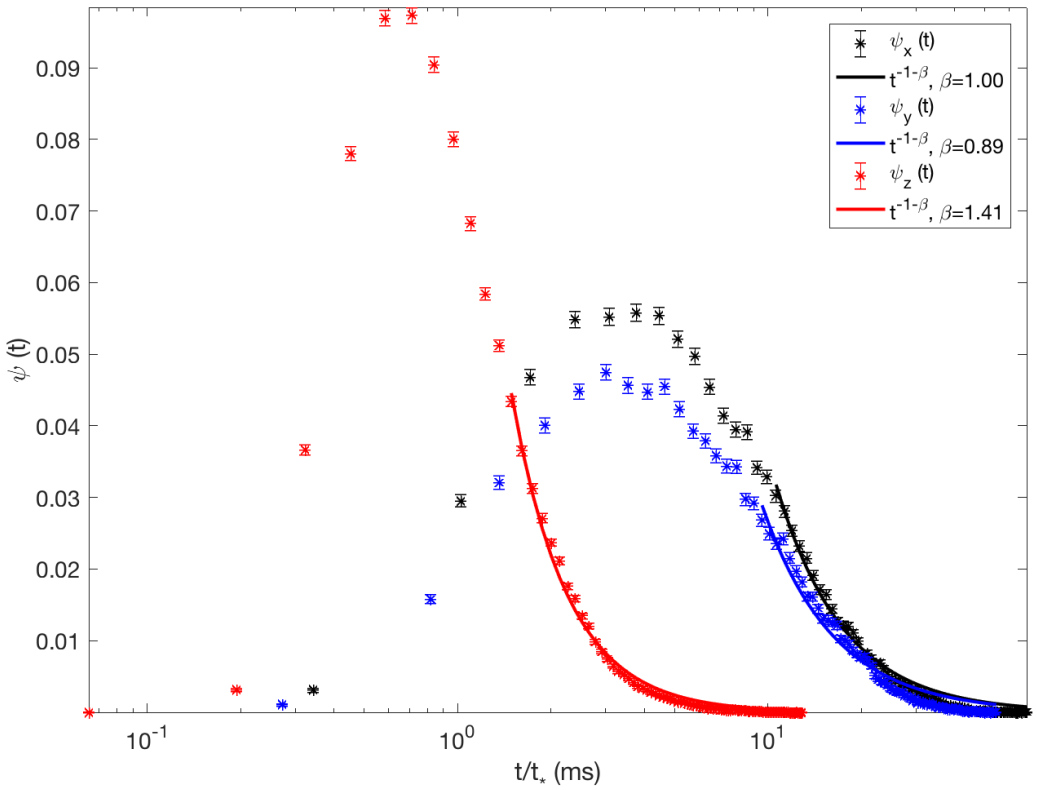

Figure 7.17: Transition probability distributions measured in experiment 2_ReMid with exponential fits to late-time tails.

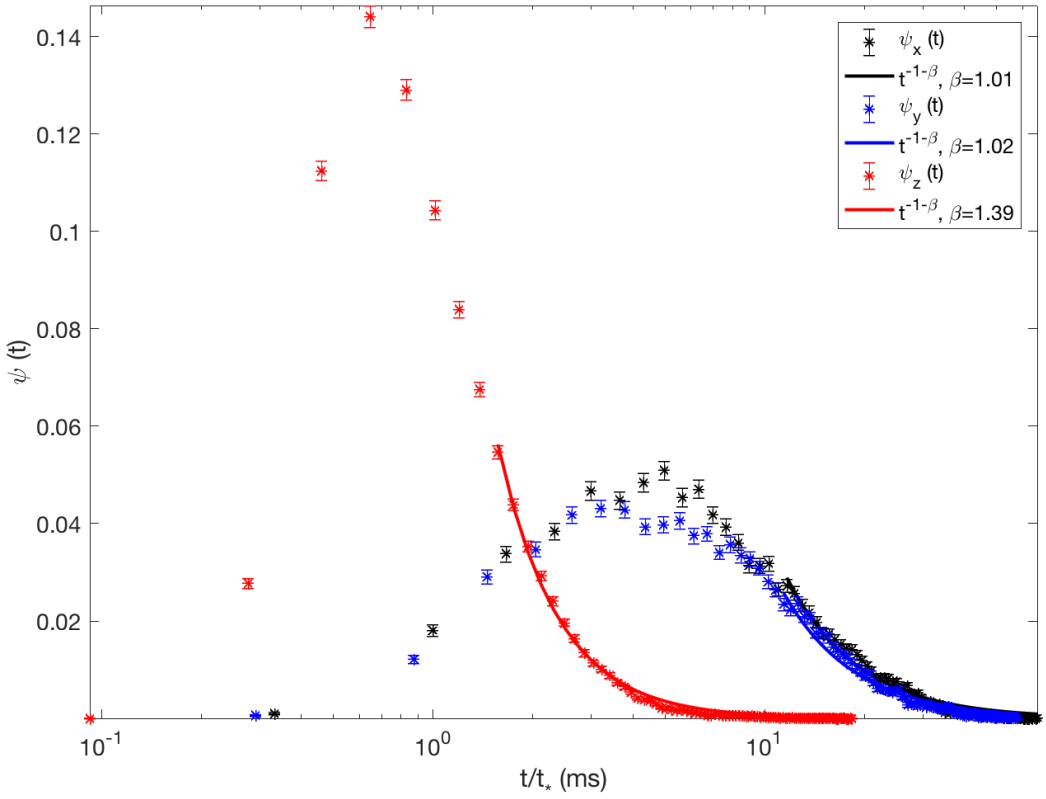

Figure 7.18: Transition probability distributions measured in experiment 2_ReHigh with exponential fits to late-time tails.

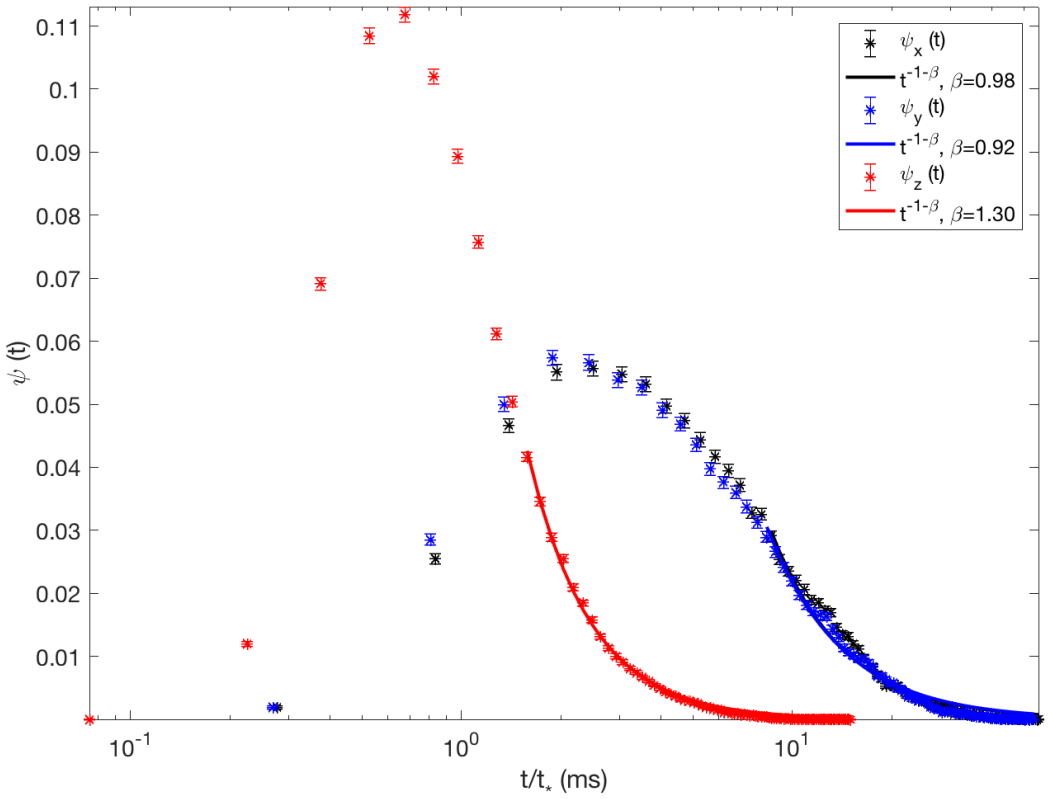

Figure 7.19: Transition probability distributions measured in experiment 2,4_ReMid with exponential fits to late-time tails.

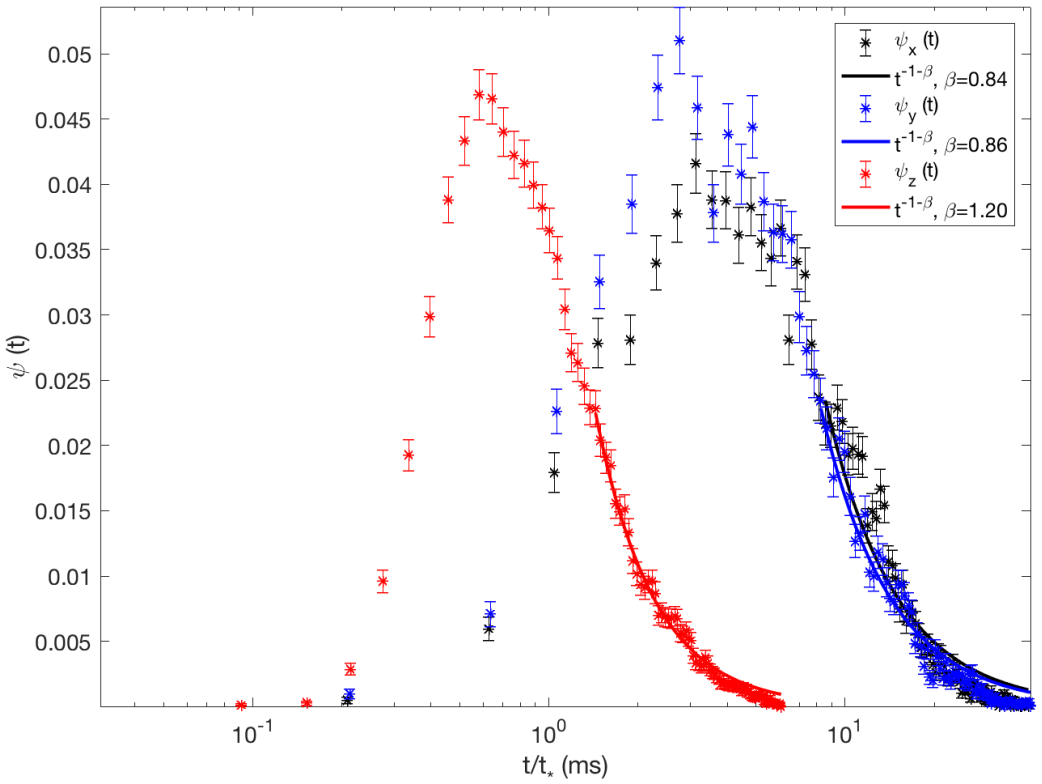

Figure 7.20: Transition probability distributions measured in experiment 2,4,8_ReMid with exponential fits to late-time tails.

Table 7.7: Fitted values of scaling exponent β in CTRW transition probability for each packed bed experiment. Subscripts indicate direction of transition being considered.

Exp.	β_x	β_y	β_z
2_ReLow	0.89 ± 0.23	1.02 ± 0.28	1.39 ± 0.14
2_ReMid	1.00 ± 0.10	0.89 ± 0.12	1.41 ± 0.07
2_ReHigh	1.01 ± 0.11	1.02 ± 0.12	1.39 ± 0.06
2,4_ReMid	0.98 ± 0.11	0.92 ± 0.09	1.30 ± 0.04
2,4,8_ReMid	0.84 ± 0.19	0.87 ± 0.13	1.20 ± 0.08

between the two regimes of anomalous dispersion previously discussed. Within uncertainty, no significant differences are seen among the transverse scaling exponents of each case.

7.3.2 Mean-Squared Displacement

The spreading of the tracers is quantified by the mean-squared displacement (MSD), σ_i^2. For the x-direction, this is defined by

$$\sigma_x^2(t) = \langle (x(t) - \langle x(t) \rangle)^2 \rangle, \tag{7.4}$$

and similarly for the y- and z-directions. Once again, angle brackets indicate averaging over all particles. To calculate this, each point in a trajectory is considered a starting point $\mathbf{x}(0)$, and displacements from this point $(\mathbf{x}(t) - \mathbf{x}(0))$ are considered. This quantity is the same as the width of the walker distribution, σ^2, that was discussed in Section 2.2.

As the filtered positions considered in this work are calculated via convolution, positions within each trajectory are not independent, and correlated uncertainties will cause a quantifiable bias in MSD calculations. This was noted by Berg et al. [66] for corrections to the Lagrangian velocity structure function and will be discussed again for corrections to velocity correlations in this work.

One can consider a measured position x_{meas} as $x_{meas} = x_{true} + \epsilon$, where x_{true} is the true position of the tracer, and ϵ is the random error. If one then assumes that $\langle \epsilon \rangle = 0$ and $\langle \epsilon^2 \rangle = \delta^2$, where δ is the average measurement uncertainty, one can then determine that

$\sigma^2_{meas} = \sigma^2_{true} + \Delta\sigma^2$, where

$$\Delta\sigma^2(t) = \sum_{q=-L}^{L+t} k_q^2 \delta^2 \tag{7.5}$$

with weights

$$k_q = \left\{ \begin{array}{cc} -A \exp \frac{-q^2}{w^2}, & q \in [-L, t-L-1] \\ A\left(\exp \frac{-(q-t)^2}{w^2} - \exp \frac{-q^2}{w^2}\right), & q \in [t-L, L] \\ A \exp \frac{-(q-t)^2}{w^2}, & q \in [L+1, L+t] \end{array} \right\}, \tag{7.6}$$

and the normalization constant A being that described in Equation 3.12. In this formulation, L is the half-width of the filter kernel support (i.e. the total support is $2L+1$ time steps) and w is the filter size. For our filter, we set $L = 2w$. With the filter width of 2 time steps used herein, L will be 4 time steps.

The term $\Delta\sigma^2$ must be subtracted from the calculated MSD to recover the true value. The shape of this correction term is shown in Figure 7.21. In the current work, the correction term is found to be several orders of magnitude smaller than the actual MSD curve in every case, but it is accounted for nonetheless.

Mean-squared displacement curves for all cases are shown in Figures 7.22-7.26. Within these curves we look for different exponential scaling regimes, indicated by straight portions in these log-log plots. Different exponential scalings are shown by black lines to indicate various scaling regimes. A number of interesting features appear in these curves.

First, it appears that in most cases, the axial (z-) MSD scales as t^2 up to one bead transit time. The exception to this is the case 2,4,8_ReMid, which appears to show a shallower scaling of $t^{7/4}$ that persists to 2-3 bead transit times. At intermediate time lags (from $t/t^* \approx 1$ to $t/t^* \approx 5$, all cases but this one exhibit an axial scaling of $t^{3/2}$. This scaling was previously observed by Kang et al. [124]. Finally, at about $t/t^* = 10$, we see a transition to Fickian transport in which the growth of σ^2 becomes linear in time. This late time transition to Fickian transport is in agreement with the model for the CTRW proposed by Edery et al. [43].

In most cases, the transverse MSD transitions to a subdiffusive $t^{3/5}$ scaling after about 1 bead transit. In the case 2,4,8Re_Mid, we instead see a transition to $t^{4/5}$ scaling that persists

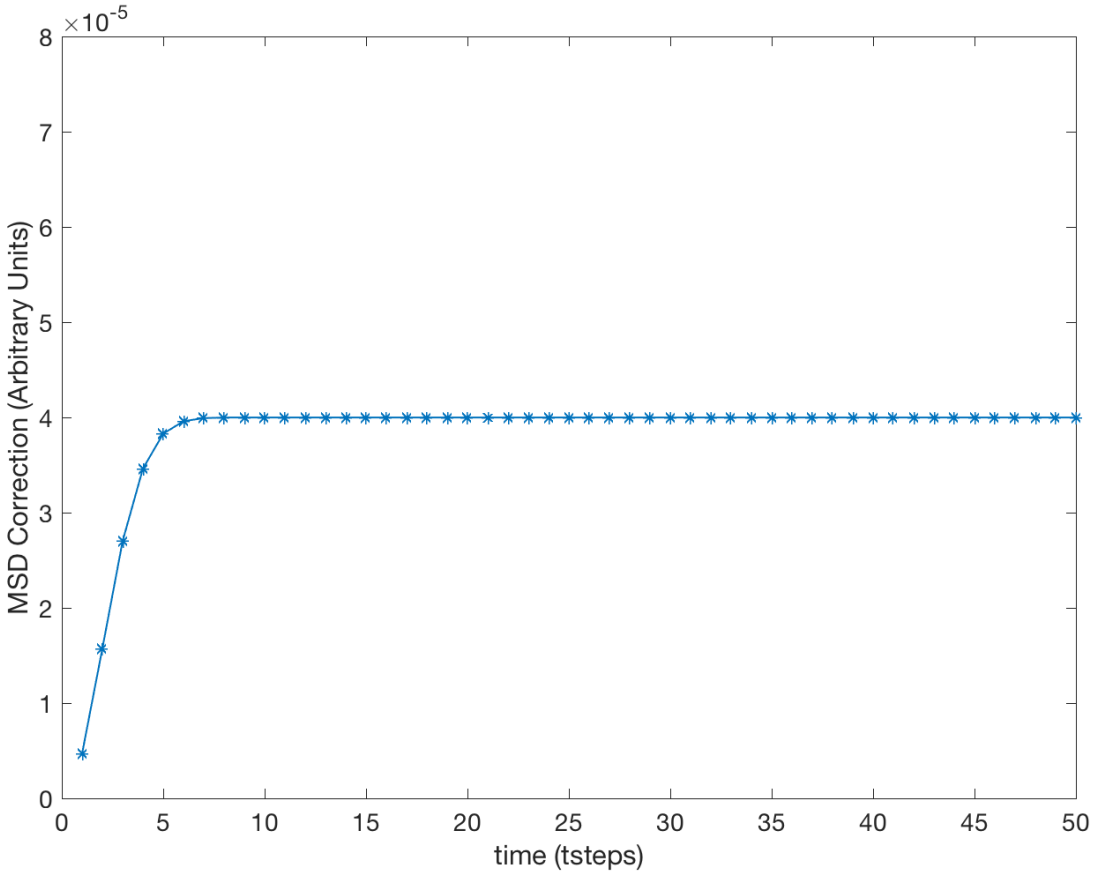

Figure 7.21: Correction to mean-squared displacement caused by correlated uncertainties for Gaussian filter of size $\sigma = 2$ time steps. Vertical axis is in arbitrary units as magnitude of correction scales with measurement uncertainty. 100 ms time steps were used for this work.

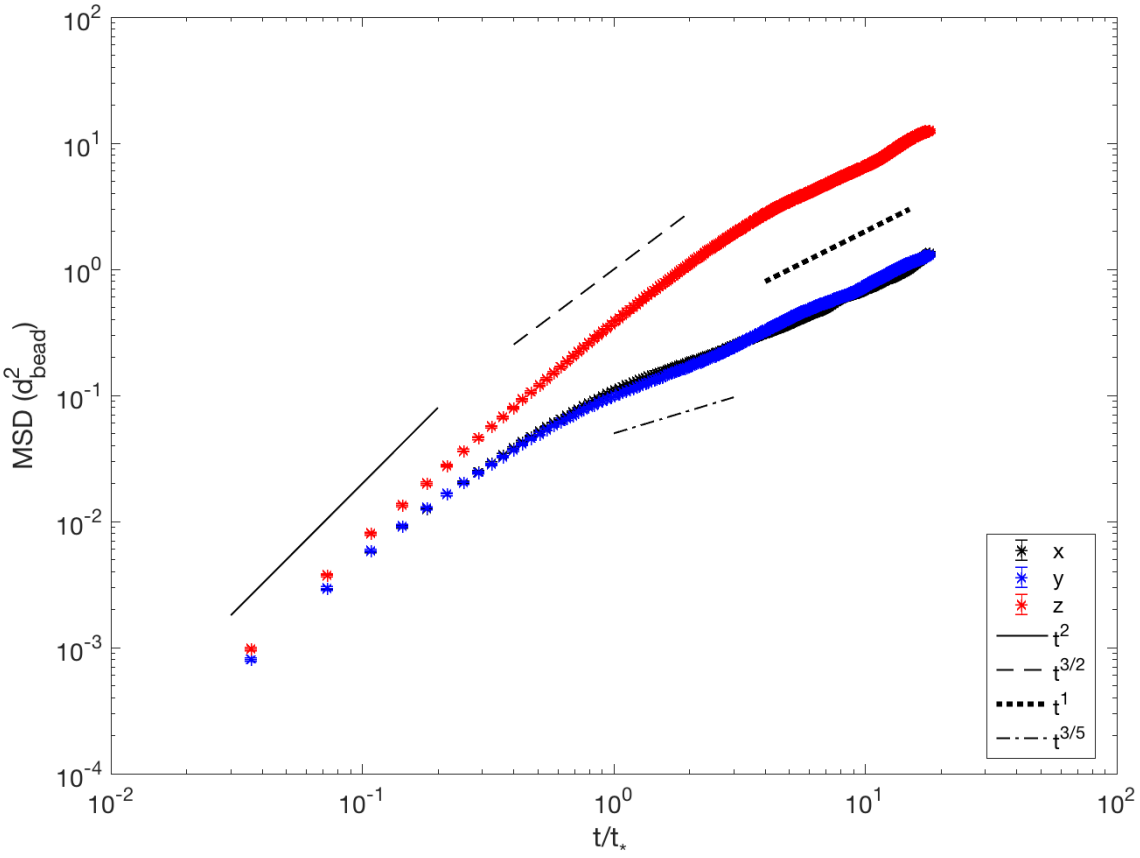

Figure 7.22: Mean-squared displacement curves for case 2_ReLow with different exponential scalings shown.

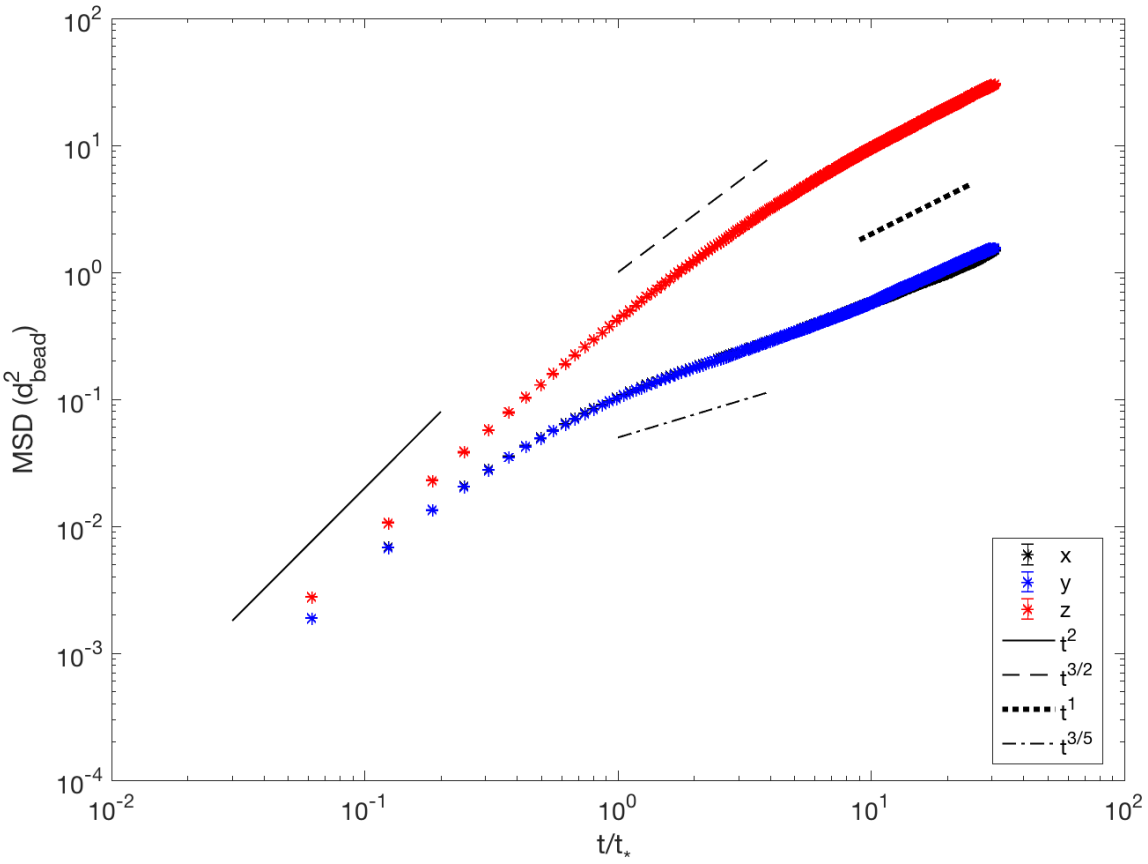

Figure 7.23: Mean-squared displacement curves for case 2_ReMid with different exponential scalings shown.

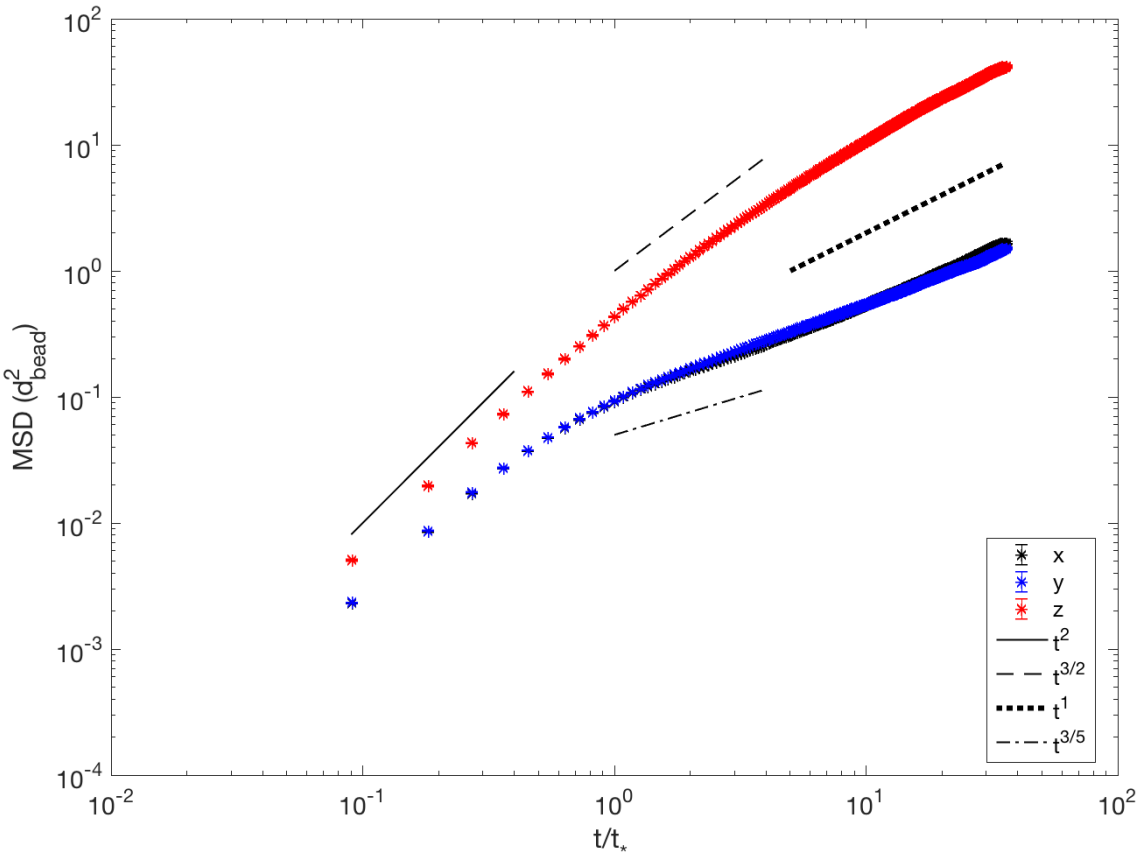

Figure 7.24: Mean-squared displacement curves for case 2_ReHigh with different exponential scalings shown.

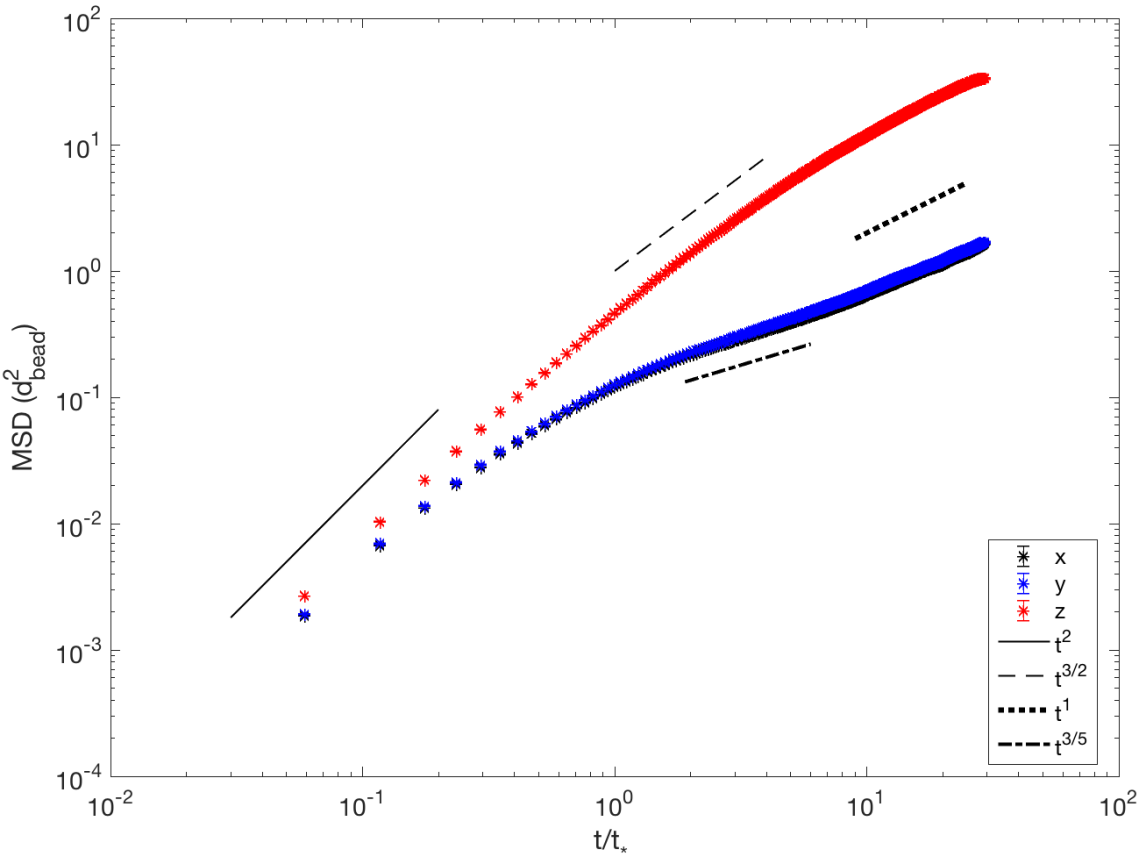

Figure 7.25: Mean-squared displacement curves for case 2,4_ReMid with different exponential scalings shown.

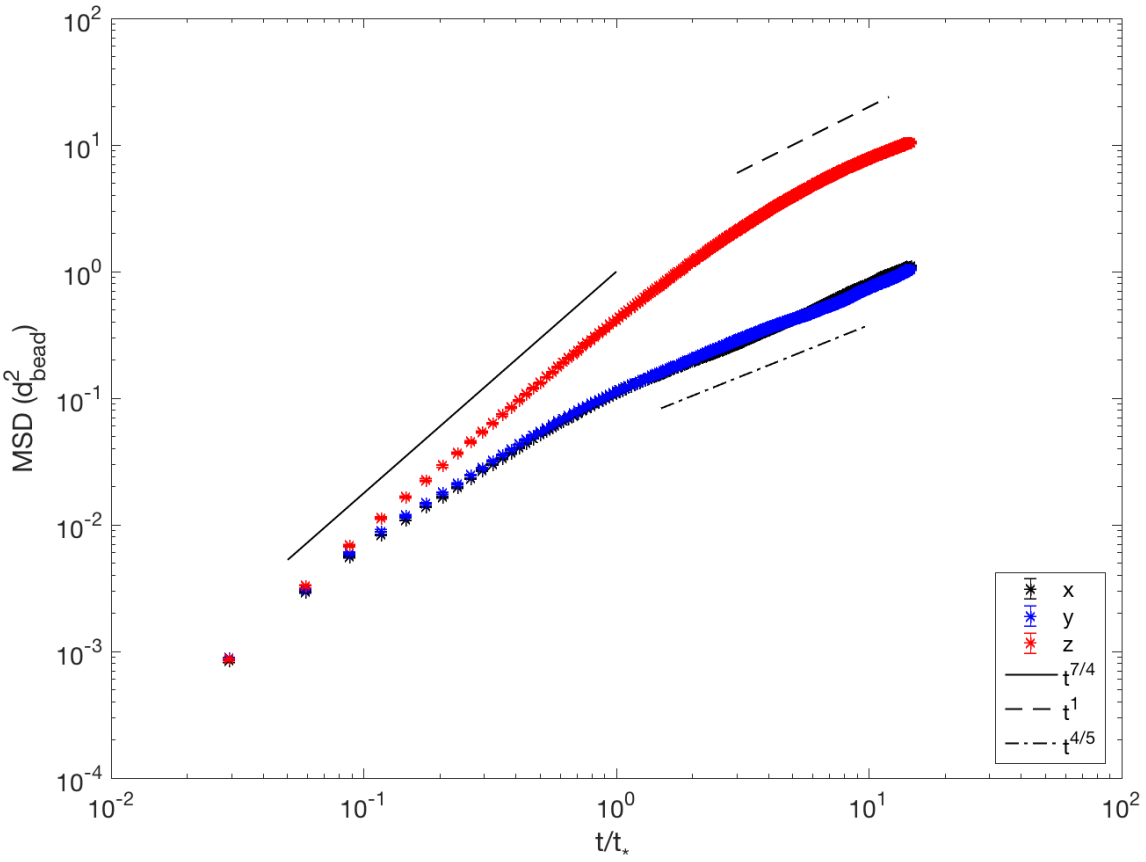

Figure 7.26: Mean-squared displacement curves for case 2,4,8_ReMid with different exponential scalings shown.

to late times. This $t^{4/5}$ in the transverse directions was previously observed by Kang et al. [124]. In the other cases, at around $t/t^* = 10$, there is once again a transition to normal, Fickian spreading.

These observations indicate that the transport of these flow tracers is anomalous (i.e. non-Fickian); however, we do observe a transition to normal transport at late times, indicating that the abnormal spreading of tracers happens in the first 10 or so bead transits. Also, while the different bead packings yield different transition probability scaling exponents β, we do not observe significant differences in the MSD curves of the 2_ReMid and 2,4_ReMid cases, yet the case 2,4,8_ReMid is quite different than these two. Thus, while the scaling exponents $\beta < 2$ do seem to indicate the presence of anomalous transport, it is unclear if differences in β correspond to differences in tracer spreading. Recall that the 2,4,8_ReMid experiment had a lower measured Reynolds number than the other ReMid cases and suffered from a biasing of trajectories toward the top of the test section. It is unclear how these affect the MSD curves relative to the other experiments.

7.4 Velocity Correlations

7.4.1 Autocorrelation

We seek to examine velocity correlations in the packed bed experiments. The first set of statistics are considered Lagrangian (i.e. "going with the flow") in that they will compare different velocities along each trajectory. The first quantity considered is the Lagrangian velocity autocorrelation, $\rho(\tau)$, defined by

$$\rho(\tau) = \frac{\langle v'(t)v'(t+\tau)\rangle}{\langle v'(t)^2\rangle}, \tag{7.7}$$

where the quantity v' is the fluctuating component of the velocity.

As individual velocities are calculated from a convolution involving many positions, a correction must also be applied to the autocorrelation calculation to account for correlated uncertainties. Before normalization by the mean-squared velocity fluctuation, this correction

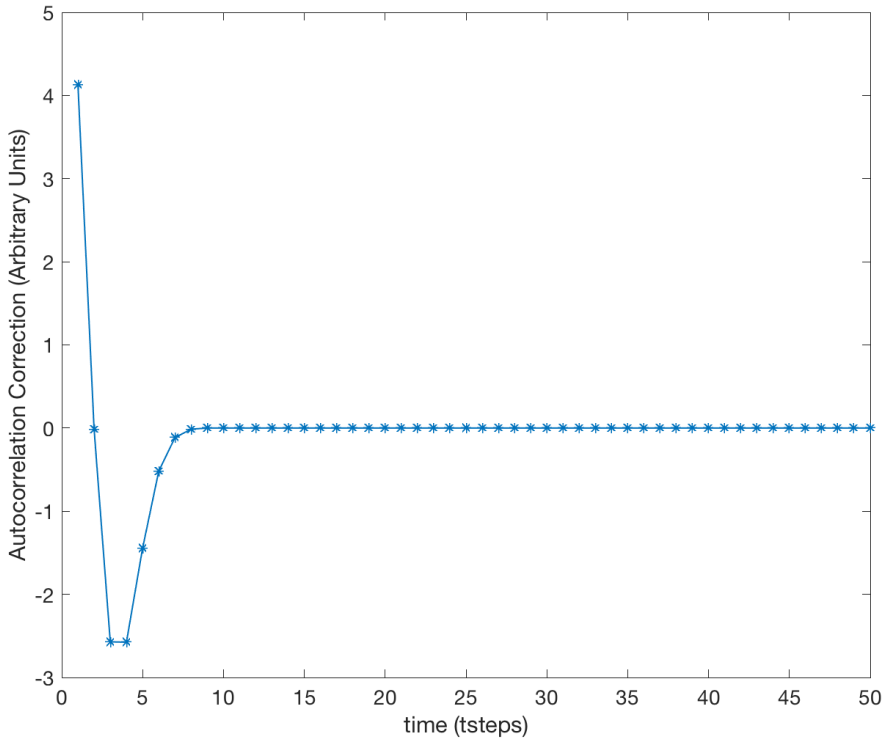

Figure 7.27: Correction to velocity autocorrelation caused by correlated uncertainties for Gaussian filter of size $\sigma = 2$ time steps. Vertical axis is in arbitrary units as magnitude of correction scales with measurement uncertainty. 100 ms time steps were used for this work.

$\Delta\rho(\tau)$ is of the form

$$\Delta\rho(\tau) = \delta^2 \sum_{q=\tau-L}^{L} \left(A' q \exp \frac{-q^2}{w^2} \right) \left(A'(q-\tau) \exp \frac{-(q-\tau)^2}{w^2} \right), \tag{7.8}$$

where A' is the normalization constant from Equation 3.13. The shape of this correction is shown in Figure 7.27.

Unlike the MSD correction, it is found that the correction that must be applied to the autocorrelation is significant at short time lags. The autocorrelation functions for the case 2_ReMid are shown before and after correction in Figure 7.28. Here one can see the "kink" caused by this defect at short time lags in the transverse directions.

To apply this correction, one must know the average value of the uncertainty δ in each spatial direction. When doing so, the calculated uncertainty values given in Table 7.2 were used, but it was found that these did not fully remove the kink from early time lags. Using

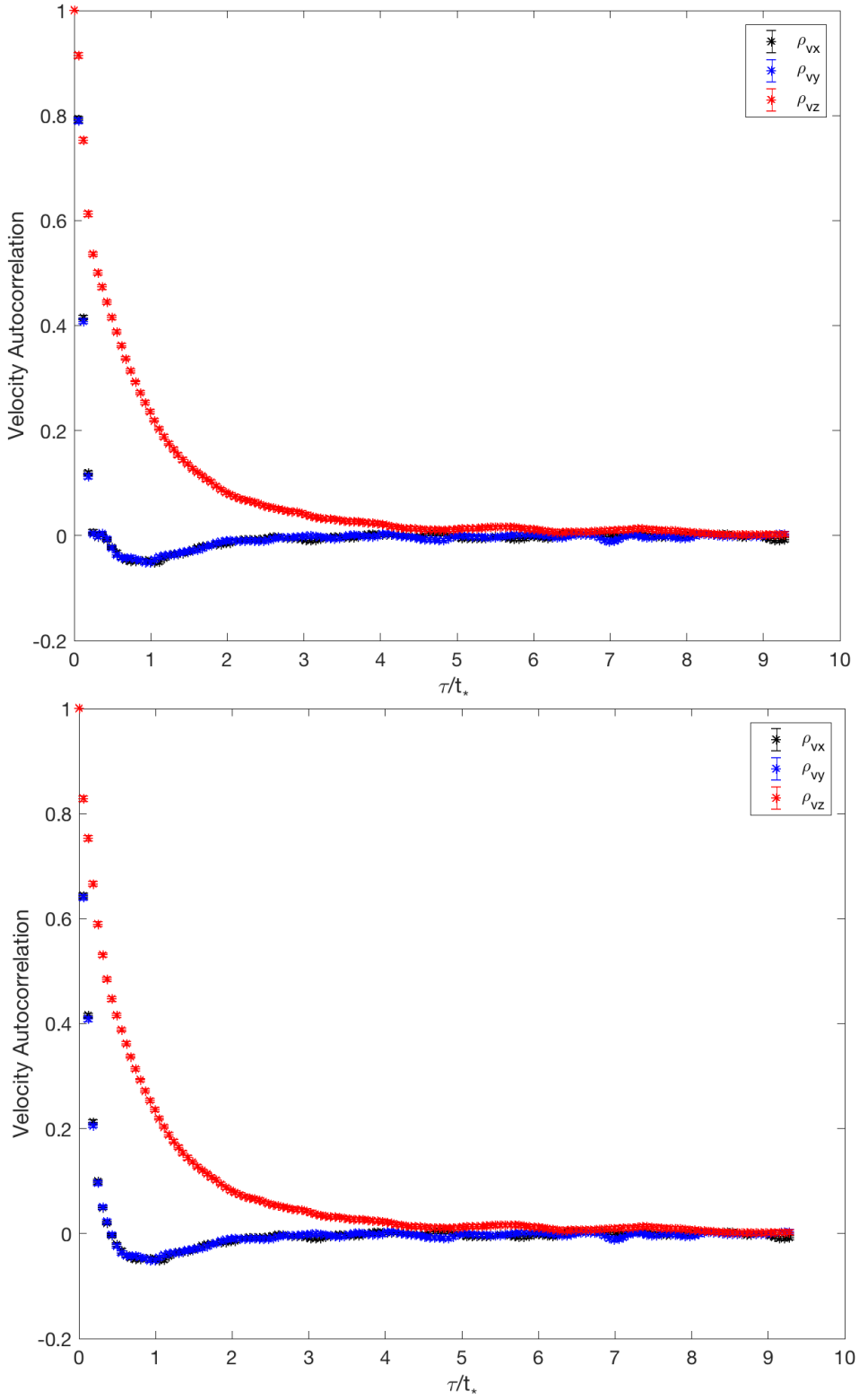

Figure 7.28: Velocity autocorrelation curves of 2_ReMid case before (top) and after (bottom) correction for correlated uncertainties.

Table 7.8: Uncertainty values in each spatial direction for each experiment determined from correction to autocorrelation and Lagrangian velocity structure function.

Exp.	Δx (mm)	Δy (mm)	Δz (mm)
2_ReLow	0.18	0.18	0.13
2_ReMid	0.19	0.19	0.17
2_ReHigh	0.19	0.19	0.16
2,4_ReMid	0.24	0.24	0.17
2,4,8_ReMid	0.23	0.24	0.5

this kink in the autocorrelation function and a similar aberration seen in the Lagrangian velocity structure function (described later in this section), the values of δ for each spatial direction were varied in 0.01 mm steps until the features of the correction were removed. In doing so, new uncertainty values were found and are given in Table 7.8. These values for average uncertainty are slightly higher than those determined by the fitting of Gaussians to each particle image during reconstruction (see Section 3.2). It is possible that the background created by other particles and ambient activity causes an overestimation of the number of coincidence lines used in each position calculation, leading to an underestimation of uncertainty. The exact cause of the discrepancy between the calculated uncertainties and those that appear to be present in the data is unknown and will be discussed in further detail in Section 8.1.

After this correction has been applied, the autocorrelation function can be plotted for each case. Figures 7.29-7.31 show the calculated autocorrelations for each experiment and each spatial direction. Curves from different experiments are overlaid to reveal differences.

It is evident that transverse velocities decorrelate more quickly than the axial velocity, with axial velocity correlations remaining nonzero out to 5-6 bead transits in some cases. The transverse autocorrelations also display a significant negatively correlated region at around 1 bead transit caused by the turning back and forth of trajectories as they pass through the packed bed pore structure. Furthermore, the higher Reynolds number cases are seen to remain correlated longer than the lower Reynolds number cases.

To quantify some of these differences between cases, we look at the integral time scale, T, defined by

$$T = \int_0^\infty \rho(\tau)\ \mathrm{d}\tau. \tag{7.9}$$

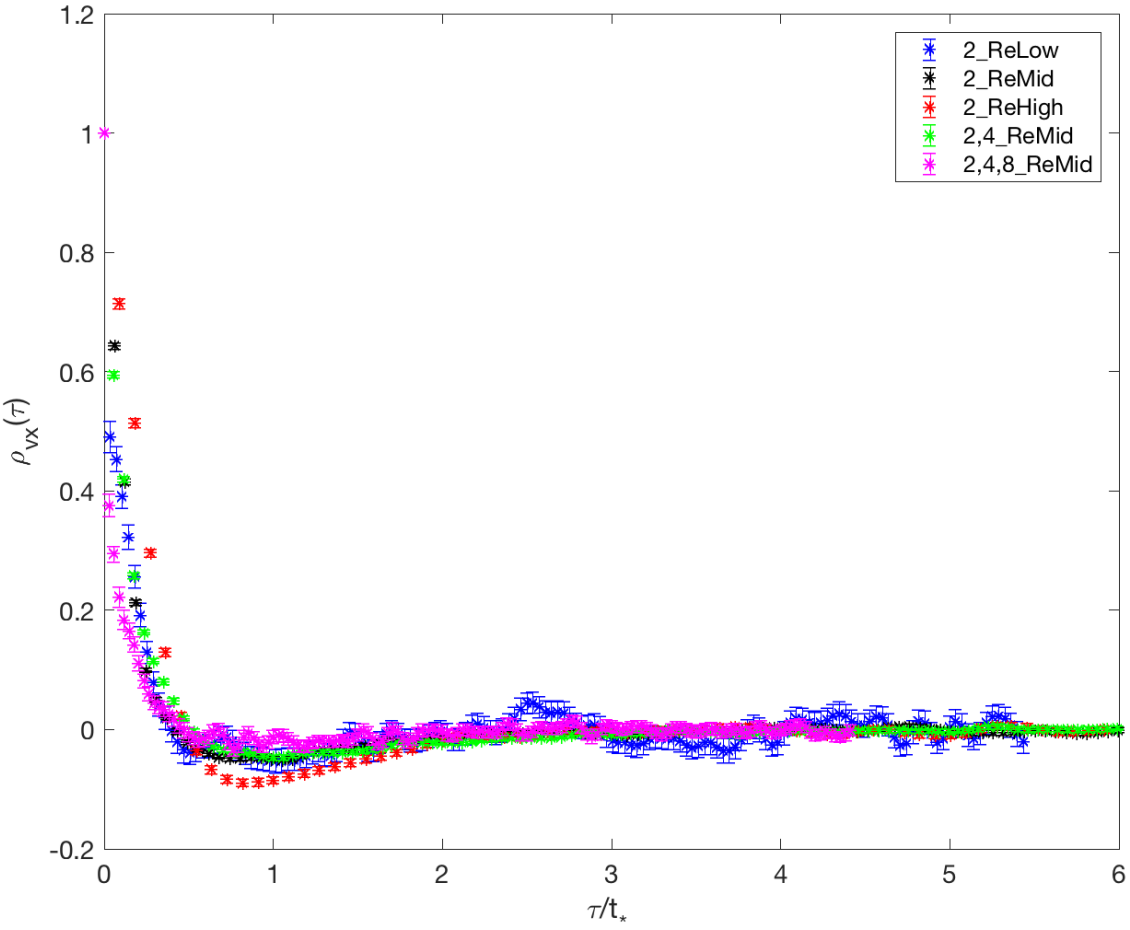

Figure 7.29: Measured x-velocity autocorrelation curves for all packed bed experiments.

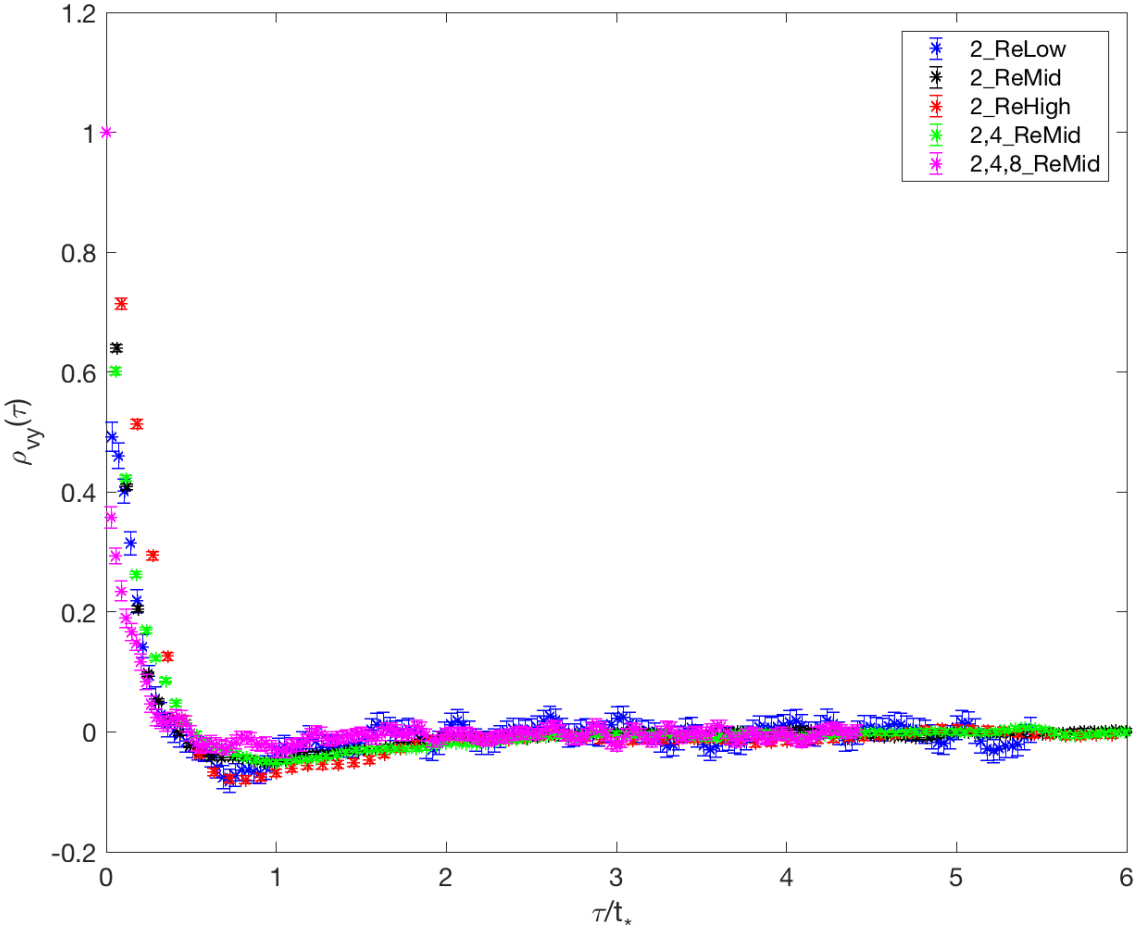

Figure 7.30: Measured y-velocity autocorrelation curves for all packed bed experiments.

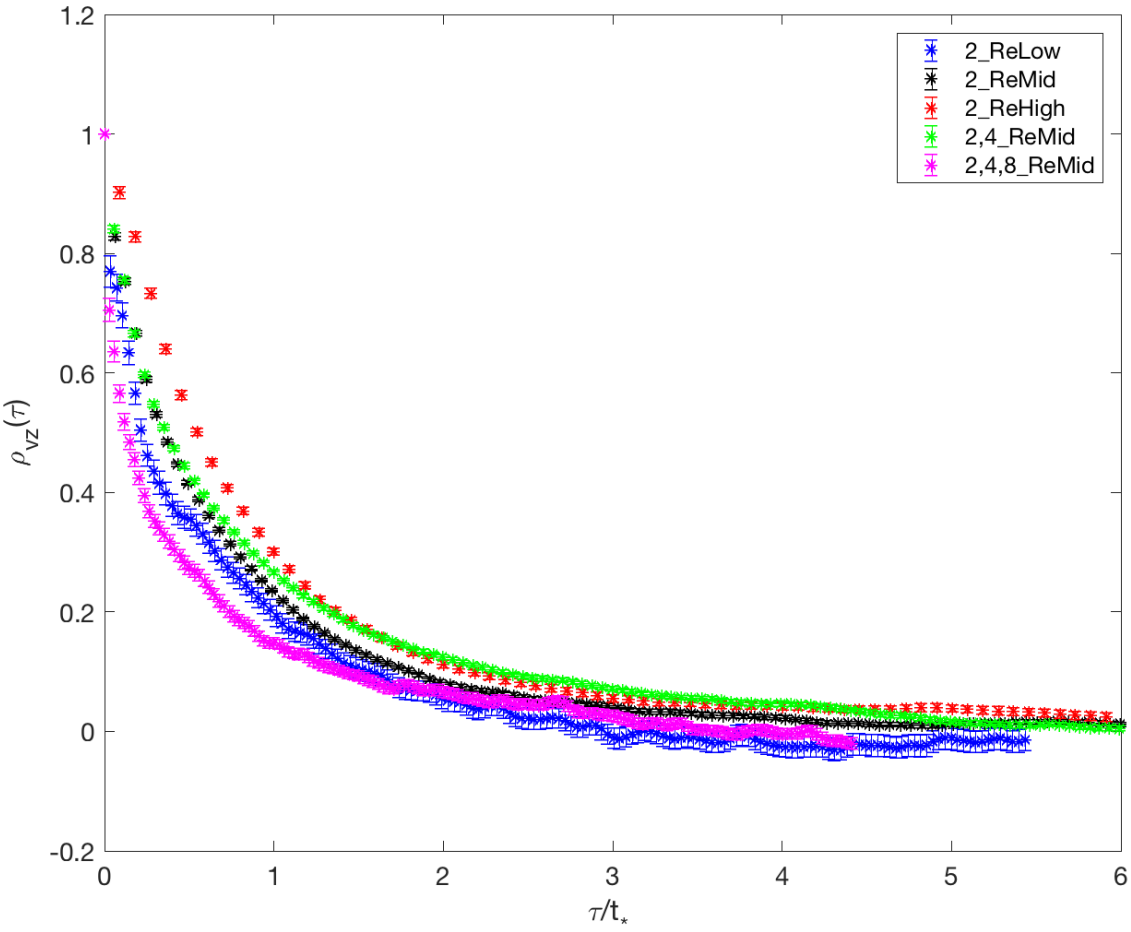

Figure 7.31: Measured z-velocity autocorrelation curves for all packed bed experiments.

Table 7.9: Integral time scales measured in packed bed experiments. Shown are both the integral time scales in milliseconds and those normalized by the bead-transit time t^*.

Exp.	T_x (ms)	T_y (ms)	T_z (ms)	T_x/t^*	T_y/t^*	T_z/t^*
2Re_Low	160	140	1380	0.06	0.05	0.51
2Re_Mid	88	83	1210	0.06	0.05	0.75
2Re_High	95	94	1200	0.09	0.09	1.1
2,4Re_Mid	100	110	1470	0.06	0.06	0.86
2,4,8Re_Mid	150	134	1580	0.04	0.04	0.47

Table 7.9 shows the integral times calculated for each case. These are calculated by numerical integration with the Matlab *cumtrapz* function. Here we see that the transverse integral time scale is generally an order of magnitude less than the axial integral scale. Also, we see that when these are normalized by the bead transit time, there is a clear trend of increased normalized integral time scale with increased Reynolds number (recall that the case 2,4,8Re_Mid has a significantly lower Reynolds number than the other Re_Mid cases). Thus when Reynolds number is increased, both axial and transverse velocity fluctuations will remain self-correlated after more bead passes.

7.4.2 Lagrangian Structure Functions

Next, we consider the 2nd-order Lagrangian velocity structure function, $D_{ii}(\tau)$, defined as

$$D_{ii}(\tau) = \langle (v_i(t+\tau) - v_i(t))^2 \rangle. \tag{7.10}$$

This quantity can be viewed as a velocity-space analogue to the MSD. Once again, it is found that this quantity must be corrected for correlated uncertainties. The correction $\Delta D_{ii}(\tau)$ is calculated as

$$\Delta D_{ii}(\tau) = \sum_{q=-L}^{L+\tau} k_q^2 \delta^2 \tag{7.11}$$

with weights

$$k_q = \left\{ \begin{array}{cc} -A'q \exp\frac{-q^2}{w^2}, & q \in [-L, t-L-1] \\ A'\left((q-\tau)\exp\frac{-(q-t)^2}{w^2} - q\exp\frac{-q^2}{w^2}\right), & q \in [t-L, L] \\ A'(q-\tau)\exp\frac{-(q-t)^2}{w^2}, & q \in [L+1, L+t] \end{array} \right\}, \tag{7.12}$$

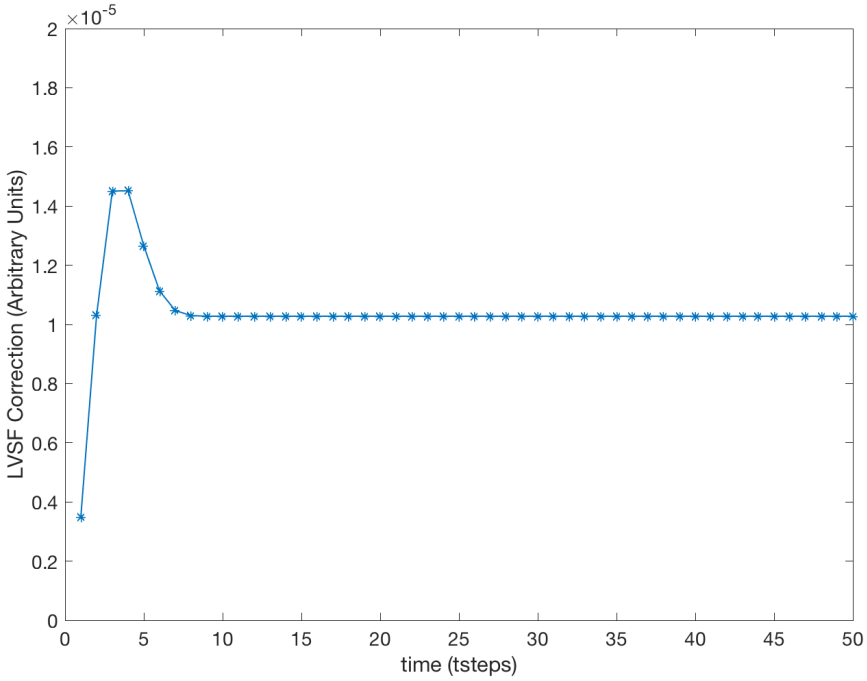

Figure 7.32: Correction to Lagrangian velocity structure function caused by correlated uncertainties for Gaussian filter of size $\sigma = 2$ time steps. Vertical axis is in arbitrary units as magnitude of correction scales with measurement uncertainty. 100 ms time steps were used for this work.

The shape of this correction is shown in Figure 7.32.

The uncertainty values given in Table 7.8 are used once again for this correction. The Lagrangian structure functions for case 2_ReMid are shown before and after correction in Figure 7.33. Here, the "hump" observed at short time lags is caused by this correlation of uncertainties and is used along with the autocorrelation curves to determine the magnitude of the correction.

Figures 7.34-7.36 show the corrected structure functions in each direction. It can be seen that in each case, the higher Reynolds number cases have greater magnitude than the lower Reynold number cases, indicating greater velocity displacements.

Before we continue the analysis of these structure functions, let us first consider the scaling ideas proposed by Kolmogorov in his seminal work on the statistical nature of turbulence [125]. Kolmogorov, examining the 2nd-order Eulerian velocity structure function (discussed later), proposed that for high Reynolds number, homogeneous, isotropic turbulence, statistical quantities at intermediate length scales should be uniquely determined

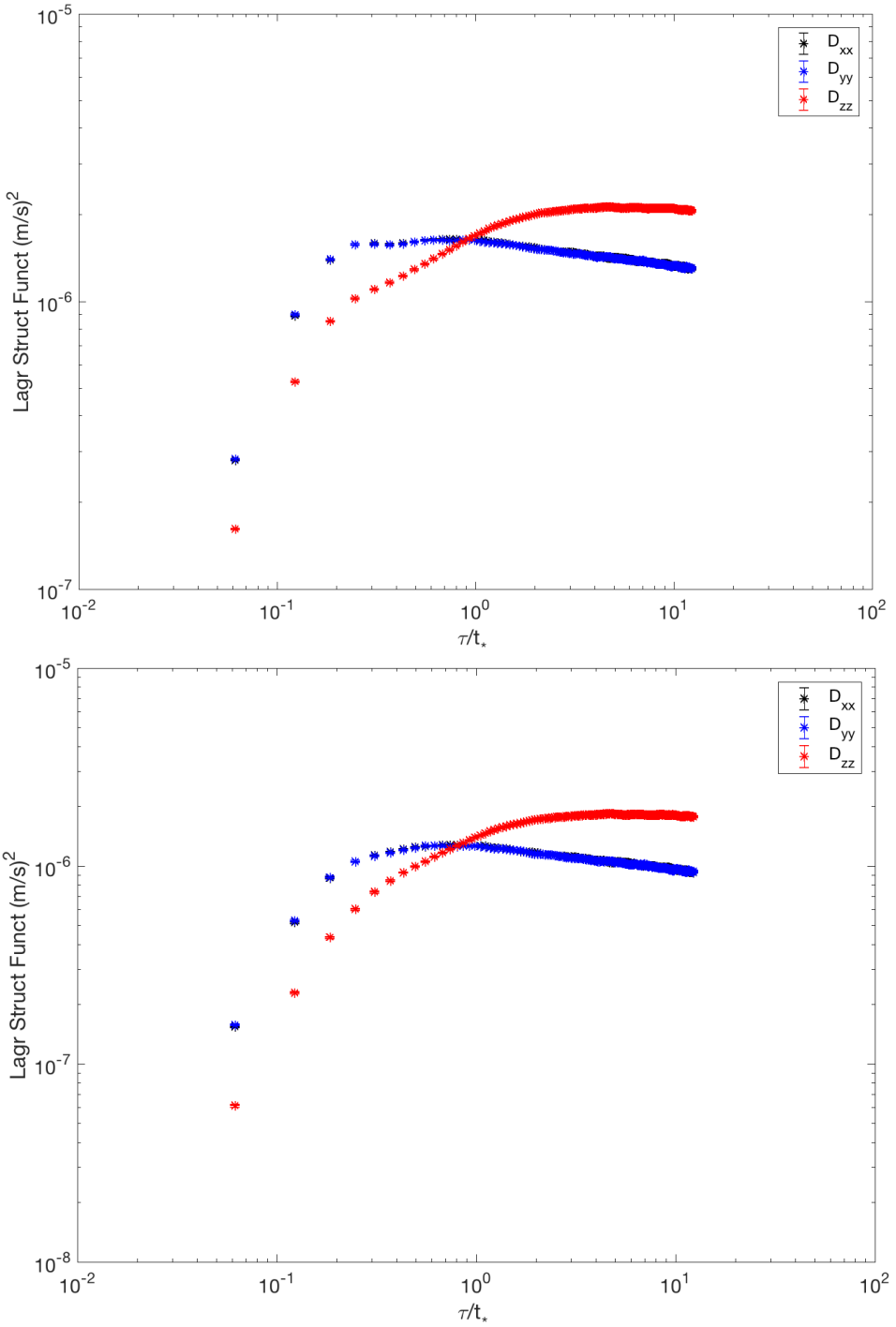

Figure 7.33: Lagrangian velocity structure functions of 2_ReMid case before (top) and after (bottom) correction for correlated uncertainties.

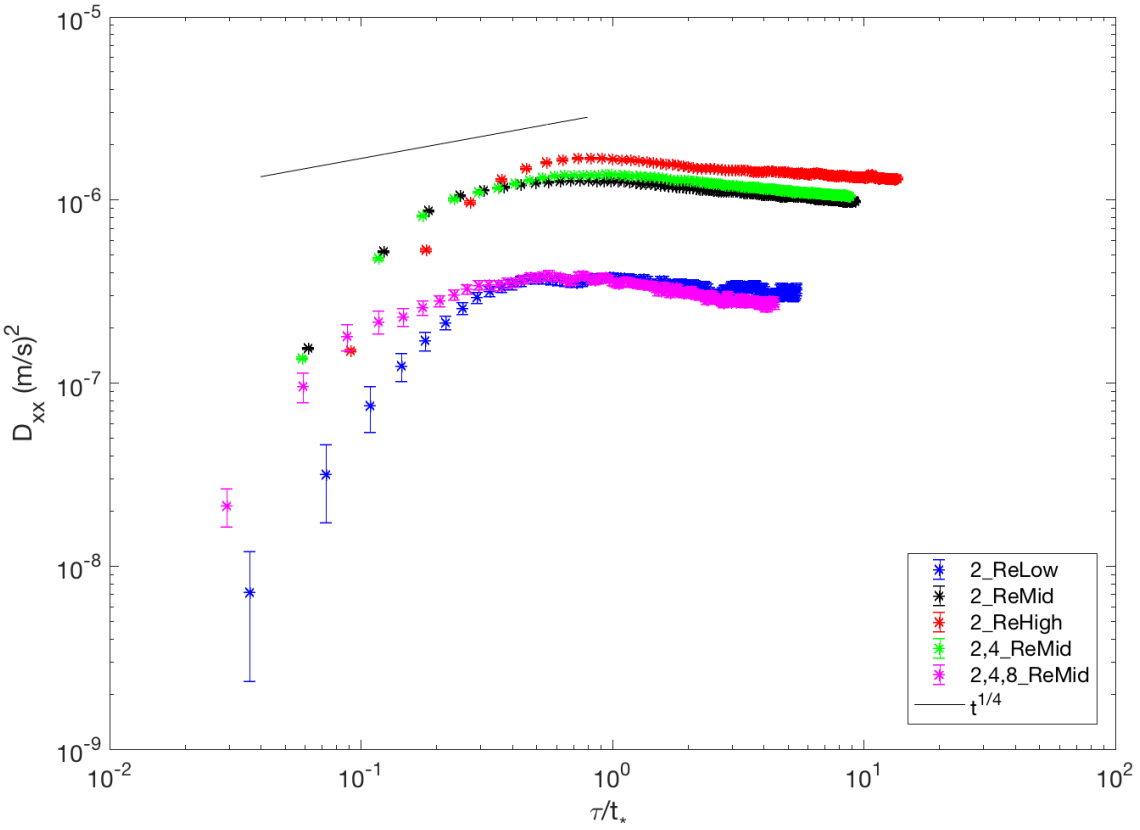

Figure 7.34: Measured x-direction Lagrangian velocity structure functions with $\tau^{1/4}$ scaling for comparison.

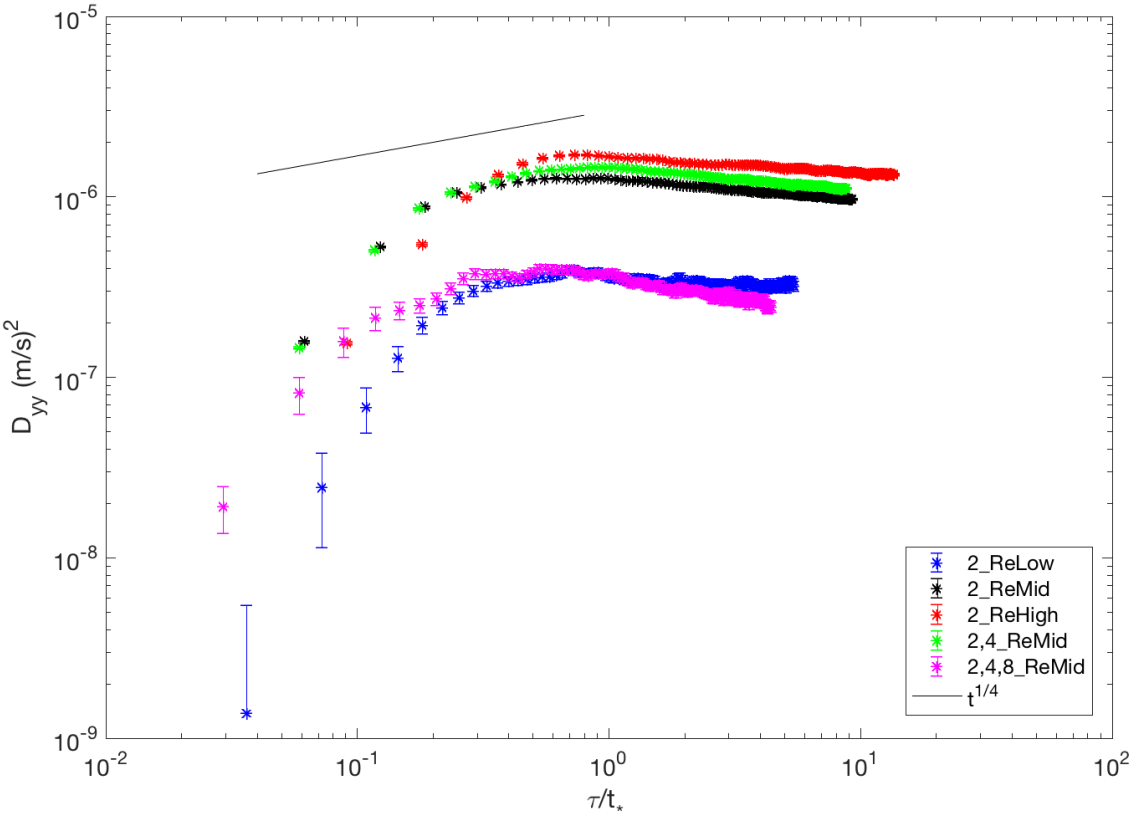

Figure 7.35: Measured y-direction Lagrangian velocity structure functions with $\tau^{1/4}$ scaling for comparison.

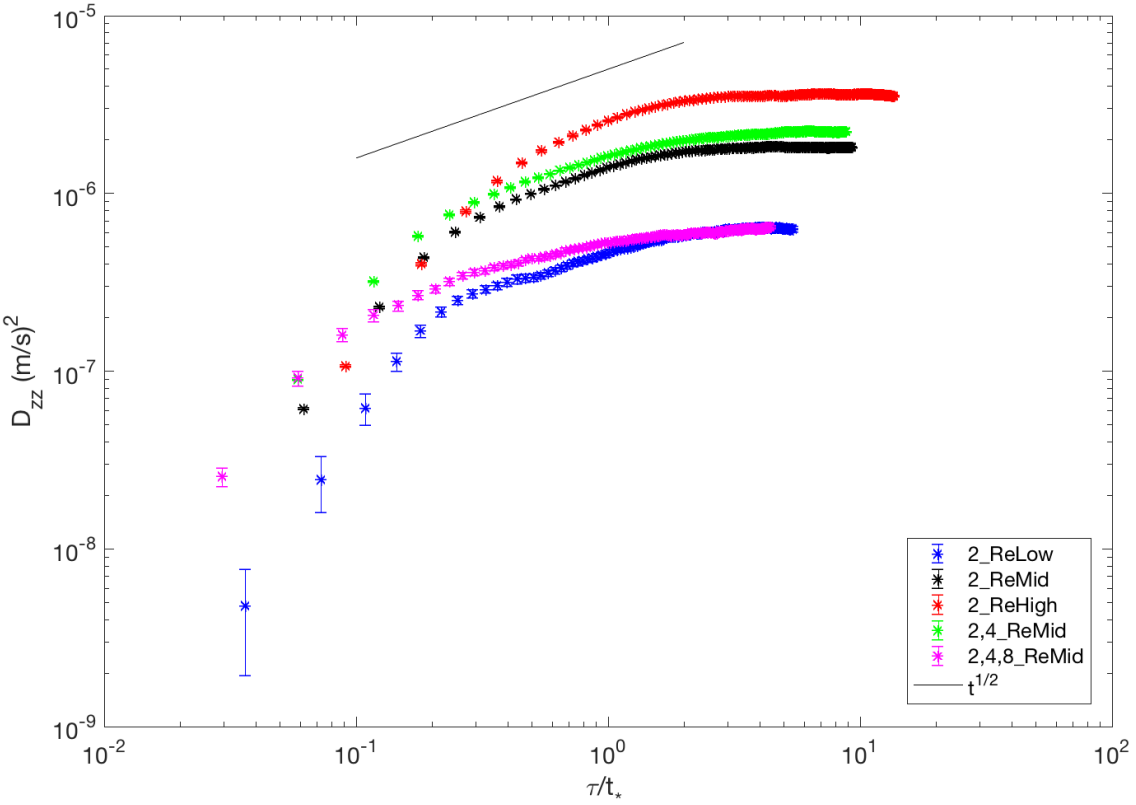

Figure 7.36: Measured z-direction Lagrangian velocity structure functions with $\tau^{1/2}$ scaling for comparison.

by the turbulent kinetic energy dissipation rate $\epsilon = \nu\langle\frac{\partial v_i'}{\partial x_j}\frac{\partial v_i'}{\partial x_j}\rangle$. As such, dimensional analysis can be used to determine universal scaling laws for such flows.

In the case of porous media flow, a direct analogue to turbulent dissipation rate is not known. Instead, we look to renormalize these distributions using the average bead diameter d_{bead} and the RMS values of the velocity fluctuations $\sqrt{\langle v_i'^2\rangle}$, denoted simply as $\bar{v_i'}$ hereafter. If a Kolmogorov-esque scaling holds, and statistical quantities are determined by these quantities, there should be some intermediate time range in which D_{ii} scales as

$$D_{ii}(\tau) = C_i \bar{v_i'}^l d_{bead}^m \tau^n, \tag{7.13}$$

with $l+m+n = 2$, by dimensional analysis. The constant C_i should then be nearly universal across all porous media flows.

As these exponents cannot be directly determined from dimensional analysis, we instead look to the data for any scaling. In the case of the transverse velocity components, there appears to be a region of $t^{1/4}$ scaling. If universal scaling holds with this exponent, then at intermediate time lags, dimensional analysis suggests

$$D_{xx}(\tau) = C_x \bar{v_x'}^{9/4} d_{bead}^{-1/4} \tau^{1/4} \tag{7.14}$$

and similarly for the y-direction. In the axial direction, a $t^{1/2}$ scaling region is observed, suggesting a structure function of the form

$$D_{zz}(\tau) = C_z \bar{v_z'}^{5/2} d_{bead}^{-1/2} \tau^{1/2} \tag{7.15}$$

at intermediate time lags.

To check for these scaling regions, we plot the transverse direction structure functions divided by $(\bar{v_i'}^{9/4} d_{bead}^{-1/4} \tau^{1/4})$ in Figures 7.37 and 7.38 and the axial structure functions divided by $(\bar{v_z'}^{5/2} d_{bead}^{-1/2} \tau^{1/2})$ in Figure 7.39. In these, we look for a plateau region at intermediate time lags, indicating the proposed scaling. The coefficients C_i are the heights of these plateaus. If all curves collapse to have the same height, it suggests that the scaling coefficient C_i may be universal.

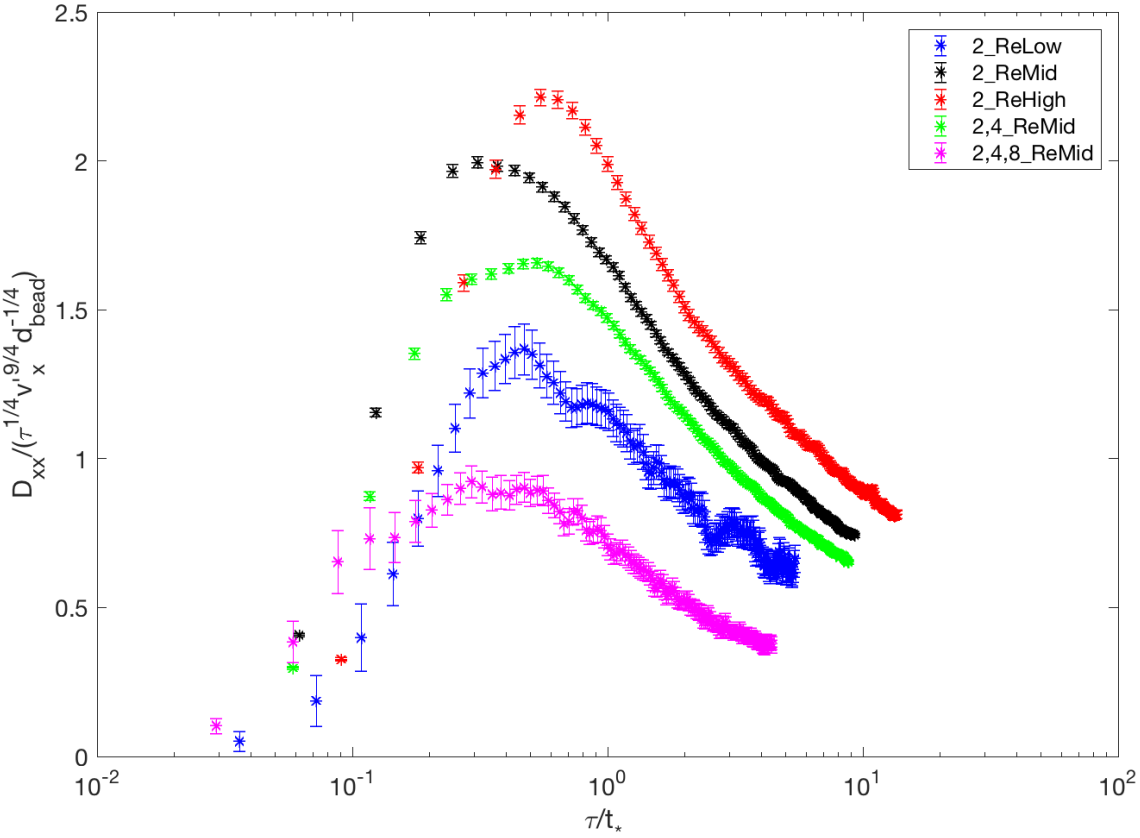

Figure 7.37: Measured x-direction Lagrangian velocity structure functions compensated by $(\tau^{1/4} v_x'^{9/4} d_{bead}^{-1/4})$.

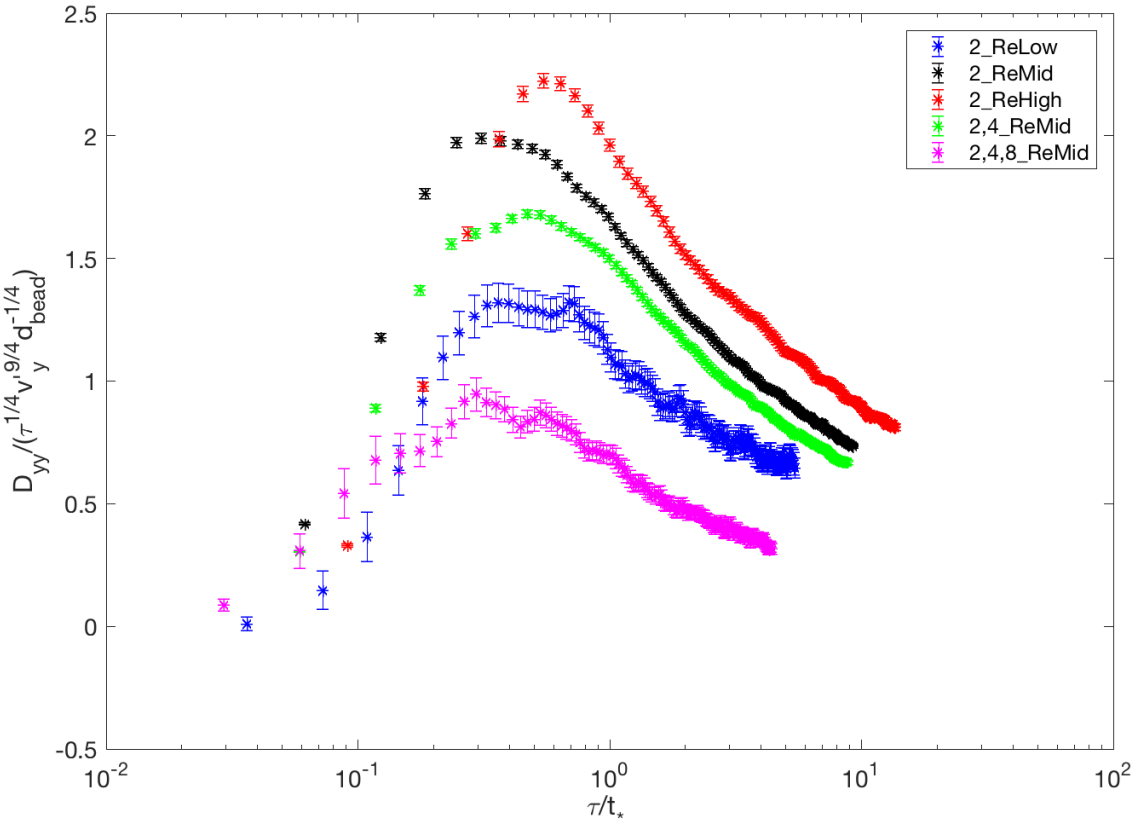

Figure 7.38: Measured y-direction Lagrangian velocity structure functions compensated by $(\tau^{1/4}v_y'^{9/4}d_{bead}^{-1/4})$.

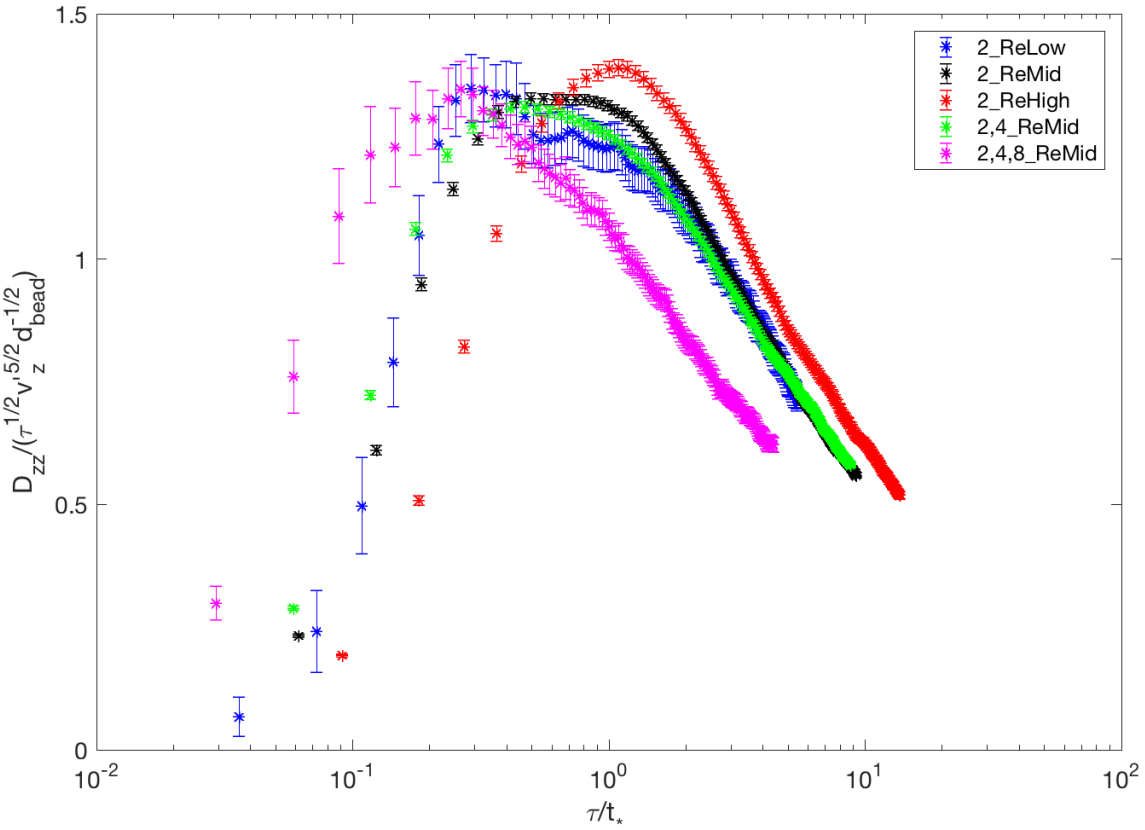

Figure 7.39: Measured z-direction Lagrangian velocity structure functions compensated by $(\tau^{1/2}v_z^{5/2}d_{bead}^{-1/2})$.

In the transverse directions, the plateau region does not appear in the case 2_ReHigh, and is seen to become more pronounced with decreasing Reynolds number in the 2 mm cases. In the mixed bead cases, the plateau region appears to be present, but is less pronounced. The coefficients C_x and C_y are also not observed to universal. Instead, it appears that these increase with increased Reynolds number and decrease with increased number of bead sizes. In the cases showing plateaus, it appears that the scaling region lasts from time lags of approximately 0.3 to 0.8 bead transit times, indicating that it appears after the integral time scale for transverse velocities. Normalizations by the RMS axial velocity fluctuation were also attempted, but did not show collapse to a universal form.

In the axial direction, a plateau region appears in all but the case 2_ReHigh, with it being most pronounced for the case 2_ReMid. Contrary to the transverse structure functions, in this case we do see that the compensated structure functions collapse to a form showing a universal scaling coefficient $C_z \approx 1.3$. Even in the 2_ReHigh case which does not exhibit a

plateau region, the peak of the curve is also near this value. In these curves, the plateau region appears to occur at lesser time lags with lower Reynolds numbers, with no direct connection between this region and the integral time scale for axial velocity fluctuations being established.

7.4.3 Eulerian Structure Functions

Lastly we examine the 2nd-order Eulerian velocity structure function, the quantity originally considered by Kolmogorov [125]. This quantity is of importance to turbulence research as an equation describing its evolution can be directly derived from the Navier-Stokes equations, and it is related to interscale turbulent kinetic energy transfer [126].

To define this quantity, we consider two points in space $\mathbf{x}$ and $\mathbf{x}'$ separated by a vector $\mathbf{r}$. The longitudinal velocity increment is then defined as

$$\delta v_{LL} = (\mathbf{v}(\mathbf{x}) - \mathbf{v}(\mathbf{x}')) \cdot \mathbf{r}/r, \tag{7.16}$$

and the transverse velocity increment is defined as

$$\delta v_{NN} = \sqrt{(\mathbf{v}(\mathbf{x}) - \mathbf{v}(\mathbf{x}'))^2 - \delta v_{LL}^2}. \tag{7.17}$$

As such, δv_{LL} is the velocity increment in the direction aligned with the displacement vector, and δv_{NN} is the magnitude of the velocity increment in the plane perpendicular to the displacement vector. Given these quantities, we can then define the longitudinal and transverse 2nd-order Eulerian velocity structure functions as

$$D_{LL} = \langle (\delta v_{LL})^2 \rangle \tag{7.18}$$

and

$$D_{NN} = \langle (\delta v_{NN})^2 \rangle, \tag{7.19}$$

respectively.

To calculate this quantity, it is required that the velocity of the flow be detected at many points during a single time step (hence it being an "Eulerian" quantity that examines a spatially fixed region and does not move with the flow). Because of this, Eulerian structure functions are not calculated for the cases 2_ReLow and 2,4,8_ReMid as too few simultaneous trajectories were detected. Also, the resolving power of the M-PEPT technique prevents us from calculating this quantity for short displacements. Recall that for the M-PEPT reconstruction of the remaining cases, a CL-counting grid of 1 mm voxels and a local maxima search radius of 3 voxels were used. This implies that the shortest particle separation that can be resolved is 3 mm, limiting the distances over which the structure function can be calculated. As this quantity is calculated between velocity measurements from different trajectories, no correction for correlated uncertainties needs to be applied.

Eulerian velocity structure functions are calculated for the cases 2_ReMid, 2_ReHigh, and 2,4_ReMid and are plotted in Figures 7.40 and 7.41. It is observed that the magnitude of the velocity increments is greater for the higher Reynolds number case and also for the mixed bead case. Once again, these are examined for any exponential scaling regions at intermediate length scales. Here, we normalize the structure functions by the the quantity $\bar{v'} = \sqrt{\bar{v}_x'^2 + \bar{v}_y'^2 + \bar{v}_z'^2}$, as the velocity increments described are a combination of axial and transverse velocities.

In the case of the longitudinal structure function, an $r^{2/3}$ region is seen. This is the same scaling predicted by Kolmogorov for homogeneous, isotropic turbulence [125], but it is believed that this is purely coincidental. Using the previously described formalism, we predict that at intermediate displacements, the structure functions should scale as

$$D_{LL}(r) = C_L \bar{v'}^2 d_{bead}^{-2/3} r^{2/3}. \tag{7.20}$$

In the transverse case, an $r^{1/3}$, region appears to exist, implying scaling of the form

$$D_{NN}(r) = C_N \bar{v'}^2 d_{bead}^{-1/3} r^{1/3}. \tag{7.21}$$

To further examine these, compensated structure functions are plotted in Figures 7.42 and 7.43.

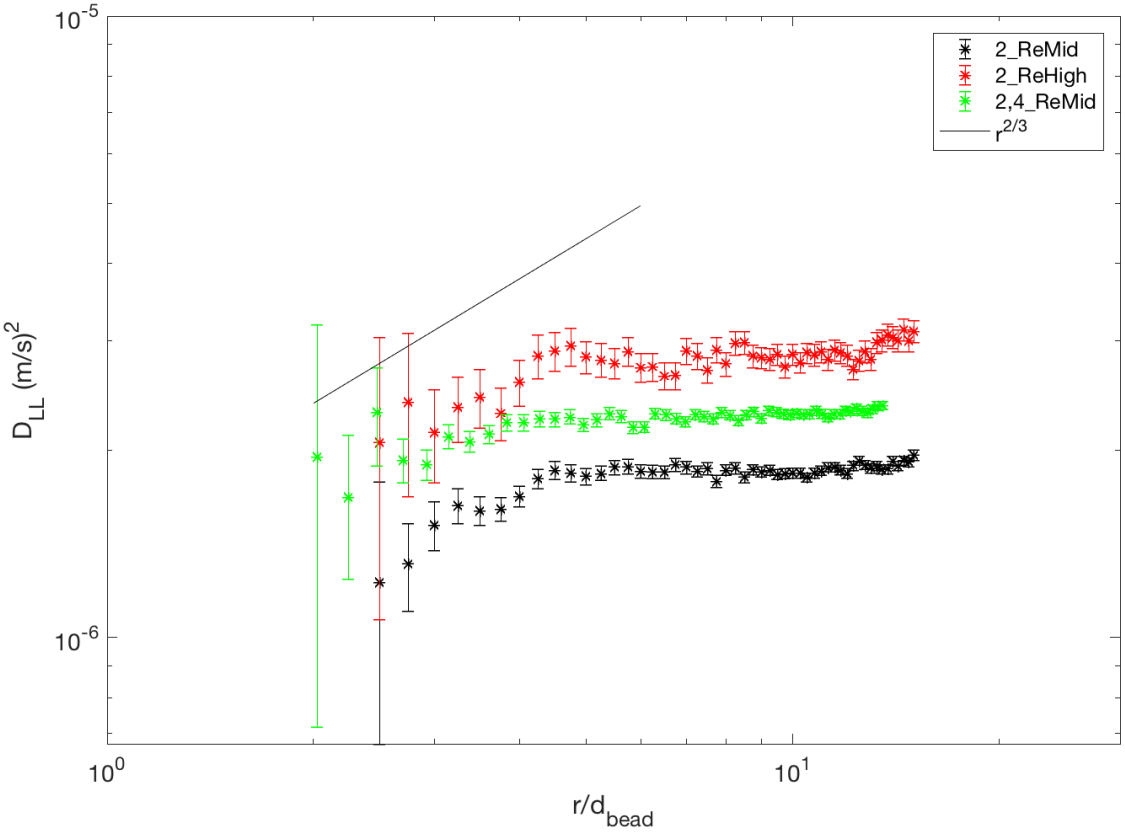

Figure 7.40: Measured longitudinal Eulerian velocity structure functions with $r^{2/3}$ scaling for comparison.

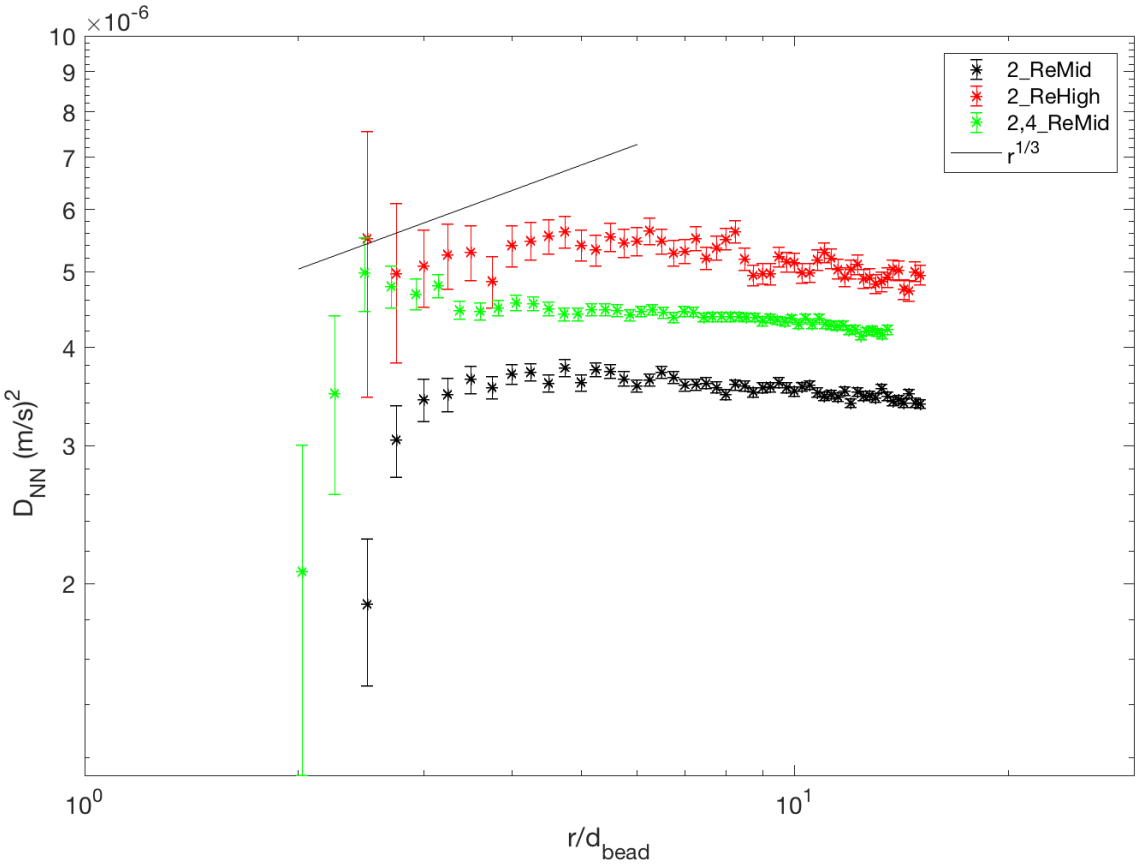

Figure 7.41: Measured transverse Eulerian velocity structure functions with $r^{1/3}$ scaling for comparison.

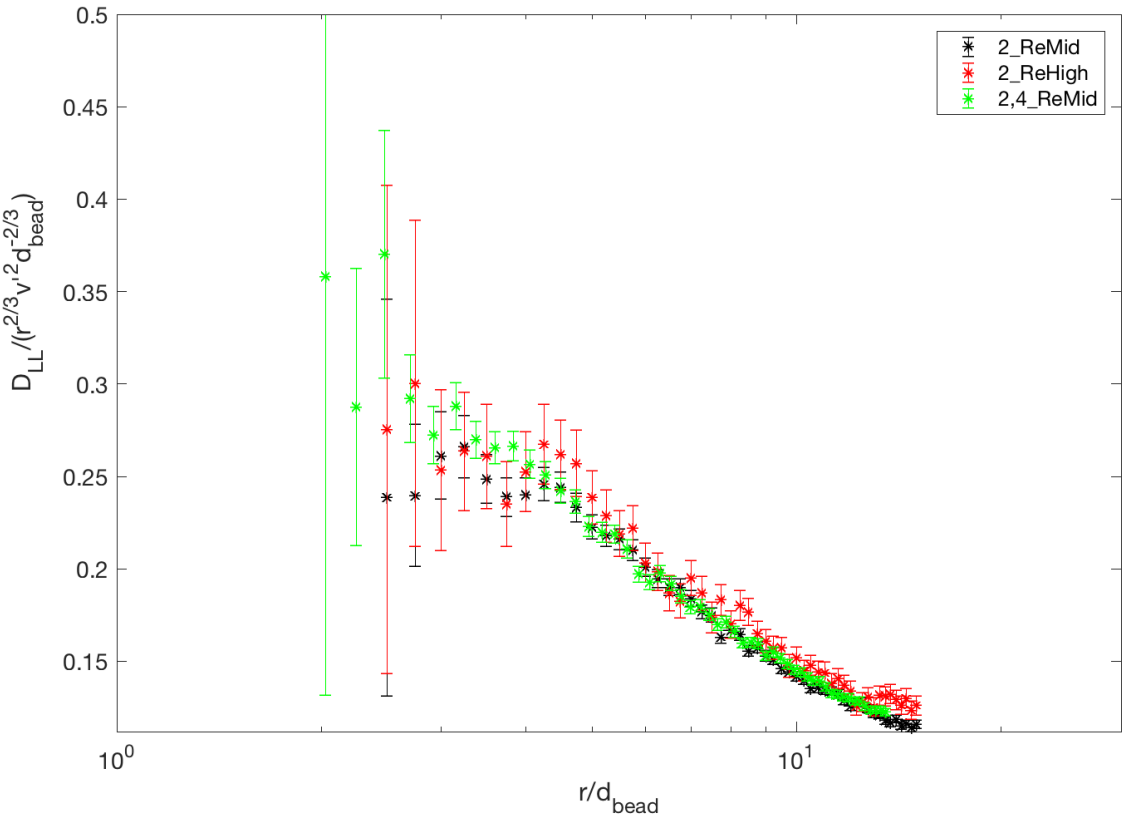

Figure 7.42: Longitudinal Eulerian velocity structure functions compensated by $(r^{2/3}\bar{v}'^2 d_{bead}^{-2/3})$.

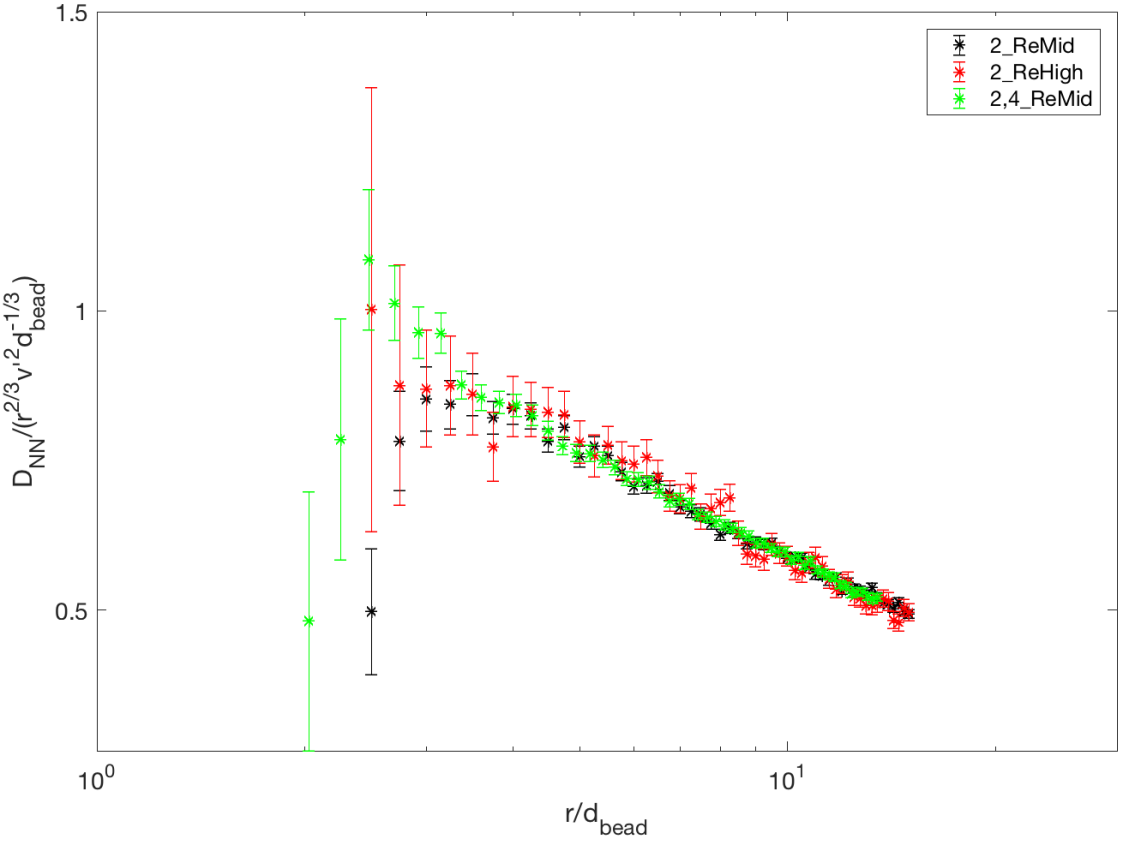

Figure 7.43: Transverse Eulerian velocity structure functions compensated by $(r^{1/3}\bar{v}'^2 d_{bead}^{-1/3})$.

It is seen that in both cases, the curves collapse onto the same form after about 3 bead diameters. The plateau region also seems to be most evident in the 2 mm cases, existing between 3 and 5 bead diameters. In contrast, the compensated structure functions of the mixed bead case seem to peak at around 2.5 bead diameters, and do not show a well-defined plateau region. In the 2 mm cases, scaling coefficients of $C_L \approx 0.25$ and $C_N \approx 0.8$ emerge, but the peak of the compensated structure function is noticeably higher in the 2,4 mm bead case. As such, this scaling seems to be restricted to the cases of uniform bead size.

Chapter 8

Discussion and Conclusion

8.1 PEPT Discussion

Positron emission particle tracking has been employed for over two decades to study flowing media in environments lacking optical access. Despite this, the majority of PEPT experiments have used a single tracer particle, limiting the amount of data that can be collected. In this work, a new technique for multiple-particle PEPT has been introduced and demonstrated. The FPI reconstruction method allows tracking of an arbitrary number of tracer particles and takes account of tracers entering and leaving the field of view of the detector system. In this way, it enables experiments using hundreds of tracers in a recirculating flow loop, such as the primary experiment described in this work. In this work over 80 tracers are tracked simultaneously in an experiment, an order of magnitude improvement over the number of particles tracked by the previous leading M-PEPT reconstruction method [8, 19]. Furthermore, the FPI method has enabled the use of PEPT for studies ranging from yeast cell migration [89] to Reynolds stress and turbulent kinetic energy budget measurements in turbulent shear flows [81].

This work has demonstrated the utility of the FPI method and explored its limitations. Based on the knowledge gained, future improvements are suggested. The first of these is a new means of calculating uncertainty during particle location. While the current calculated uncertainty (Table 7.2) is close to the actual amount of random noise in the particle tracking data (Table 7.8), the differences are still significant. As noted, it is possible that this is caused

by an overestimation of the number of CL used for each particle position reconstruction. It is also possible that sources beyond the reconstruction method (positron range, photon scattering, etc.) are contributing to the uncertainty in a way that the image reconstruction does not take into account. An improved method for uncertainty calculation is desired, and is a line of current work.

Another apparent limitation of the FPI method is the difficulty associated with finding particles that are close together. Figure 8.1 shows an example axial slice from the CL counting grid from the 2_ReMid case. Here, a $1 \times 1 \times 1$ mm^3 grid is used for line counting and the grid has been smoothed via background subtraction and convolution with a Gaussian kernel of width $2w + 1$ voxels with $w = 3$. Solid circles indicate the $w = 3$ voxels radii employed in this experiment for local maxima search and position calculation, while dashed circles show the same for $w = 4$. In the case of $w = 4$, only one of these particles would be detected, as the other maximum falls within the search radius. In the case of $w = 3$, both particles would be detected, but the overlap of the particle images would cause both positions to be biased toward their mutual center. It is desired that improvements are made to the FPI method to eliminate this sensitivity to the selection of w, remove the biasing cause by close approaching particles, and allow resolving of even closer approaching particles.

The first proposed solution is the use of smaller voxels, but this introduces two problems. First, both the memory cost of storing the line grid and the computational cost of searching the grid for maxima scale as l^{-3}, where l is the side-length of the voxels used. The majority of M-PEPT reconstruction runtime is occupied by position reconstruction. Thus, going from 1 mm voxels to 0.5 mm voxels would increase computational time roughly 8-fold.

The second issue with decreasing voxel size is uneven sampling of the voxel space by the possible combinations of detector elements used for coincidence determination. Figure 8.2 shows all possible coincidence lines that can be drawn between detector elements in a 24 element detector ring, as shown in [63]. This pattern creates an uneven sampling of voxels by coincidence lines that is most extreme near to, but not right at the transverse center of the field of view. A similar defect exists for parallel plate or rectangular detector geometries, but the pattern will be different. This defect is decreased when more detector elements are in each ring (recall that there are 320 individual crystals in each ring of the Inveon) but

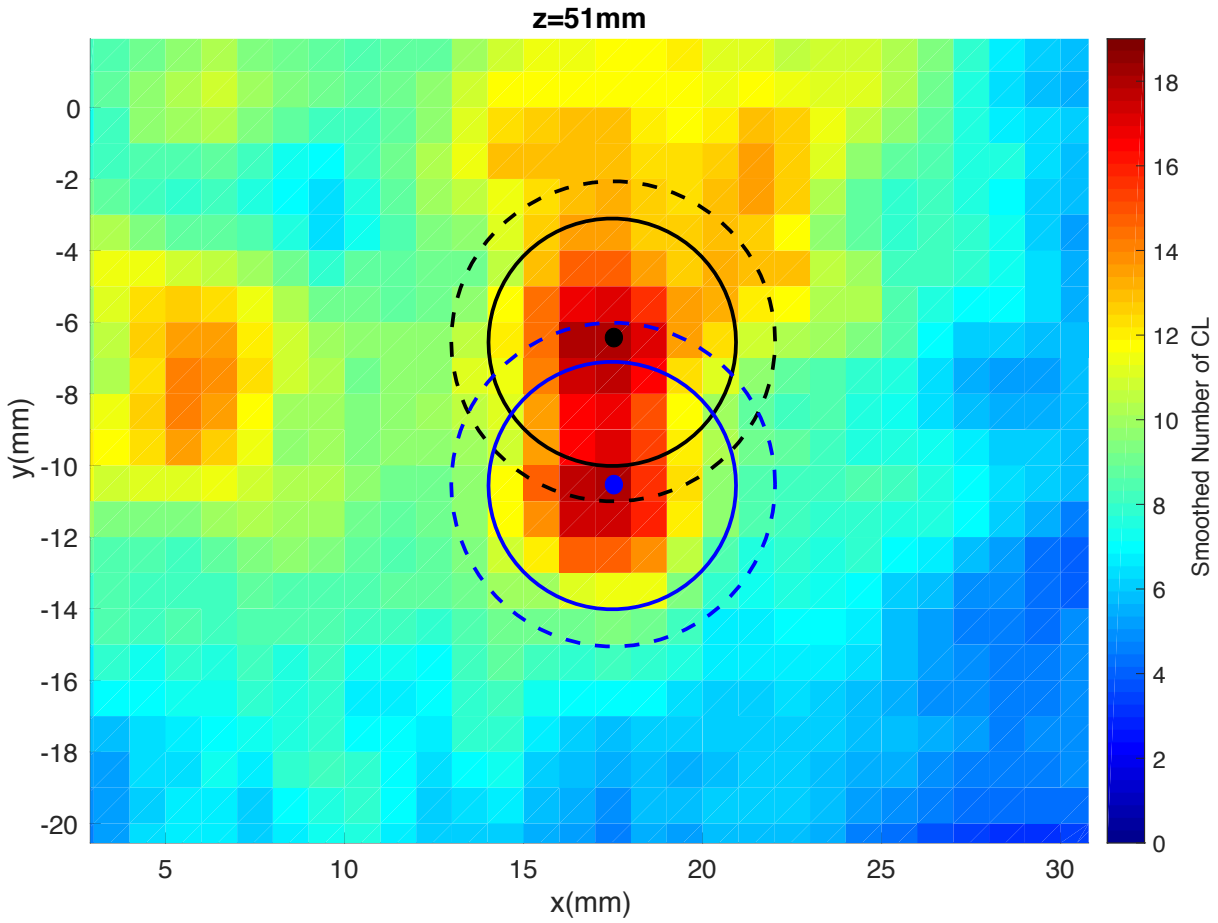

Figure 8.1: Axial frame from smoothed CL grid showing images of close particles. Dots indicate local maxima, and solid and dashed circles indicate search regions used in local maxima calculation with $w = 3$ and $w = 4$ voxels, respectively.

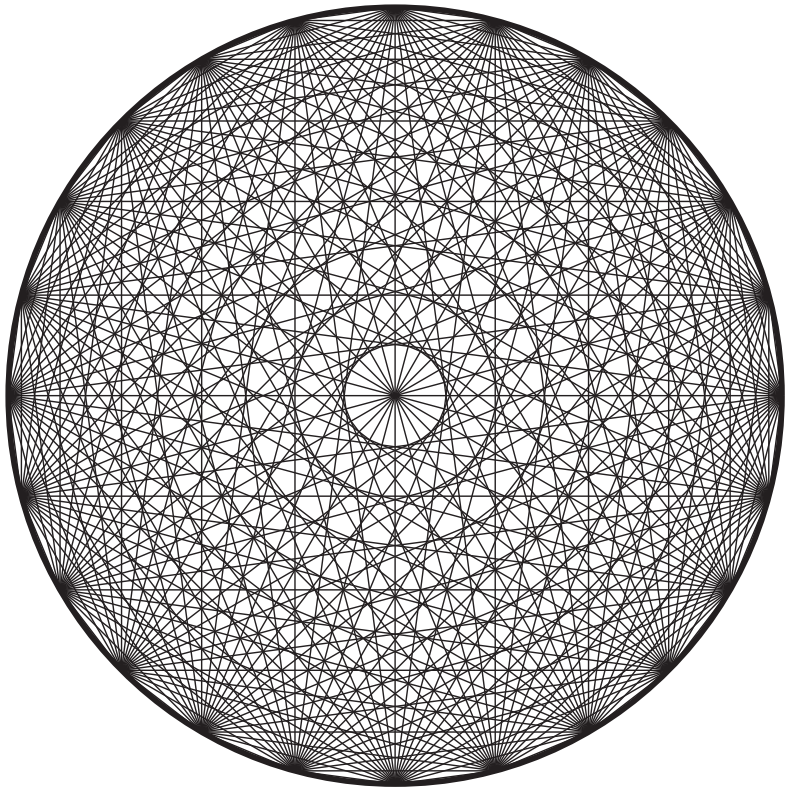

Figure 8.2: All possible combinations of coincidence lines for a single axial slice of a ring-type PET scanner with 24 detector elements [63].

becomes more pronounced when smaller voxels are used, relative to the individual crystal size. Because of this, 1 mm voxels seem to provide the best results for the Inveon, which has 1.51×1.51 mm^2 crystal faces. Recall from Section 3.2 that in the smoothing of the CL counting grid, a Gaussian half-width of $\lambda = \frac{Crystal\ Width}{2\times(Grid\ Size)}$ is used. This width is chosen in an attempt to "spread out" the effects of each CL onto multiple grid elements but testing has shown that it does not entirely eliminate the effect of this CL sampling pattern. It is possible that an improved filtering scheme or a calibration routine could be implemented for PEPT as a means to overcome this sampling issue. Furthermore, the design of detectors with smaller individual elements may also allow the use of smaller voxels for reconstruction.

In lieu of reducing the voxel size, it is suggested that modern optical particle tracking techniques designed for dense particle number images be ported for use in PEPT. The use of CL-count voxels makes the adaptation of 2D optical particle tracking techniques to 3D

PEPT reconstruction straightforward. One possible method to be explored is the "shake-the-box" technique of Schanz et al. [127]. In this method, particle identification and linking are performed simultaneously, with particle images from a frame i being "shaken" to search for those in frame $i+1$. If a particle from frame i is detected in frame $i+1$, its virtual image (based on the pixel/voxel distribution seen in frame i) is subtracted from that frame so that nearby particles can be identified without interference. For 2-D PTV, it has been demonstrated that this method can be used to identify and track over 99% of particles at particle densities up to 0.125 particles per pixel (average separation 2.8 pixels) [127]. It is unclear if similar performance can be achieved in PEPT, but it is believed that improvements over the current version of M-PEPT would be seen.

As a means to test the performance of M-PEPT routines, it is desired that synthetic particle images be created. Such synthetic datasets establish a ground truth against which to test, providing easy quantification of position calculation error and numbers of false-positives and true-negatives. Ideally, the creation of synthetic datasets would account for all physical processes that happen between positron-emission from a tracer to the creation of the listmode files including positron range, photon scattering by the medium, and response of the detector system.

The Geant4 Application for Tomographic Emission (GATE [60]) platform has been used to create a model of the Siemens Iveon that includes detector electronic response [61]. However, work using this [113, 25] and other [62] models of the Inveon has shown sensitivity profiles of simulated machines that differ from those measured with physical scanners. Such models can still be used for testing PEPT methods, but it requires the application a correction to account for the improper response to the amount of activity being simulated [25]. It is desired that the cause of this mismatch between simulation and reality be found and corrected. In doing so, it would be possible to properly simulate both current machines for methods testing and experimental design and novel detector geometries for design of future PEPT systems. Full simulation of a PEPT experiment has been explored by our group [128] and is an open line of research.

This design of new detectors is one of two technological advancements proposed for PEPT. It is desired that new detectors have increase sensitivity over current scanners without any

degradation of spatial resolution. Contemporary, small-animal PET scanners, such as the Perkin-Elmer G8, show improved sensitivity over the Inveon (near 9% at the center the FOV with 350-650 keV energy window [129]). However, this scanner has a closed-box geometry that would make it impractical for studies in most engineering flow systems and fundamental fluid dynamics apparatuses. The G8 is being explored as means of continuing the study of cell tracking in small-animal models. As such, it is desired that any detector system designed specifically for PEPT be modular in nature, giving flexibility for use in many experimental setups.

Lastly, the creation of new tracers would improve PEPT performance for flow measurements. To serve as a flow tracer for Lagrangian flow measurements, it is desired that any tracer particle be significantly smaller that the smallest present flow scales to prevent particle inertia from biasing results [130, 131, 132]. In the case of PEPT, this creates a problem as the use of a smaller tracer is accompanied by a decrease in activity and thus reconstruction accuracy. To overcome this, new tracers are desired that are smaller than those currently used but of similar or greater activity. One way to do this is to switch from surface-activation to a volumetric activation so that the number of positron-emitting atoms in a particle makes up a much greater fraction of the whole.

Fabrication of such tracers has been a line of research within our group and has proven a significant challenge. At its heart, this is a radiochemical problem requiring careful control of input parameters to create particles of the proper chemical composition and size. The most promising efforts involve creation of gallium-hydroxide particles by precipitating $Ga(OH)^3$ from a solution of Ga, HCl, and NaOH, but these have not been tested using the radioactive species ^{68}Ga. This isotope can be produced using commercial elution generators, but the concentration of ^{68}Ga in the eluent is likely too low to fabricate high-activity tracers. Fabrication of ^{64}Cu tracers was explored in collaboration with the University of Missouri, Columbia due to their proximity to the United State's primary source of ^{68}Cu, the Missouri University Research Reactor (MURR), but this research was halted due to lack of funding.

Such small, volumetrically activated particles not only have the potential to increase measurement resolution while mitigating inertial effects, they also would not leach their radiolabel during use, as is observed for the tracers used in this work. If such tracers are

stable at high temperatures, they may also be useful for studies in liquid metal flows, whose typical opacity makes them inaccessible to optical measurements. In the opinion of the author, the creation of durable, high-activity, small-volume tracers is the "holy grail" of PEPT advancement.

8.2 Porous Media Discussion

In the experiments described herein, new information on porous media flows has been discovered, and limitations of the methods employed have been found. Leaching and trapping of particles prevented the collection of sufficient data in two of the cases investigated. The experiments performed proved inconsistent, and while the same preparations were made for each test, the data showed no clear indication why some experiments were successful while others were not. The cases 2_ReLow and 2,4,8_ReMid should be repeated in the future, and cases exploring multiple Reynolds numbers should be conducted in the mixed-bead cases.

The current set of experiments demonstrates tracking of particles over more than 50 bead diameters. Recent experiments using index of refraction matched materials have used optical particle tracking to reveal sub-pore-scale dynamics of particles in porous media flow [47]; however, these only tracked particles over a few pore lengths. Moroni and Cushman [46] tracked particles over 11 bead diameters in a packed bed configuration, but this is the first work describing dynamics over dozens of bead passes.

In examining velocity and acceleration statistics, it is observed that in all cases, velocity and acceleration distributions are distinctly non-Gaussian. This has been previously observed in both porous media experiment [47] and simulation [124]. For porous media flows, Kang et al. [124] demonstrated a link between this velocity intermittency and anomalous transport. The acceleration PDFs measured herein are also similar to those observed in turbulent flows [64, 65, 66, 130].

It is observed that in all cases, the tails of the transition time distributions decay algebraically with tails $\psi(t) \sim t^{-1-\beta}$ with $\beta < 2$. When considered under the continuous time random walk paradigm, anomalous transport arises from these long waiting times between transitions. We also see that for transitions in the axial direction, the scaling exponent β_z

decreases in the mixed bead cases, implying that these long transition time events become more frequent. This decrease of β with increased number of bead sizes has been observed by Levy and Berkowitz [34], who studied tracer spreading in the mean-flow direction. In past experiments, the long time scaling of $\psi(t)$ was inferred by measuring concentration profiles, but using PEPT, we have succeeded in directly measuring this quantity. This confirms the validity of the underlying postulate of the CTRW model regarding random walkers with a propensity to wait for long periods before taking their steps.

In these experiments, anomalous transport is demonstrated by the regions of nonlinear scaling in the mean-squared displacement curves. In all cases, nonlinear scaling is seen at early times with a late time transition to Fickian transport. Many of the scaling regimes observed match those observed in the simulations of Kang et al.[124]; however, they observed anomalous scaling persisting to late times. In these simulations, only advective transport was considered, implying that this transition to Fickian transport is likely caused by diffusive processes. This late time recovery of normal transport is built into the CTRW transition time distribution model proposed by Edery et al. [43].

In the current work, no direct correlation is seen between the observed nonlinear scaling regimes and the degree of bead heterogeneity. It is expected that the decreased β_z observed in the mixed bead cases would lead to transport that is somehow more anomalous. In the case of the 2,4,8_ReMid experiment, we do see anomalous scaling persist to late times in the transverse directions, but the transverse transition time decay exponents β_x and β_y are the same as those observed in other cases, within uncertainty. In fact, we see a quicker transition to linear scaling in the axial direction than in the case 2_ReLow (the case with the most similar Reynolds number). Furthermore, little to no difference is observed between the axial MSD curves of the cases 2_ReMid and 2,4_ReMid, despite these two showing different axial transition time decay exponents β_z

Perhaps the most interesting findings of this study are those related to velocity correlations. The transverse velocity fluctuations quickly decorrelate while correlations between axial velocity fluctuations persist to 4 (in the low Reynolds number cases) to 6 (in the high Reynolds number cases) bead transits.

In the case of the Lagrangian velocity structure functions, the axial structure functions are seen to collapse and suggest the possibility of universal scaling

$$D_{zz}(\tau) = C_z \bar{v_z'}^{5/2} d_{bead}^{-1/2} \tau^{1/2} \tag{8.1}$$

with coefficient $C_x \approx 1.3$. This is the first time that such scaling has been observed in porous media flows and should be measured for a number of other porous media to test the assumption of universality.

For the Eulerian structure functions, scalings of the form

$$D_{LL}(r) = C_L \bar{v'}^2 d_{bead}^{-2/3} r^{2/3} \tag{8.2}$$

and

$$D_{NN}(r) = C_N \bar{v'}^2 d_{bead}^{-1/3} r^{1/3} \tag{8.3}$$

are seen for the longitudinal and transverse structure functions, respectively, in the 2 mm packed bed experiments with coefficients $C_L \sim 0.25$ and $C_N \sim 0.8$. This does not hold for the case 2,4_ReMid. This has not been previously measured in porous media flows. Future experiments should be conducted with more bead configurations, denser particle seeding, and higher resolving power to see if this scaling appears in any other cases and if it persists to shorter length scales.

We note that in both cases, the universal forms found required knowledge of the average pore size and the RMS velocity fluctuation, $\bar{v'}$. Holzner et al. [47] showed that their measured velocity distributions could be predicted using knowledge of the pore size distributions in their porous media. Thus, it is possible (and perhaps likely) that the primary controlling factor in these statistical quantities is the pore size distribution. If the observed scalings are universal, information on the pore distribution in a sample (acquired through X-ray computed tomography or other means) may be sufficient for predicting both Eulerian and Lagrangian velocity increments.

Links between porous media flows at low Reynolds numbers and high Reynolds number turbulent flows are present as evidenced by the similar acceleration distributions and

longitudinal Eulerian structure function scaling. This may be caused by correlated structures that exist in each system. In turbulent flows, this is referred to as the "energy cascade" in which turbulent kinetic energy is produced at the largest scales of the flow and transferred through the break-up of correlated structures, called eddies, to the smallest scales of the flow where energy is dissipated by viscous heating [133]. It is not expected that the same mechanism is present in porous media flows, but it is possible that random pore networks can create flow paths that resemble eddies of different sizes.

Recall that an evolution equation for the 2nd order Eulerian structure function can be derived directly from the Navier-Stokes equation [126]. This equation is often referred to as von Kármán-Howarth-Monin (KHM) equation [134, 135] and can be used to derive Kolmogorov's 4/3-Law for the 3rd-order Eulerian velocity structure function, $D_{LLL}(r) = -\frac{4}{3}\epsilon r$, at intermediate length scales r, where ϵ is again the turbulent kinetic energy dissipation rate [136]. We note that in the present work 3rd-order structure functions were calculated, but the uncertainties were too large for any structure to be seen.

It is desired that an equivalent equation be derived for porous media flows, but it is unclear if this is possible. Such an equation would likely require information on the geometry of the media, and thus a general form may not exist. It may be that for homogeneous pore spaces, such as the 2 mm cases shown here, a simplified solution exists, and this could be why power-law scaling appears to exist for the Eulerian structure functions of the 2 mm cases and not the 2,4 mm case. These and other musings on theoretical descriptions of flow in porous media are left to future work.

8.3 Concluding Remarks

A novel method for PEPT with multiple tracers has been introduced, tested, and used for measurements ranging from individual-cell tracking to secondary flow identification in twisted tape swirled flow. This method has been demonstrated for tracking over 80 particles simultaneously, and in theory allows for the tracking of an arbitrary number of tracers. This creates many new opportunities for the use of PEPT for flow measurement in systems where optical flow measurements are prohibitively difficult. With further advancements of this

method along with the advent of novel detectors and tracers for PEPT, it is possible that this technique will become widely used in the experimental fluid dynamics community.

In the experiment detailed herein, PEPT was used to confirm the nature of random walk statistics in porous media. It is seen that as tracers move across beads in each test section, the probability distributions of their transit times have long tails, indicating the presence of long waiting times between each step. This leads to the non-Fickian dispersion of particles observed in this work, but it is not clear if there exists a direct correspondence between the decay exponents of the transition time distributions and the scaling regimes of the tracer spreading. Establishment of such a connection is left to future work. Furthermore, it is observed that at late times, Fickian spreading is recovered, likely due to the influence of molecular diffusion processes.

Finally, we observe scaling regimes in both Eulerian and Lagrangian velocity structure functions that have not been previously presented. A universal scaling law may be present in the axial Lagrangian structure function, and a scaling regime appears to exist in the Eulerian structure functions of the single-bead cases. These both warrant further experimental and theoretical investigation.

The author is grateful to his advisors, committee members, coworkers, and all who have aided in this research in any manner. To anyone who has read this work, either in part or in whole, I thank you for your time and attention, and I hope that this work has served its purpose as a tool for your study, your work, or simply the whetting of your curiosity.

Bibliography

[1] R. Kotzé et al. Optimisation of pulsed ultrasonic velocity system and transducer technology for industrial applications. *Ultrasonics*, 53:459, 2013. 1

[2] N.P. Ramskill et al. Magnetic resonance velocity imaging of gas flow in a diesel particulate filter. *Chem. Engr. Sci.*, 158:490, 2017. 1

[3] U. Hampel et al. High resolution gamma ray tomography scanner for flow measurement and non-destructive testing applications. *Rev. Sci. Instr.*, 78(10374):1, 2007. 1

[4] H. Bashiri et al. Investigation of turbulent fluid flows in stirred tanks using non-intrusive particle tracking technique. *Chem. Engr. Sci.*, 140:233, 2016. 1

[5] M. Sahimi. Flow phenomena in rocks: form continuum models to fractals, percolation, cellular automata, and simulated annealing. *Rev. Mod. Phys*, 64(4):1393, 1993. 2, 14

[6] R. F. Shaw. Signalling particles for introduction into blood flowing through a vessel of interes. U.S. Patent No. 4,224,303, 1980. 3, 70

[7] D. J. Parker et al. Positron emission particle tracking - a technique for studying flow within engineering equipment. *Nucl. Instr. Meth. Phys. Res. A*, 326:592, 1993. 5, 42, 44, 46

[8] Z. Yang et al. Multiple-particle tracking - an improvement for positron particle tracking. *Nucl. Instr. Meth. Phys. Res. A*, 564:332, 2006. 6, 8, 24, 175

[9] Y. F. Chang et al. Using a pet camera to track individual phases in process equipment with high temporal and spatial resolutions: Algorithm development. In *2012 IEEE International Instrumentation and Measurement Technology Conference Proceedings*, 2012. 6, 7, 9

[10] Y. F. Chang and A. C. Hoffman. A lagrangian study of liquid flow in a reverse-flow hydrocyclone using positron emission particle tracking. *Exp. Fluids*, 56(4):1, 2015. 7, 9, 105

[11] M. Bickell et al. A new line density tracking algorithm for pept and its application to multiple tracers. *Nucl. Instr. Meth. Phys. Res. A*, 682:36, 2012. 7, 24, 25, 27, 42, 44

[12] R. D. WIldman et al. Single-particle motion in three-dimensional vibrofluidized granular beds. *Phys. Rev. E*, 62(3):3826, 2000. 8

[13] F. Chiti et al. Using positron emission particle tracking (pept) to study the turbulent flow in a baffled vessel agitated by a rushton turbine: Improving data treatment and validation. *Chem. Engr. Res. Des.*, 89:1947, 2011. 8

[14] W. D. Griffiths et al. The use of positron emission particle tracking (pept) to study the movement of inclusions in low-melting-point alloy castings. *Metallurg. Mat. Trans. B*, 43B:370, 2011. 8

[15] O. Mihailova et al. Laminar mixing in a smx static mixer evaluated by positron emission particle tracking (pept) and magnetic resonance imaging (mri). *Chem. Engr. Sci.*, 137:1014, 2015. 8

[16] R. Pérez-Mohedano et al. Positron emission particle tracking (pept) for the anaylsis of water motion in a domestic dishwasher. *Chem. Engr. J.*, 259:724, 2015. 8, 9

[17] D. Boucher et al. Observation of iron ore beneficiation within a spiral concentrator by positron emission particle tracking of large (ϕ=1440 μm) and small (ϕ= 58μm) hematite and quartz tracers. *Chem. Engr. Sci.*, 140:217, 2016. 8

[18] D. J. Parker. Positron emission particle tracking and its application to granular media. *Rev. Sci. Instr.*, 88:051803, 2017. 8, 12, 14

[19] Z. Yang et al. Study on solids translational and rotational motions in rotating cans. *LWT-Food Sci. Technol.*, 57:383, 2014. 8, 175

[20] T. S. Volkwyn et al. Studies of the effect of tracer activity on time-averaged positron emission particle tracking measurements on tumbling mills at pept cape town. *Minerals Engr.*, 24:261, 2011. 8, 13

[21] A.J. Morrison et al. The shape and behaviour of a granular bed in a rotating drum using eulerian flow fields obtained from pept. *Chem. Engr. Sci.*, 152:186, 2016. 8

[22] Y. F. Chang et al. Pept: An invaluable tool for 3-d particle tracking and cfd simulation verification in hydrocyclone studies. *EPJ Web Conf.*, 50:05(001):1, 2013. 9

[23] B.V. Balakin et al. Non-invasive studies of multiphase flow in process equipment. positron emission particle tracking technique. *IOP Conf. Ser.: J. Phys.: Conf. Ser.*, 281(012039):1, 2017. 9

[24] C. W. Chou. Application of pept to track a single labelled red blood cell in vitro. Master's thesis, University of Birmingham, 2006. 9

[25] K. S. Lee et al. Single-cell tracking with pet using a novel trajectory reconstruction algorithm. *IEEE Trans. Med. Imag.*, 34(4):994, 2015. 9, 39, 71, 179

[26] Y. Ouyang et al. Evaluation of a bgo-based pet system for single-cell tracking performance by simulation and phantom studies. *Mol. Imag.*, 15:1, 2016. 10, 71

[27] L. Jodal et al. Positron range in pet imaging: an alternatice approach for assessing and correcting the blurring. *Phys. Med. Biol.*, 57:3931, 2012. 10

[28] L. Jodal et al. Positron range in pet imaging: non-conventional isotopes. *Phys. Med. Biol.*, 59:7419, 2014. 10

[29] X. Fan et al. Labelling a single particle for positron emission particle tracking using direct activation and ion-exchange techniques. *Nucl. Instr. Meth. Phys. Res. A*, 562: 345, 2006. 11, 12, 86, 87

[30] D. J. Parker and X. Fan. Positron emission particle tracking - application and labelling techniques. *Particuology*, 6:16, 2008. 11

[31] Q. Bao et al. Performance evaluation of the inveon dedicated pet pre- clinical tomograph based on the nema nu-4 standards. *J. Nucl. Med.*, 50:401, 2009. 12, 39, 77, 82, 84

[32] A. Nissan and B. Berkowitz. Inertial effects on flow and transport in heterogeneous porous media. *Phys. Rev. L.*, 120(054504):1, 2018. 15

[33] Z. Zeng and R. Grigg. A criterion for non-darcy flow in porous media. *Transp. Por. Med.*, 63:57, 2006. 15

[34] M. Levy and B. Berkowitz. Measurement and analysis of non-fickian dis- persion in heterogeneous porous media. *J. Contaminant Hydrology*, 64:203, 2003. 15, 19, 20, 22, 137, 182

[35] D. del Castillo-Negrete et al. Nondiffusive transport in plasma turbulence: A fractional diffusion approach. *Phys. Rev. Letters*, 94(065003):1, 2005. 15

[36] Q. Yuan et al. Nonlinear simulation of miscible displacements with concentration-dependent diffusion coefficient in homogeneous porous media. *Chem. Engr. Sci.*, 172: 528, 2017. 15

[37] K. Pearson. The problem of the random walker. *Nature*, LXXII:294, 1905. 16

[38] F. Reif. *Fundamentals of Statistical and Thermal Physics*. Waveland Press, Inc., 1st edition, 2009. 16

[39] B. Berkowitz and H. Scher. Anomalous transport in random fracture networks. *Phys. Rev. Letters*, 79(20):4038, 1997. 17, 20

[40] B. Berkowitz et al. Anomalous transport in laboratory-scale, heterogeneous porous media. *Water Resources Res.*, 36(1):149, 2000. 17, 19, 20, 21

[41] E. W. Montroll and H Scher. Random walks on lattices. iv. continuous- time walks and influence of absorbing boundaries. *J. Stat. Phys*, 9(2):101, 1973. 17

[42] H. Scher and E. W. Montroll. Anomalous transit-time dispersion in amor- phous solids. *Phys. Rev. B*, 12(6):2455, 1975. 18

[43] Y. Edery et al. Anomalous reactive transport in porous media: Experiments and modeling. *Phys. Rev. E*, 91:052130–1, 2015. 20, 21, 88, 144, 182

[44] S. E. Silliman. Laboratory evidence of the scale effect in solute transport through saturated porous media. Master's thesis, Univ. of Arizona, Tucson, 1981. 20

[45] S. E. Silliman and E. S. Simpson. Laboratory evidence of the scale effect in dispersion of solutes in porous media. *Water Resources Res.*, 23(11):2145, 1987. 20, 21

[46] M. Moroni and J. H. Cushman. Statistical mechanics with three-dimensional particle tracking velocimetry experiments in the study of anomalous dispersion. ii. experiments. *Phys. Fluids*, 13(1):81, 2001. 22, 76, 181

[47] M. Holzner et al. Intermittent lagrangian velocities and accelerations in three-dimensional porous medium flow. *Phys. Rev. E*, 92(013015):1, 2015. 22, 23, 76, 130, 133, 181, 183

[48] C. Wiggins et al. A novel clustering approach to positron emission particle tracking. *Nucl. Instr. Meth. Phys. Res. A*, 811:18, 2016. 25, 48, 115

[49] J. MacQueen. Some methods for classification and analysis of multivariate observations. In *Proc. of Fifth Berkeley Symposium on Mathematics Statistics and Probability*, 1967. 25

[50] G. Hamerly and C. Elkan. Learning the k in k-means. In *Proc. of Advances in Neural Information Processing Systems 16*, 2003. 25

[51] H. Anton. *Elementary Linear Algebra*. Wiley and Sons, Inc, 10th edition, 2010. 26

[52] T. Anderson and D. Darling. Asymptotic theory of certain 'goodness of fit' criteria based on stochastic processes. *Ann. Math. Stat.*, 23:193, 1952. 26

[53] M. A. Stephens. Edf statistics for goodness of fit and some comparisons. *J. Am. Stat. Assoc.*, 69:730, 1974. 27, 32

[54] Y. C. Tai et al. Performance evaluation of the micropet p4: a pet system dedicated to animal imaging. *Phys. Med. Biol.*, 46:1845, 2001. 27, 29, 50

[55] C. Wiggins et al. A feature point identification method for positron emission particle tracking with multiple tracers. *Nucl. Instr. Meth. Phys. Res. A*, 843:22, 2017. 32, 36, 115

[56] S. Tong et al. Image reconstruction for pet/ct scanners: past achieve- ments and future challenges. *Imaging Med.*, 2:529, 2010. 32

[57] J. C. Crocker and D.G. Grier. Methods of digital video microscopy for col- loidal studies. *J. Colloid Interf. Sci.*, 179:298, 1996. 32, 34

[58] I. F. Sbalzarini and P. Koumoutsakos. Feature point tracking and trajectory analysis for video imaging in cell biology. *J. Struct. Biol.*, 179:298, 2005. 32, 34, 50

[59] M. R. Brady. Subpixel resolution schemes for multiphase flows. Master's thesis, Virginia Polytechnic Institute and State University, 2006. 36

[60] S. Jan et al. Gate: a simulation toolkit for pet and spect. *Phys. Med. Biol.*, 49:4543, 2004. 39, 179

[61] S. Lee et al. Development and validation of a complete gate model of the siemens inveon trimodal imaging platform. *Mol. Imag.*, 12:1, 2013. 39, 179

[62] L. Lu et al. Performance evaluation of the inveon pet scanner using gate based on the nema nu-4 standards. In *Proceedings of IEEE Nuclear Science Sym- posium and Medical Imaging Conference*, 2013. 39, 179

[63] W. W. Moses. Fundamental limits of spatial resolution in pet. *Nucl. Instr. Meth. Phys. Res. A*, 648:S236, 2011. 46, 105, 106, 110, 176, 178

[64] G. A. Voth et al. Measurement of particle accelerations in fully developed turbulence. *J. Fluid Mech.*, 469(121), 2002. 46, 133, 181

[65] N. Mordant et al. Experimental lagrangian acceleration probability density function measurement. *Phycisa D*, 193:245, 2004. 46, 133, 181

[66] J. Berg et al. Experimental lagrangian structure functions in turbulence. *Phys. Rev. E*, 80:026316, 2009. 46, 111, 143, 181

[67] H. Kuhn. The hungarian method for the assignment problem. *Nav. Res. Logist. Q.*, 2: 83, 1955. 49

[68] H. Kuhn. Variants of the hungarian method for assignment problems. *Nav. Res. Logist. Q.*, 3:253, 1956. 49

[69] J. Munkres. Algorithms for the assignment and transportation problems. *J. Soc. Ind. Appl. Math.*, 5:32, 1957. 49

[70] Y. A. Hassan and R. E. Canaan. Full-field bubbly flow velocity measurements using a multiframe particle tracking technique. *Exp. Fluids*, 12:49, 1991. 49

[71] S. J. Baek and S. J. Lee. A new two-frame particle tracking algorithm using match probability. *Exp. Fluids*, 22(1):23, 1996. 49

[72] K. Ohmi and H. Y. Li. Particle-tacking velocimetry with new algorithms. *Meas. Sci. Technol.*, 11(6):603, 2000. 49

[73] N. Patel et al. Positron emission particle tracking in pulsatile flow. *Exp. Fluids*, 58 (42):1, 2017. 49, 205, 206

[74] S. Langford et al. Positron emission particle tracking (pept) for fluid flow measurements. *Nucl. Engr. Des.*, 302:81, 2016. 53

[75] S. Langford et al. Positron emitting particle tracking (pept) for fluid flow measurements. In *Proc. of American Nuclear Societ Student Conference 2015*, 2015. 54

[76] E. Clark et al. Multiphysics analysis of the wendelstein 7-x actively cooled scraper element. *Fus. Sci. Technol.*, 68:635, 2015. 55

[77] A. Cardella et al. Design, manufacturing and thermo-mechanical testing of a relevant size monoblock divertor prototype. In *Proc. 18th Sump. on Fusion Technology*, volume 1, page 283, 1994. 55

[78] E. Clark et al. Computational investigatin of the thermal-hydraulic performance for twisted tape enabled high heat flux components. *Fus. Sci. Technol.*, 72:278, 2017. 55

[79] E. B. Clark. *Computational Thermal-Hydraulics Modeling of Twisted Tape Enabled High Heat Flux Components*. PhD thesis, Univ. of Tennessee, 2017. 55

[80] A. Hasanpour et al. A review study on twisted tape inserts on turbulent flow heat exchangers: The overall enhancement ratio criteria. *Internat. Comm. Heat Mass Transfer*, 55:53, 2014. 56

[81] C. Wiggins et al. Qualification of multiple-particle positron emission particle tracking (m-pept) technique for measurements in turbulent wall-bounded flow. *Chem. Engr. Sci.*, 204:246, 2019. 60, 87, 105, 175

[82] O. Reynolds. An experimental investigation of the circumstances which determine whether the motion of water shall be direct of sinuous, and of the law of resistance in parallel channel. *Proc. Royal Soc. London*, 35:84, 1883. 60

[83] M. Hultmark et al. Turbulent pipe flow at extreme reynolds numbers. *Phys. Rev. Letters*, 108(094501):1, 2012. 60

[84] M. Hultmark et al. Logarithmic scaling of turbulence in smooth- and rough-walled pipe flow. *J. Fluid Mech.*, 728:376, 2013. 60

[85] B. J. Rosenberg et al. Turbulence spectra in smooth- and rough- wall pipe flow at extreme reynolds numbers. *J. Fluid Mech.*, 731:46, 2013. 60

[86] X. Wu and P. Moin. A direct numerical simulation study on the mean velocity characteristics in trubulent pipe flow. *J. Fluid Mech.*, 608:81, 2008. 60, 61, 63, 64, 65, 66

[87] G. K. El Khuory et al. Direct numerical simulation of turbulent pipe flow at moderately high reynolds numbers. *Flow Turb. Combust.*, 91:475, 2013. 60, 61, 63, 64, 65, 66, 67

[88] N. Stelzenmuller et al. Lagrangian acceleration statistics in a turbulent channel flow. *Phys. Rev. Fluids*, 2(054602):1, 2017. 60, 66, 68, 69

[89] S. T. Langford et al. Three-dimensional spatiotemporal tracking of fluorine- 18 radiolabeled yeast cells via positron emission particle tracking. *PLoS ONE*, 12(7): e0180803, 2017. 61, 71, 175

[90] M. Zagarola and A.J. Smits. Mean-flow scaling of turbulent pipe flow. *J. Fluid Mech.*, 373:33, 1998. 63

[91] J. L. G. Oliveira et al. Lagrangian and eulerian statistics of pipe flows mea- sured with 3d-ptv at moderate and high reynolds numbers. *Flow Turb. Combust.*, 91:105, 2013. 68

[92] N. Adonai et al. vivo cell labeling with 64cu– pyruvaldehyde-bis(n4-methylthiosemicarbazone) for imaging cell trafficking in mice with positron-emission tomography. *Proc. Nat. Acad. Sci.*, 99:3030, 2002. 70

[93] R. J. Melder et al. A method for labelling cells for positron emissino tomograpy (pet) studies. *J. Immun. Meth.*, 175:79, 1994. 70

[94] A. Aicher et al. Assessment of the tissue dis- tribution of transplanted human endothelial progenitor cells by radioactive labeling. *Circ.*, 107:2134, 2003. 70

[95] Y. Zhang et al. 18f-fdg cell labeling may underestimate transplanted cell homing: more accurate, efficient, and stable cell labeling with hexadecyl-4-[18f]fluorobenzoate for in vivo tracking of transplanted human progenitor cells by positron emission tomography. *Cell Transpl.*, 21:1821, 2012. 70, 75

[96] B. Ma et al. A simple method for stem cell labelling with fluorine 18. *Nucl. Med. Biol.*, 32:701, 2005. 70, 75

[97] A. L. Goertzen et al. On the imaging of very weak sources in an lso pet scanner. In *Proc. of IEEE Nuclear Science Symposium 2006*, 2006. 71, 72, 82

[98] S. Li. et al. Eukaryotic resistance to fluoride toxicity mediated by a widespread family of fluoride export proteins. *Proc. Nat. Acad. Sci.*, 110:19018, 2013. 71

[99] *A General Monte Carlo N-Particle (MCNP) Transport Code.* Los Alamos National Laboratory, 2016. 74

[100] N. A. R. Gow and B. Yadav. Microbe profile: candida albicans: a shape-changing, opportunistic pathogenit fungus of humans. *Microbiology*, 163:1145, 2017. 75

[101] P. W. Doherty et al. The use of indium-111 labeled leuiocytes for absecess detection. *Clin. Nucl. Med.*, 3:108, 1978. 75

[102] C. Heyn et al. In vivo mri of cancer cell fate at the single-cell level in a mouse model of breast cancer metastasis to the brain. *Magn. Res. Med.*, 56:1001, 2006. 75

[103] M.F. Kircher et al. Noninvasive cell-tracking methods. *Nat. Rev. Clin. Oncol.*, 8:677, 2011. 75

[104] *Inveon Operator Manual: Inveon Scanners and Inveon Acquisition Workplace 2.0.* Siemens Medical Solutions USA, Inc., 2014. 77, 82

[105] B. E. Atkins et al. A data acquisition, event processing and coincidence determination module for a distributed parallel processing architecture for pet and spect imaging. In *Proc. of IEEE Nuclear Science Symposium 2006*, 2006. 77, 79, 80, 81

[106] R. A. Mintzer and S. B. Siegel. Design and performance of a new pixelated- lso/pspmt gamma-ray detector for high resolution pet imaging. In *Proc. of IEEE Nuclear Science Symposium 2007*, 2007. 77, 78, 79

[107] S. S. Gleason et al. A new highly versatile multimodality small animal imaging platform. In *Proc. of IEEE Nuclear Science Symposium 2006*, 2006. 77

[108] D. Hu et al. A neural network based algorithm for building crystal look- up table of pet block detector. In *Proc. of IEEE Nuclear Science Symposium 2006*, 2006. 77

[109] D. F. Newport et al. Quicksilvertm : A flexible, extensible, and high-speed architecture for multi-modality imaging. In *Proc. of IEEE Nuclear Science Symposium 2006*, 2006. 77, 78, 79

[110] M. W. Lenox et al. Digital time alignment of high resolution pet inveon block detectors. In *Proc. of IEEE Nuclear Science Symposium 2006*, 2006. 77

[111] A. R. McFarland et al. Continuously sampled digital pulse processing for inveon small animal pet scanner. In *Proc. of IEEE Nuclear Science Symposium 2007*, 2007. 77

[112] A. R. McFarland et al. A compactpci based event routing subsystem for pet and spect data acquisition. In *Proc. of IEEE Nuclear Science Symposium 2006*, 2006. 77, 81

[113] R. A. Santos Torres. *Evaluation of Inveon Pre-Clinical Positron Emission Tomography (PET) Scanner Geant4 Application for Tomographic Imaging (GATE) Model for Multi-Positron Emission Particle Tracking (M-PEPT)*. PhD thesis, Univ. of Tennessee, 2017. 81, 83, 179

[114] A. Rosato et al. Why the brazil nuts are on top: Size segregation of particulate matter by shaking. *Phys. Rev. Letters*, 58(10):1038, 1987. 94

[115] J. F. Swindells et al. Viscosities of sucrose solutions at various temperatures: Tables of recalculated values. Technical report, United States Department of Commerce, 1958. 96

[116] E. M. Moore. Positron emission particle tracking software maturation project. Master's thesis, Univ. of Tennessee, 2017. 103

[117] C. Willert. Stereoscopic digital particle image velocimetry for application in wind tunnel flows. *Meas. Sci. Technol.*, 8:1465, 1997. 105

[118] S. M. Soloff et al. Distrotion compensation for generalized stereoscopic particle image velocimetry. *Meas. Sci. Technol.*, 8:1441, 1997. 105

[119] C. W. H. Van Doorne and J. Westerweel. Measurement of laminar, transitional and trubulent pipe flow using stereoscopic-piv. *Exp. Fluids*, 42:259, 2007. 105, 107

[120] S. Gesemann et al. From noisy particle tracks to velocity, acceleration and pressure fields using b-splines and penalties. In *18th International Symposium on the Application of Laser and Imaging Techniques to Fluid Mechanics*, 2016. 112

[121] J. M. Lawson et al. Bias in particle tracking acceleration measurement. *Exp. Fluids*, 59(172):1, 2018. 112

[122] D. McWhirter et al. Magnetohydrodynamic flows in porous media ii: Experimental results. *Fus. Technol.*, 34(1):187, 1998. 129

[123] A. Lachhab et al. Particle tracking experiments in match-index-refracton porous media. *Ground Water*, 46(6):865, 2008. 129

[124] P. K. Kang et al. Pore-scale intermittent velocity structure underpinning anomalous transport through 3-d porous media. *Geophys. Res. Let.*, 41:6184, 2014. 144, 151, 181, 182

[125] A. N. Kolmogorov. The local structure of turbulence in incompressible viscous fluid for very large reynolds numbers. *Proc. USSR Acad. Sci.*, 30:299, 1941. 159, 168, 169

[126] P. C. Valente and J. C. Vassilicos. The energy cascade in grid-generated non-equilibrium decaying turbulence. *Phys. Fluids*, 27(045103):1, 2015. 168, 184

[127] D Schanz et al. Shake-the-box: Lagrangian particle tracking at high particle image densities. *Exp. Fluids*, 57(70):1, 2016. 179

[128] M. Herald et al. Simulated time-dependent data to estimate uncertainty in fluid flow measurements. *Nucl. Engr. Des.*, 337:221, 2018. 179

[129] Z. Gu et al. Performance evaluation of g8, a high-sensitivity benchtop preclinical pet/ct tomograph. *J. Nucl. Med.*, 60(1):142, 2019. 180

[130] J. Bec et al. Acceleration statistics of heavy particles in turbulence. *J. Fluid Mech.*, 550:349, 2006. 180, 181

[131] J. de Jong et al. Measurement of inertial particle clustering and relative velocity statistics in isotropic turbulence using holographic imaging. *Internat. J. Multiph. Flow*, 36:324, 2010. 180

[132] J. P. L. C. Salazar and L. R. Collins. Inertial particle relative velocity statistics in homogeneous isotropic turbulence. *J. Fluid Mech.*, 696(45), 2012. 180

[133] S. B. Pope. *Turbulent Flows*. Cambridge University Press, 2003. 184

[134] T. von Kármán and L. Howarth. On the statistical theory of isotropic turbulence. *Proc. Royal Soc. London A*, 164(917):192, 1938. 184

[135] A. S. Monin and A. M. Yaglom. *Statistical Fluid Mechanics*, volume II. MIT Press, 1975. 184

[136] A. N. Kolmogorov. Dissipation of energy in locally isotropic turbulence. *Proc. USSR Acad. Sci.*, 32:16, 1941. 184

[137] S. T. Langford. Jet flow validation of positron emission particle track- ing utilizing high speed video. Master's thesis, Univ. of Tennessee, 2016. 201

[138] S. Langford et al. Positron emission particle tracking (pept) validation for jet flow. In *Proc. of the 24th International Conference on Nuclear Engineering*, 2016. 201

[139] N. Patel. A characterization of pulsatile flow by positron emission particle tracking. Master's thesis, Univ. of Tennessee, 2017. 205

Appendices

A Other M-PEPT Experiments

A number of other PEPT experiments have been performed at the University of Tennessee during the author's tenure. While these do not highlight specific capabilities of M-PEPT reconstruction, like those described in Chapter 4, they do show some of the possible applications of PEPT. These experiments have been performed by many members of the research group of Arthur Ruggles, and in all cases, the author analyzed list mode data using M-PEPT to reconstruct particle trajectories. Brief descriptions of each experiment follow.

A.1 Channel with Baffle Plates

The second experiment in which G-means was used for reconstruction was a measurement of the flow of water between a series of baffle plates in a rectangular channel. This work was the subject of a Master's Thesis by Seth Langford [137] and of a conference paper [138] by Langford and others, including the current author. The author was involved in performing the experiment and analyzed list mode files to reconstruct particle trajectories.

In this study, flow of water at volume flow rate 0.62 L/s (Re=23,500 in constrained region) was driven by pump, and PEPT measurements were made with a Siemens Inveon Preclinical PET scanner. Ion exchange resins were activated to ∼1 mCi per particle with ^{18}F and used in this study. Data were collected for 30 minutes.

G-means was used with an A-D critical value of 20, 2×2×2 mm^3 grid, and time steps of 1 ms to reconstruct trajectories. A total of ∼4,000 trajectories were reconstructed, as seen in Figure A.2. Here, one observes acceleration of trajectories in the restricted region and a large recirculation region between the baffle plates.

An optical PTV study was performed to test the efficacy of the PEPT measurement. Velocities were calculated from divided differences of the trajectories and averaged onto a 2-D Eulerian (spatially fixed) grid as described in [137]. The time-averaged downstream velocity measured by each technique is shown in Figure A.3. It is found that both PEPT and PTV measured similar mean-flow characteristics throughout the region of interest in the test section. This validation against an established optical flow diagnostic technique

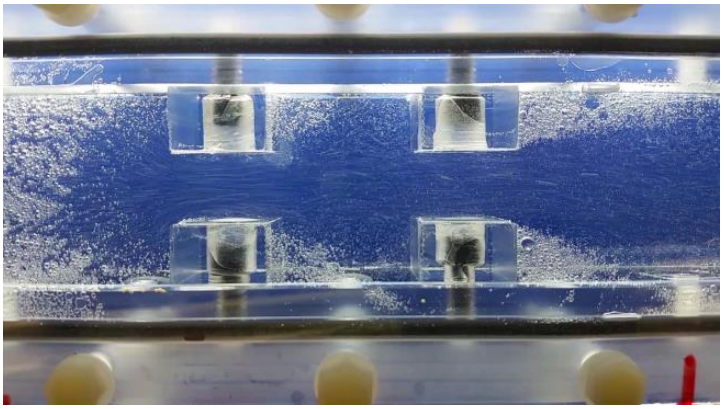

Figure A.1: Test section region of interest in baffle flow experiment.

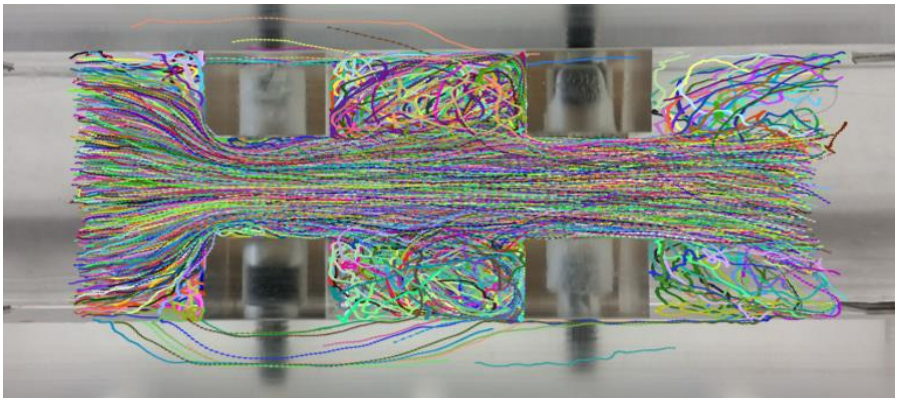

Figure A.2: Trajectories of particles in baffle induced flow. Trajectories outside of flow region are from particles traversing gap between test section walls and lid.

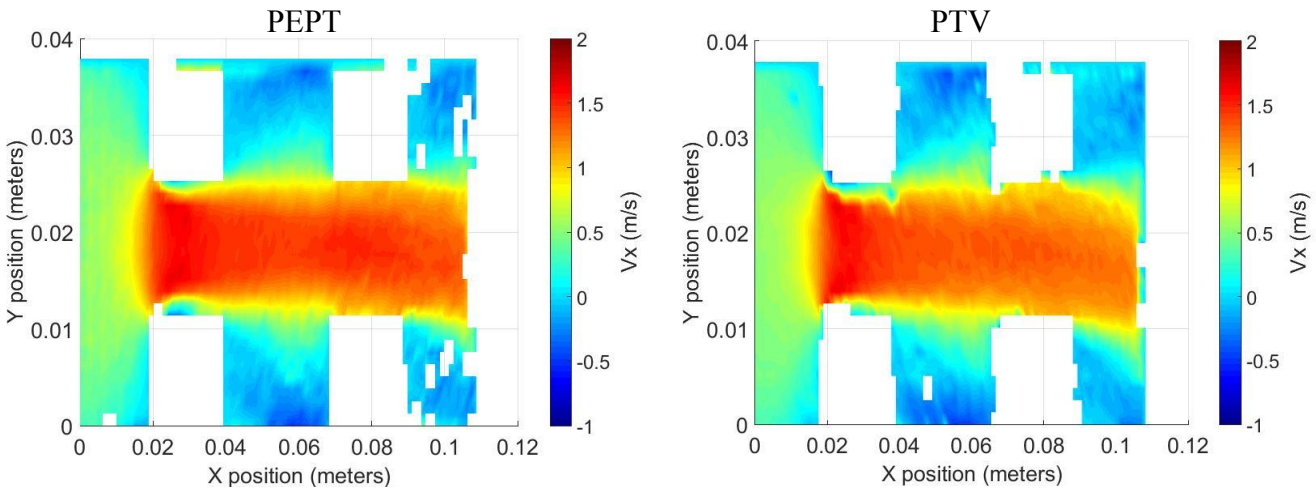

Figure A.3: Time-averaged downstream (x-) velocity measured via PEPT (left) and PTV (right) in baffle flow experiment. In this figure, the x-direction is the downstream direction, and the y-direction is the horizontal transverse.

demonstrated the utility of this PEPT technique for measurements in turbulent flow with complex geometry and steep velocity and acceleration gradients.

A.2 Heat Exchanger

The first experiment conducted in an opaque test section using our M-PEPT methods was a study of flow in the shell-side of a stainless steel, tube-in-shell heat exchanger. The author did not participate in the conducting of this experiment but performed all trajectory reconstruction and subsequent analysis. Photographs of this heat exchanger are seen in Figure A.4. Note that on the shell-side, flow goes around these tubes and not through them, creating very complicated flow paths. The outer shell of this heat exchanger is approximately 1/4-inch thick.

In this study, ion exchange resins of diameter 690 μm and activity $\sim$1 mCi were used as flow tracers. It was found that these often got stuck in the test section, so density-matching was used to mitigate this defect. A sucrose solution of density 1.225 g/cc was used as the working fluid, and flow was pumped through the test section with a Reynolds number of 2,300. An 8-minute scan of this flow apparatus was performed with Siemens Inveon PET scanner.

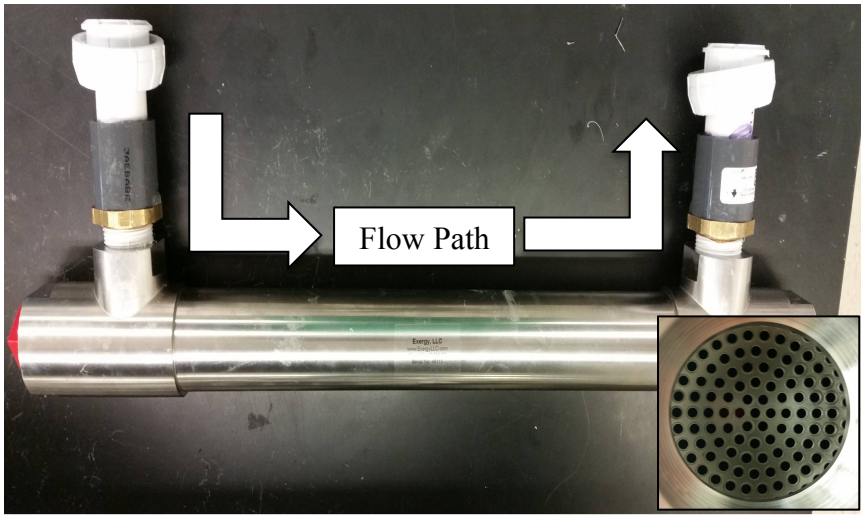

Figure A.4: Photograph of stainless steel heat exchanger studied via PEPT. Inset photo shows structure of tubes.

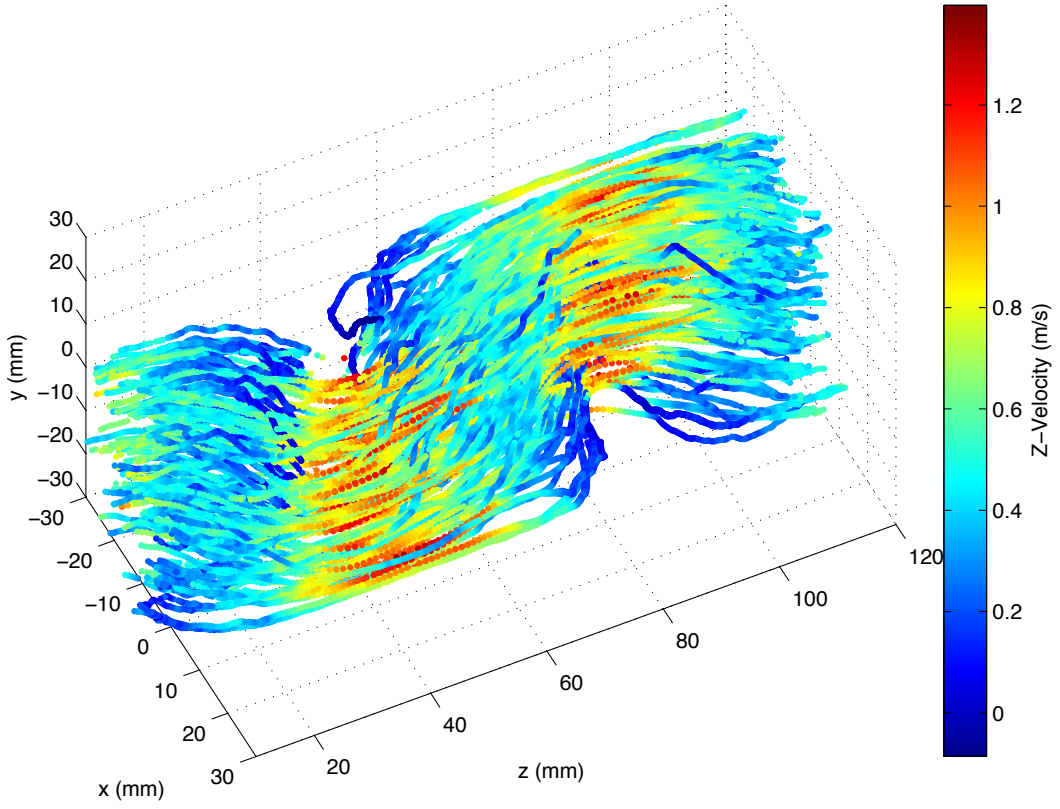

Figure A.5: Trajectories measured in heat exchanger experiment, colored by downstream velocity.

Trajectories were reconstructed using the FPI method with 1 ms time steps, and trajectories were filtered and differentiated via convolution with the kernels described by Equations 3.12 and 3.13. The measured trajectories, colored by downstream velocity, are shown in Figure A.5. These trajectories reveal the presence of structural baffle plates in the test section that were unknown to the researchers before this study. PEPT captures the acceleration of the flow as it passes around these baffles and the complicated paths taken by particles as they pass around the tubes. This experiment demonstrated the ability of PEPT to image complex flow structures in a stainless steel system. This capability is portable to more detailed studies of flow in heat exchangers and other engineering equipment.

A.3 Pulsatile Flow

Pulsatile flow was examined with PEPT to test the efficacy of the method for measurements of blood flow. This work has been detailed in a Master's Thesis by Nitant Patel [139] and in a publication by Patel et al. [73]. The current author was involved in the planning and conducting of this experiment, performed M-PEPT trajectory reconstruction, and assisted in subsequent analysis of this experiment.

In this work, pulsatile flow of water was studied in an elastic tube of inner diameter 19 mm (3/4-inch). This tube size is comparable to the size of an adult human aorta. The tube was studied in both an open and "pinched" configuration (see Figure A.6) to simulate flow in an artery with and without stenosis. Ion exchange resins of activity ∼0.2 mCi were used for these experiments, and scans were performed with a Siemens Inveon PET scanner for 50 minutes (pinched geometry) and 65 minutes (open geometry). Flow was driven by pump at a Reynolds number of ∼20,000, based on the diameter of the unpinched tube.

Pulsing was generated at frequency 2 Hz by the rotation of a motorized ball valve upstream of the test section. Reflective tape was attached to the shaft of the valve drive, and a laser photodiode was used to send trigger signals to the PET scanner with each rotation of the ball valve. Trigger words are inserted into the coincidence event listmode stream with each signal, and these were used to segment the reconstructed data into pulse cycles.

Data were reconstructed using the FPI method with 1 ms time steps. After reconstruction, data were sorted into 20 temporal bins depending on their place within each pulse cycle



Figure A.6: Elastic tube pinched with spring clamp in pulsatile flow experiment.

(i.e. the time since the most recent trigger event). Trajectories from frames corresponding to full flow, flow reversal, and flow recovery are shown in Figure A.7 (open geometry) and Figure A.8 (pinched geometry). The reader is referred to the online version of the original work by Patel et al. [73] for animations of the flow pulsing.

These trajectories show interesting features within the pulse cycle. In both cases, full flow reversal was seen when the valve closes. In the pinched geometry case, a large recirculation region was seen downstream of the obstruction, and mean axial flow remained negative in this region throughout the pulse cycle. Flow modulation downstream of the obstruction persisted beyond the field of view of the scanner.

This experiment demonstrated the applicability of PEPT for pulsatile flow studies, including hemodynamics, and was the first PEPT experiment conducted in a transient flow system. As PEPT does not require optical clarity, surrogate fluids are not needed, and experiments can be conducted using blood as the working fluid. Furthermore, if a safe bloodborne tracer can be fabricated, PEPT may be used a diagnostic tool for identifying blockages by looking for recirculation regions like the ones noted in the pinched geometry case.

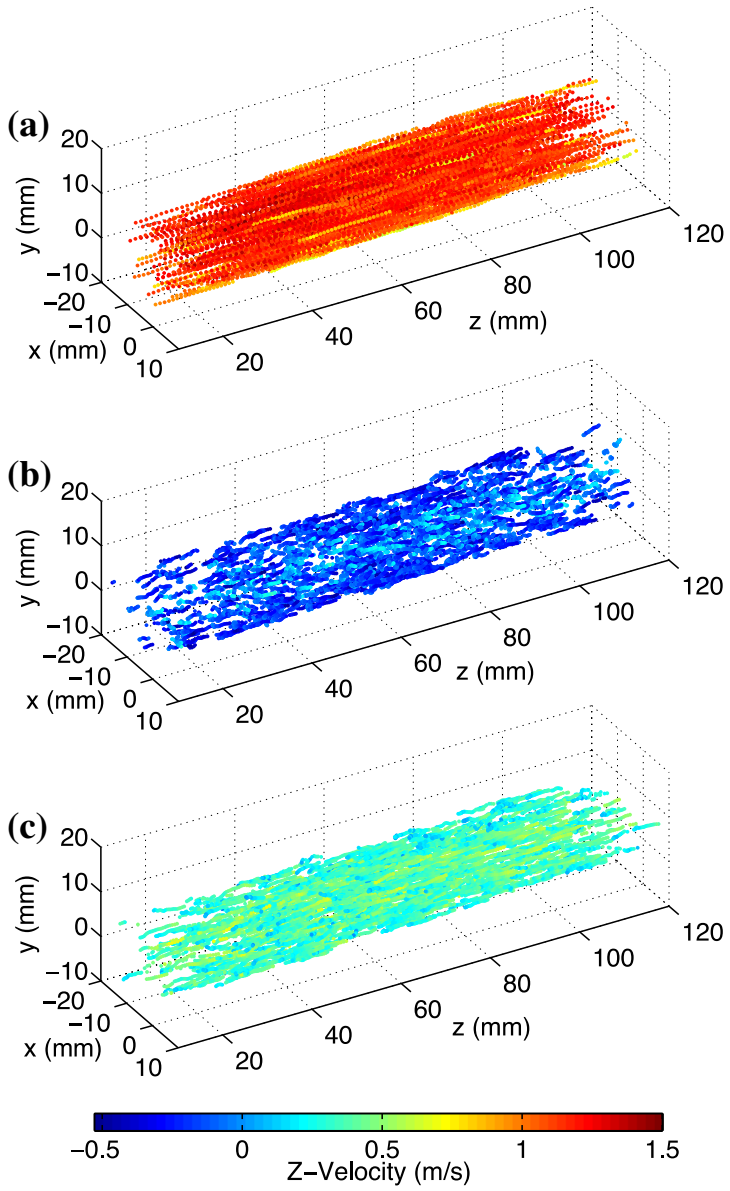

Figure A.7: Trajectories from three frames of pulse cycle from open geometry pulsatile flow experiment, colored by downstream velocity. Frames show full flow (a), flow reversal (b), and flow recovery (c) portions of pulse cycle.

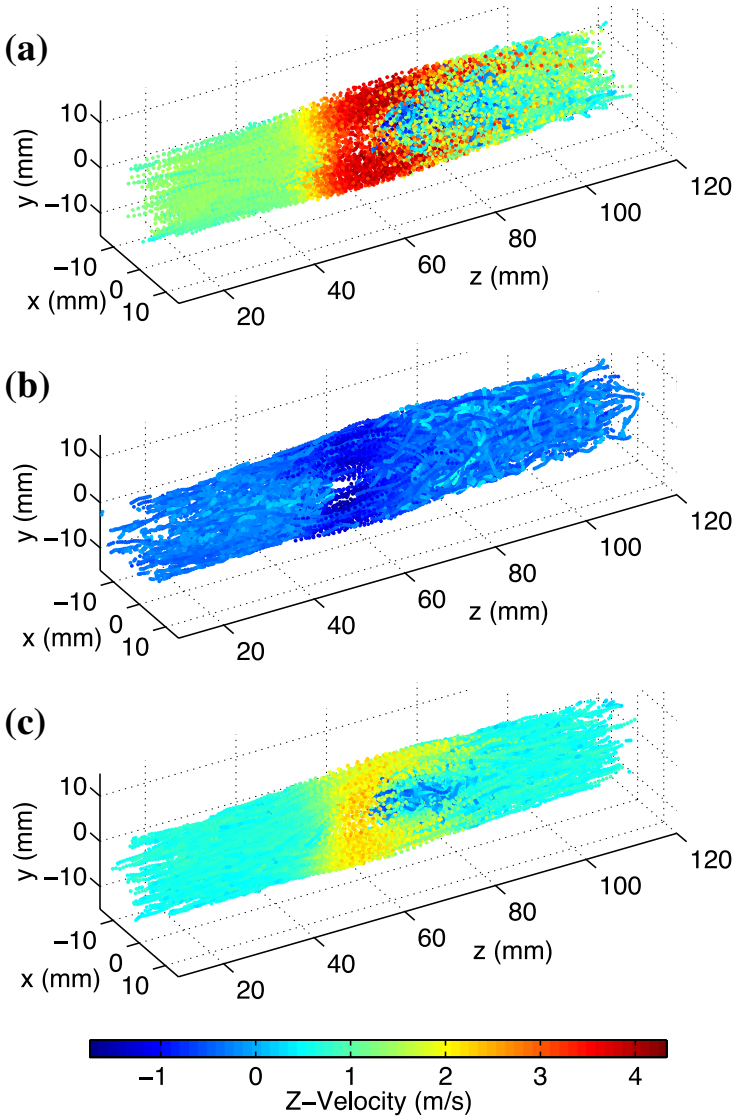

Figure A.8: Trajectories from three frames of pulse cycle from pinched geometry pulsatile flow experiment, colored by downstream velocity. Frames show full flow (a), flow reversal (b), and flow recovery (c) portions of pulse cycle.

B Particle Activation Procedure

The procedure used for activating particles is documented here. As an example, the activation procedure used for the 2 mm packed bed test of October 19, 2018 is included. In this activation, anion exchange resins were activated to 44 μCi per particle at the University of Tennessee Medical Center using the procedures described in Section 5.2. The full procedure follows.

Activation Procedure: 10/19/2018

Goal: 1 tube with ~500 activated particles

Items Needed:

- Small (5-50 uL) Pipette
- Large (100-1000 uL) Pipette
- Small and Large Pipette tips
- Microcentrifuge
- Supply of Deionized (DI) Water
- Supply of Sugar DI Water
- 2 Cylindrical Centrifuge Tubes, labeled **C**, **X**
- 2 Conical Eppendorf Tube with filter, labeled **A, B**
- Eppendorf Tube tray
- Gloves
- Labcoats
- Goggles
- Extra Cylindrical centrifuge tubes
- Counting Well (at Medical Center)
- Bottle with 100 mL Deionized Water, labeled **W**
- Rad Waste Bottle
- Calculator
- Tungsten Eppendorf Tube Shield
- Trash Bag(s)
- Saran Wrap
- Bench Paper (at Medical Center)
- Geiger Counter (at Medical Center)

Procedure

1) Prepare stock solution of particles in tube **A** (Morning of activation)
   - -Prepare particle suspension: ~100 particles/uL in DI sugar water
     - Note: ~4,000 particles per milligram
   - -Transport to UTKMC

2) Preparation (at Medical Center)
   - -Put on gloves
   - -Take initial baseline radiation survey in hot lab
     - -Inspect fume hood, countertop, counting well, bricks
     - -Note any areas of contamination; cover with bench paper
   - -Apply bench paper in hood, if not placed
   - -Apply saran wrap to counting well handle and microcentrifuge
   - -Set up trash bag
   - -Place Geiger counter near counting well for hand checks
   - **NOTE**: Perform hand checks if contamination is suspected
   - -Place Equipment into fume hood
     - -Open all lids

3) Activation

-Change gloves
-Agitate tube **A**
-Move 5 uL (500 particles) from tube **A** onto filter in tube **B**
-Add additional 5 uL of DI water to tube **B**
-Measure activity of syringe
-Inject activation medium into tube **B** (should be ~30 mCi in 30 uL)
-Measure activity remaining in syringe
-Dispose of syringe
-Measure activity of Tube **B**
-Activate for 20 minutes, shaking every few minutes.
    -Change gloves after each agitation
-Add 200 uL DI water to **B**, shake.
-Prepare 230 uL water balance in tube **X** and place in centrifuge
-Centrifuge **B** at 5000 RCF for 40 seconds
-Place 200 uL DI water on filter in tube **B**
-Move filter from tube **B** to tube **A**
-Measure and record activity of wastewater
-Dispose of wastewater
-Rinse bottom of vial **B** and dispose of rinse water
-Place filter back into tube **B**
-**Repeat until wastewater is clean:**
    -Centrifuge **B** at 5000 RCF for 40 seconds
    -Place 200 uL DI water on filter in tube **B**
    -Move filter from tube **B** to tube **A**
    -Measure and record activity of wastewater
    -Dispose of wastewater
    -Rinse bottom of vial **B** and dispose of rinse water
    -Place filter back into tube **B**
-Centrifuge **B** at 5000 RCF for 40 seconds
-Place 200 uL DI SUGAR water on filter in tube **B**
-Move filter from tube **B** to tube **A**
-Measure and record activity of wastewater
-Dispose of wastewater
-Rinse bottom of vial **B** and dispose of rinse water
-Place filter back into tube **B**
-Measure and Record Activity of **B**
    -Record approximate activity per particle
-Agitate tube **B**
-Pipette contents of **B** into tube **C**
Perform 2 more times:
    -Add 200 uL Sugar DI water to **B**, shake.
    -Pipette contents of **B** into tube **C.**
-Measure and record activity of **C**
    -Record estimated number of particles in **C**
-Measure and record activity of **B**
    -Estimate Losses

-Place **C** in shielded cask, to be transported by Rad Safety

4) Clean up

NOTE: Clean up to be performed by personnel remaining at UT Medical Center after transport of Activity. All personnel must survey hands, coats, shoes, and any personal belongings that may have been contaminated before leaving.

-Change gloves
-Remove saran wrap and bench paper and place in trash bag
-Place Equipment on cart in hallway
-Survey Lab
    -Hood, bricks, counting well, countertop, hallway
    -Take swipes on countertop and equipment
-Place trashbag on cart
-Move cart to room at end of hallway
-Put radioactive materials label on cart
-Survey labcoats, shoes, hands, glasses, etc.
-Report any contamination to UTKMC personnel
-Return to UTK

C Experimental Procedure

The procedure used for packed bed flow experiments is documented here. As an example, the experimental procedure used for the 2 mm packed bed test of October 19, 2018 is included. In this experiment, flow of 110 mL/min. is delivered to the test section. This procedure includes descriptions of activities performed before, during, and after each experiment and uses the test section and flow loop described in Section 5.3. The full procedure follows.

Equipment

- Flow loop with instrumentation
- Test section
- Inveon (PET Scanner)
- Fluid barrier
- Tanks (header and injection)
- Cart
- Table
- Portable shielding
- Styrofoam and plastic blocks
- Pump body, head, controller
- Buckets
- Mop
- Gloves
- 1 extension cord
- DAQ computer
- Activated particles in microfuge tube
- Glycerin
- Geiger counter
- Paper Towels
- 2 gallons of DI Sugar Water
- Squirt Bottle of DI Sugar Water
- Thermometer
- Magnetic stirrer/hot plate
- Adjustable stand

Testing Procedure

Day Before

- Turn on the scanner and move bed to the bottom and fully out position
    - If scanner gets turned off, do not turn it back on without first removing the test section and bore protector from the scanner bore
    - The following loop cleaning procedure can be implemented couple of days before the experiment.
    - Loop Cleaning Procedure

        - Ensure tanks and tubing mostly dry
        - Assemble the flow loop: Use plugs in lieu of pressure transducer
        - Fill the tanks with DI water
        - Plug in the pump to the power strip
        - Turn on the pump and let the water fill test section and go through all the tubing
        - Leave the pump on for few minutes so the loop will be rinsed with DI water
        - Run the pump in reverse to remove most water from test section
        - Drain remainder of test section via drain plugs
        - Ensure the loop is dry

- Place the fluid barrier in scanner bore
- Ensure the test section is aligned at appropriate position in the scanner
- Assemble the loop with test section outside bore (bed out position. Vent (outlet) should be on bed side of scanner

- Ensure that the test section is straight, level, and centered with respect to the bore

- Ensure the tanks are elevated above the test section via plastic blocks
    - Place injection tank on magnetic stirrer
- Ensure that the pump and instrumentations are plugged into the two different power strips with an on/off switch that is beyond the shielding plates
    - On the first power strip plug the Pump
    - On the second power strip plug in the pressure transducers

- Ensure that vent is vertical; pressure taps are on workbench side.
- Leave test section outside bore
- Put shielding in place

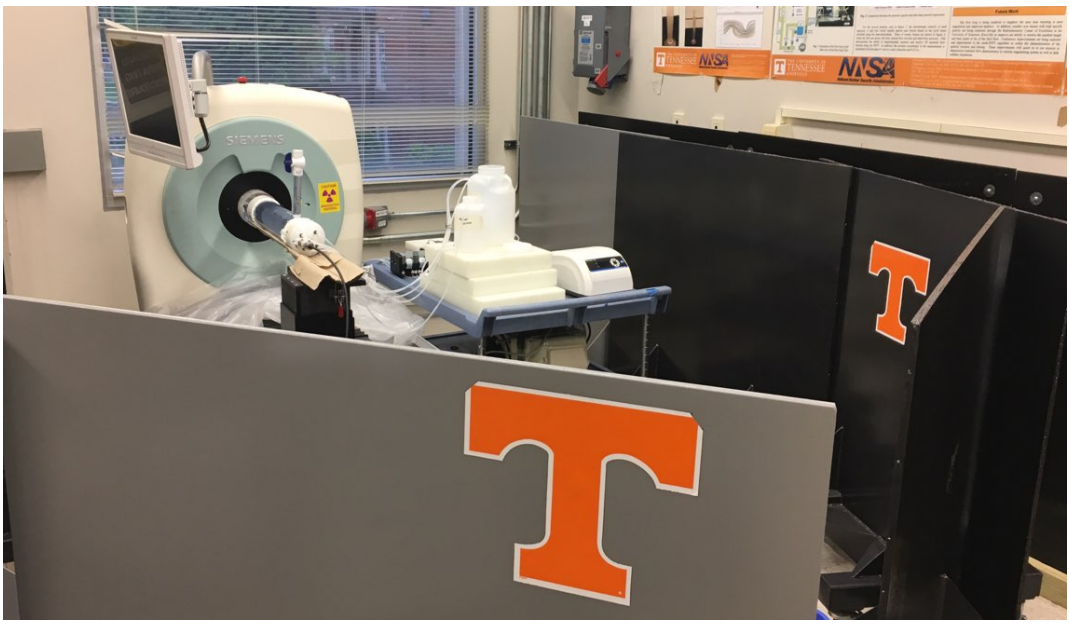

Activating the instrumentation

- Turn off pump and all the instrumentations
- Close and return the day of the test to ensure flow loop is not leaking and is still water solid

Day of the Test

Test Section Test

- Begin the following protocol approximately two hours before the particles arrive at the lab
- Check density and temperature of Sugar Water and record
- Leave until particles arrive

After Particles arrive:

- Fill the tanks (to top of tape)
    - ~1 gallon in header tank
    - ~32 oz in injection tank
- Ensure all lines are properly connected
- Turn on the pump, select the desired speed (~167 RPM), and press start.
- Allow test section to fill.
    - Start with return lines above tank water lines
    - When water gets above pressure lines, ensure they are water solid
        - ***May not be possible
- Close vent valve as water begins to fill vent line.
    - Tilt to ensure that bubbles are vented out.
- Ensure that there are no leaks and that the loop is water solid
    - If leak is observed, drain loop, and dry and caulk the area of the observed leak(s). Wait for caulk to set up (~20 min) before refilling tank.
- Fill injection tank so that its total volume is ~1 liter
- Make sure both tank levels are relatively high and return lines are below water line
- Actuate pump and vent valve to remove bubbles if needed
- Turn pump off
- Move bed of scanner into bore such that injection needle is aligned with beginning of FOV

Particle Dump

- Put on gloves
- Drop glycerin into microfuge tubes and shake
- Dump tracers into injection tank.
- Rinse the walls and with DI water if needed
- Agitate injection tank to suspend particles.
- Change gloves
- Turn on magnetic stirrer to lowest setting
- Survey area/equipment for contamination

- Data Acquisition

- Turn on the pump
- Start work flow on the Inveon and begin acquiring data
    - Make sure there is no histogramming in workflow

- Repeat the Data acquisition and previous step for following runs
    - Agitate both tanks between runs

Runs	Scan Time (min)	Total Flow Rate (mL/min)	Energy Window (keV)
1	30	110	425-625
2	30	110	425-625
3	30	110	425-625
4	30	110	425-625

- Once test is complete, shut off the pump and tanks
- Place any potentially contaminated materials on cart behind shielding and label
- Use bed motion controls to remove test section from bore
- Run pump in reverse to drain test section to ~1/2 full
- Return after 24-48 hours

Expected Radiation Activity (assuming 30 mCi initial activity)

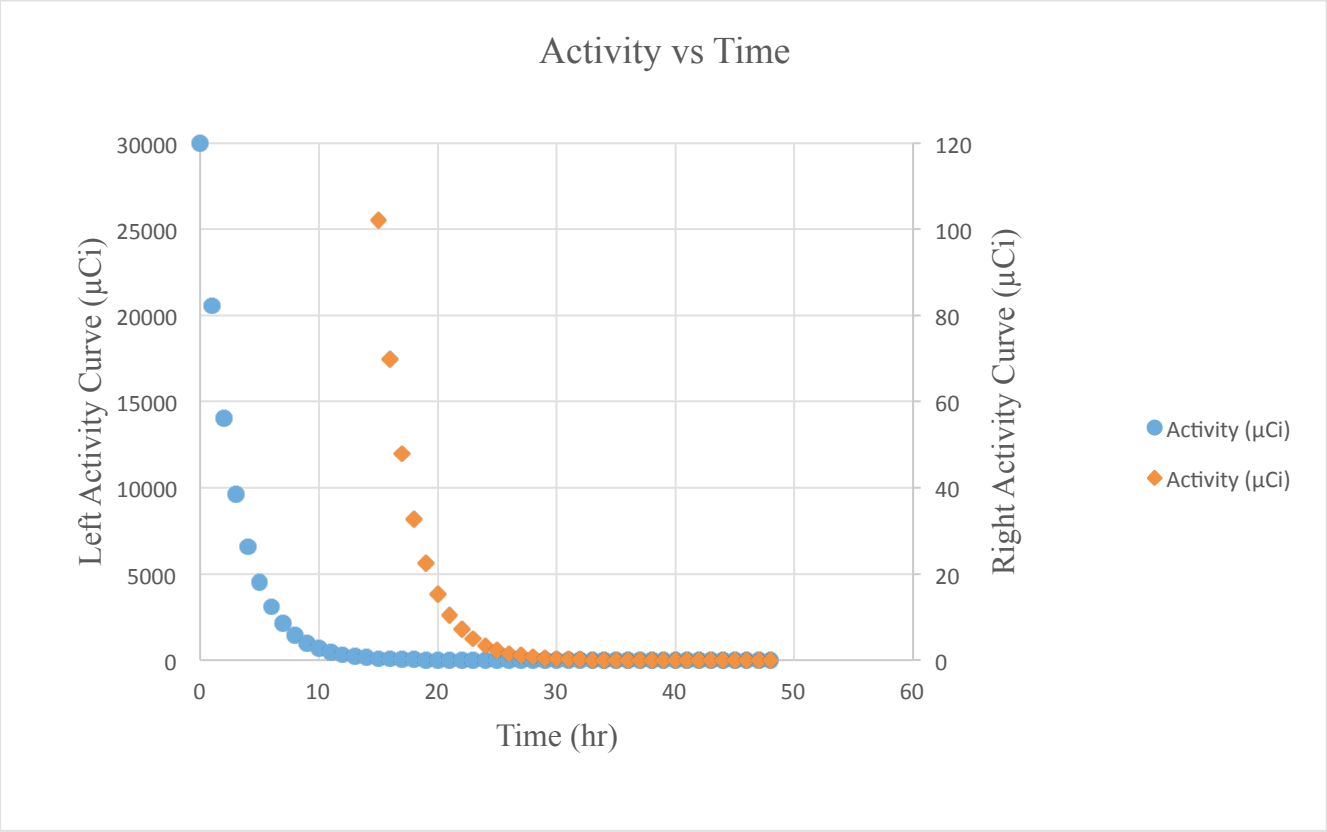

Day after the Test

Clean up

- Ensure return lines are not submerged in tanks
- Run pump in reverse to begin emptying test section. Monitor tank levels to ensure no spilling.
- After the test section is drained below inlets, place bucket under drain plug, remove drain plug, and drain
- Gently tilt the flow loop to get all the water out
- Once test section is empty, remove inlet lines and remove test section from FOV in such a manner as to reduce the risk of spilling water on the Inveon

Vita

Cody Wiggins is a native of Alcoa, Tennessee and the son of Donna and Kenny Wiggins. He attended Maryville Christian School, where he competed in baseball and a number of academic competitions until his graduation in 2010. In the Fall of 2010, Cody enrolled at the University of Tennessee, Knoxville in the Department of Nuclear Engineering.

Cody began research with Dr. Arthur Ruggles in November of 2012, studying the mixing of parallel jets impinging on an ambient body of water. He began his study of repurposing positron emission tomography equipment for flow interrogation under Dr. Ruggles, with the first versions of in-house PEPT reconstruction software appearing in the Spring of 2014. He graduated with a Bachelor of Science degree in Nuclear Engineering with minors in Mathematics and Physics in the Spring of 2014, and began graduate studies in Physics at the University of Tennessee the following Fall.

At the beginning of his graduate tenure, the first working versions of multiple-particle PEPT reconstruction software were designed, prompting Cody's decision to continue his pursuit of a Physics Ph.D. under Dr. Kate Jones while conducting research on PEPT development under Dr. Ruggles. The development and deployment of new methods for PEPT has remained the focus of Cody's research and are the primary topics of the preceding document. His work has been generously supported by a Nuclear Engineering University Program (NEUP) Integrated University Program (IUP) graduate fellowship. Cody will receive his Ph.D. in Physics during the Summer of 2019 and continue his PEPT research as a postdoctoral researcher in the Department of Mechanical and Nuclear Engineering at Virginia Commonwealth University.